Université de Montréal

Développement de nouveaux matériaux organométalliques pour des applications dans le domaine de la conversion d'énergie solaire

par
André Yvon-Bessette

Département de Chimie
Faculté des Arts et des Sciences

Mémoire présenté à la Faculté des Études Supérieures
en vue de l'obtention du grade de
Maîtrise ès sciences (M.Sc.) en chimie

Avril 2012

Université de Montréal
Faculté des études supérieures et postdoctorales

Ce mémoire intitulé :

Développement de nouveaux matériaux organométalliques pour des applications dans le domaine de la conversion d'énergie solaire

Présenté par :
André Yvon-Bessette

a été évalué par un jury composé des personnes suivantes :

Pr André Beauchamp, président-rapporteur
Pr Garry S. Hanan, directeur de recherche
Pr Frank Schaper, membre du jury

Résumé

Dans un contexte où l'approvisionnement énergétique mondial du 21^{e} siècle est un enjeu majeur, le développement de sources d'énergie renouvelables suscite l'attention croissante de la communauté scientifique et industrielle. L'énergie solaire est définitivement l'une des meilleures alternatives aux combustibles fossiles en tant que source d'énergie du monde de demain. Ce mémoire traite donc du développement de nouveaux matériaux organométalliques pour des applications de photorécoltage d'énergie en photovoltaïque et en production d'hydrogène. Le premier chapitre présente la synthèse assistée par microondes de quatre nouveaux complexes de Co(II), Ni(II), Cu(II) et Zn(II) basés sur le ligand tétra-*p*-méthoxyphényl-azadipyrrométhène (ADPM) avec des rendements variant de 89% à quantitatif. Ces complexes sont mis en relation avec d'autres complexes homoleptiques connus portant le tétraphényl-ADPM comme ligand ainsi qu'avec leurs chélates de BF_2^+ pour une meilleure compréhension des tendances engendrées par la substitution de l'agent coordonnant et/ou des substituants *p*-méthoxy. Pour ce faire, le comportement électrochimique et photophysique est présenté. De façon générale, la présence des quatre groupements *p*-méthoxy semble rendre les dérivés de cet ADPM plus susceptibles à la dégradation électrochimique en conditions d'oxydation et induire un déplacement bathochromique des propriétés optiques d'absorption et d'émission. Les structures rayons X du ligand tétra-*p*-méthoxyphényl-ADPM et de son complexe homoleptique de Co(II) sont aussi discutées. Cette étude a été effectuée dans l'espoir de fournir des informations utiles sur la stabilité des ADPM aux chercheurs du domaine photovoltaïque en quête de nouveaux chromophores dans le proche infrarouge (NIR). Le deuxième chapitre présente quant à lui les propriétés de senseur envers les anions F^-, OAc^- et $H_2PO_4^-$ de deux nouveaux complexes neutres de Re(I) de type mono- et dinucléaire basés sur une phénanthroline substituée en position 5 contenant un récepteur thio-urée. Ces composés ont été obtenus dans des rendements de 81% et 60%, respectivement. L'effet de la formation de ponts hydrogène lors de l'ajout d'anions versus la déprotonation du récepteur a été évalué par des titrations UV/Vis et RMN ^{1}H et semble indiquer que la

formation de la base conjuguée du récepteur est favorisée pour ce type de système. De plus, la structure rayons X d'un des précurseurs est présentée et permet une discussion sur la chiralité des complexes mono- et dinucléaire obtenus. L'obtention d'un complexe bimétallique par autoassemblage ouvre la voie à la préparation d'antennes moléculaires pour des systèmes de photosynthèse artificielle.

Mots-clés : Conversion d'énergie solaire, Photovoltaïque, Production d'hydrogène, Chimie de coordination, Azadipyrrométhène, Complexes homoleptiques, Cobalt, Nickel, Cuivre, Zinc, Complexes neutres de Re(I), Détection d'anions, Électrochimie, Photophysique, Structures rayons X.

Abstract

The world's energy supply is rapidly becoming the major issue of the 21st century. Instead of the *status quo* approach of finding and extracting more hydrocarbons from the ground, the development of renewable energy sources is attracting much interest from both the scientific and industrial communities. Solar energy is definitively one of the best sources to power the World of tomorrow. In such a framework, this dissertation discusses the development of new organometallic materials able to harvest solar energy for photovoltaic or H_2 photoproduction applications. The first chapter presents the synthesis by a microwaves-assisted methodology of four new homoleptic complexes of Co(II), Ni(II), Cu(II) and Zn(II) based on the tetra-*p*-methoxyphenyl-azadipyrromethene (ADPM) ligand in yields ranging from 89% to quantitative. Those complexes are put in relation with already known ADPM homoleptic complexes of the same M(II) series and related BF_2^+ chelates (Aza-BODIPY) for a better understanding of trends arising from substitution of the chelate and/or electron-donating effect of the *p*-methoxy substituents. This is achieved by the study of electrochemical behavior of the compounds and their photophysical properties. From a general point of view, the presence of the four *p*-methoxy substituents leads to an electrochemical decomposition of the derivatives based on that ADPM in oxidative conditions, along with a bathochromic shift of the optical properties. X-Ray structures for the tetra-*p*-methoxyphenyl-ADPM ligand and related Co(II) complex are also discussed. Hopefully, this study will provide useful insights to researchers on the substituents to install for stable ADPM derivatives in their quest for NIR chromophores utilizable for photovoltaic application. The second chapter report anion sensing properties toward F^-, OAc^- and $H_2PO_4^-$ of new neutral mononuclear and dinuclear Re(I) complexes based on a 5-substituted phenanthroline moiety bearing a thiourea hydrogen-bonding receptor. Those complexes were obtained in 81% and 60% yields, respectively. The effect of hydrogen-bonding versus deprotonation of the thiourea receptor upon addition of the anions was also evaluated by UV/vis and ^1H NMR titration techniques. Observations made support the hypothesis that formation of the conjugated base of the receptor is favored. In addition, an

X-ray structure of the Re(I) precursor complex is reported and the chirality of the mononuclear and dinuclear complexes is discussed. Achievement of a bimetallic complex by self-assembly paves the way for the preparation of light-harvesting molecular antennae utilizable in artificial photosynthesis systems.

Keywords : Solar energy conversion, Photovoltaic, Hydrogen production, Coordination chemistry, Azadipyrromethene, Homoleptic complexes, Cobalt, Nickel, Copper, Zinc, Neutral Re(I) complexes, Anion sensing, Electrochemistry, Photophysic, X-Ray structures.

Table des matières

Liste des tableaux

Liste des figures

Liste des abréviations

A	Accepteur
Abs	Absorbance
ADPM	Azadipyrrométhène
Aza-BODIPY	Chélate BF_2^+ d'un azadipyrrométhène
BHJSC	Bulk-heterojunctions Solar Cells
BODIPY	Chélate BF_2^+ d'un dipyrrométhène
br	Broad
calcd	Calculated
C_{XX}	Dérivé fullerène contenant XX carbones
CV	Voltammétrie cyclique
Δ	Chaleur
δ	Déplacement chimique
d	Doublet
d	Orbitales *d*
D	Donneur
D-A	Donneur-Accepteur
DCM	Dichlorométhane
DFT	Density-Functional Theory
DPM	Dipyrrométhène
DPV	Differential pulse voltammetry
DSSC	Dye-Sensitized Solar Cells
E	Energie
e^-	électron

E_d	Différence d'énergie entre les LUMO du D et de l'A
E_g	Séparation de bande (Band-Gap Energy)
eq	Équivalents
ESI	Electronic supporting informations
ETA	Extremely Thin Absorber
eT	Energy transfer
fac	Facial
FF	Fill Factor
GmbH	Société à responsabilité limitée allemande
h+	Trou positif
HOMO	Highest Occupied Molecular Orbital
HR-ESIMS	High-Resolution Electro Spray Ionization Mass Spectrometry
HRMS	High-Resolution Mass Spectrometry
hν	Irradiation lumineuse
IR	Infrarouge
ITO	Indium Tin Oxyde
J	Constante de couplage
J_{sc}	Densité de courant du petit circuit (Short-circuit current density)
J_{mp}	Courant de la cellule solaire
J_L	Courant généré par la lumière
J-V	Courbe courant-voltage
λ_{ab}	Longueur d'onde de l'absorption
λ_{max}	Longueur d'onde de l'absorption maximale
L	Ligands
LC	Chromatographie liquide (Liquid chromatography)

L_D	Distance de diffusion de l'exciton
LX	Ligand bidentate de type neutre (L) et anionique (X)
LUMO	Lowest Unoccupied Molecular Orbital
M	Métal
MSD	Détecteur par spectroscopie de masse (Mass spectroscopy detector)
m/z	Masse sur charge
n	Semi-conducteur de type négatif
n	Normal / linéaire
η	Efficacité de conversion solaire (power-conversion efficiency)
NA	Non disponible (Non-available)
NIR	Proche infrarouge (Near-Infrared)
NMR	Résonance magnétique nucléaire
OAc	Acétate
OPV	Organic Photovoltaic Devices
OMP	Organometallic Polymers
Ox	Oxydation
p	Semi-conducteur de type positif
p	para-
PCBM	[6,6]-phenyl-C61-butyric acid methyl ester
PCE	Power Conversion Efficiency
PDI	Perylenediimide
PEDOT:PSS	Poly(3,4-ethylene-dioxythiophene):poly(styrenesulfonate)
PHJSC	Planar-Heterojunctions Solar Cells
P_{in}	Puissance à l'entrée
P_{out}	Puissance à la sortie

ppm	Parties par million
PSII	Photosystème II
q	Quadruplet
Red	Réduction
RMN	Résonance magnétique nucléaire
rpm	Révolutions par minute
r.t.	Température ambiante (Room temperature)
s	Singulet ou seconde
SCE	Électrode au calomel saturée de KCl
t	Triplet
TBAP	Tetrabutylammonium hexafluorophosphate
THF	Tétrahydrofurane
TOF	Temps de vol (Time of flight)
TW	Térawatt
UV	Ultraviolet
vis	Visible
V_B	Gain en voltage généré à l'intérieur de la cellule solaire
V_{OC}	Voltage du circuit ouvert (Open-circuit voltage)
V_{MP}	Voltage de la cellule solaire
$V_{built\text{-}in}$	Built-in Potential

Au Pr Serge Lacelle, qui a su m'inspirer par
son amour des Sciences et de la Nature

« C'est le rôle essentiel du professeur
d'éveiller la joie de travailler et de connaître. »
- Albert Einstein (1879-1955)

« L'imagination est plus importante que le savoir. »

- Albert Einstein

Remerciements

Tout d'abord, je souhaite remercier les organismes subventionnaires suivants d'avoir rendu possible la réalisation de mes travaux de M.Sc. industrielle avec la compagnie Saint-Jean Photochimie Inc. (SJPC) dans le cadre d'une bourse BMP-Innovation:

- Fonds québécois de la recherche sur la nature et les technologies (FQRNT)
- Conseil de recherches en sciences naturelles et génie (CRSNG)
- Université de Montréal (Bourse FESP – Chimie)

Mes remerciements vont aussi au Pr Garry S. Hanan pour m'avoir accueilli dans son groupe de recherche et avoir cru dès le début de cette aventure à la possibilité d'une collaboration fructueuse avec un partenaire industriel comme SJPC. Sans son appui et sa grande flexibilité, il apparaît clair à mes yeux que d'intéressantes découvertes scientifiques ainsi qu'un encadrement hors du commun et enrichissant n'auraient pu s'offrir à moi.

Je souhaite également remercier toute l'équipe de R&D chez SJPC de m'avoir supporté et conseillé dans les diverses phases de recherche de ma M.Sc. Plus particulièrement, je souhaite exprimer toute ma gratitude à mon directeur de recherche, le Dr Denis Désilets, pour la confiance indéfectible dont il a fait preuve à mon égard ainsi que son support constant face aux différents obstacles qui se sont présentés en cours de route. Aussi, je ne saurais être plus redevable à Francis Bélanger pour sa supervision passionnée, son soutient et ses enseignements quotidiens des multiples aspects du chimiste de synthèse. Je me dois également de faire une mention toute spéciale à trois collègues et amis qui m'ont

aidé d'une multitude de façons au fil des jours : Sylvain Boucher, Ian Marcotte et Khalil Feghali. Merci à vous tous pour la belle atmosphère de camaraderie qui fait de SJPC un endroit si extraordinaire à œuvrer!

Je voudrais aussi souligner l'aide précieuse des membres du groupe Hanan que j'ai eu la chance de côtoyer et qui m'ont aidés dans mon exploration de la recherche académique. Plus particulièrement : le Dr Samik Nag, la Dr Marie-Pierre Santoni, Daniel Chartrand, Mihaela Cibian, Amlan K. Pal, la Dr Janaina G. Ferrera et Ludwig Chenneberg. De plus, j'ai eu le plaisir de superviser Andrew O'Connor lors de la session d'hiver 2012. Sa rencontre fût un réel plaisir et un enrichissement personnel à plusieurs égards.

L'aide de Marie-Christine Tang, Karine Venne et Alexandra Furtos du service de spectroscopie de masse ainsi que de Cédric Malveau, Antoine Hamel et Geneviève Beaudry-Dubois de celui de RMN a aussi été vivement appréciée.

À titre plus personnel, je tiens à remercier du fond de mon cœur mon père, Gilles Bessette, pour tous les efforts et sacrifices qu'il a fait pour me permettre d'être la personne épanouie que je suis aujourd'hui. Merci Pa! Je tiens aussi à remercier deux personnes toutes spéciales qui ont partagées ma vie au cours de mes travaux de M.Sc. Merci à Vanessa Dagenais pour avoir été là dans les moments éprouvants et les incertitudes du début. Un immense merci à Anne-Catherine Bédard qui partage aujourd'hui mes plus grandes aspirations et qui me donne foi à un avenir emplie de bonheur. Je t'aime ma Chérie!

Introduction

I.1 – Mise en contexte

Dans un contexte économique où l'approvisionnement énergétique mondial du 21e siècle est un enjeu majeur, le développement de sources d'énergie renouvelables suscite l'attention croissante de la communauté scientifique et industrielle. À cet égard, Jacobson et Delucchi publiaient en 2009 dans la revue *Scientific American* le premier plan pour fournir, d'ici 20 ans, 100% de l'énergie consommée sur Terre provenant de sources renouvelables.[1] Dans ce plan audacieux, ils calculaient qu'environ 30% des 11.5 térawatts (TW) de l'énergie mondiale consommée à chaque instant devrait être le fruit de l'énergie solaire. De façon similaire, Grätzel mentionnait déjà en 2001 dans la revue *Nature* que recouvrir 0.1% de la surface terrestre avec des cellules solaires ayant 10% d'efficacité de conversion devrait satisfaire la demande énergétique mondiale de l'époque.[2] Plus récemment, Armaroli et Balzani discutaient dans un article de revue de la littérature l'idée d'un monde propulsé à l'électricité comme l'un des défis majeurs du 21e siècle,[3] alors qu'un éditorial dans *Nature Materials* pointait une voie à suivre pour que les énergies solaires deviennent compétitives face à leurs rivales fossiles.[4] Signe concret qu'il s'agit bel et bien d'un enjeu stratégique marqué, le *US Department of Energy* a fondé en 2010 le programme *SunShot*, doté d'un budget annuel de près de 300 millions de dollars US pour permettre l'abaissement du coût des énergies solaires en deçà des 6 cents par kilowatt-heure (kWh) d'ici 2020.[5]

Dans les faits, l'étude de systèmes pour la conversion de l'énergie solaire se fait principalement selon deux grands axes, soit en énergie électrique (effet photovoltaïque) ou bien en énergie chimique (*i.e.* la photoproduction d'hydrogène moléculaire). Dans le cadre de ce mémoire, le développement de nouvelles molécules organométalliques pour des applications dans ces deux domaines de la photoconversion d'énergie solaire sera discuté.

Dans le premier chapitre, l'utilisation comme ligand bidenté de type LX de la famille de chromophore des azadipyrrométhènes (ADPM) sera présentée dans le contexte de leur complexation homoleptique sur les métaux de transition Co(II), Ni(II), Cu(II) et Zn(II). Ces complexes présentant un vif potentiel pour des applications dans le domaine du photovoltaïque organique (*Organic Photovoltaic*; OPV),[6] leurs niveaux énergétiques révélés par électrochimie ainsi que leurs propriétés photophysiques seront au cœur de la discussion soumise pour publication dans le périodique *Inorganic Chemistry*.

Le deuxième chapitre portera sur la préparation de complexes neutres de Re(I) basés sur un noyau phénanthroline substitué en position 5 pour permettre leur autoassemblage via la formation de liens thio-urées. La présence de ce type de lien permettant *a priori* leur utilisation en tant que senseurs d'anions via la formation de ponts hydrogène, l'étude de cette application est centrale à la discussion qui a été acceptée pour publication dans le périodique *Supramolecular Chemistry*. Cependant, la formation de liens thio-urées ayant permis l'édification de façon contrôlée d'un complexe bimétallique, cette voie synthétique apparaît toute désignée pour la formation d'antennes moléculaires visant l'absorption de l'énergie solaire à l'intérieur de systèmes pour la photosynthèse artificielle.

La suite de l'introduction comportera quant à elle deux sections distinctes présentant un survol de chacune des deux applications de la photoconversion d'énergie étudiées dans ce mémoire. Cela a pour objectif premier de familiariser le lecteur face à leur principe de fonctionnement général ainsi qu'à les sensibiliser dans un deuxième temps aux exigences particulières de chacune des applications. Ces deux sections suivront l'ordre dans lequel les chapitres sont présentés.

I.2 – Le domaine du photovoltaïque organique (OPV)

I.2.1 – Contexte général

Les cellules photovoltaïques sont le fruit de l'application du concept plus général de l'effet photovoltaïque observé pour la première fois en 1839 par le physicien français Alexandre-Edmond Becquerel.[7] Cet effet est intimement lié à celui photoélectrique découvert en 1887 par le physicien allemand Heinrich Rudolf Hertz et qui consiste en l'émission d'électrons par un matériau lorsqu'il est exposé à la lumière ou à un rayonnement électromagnétique de fréquence suffisamment élevée.[8] L'expérience type de cet effet consiste à éclairer une plaque métallique qui émet des électrons en retour. Il fut expliqué pour la première fois en 1905 par le physicien allemand Albert Einstein, qui utilisa pour ce faire les concepts de photons et de quantum d'énergie. Cette découverte lui valut d'ailleurs le prix Nobel de physique en 1921.[9]

Dans le cas des cellules photovoltaïques, le fonctionnement est basé sur les semi-conducteurs, qui ont la capacité de générer un trou positif dans la couche de valence du matériau lorsqu'un électron est photo-excité vers la couche de conduction.[10] Les dispositifs solaires de premières générations basés sur des jonctions dans l'état solide (*solid-state junction*), souvent faient de Si, présentent des rendements de conversion solaire intéressants. En effet, les plus récents dispositifs à base de Si cristallin oscillent autour de 25% de conversion, alors que ceux à base de couche mince de GaAs atteignent 28%.[11] Cependant, ces cellules sont chères à produire et nécessitent beaucoup d'énergie lors de

leur fabrication. De plus, la rigidité des panneaux solaires produits les limite à des applications spécifiques.[2]

Heureusement, le domaine du photovoltaïque évolue rapidement et une riche variété de technologies compétitionnent actuellement pour émerger. Pour ne nommer que les principales nouvelles générations de cellules, mentionnons : les cellules photoélectrochimiques basées sur des jonctions nanocristallines ou des réseaux interpénétrants (interpenetrating networks); les cellules tandems pour le clivage d'eau par la lumière visible; les cellules hétérojonctions solides sensibilisées par des colorants et celles de type absorbant extrêmement mince (ETA); les jonctions molles ainsi que les cellules solaires organiques. En bref, ce domaine est passablement actif et certaines de ces cellules se retrouvent déjà à l'échelle commerciale.

En 2009, Brabec a étudié les aspects économiques entourant l'OPV dans le cadre d'une revue de la littérature.[12] Il concluait qu'une technologie à faible coût de production comme l'OPV serait compétitive avec les autres sources d'énergie lorsqu'une efficacité de conversion de 7% et une durée de vie du module de 7 ans seraient atteintes. Les dispositifs à la fine pointe de l'art atteignent actuellement 9.1% pour les cellules solaires organiques basées sur des hétérojonctions (*bulk-heterojunction solar cells*; BHJSC) de type polymère/fullerène dans une architecture inverse tel que rapporté par la compagnie américaine Polyera[13] et de 9.8% pour des cellules d'architecture tandem basées sur des oligomères déposés en phase vapeur qui sont fabriquées par l'Allemande Heliatek GmbH.[14] De son côté, le nobélisé Alan J. Heeger et ses collaborateurs ont récemment rapporté dans

Nature Materials des BHJSC basées sur des oligomères déposés en solution atteignant 6.7% d'efficacité.[15] D'aussi hautes efficacités de conversion sont très prometteuses pour le domaine de l'OPV dans la mesure où il possède de surcroit trois avantages marqués sur les technologies compétitrices :

1. Flexibilité de la cellule permettant de l'enduire virtuellement n'importe où en tant que couche mince.
2. Faible poids du module.
3. Faible coût de production.

Plusieurs familles de molécules sont présentement utilisées à l'échelle industrielle en OPV, notamment les dérivés de thiophène et de carbazole.[12] Cependant, la quête de nouvelles familles de molécules est incessante dans l'objectif de résoudre les quelques limitations qui restreignent encore l'obtention de bonnes efficacités de conversion dans les modules plastiques de grande surface, tel que discuté récemment par Leclerc *et coll.*[16] Une bonne source d'inspiration pour la conversion d'énergie solaire demeure définitivement la Nature, avec sa magnifique machine photosynthétique qui révèle encore à la communauté scientifique de nouveaux secrets sur son fonctionnement.[17] Les porphyrines sont des chromophores essentiels dans le photorécoltage des photosystèmes naturels, s'avérant de ce fait des candidats intéressants pour l'OPV.[18-21] En fait, les porphyrines recommencent à attirer l'attention des chercheurs aujourd'hui, mais ce regain se produit plusieurs années après le tout premier exemple de cellule solaire organique rapportée en 1975 par Tang et Albrecht.[22] Ce premier dispositif était constitué de chlorophylle-a en tant que couche

photoactive prise en sandwich entre deux électrodes et avait mené à une efficacité de conversion d'environ 0.001%.

En raison de leur structure représentant des demi-porphyrinoides, les dipyrrométhènes (DPM) et les azadipyrrométhènes (ADPM) représentent aussi des candidats intéressants pour l'OPV. Dans les faits, leurs propriétés photophysiques sont similaires aux porphyrinoides, en plus de présenter plusieurs avantages synthétiques. Premièrement, ils évitent l'étape à faible rendement de macrocyclisation des porphyrines et sa difficile purification, ce qui est un point important à considérer du point de vue commercial. Deuxièmement, les DPM et ADPM offrent plusieurs leviers synthétiques permettant l'ajustement des propriétés photophysiques par la variation des substituants. Troisièmement, ils présentent une plus grande versatilité face à la géométrie de coordination des métaux de transition grâce à leur motif bidenté, comparativement à celle plan carré forcée par les porphyrinoids tétradentés. Pour toutes ces raisons et aussi parce que les ADPM ont tendance à absorber plus loin dans le proche infrarouge (near-IR, NIR) que les DPM, notre choix s'est arrêté sur les dérivés azadipyrrométhènes dans le contexte de complexes homoleptiques pour des applications potentielles en OPV, tel qu'il sera discuté dans le chapitre 1.

I.2.2 – Principe de fonctionnement des cellules en OPV

Le schéma général d'une cellule solaire hétérojonction (Figure I.1) consiste en deux semi-conducteurs, l'un de type n et l'autre de type p, qui sont déposés soit en couches planes ou bien sous forme BHJSC entre une cathode d'aluminium et une anode transparente d'oxyde d'indium-étain (ITO). De plus, une couche de PEDOT:PSS est intercalée entre l'anode et la couche d'hétérojonctions pour augmenter la qualité de la surface de contact et des transferts de charge qui se déroulent à cette interface. Le matériau de type n est généralement constitué de dérivés de fullerène, comme le PCBM ou le $PC_{71}BM$ (Figure I.2), car ces derniers offrent une LUMO base en énergie qui agit comme un accepteur (A) d'électron (e^-) et transporte la charge négative vers la cathode. La couche photoactive de type p est celle qui agit comme électron donneur (D), et donc comme un transporteur de trous positifs (h^+). Cette couche peut être basée sur de petites molécules (ou des oligomères) dans le cas des hétérojonctions planes ou bien sur des polymères formant des nanodomaines avec les dérivés de fullerène dans le cas des BHJSC.

Figure I.1 – Représentation schématique d'une cellule solaire organique (gauche) et plus spécifiquement de type hétérojonction plane (haut) et BHJSC (bas).

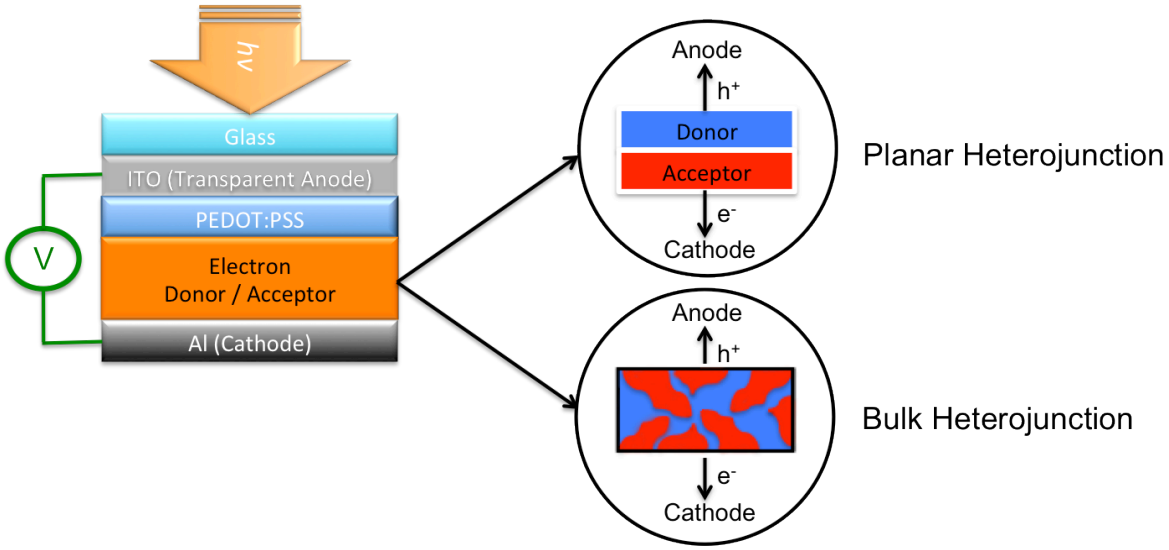

Figure I.2 – Structure chimique du PCBM et du $PC_{71}BM$.

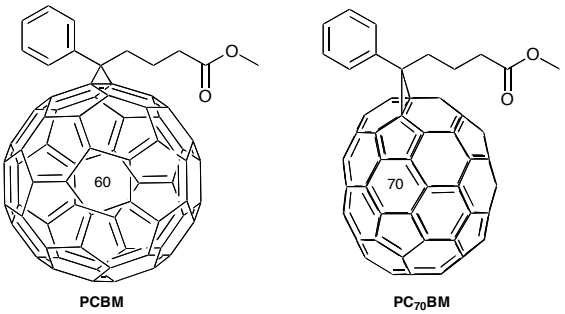

Tel qu'expliqué par Hsu *et coll.*, le mécanisme de fonctionnement des cellules solaires de type D-A hétérojonctions survient en quatre temps.[23] Premièrement, il y a une photoexcitation dans le matériel donneur qui mène à la création d'une paire électron-trou, appelé un exciton. Dans un deuxième temps, l'exciton diffuse vers l'interface de l'hétérojonction D-A. Si la distance à parcourir est supérieure à la distance de diffusion maximale (max L_D), il y aura une recombinaison de la paire électron-trou anéantissant tout autre processus. La troisième étape du mécanisme consiste en la dissociation de l'exciton à l'interface D-A. En fait, cette étape est le passage de l'électron de la LUMO du D vers celle de l'A. De son côté, le trou réintègre la HOMO du donneur. Finalement, la quatrième étape consiste au transport des charges générées à l'étape précédente vers leur électrode respective. Dans l'ensemble, ce mécanisme mène à la génération par la lumière d'un courant électrique pouvant être converti en travail utile.

Pour s'assurer d'une bonne compréhension des différents paramètres intercorrélés affectant les performances photovoltaïques, la Figure I.3 présente les énergies relatives des orbitales HOMO et LUMO pour le donneur et l'accepteur ainsi que les principaux défis de chacun pour l'amélioration du rendement de conversion solaire. La séparation de bande (band-gap; E_g) correspond à la l'énergie requise pour exciter un électron de la HOMO vers la LUMO du donneur. Évidemment, cette énergie (E) est fournie par la lumière (*hv*) dans le cas d'une application photovoltaïque. Le gain en voltage généré à l'intérieur de la cellule (V_B) est linéairement dépendant du voltage du circuit ouvert (open-circuit voltage; V_{OC}). Finalement, la différence d'énergie entre les LUMO du D et de l'A (E_d) est la force motrice pour le transfert d'électron. Elle doit être d'environ 0.3-0.4 eV pour assurer une bonne

dissociation de l'exciton en une paire de charges à l'interface D-A.[24] La Figure I.3 présente aussi un relai électronique (Relay), un additif récent dans les dispositifs de type BHJSC qui consiste en un colorant agissant comme photosensibilisateur.[25] Cet additif tend à augmenter à la fois le rendement de conversion énergétique de la cellule solaire et la panchromaticité de l'absorption solaire vers la région du NIR. Ce point est particulièrement important dans la mesure où environ 50% de l'intensité de la radiation du Soleil atteignant la surface terrestre se situe entre 700 et 2000 nm et que le cœur du flux solaire est entre 600 et 800 nm (Figure I.4).[26,27]

Figure I.3 – Principes de l'OPV et défis pour les nouvelles générations de matériaux.

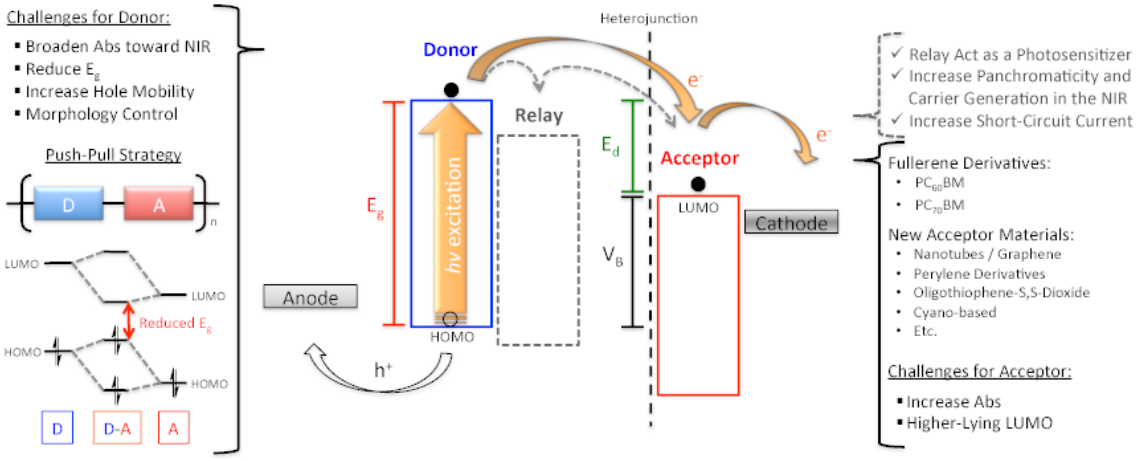

Figure I.4 – Spectre de la radiation solaire. [28]

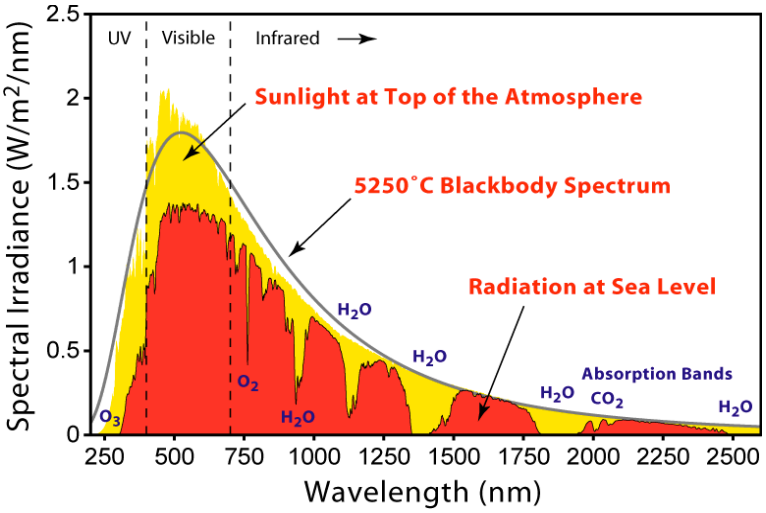

Pour déterminer l'efficacité de conversion du pouvoir (power-conversion efficiency; η) de la cellule solaire, les courbes de Courant-Voltage (J-V) dans le noir et sous illumination solaire sont utilisées comme méthode de caractérisation directe. Tel que présenté récemment par Mishra et Bäuerle dans une revue de la littérature,[27,29] les paramètres essentiels déterminant la performance de la cellule solaire sont représentés dans la figure I.5 (J_{SC} = short-circuit current density; FF = fill factor; V_{mp} et J_{mp} sont le voltage et le courant, respectivement, auquel le pouvoir à la sortie du dispositif atteint son maximum; J_L est le courant généré par la lumière). Ainsi, l'équation de η est définie comme le ratio du pouvoir maximum à la sortie (P_{out}) sur celui à l'entrée (P_{in}).

Figure I.5 – Courbes de Courant-Voltage (J-V) caractérisant les cellules solaires. [27]

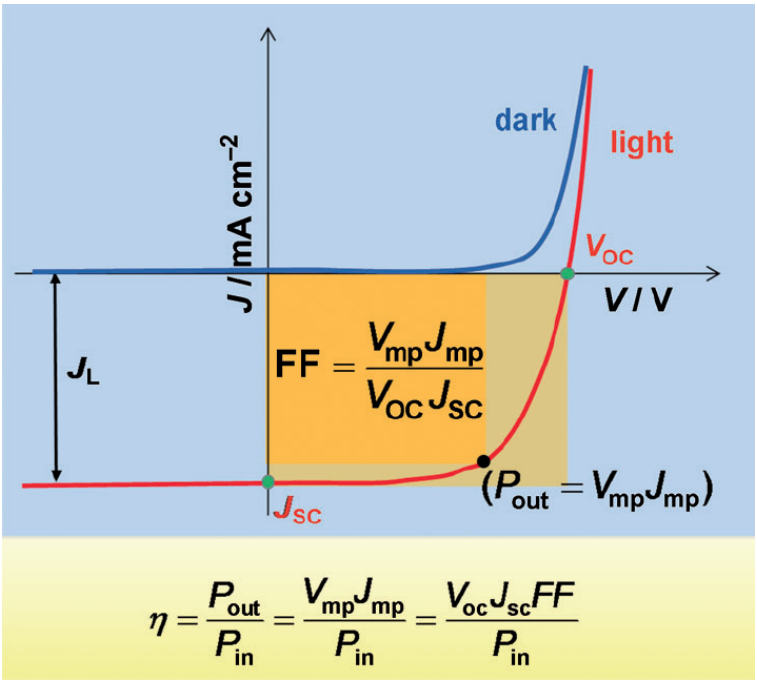

I.3 – Le domaine de la photosynthèse artificielle

Tel que mentionné à la section I.2, la Nature possède une mécanique magnifique pour faire la photosynthèse qui inspire de nombreux chercheurs. Sa capacité à utiliser l'énergie solaire pour entreposer annuellement environ 100 TW sous forme de biomasse est certes impressionnante, mais ne peut malheureusement pas être répliquée de façon identique par l'Homme.[30] Qu'à cela ne tienne, son étude a permis de déterminer que la photosynthèse naturelle implique deux grands processus distincts, l'un permettant la réduction du CO_2 pour former des carbohydrates et l'autre procédant au craquage de H_2O en H_2 et O_2 (*water splitting*). Ce dernier processus est multiélectronique et survient dans le photosystème II (PSII). Le PSII possède un centre de réaction métallique à base de Mn_4CaO_4 entouré d'antennes moléculaires pour collecter l'énergie lumineuse avant de la lui transférer.[31] Les antennes sont notamment composées de chlorophylles ainsi que de dérivés de porphyrines. Fait à mentionner, toute cette architecture moléculaire complexe se met en place de façon autoassemblée. Les interactions faibles telles celles des ponts hydrogène, dipôle-dipôle et électrostatiques y jouent toutes un rôle majeur en assurant la cohésion du système et des transferts électroniques / énergétiques qui se produisent entre les sous-unités.

Des systèmes hétérogènes et homogènes de photosynthèse artificielle pour la production d'hydrogène moléculaire sont au cœur de la recherche actuelle dans ce domaine.[32] En effet, le stockage de l'énergie solaire sous la forme de molécules de H_2 hautement énergétiques et dont la combustion redonne comme sous-produit de l'eau

s'avère être l'une des meilleures options disponible pour contrer les gaz à effet de serre engendrés par les combustibles fossiles tout en assurant un approvisionnement énergétique renouvelable.

Plusieurs défis guettent toutefois les scientifiques en ce qui a trait au développement de systèmes biomimétiques efficaces. Premièrement, les processus multiélectroniques lors du clivage de l'eau pour former O_2 (4 électrons nécessaires) et H_2 (2 électrons) nécessitent une accumulation de charge près du catalyseur redox qui est difficilement réalisable. Deuxièmement, la capacité à collecter de façon efficace l'énergie lumineuse par les antennes moléculaires et la transmettre de façon vectorielle vers le catalyseur redox est une étape clé qui se doit d'être maîtrisée. En effet, les antennes moléculaires requièrent l'assemblage contrôlé de plusieurs unités chromophoriques offrant une absorption complémentaire de la bande spectrale solaire et ce, avec une efficacité quantique maximale.[33,34] La raison réside dans la faible efficacité des processus de transferts énergétiques qui se trouve en compétition constante avec les recombinaisons de charges dissipant dans le système l'énergie recueillie sous forme de chaleur. Troisièmement, la transformation de cette énergie collectée pour former les molécules énergétiques par le catalyseur redox demande un choix judicieux du centre de réaction.[35-38] Ce dernier devra comporter deux catalyseurs redox adaptés, l'un pour chacune des demi-réactions de décomposition de l'eau en ses éléments constitutifs. La Figure I.6 présente une structure schématique d'un système artificiel photorécolteur d'énergie inspiré par la Nature pour permettre le clivage de l'eau ainsi que les principaux défis qui y sont associés.[32]

Figure I.6 – Structure schématique d'un système artificiel photorécolteur d'énergie pour le clivage d'eau comportant une antenne moléculaire.[32]

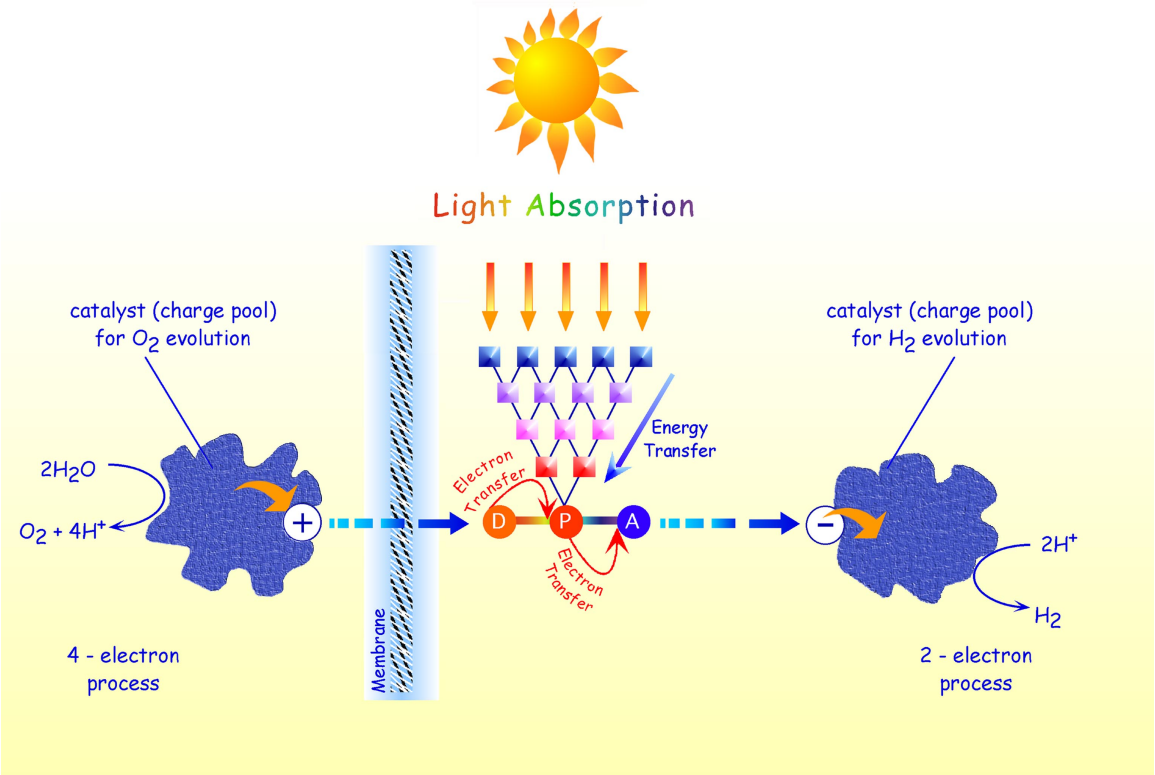

I.4 – Bibliographie de l'introduction

(1) Jacobson, M. Z.; Delucchi, M. A. *Scientific American* **2009**, *301*, 58.

(2) Gratzel, M. *Nat.* **2001**, *414*, 338.

(3) Armaroli, N.; Balzani, V. *Energy Environ. Sci.* **2011**, *4*, 3193.

(4) *Nat. Mater.* **2012**, *11*, 173.

(5) *Nat. Mater.* **2012**, *11*, 178.

(6) Il est à noter que l'appellation du domaine "photovoltaïque organique" doit être ici prise au sens large et qu'elle peut inclure la présence de complexes organométalliques dans la fabrication des cellules solaires en découlant. En effet, cette appellation commune dans le milieu scientifique est historiquement basée sur son opposition à la photovoltaïque à base de semi-conducteurs inorganiques, par exemple les cellules solaires faites de silicium cristallin.

(7) Becquerel, A. E. *C. R. Acad. Sci.* **1839**, *9*, 561.

(8) Hertz, H. R. *Ann. Phys. (Berlin)* **1887**, *33*, 983.

(9) *"The Nobel Prize in Physics 1921"* Nobelprize.org, http://www.nobelprize.org/nobel_prizes/physics/laureates/1921/, April 17th

(10) Hains, A. W.; Liang, Z.; Woodhouse, M. A.; Gregg, B. A. *Chem. Rev.* **2010**, *110*, 6689.

(11) Green, M. A.; Emery, K.; Hishikawa, Y.; Warta, W.; Dunlop, E. D. *Prog. Photovoltaics: Res. Appl.* **2012**, *20*, 12.

(12) Dennler, G.; Scharber, M. C.; Brabec, C. J. *Adv. Mater.* **2009**, *21*, 1323.

(13) *Polyera Achieves World-Record Organic Solar Cell Performance*, http://www.polyera.com/newsflash/polyera-achieves-world-record-organic-solar-cell-performance, February 23th, 2012

(14) *Heliatek achieves new world record for organic solar cells with certified 9.8 % cell efficiency*, http://www.heliatek.com/?p=1346&lang=en, February 23th, 2012

(15) Sun, Y.; Welch, G. C.; Leong, W. L.; Takacs, C. J.; Bazan, G. C.; Heeger, A. J. *Nat. Mater.* **2012**, *11*, 44.

(16) Gendron, D.; Leclerc, M. *Energy Environ. Sci.* **2011**, *4*, 1225.

(17) Scholes, G. D.; Fleming, G. R.; Olaya-Castro, A.; van Grondelle, R. *Nat. Chem.* **2011**, *3*, 763.

(18) Radivojevic, I.; Varotto, A.; Farley, C.; Drain, C. M. *Energy Environ. Sci.* **2010**, *3*, 1897.

(19) Martinez-Diaz, M. V.; de la Torre, G.; Torres, T. *Chem. Commun.* **2010**, *46*, 7090.

(20) Walter, M. G.; Rudine, A. B.; Wamser, C. C. *J. Porphyrins Phthalocyanines* **2010**, *14*, 759.

(21) Lemmetyinen, H.; Tkachenko, N. V.; Efimov, A.; Niemi, M. *Phys. Chem. Chem. Phys.* **2011**, *13*, 397.

(22) Tang, C. W.; Albrecht, A. C. *J. Chem. Phys.* **1975**, *62*, 2139.

(23) Cheng, Y.-J.; Yang, S.-H.; Hsu, C.-S. *Chem. Rev.* **2009**, *109*, 5868.
(24) Scharber, M. C.; Mühlbacher, D.; Koppe, M.; Denk, P.; Waldauf, C.; Heeger, A. J.; Brabec, C. J. *Adv. Mater.* **2006**, *18*, 789.
(25) Kubo, Y.; Watanabe, K.; Nishiyabu, R.; Hata, R.; Murakami, A.; Shoda, T.; Ota, H. *Org. Lett.* **2011**, *13*, 4574.
(26) Zeng, L.; Jiao, C.; Huang, X.; Huang, K.-W.; Chin, W.-S.; Wu, J. *Org. Lett.* **2011**, *13*, 6026.
(27) Mishra, A.; Bäuerle, P. *Angew. Chem. Int. Ed. Engl.* **2012**, *51*, 2020.
(28) *Sunlight* Wikipedia, http://en.wikipedia.org/wiki/Sunlight, April 19th 2012
(29) Il est à noter que la nomenclature des paramètres pour la caractérisation des cellules solaires provient du domaine de la physique et non de la chimie. Cela entraîne des disparités, notamment concernant le courant où le "J" est utilisé en physique plutôt que le "I" conventionnel en chimie. Se référer à la liste des abréviations.
(30) Barber, J. *Chem. Soc. Rev.* **2009**, *38*, 185.
(31) Dau, H.; Zaharieva, I. *Acc. Chem. Res.* **2009**, *42*, 1861.
(32) Balzani, V.; Credi, A.; Venturi, M. *Chem. Sus. Chem.* **2008**, *1*, 26.
(33) Huynh, M. H. V.; Dattelbaum, D. M.; Meyer, T. J. *Coord. Chem. Rev.* **2005**, *249*, 457.
(34) Alstrum-Acevedo, J. H.; Brennaman, M. K.; Meyer, T. J. *Inorg. Chem.* **2005**, *44*, 6802.
(35) Meyer Thomas, J. *Nat.* **2008**, *451*, 778.
(36) Concepcion, J. J.; Tsai, M.-K.; Muckerman, J. T.; Meyer, T. J. *J. Am. Chem. Soc.* **2010**, *132*, 1545.
(37) Dogutan, D. K.; McGuire, R.; Nocera, D. G. *J. Am. Chem. Soc.* **2011**, *133*, 9178.
(38) Lee, C. H.; Dogutan, D. K.; Nocera, D. G. *J. Am. Chem. Soc.* **2011**, *133*, 8775.

Chapitre 1

Partie A –

Azadipyrromethene Dye Derivatives in Coordination Chemistry: Structure-Properties Relationship of Panchromatic Homoleptic M(II) Complexes

Auteurs :

André Bessette [1,2], Janaina G. Ferreira [1], Martin Giguère [2], Francis Bélanger [2], Denis Désilets [2] et Garry S. Hanan [1] *.

[1] Département de Chimie, Université de Montréal, Pavillon J.-A. Bombardier, 5155 Decelles Avenue, Montréal, Québec, H3T-2B1, Canada

[2] Saint-Jean Photochimie Inc., 725 Trotter street, Saint-Jean-sur-Richelieu, Québec, J3B 8J8, Canada.

Contributions :

- **André Bessette** : Synthèse des nouveaux complexes organométalliques; caractérisation photophysique, électrochimique et structurale; rédaction de l'article.
- Janaina G. Ferreira: Résolution des structures rayons X de l'article.
- Martin Giguère: Chimiste de la compagnie St-Jean Photochimie Inc. (SJPC) ayant synthétisé les composés **1b** et **6b** fournis par SJPC.
- Francis Bélanger: Chimiste de la compagnie St-Jean Photochimie Inc. (Superviseur de stage en industrie)
- Denis Désilets: Directeur de la R&D chez SJPC. (Superviseur de stage en industrie)

Historique :

Soumis pour publication dans le journal *Inorganic Chemistry* en tant que ''Full Paper'' le 28 avril 2012. Accepté pour publication le 31 octobre 2012. DOI : 10.1021/ic300872m

1. 1 – Abstract

As a near-infrared (NIR) absorbing chromophore closely related to dipyrromethene (DPM), the azadipyrromethene (ADPM) family has attracted much interest in life sciences and optoelectronic applications. A high-yielding microwave-assisted synthesis is reported for new homoleptic complexes of Co(II), Ni(II), Cu(II) and Zn(II) based on the tetra-*p*-methoxyphenyl-ADPM ligand **1b**. These complexes are compared with other homoleptic complexes of the same M(II) series based on the tetraphenyl-ADPM **1a** and also with related BF_2^+ chelates (Aza-BODIPY, **6a-b**) for a better understanding of trends arising from substitution of the chelate and/or electron-donating effect of the *p*-methoxy substituents. The electrochemical behavior of the new compounds **2b**, **3b** and **5b** in dichloromethane revealed two pseudo-reversible reductions (**2b** = -1.09 and -1.25 V vs SCE; **3b** = -1.05 and -1.29 V; **5b** = -1.13 and -1.25 V) followed by a third irreversible process (**2b** = -1.78 V; **3b** = -1.80 V; **5b** = -1.77 V) along with two pseudo-reversible oxidations (**2b** = 0.55 and 0.80 V; **3b** = 0.56 and 0.80 V; **5b** = 0.55 and 0.80 V) followed by two close irreversible processes (**2b** = 1.21 and 1.27 V; **3b** = 1.21 and 1.28 V; **5b** = 1.22 and 1.25 V). On its side, Cu(II) homoleptic complex **4b** revealed only one pseudo-reversible reduction at -0.59 V followed by three irreversible processes at -0.95, -1.54 and -1.74 V respectively. The oxidation behavior of this complex followed other related **1b** ADPM-based homoleptic complexes with two pseudo-reversible processes (0.55 and 0.82 V respectively) and two irreversible processes (1.19 and 1.25 V respectively). The redox

processes are assigned and discussed in relation to their photophysical properties. X-Ray structures for the tetra-*p*-methoxyphenyl-ADPM ligand **1b** and related Co(II) complex **2b** are also discussed.

1. 2 – Introduction

The dipyrromethene (DPM) organic dye family has attracted increased attention due to their practical applications such as biological probes[1-6] and light-harvesting[7-11] system components. As a close parent of this intense red-absorber and near-infrared (NIR) fluorescent emitter, azadipyrromethene (ADPM) offers an opportunity to absorb and emit even further in the NIR region. Therefore, this panchromatic chromophore family is attracting interest, especially in organometallic chemistry.[12-14] In fact, ADPM exhibits similar properties to the DPM family including versatile methods of preparation,[15] even for unsymmetrical derivatives.[16-18] Consequently, fine-tuning of the optical and steric properties becomes feasible for the preparation of suitable photoactive materials for life sciences and energetic photoconversion, including photovoltaic applications.[19-30] Unlike DPM, the ADPM dye has never been isolated in its unsubstituted form, being mainly formed as tetra-aryl derivatives in the 3 and 5 positions by two distinct synthetic methods.[15] Figure 1.1 depicts both generic chromophores plus their classical boron adducts (BODIPY and Aza-BODIPY) with the position numbering and corresponding nomenclature.

The synthesis of homoleptic complexes of the d^{10} metal ions Zn(II) and Hg(II) with various substituted tetra-aryl-ADPM was recently reported by Gray and coworkers.[31] Subsequently, O'Shea *et al.* studied the spectroscopic properties of Co(II), Ni(II), Cu(II) and Zn(II) chelates **2a** to **5a** based on tetraphenyl-ADPM **1a** (Figure 1.2),[32] sixty-six years after their initial synthesis by Rogers.[33]

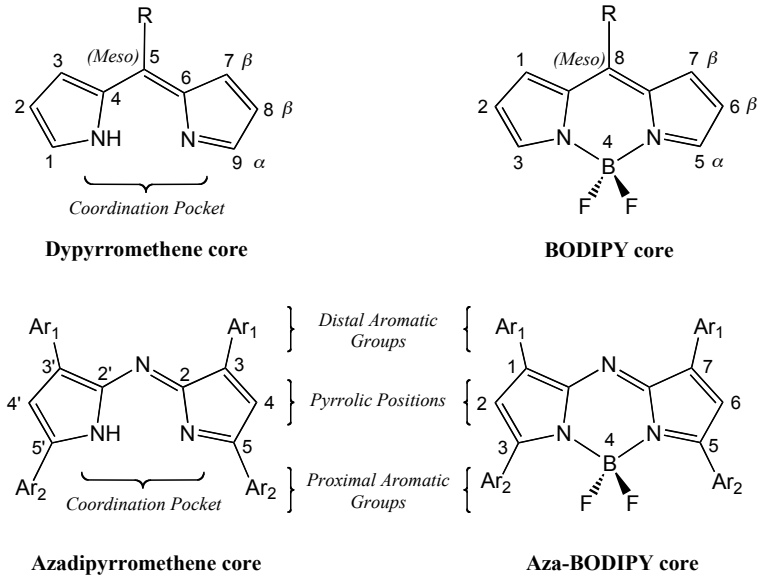

Figure 1.1 – DPM, ADPM and their corresponding boron adducts.

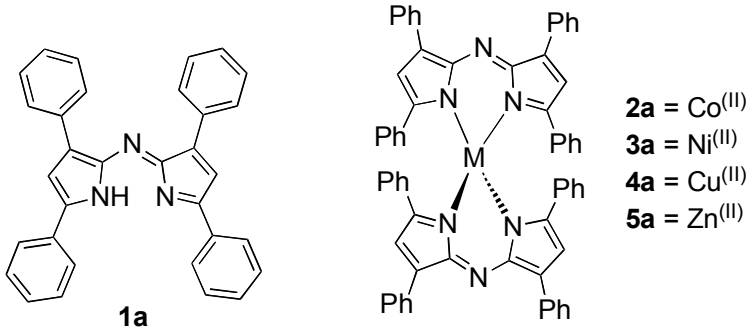

Figure 1.2 – ADPM **1a** and complexes **2a** to **5a**.

The synthesis of ADPM-based homoleptic complexes reported by the group of O'Shea, which was inspired from Rogers' initial one, was quite an improvement over Gray's approach. Although O'Shea decreased the reaction time from up to one day at room temperature in tetrahydrofuran (THF) to about one hour in hot *n*-butanol, this procedure wasn't high-yielding in every case. Herein, we report a new synthetic approach using potassium *tert*-butoxide (KO^tBu) as a strong base to deprotonate the pyrrolic unit and assisted by microwave heating. This optimization of conditions leaded to a more straightforward, high-yielding and reproducible synthesis on the timescale of minutes. This procedure allowed us to prepare new homoleptic four-coordinate complexes of Co(II), Ni(II), Cu(II) and Zn(II) **2b** to **5b** featuring the tetra-*p*-methoxyphenyl substituted ADPM **1b** also reported by Rogers[33] and absent from scientific literature since then (Figure 1.3).

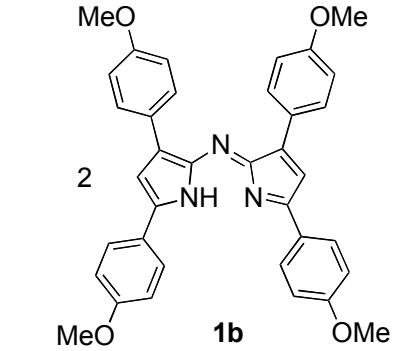

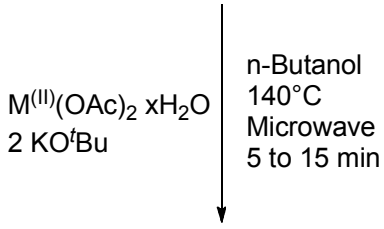

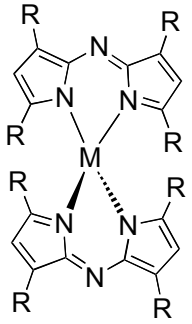

2b = $Co^{(II)}$, R = *p*-(OMe)Ph; >99%
3b = $Ni^{(II)}$, R = *p*-(OMe)Ph; 89%
4b = $Cu^{(II)}$, R = *p*-(OMe)Ph; 92%
5b = $Zn^{(II)}$, R = *p*-(OMe)Ph; 89%

Figure 1.3 – Synthesis of complexes **2b** to **5b** from ADPM **1b** assisted by microwave irradiation.

In addition to the classical characterization, such as ^{1}H and ^{13}C NMR, high-resolution mass spectrometry (HRMS) and elemental analysis; electrochemistry has been used to establish the exact energy associate with the HOMO and the LUMO levels of ligands **1a-b,** complexes **2** to **5a-b** and Aza-BODIPYs **6a-b (**Figure 1.4**)**. Due to an emergent area of ADPM coordination chemistry, the effect of metal complexation and also of substitution with electron-rich -OMe groups on the electronic properties of this dye family was still lacking from an electrochemical point of view.[30] In order to establish a general trend, the photophysical characterization of those new electron-rich tetra-*p*-methoxy compounds is also reported and compared to existing tetra-phenyl ADPM derivatives in both DCM and THF solution. Finally, X-ray structures of **1b** and **2b** are discussed in relation to existing results observed for similar homoleptic M(II) complexes in order to have insight on the effect of the electron-rich tetra-*p*-methoxyphenyl-ADPM. All together, information presented herein should permit an empirical evaluation of such panchromatic chromophores toward their incorporation in photovoltaic applications as electron-donor or photosensitizer materials.[6,29,30,34,35]

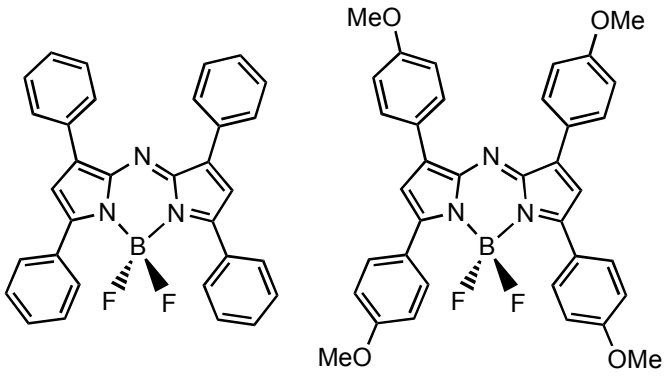

6a **6b**

Figure 1.4 – Aza-BODIPY **6a** and **6b**.

1. 3 – Experimental section

a) Materials and Instrumentation

Literature procedures were used for the synthesis of compounds **1a**, **1b, 2-5a** and **6a**.[15,32] Aza-BODIPY **6b** was obtained from Saint-Jean Photochemicals Inc. and used as received. $M(OAc)_2 \bullet xH_2O$ (M = Co, Ni, Cu, Zn; OAc = Acetate), potassium *tert*-butoxide (KO^tBu) and solvents were obtained commercially and used without further purification. Reactions were carried out under ambient atmosphere. Solvents were removed under reduced pressure using a rotary evaporator unless otherwise stated.

Microwave reactions were performed on a Biotage Initiator^{TM} Eight equipped with an auto-sampler in 20 mL flasks from the same distributor. The degree of absorption was set to normal, with 2 min of pre-stirring and a stirring rate of 600 rpm.

Nuclear magnetic resonance (NMR) spectra were recorded in $CDCl_3$ at room temperature (r.t.) on a Bruker AV400 spectrometer at 400 MHz for ^1H NMR and at 100 MHz for ^{13}C NMR, otherwise stated. Chemical shifts are reported in part per million (ppm) relative to residual solvent protons (7.26 ppm for chloroform-d) and the carbon resonance of the solvent (77.16 ppm for chloroform-d). Absorption and emission spectra were measured in CH_2Cl_2 (DCM) and THF at concentrations obeying Beer-Lambert's law at r.t. on a Cary 500i UV-vis-NIR Spectrophotometer and a Cary Eclipse Fluorescence Spectrophotometer, respectively.

High-Resolution Electro Spray Ionization Mass Spectrometry (HR-ESIMS) was performed on a Liquid Chromatography / Mass Spectrometry with a Time of Flight detector (LC/MS TOF) from Agilent by infusion of a solution in CH_2Cl_2 of compounds **2-5b** directly into the source by vacuum-aspiration.

Electrochemical measurements were carried out in argon-purged CH_2Cl_2 at room temperature with a BAS CV50W multipurpose equipment interfaced to a PC. The working electrode used was a glassy carbon electrode for every compound. The counter electrode was a Pt wire, and the pseudo-reference electrode was a silver wire. The reference was set using an internal 1 mM ferrocene/ferrocenium sample at 0.46 V vs SCE in CH_2Cl_2. The concentration of the compounds was about 1 mM. Tetrabutylammonium hexafluorophosphate (TBAP) was used as supporting electrolyte and its concentration was 0.10 M. Cyclic voltammograms (CV) were obtained at scan rates of 50, 100, 200, and 500 mV/s. For reversible processes, half-wave potentials (vs. SCE) from CV were used. To establish the potential of irreversible processes, differential pulse voltammetry (DPV) experiments were performed with a step rate of 4 mV, a pulse height of 50 mV, and a frequency of 5 Hz. Criteria for reversibility were the separation of 60 mV between cathodic and anodic peaks, the close to unity ratio of the intensities of the cathodic and anodic currents, and the constancy of the peak potential on changing scan rate.

Diffraction data were collected on a Bruker Microstar diffractometer equipped with a Platinum 135 CCD Detector, a Helios optics, a Kappa goniometer and Cu K(α) radiation. The diffraction quality of the crystals were checked several times, revealing in all cases

poor diffraction with a large amount of diffuse scattering, signaling extensive crystal disorder. Cell refinement and data reduction were done using APEX2.[36] Absorption corrections were applied using SADABS.[37] Structures were solved by direct methods using SHELXS97 and refined on F^2 by full-matrix least squares using SHELXL97.[38] All non-hydrogen atoms were refined anisotropically. Hydrogen atoms were refined isotropically on calculated positions using a riding model. For compound **1b**, the highest residual difference peak with electronic density of 1.4 e/Å^3 is essentially due to a minor spatial disorder of the N2 atom (evaluated to 18%) and was not modeled in the final structure. For the Ni(II), Co(II) and Cu(II) complexes, crystals showed high mosaicity and low diffraction, as well as high decay of standard intensities during data collection (around 20%). Due to the undesirable characteristics described above, the crystal structures of the nickel, copper and zinc complexes were not completed. However, it was possible to determine details of the connectivity and conformation from those complexes, which were similar to those obtained for the distorted tetrahedral cobalt complex **2b**. For this last complex, the structure exhibited high disorder, mainly over the methoxyphenyl rings, which was modeled as two components, with average ration of 0.7/0.3 and refined anisotropically.

Experimental uncertainties are as follows: absorption maxima, ±2 nm; molar absorption coefficient, 10%; emission maxima, ± 5 nm; redox potentials, ± 10 mV.

b) Experimental procedures and data

Bis[3,5-bis(4-methoxyphenyl)-1*H*-pyrrol-2-yl)-3,5-bis(4-methoxyphenyl)-2-ylidene)amine]Co(II) (**2b**).

A suspension of compound **1b** (116 mg, 0.203 mmol), Co(II) acetate tetrahydrate [$Co(OAc)_2 \bullet 4H_2O$] (25 mg, 0.10 mmol) and KO^{t}Bu 95% (24 mg, 0.20 mmol) in 10 mL of *n*-butanol was reacted in microwave for 15 min. under magnetic stirring. The reaction mixture was evaporated to dryness, dissolved in CH_2Cl_2 and filter through Celite. The solvent was evaporated to afford a blue-purple powder. Yield = 123 mg (> 99 %). ^{1}H NMR ($CDCl_3$, 500 MHz) δ/ppm: 7.22 (br. s.), 7.84 (br. s.), 8.73 (br. s.), 15.02 (br. s.), 15.33 (br. s.), 63.66 (br. s.). Mass Spec (*m/z*); HR-ESIMS calcd for $C_{72}H_{60}N_6O_8Co$: [M^+] 1195.3799, found: 1195.3781. Elemental Analysis: calcd: C = 72.29 %, H = 5.06 %, N = 7.03 %; found: C = 72.23 %, H = 5.07 %, N = 7.00 %. Crystals suitable for X-ray analysis were obtained from double-layer crystallization in CH_2Cl_2 and hexanes.

Bis[3,5-bis(4-methoxyphenyl)-1*H*-pyrrol-2-yl)-3,5-bis(4-methoxyphenyl)-2-ylidene)amine]Ni(II) (**3b**).

A suspension of compound **1b** (117 mg, 0.206 mmol), Ni(II) acetate tetrahydrate [$Ni(OAc)_2 \bullet 4H_2O$] (26 mg, 0.10 mmol) and KO^{t}Bu 95% (24 mg, 0.20 mmol) in 10 mL of *n*-butanol was reacted in microwave for 10 min. with magnetic stirring. The reaction mixture was evaporated to dryness, dissolved in CH_2Cl_2 and filtered through Celite. The solvent was evaporated and the resulting red-purple residue was concentrated in THF and recrystallized by slow diffusion of pentane. The solid was isolated by filtration and washed with pentane (3 X 5 mL), which afforded a red-purple powder. Yield = 109 mg (89 %). ^{1}H NMR ($CDCl_3$, 400 MHz) δ/ppm: -1.78 (d, J=7.46 Hz, 8 H), 2.79 (s, 12 H), 3.44 (s, 12 H), 6.40 (d, J=7.67 Hz, 8 H), 8.15 (br. s., 8 H), 34.53 (br. s., 8 H), 61.52 (br. s., 4 H). Mass Spec (*m/z*); HR-ESIMS calcd for $C_{72}H_{60}N_6O_8Ni$: [M^+] 1194.3821, found: 1194.3828. Elemental Analysis: calcd: C = 72.31 %, H = 5.06 %, N = 7.03 %; found: C = 72.30 %, H = 4.97 %, N = 7.08 %.

Bis[3,5-bis(4-methoxyphenyl)-1*H*-pyrrol-2-yl)-3,5-bis(4-methoxyphenyl)-2-ylidene)amine]Cu(II) (**4b**).

A suspension of compound **1b** (118 mg, 0.207 mmol), Cu(II) acetate monohydrate [Cu(OAc)2 •H2O] (21 mg, 0.10 mmol) and KOtBu 95% (25 mg, 0.21 mmol) in 10 mL of n-butanol was reacted in microwave for 5 min. with magnetic stirring. The reaction mixture was evaporated to dryness, dissolved in CH2Cl2 and filtered through Celite. The solvent was evaporated and the resulting blue-purple residue was concentrated in THF and recrystallized by slow diffusion of pentane. The solid was isolated by filtration and washed with pentane (3 X 5 mL), which afforded a blue-purple powder. Yield = 114 mg (92 %). Mass Spec (m/z); HR-ESIMS calcd for C72H60N6O8Cu: [M+] 1199.3763, found: 1199.3734. Elemental Analysis: calcd: C = 72.01 %, H = 5.04 %, N = 7.00 %; found: C = 71.79 %, H = 5.23 %, N = 6.83 %.

Bis[3,5-bis(4-methoxyphenyl)-1*H*-pyrrol-2-yl)-3,5-bis(4-methoxyphenyl)-2-ylidene)amine]Zn(II) (**5b**).

A suspension of compound **1b** (142 mg, 0.249 mmol), Zn(II) acetate dihydrate [$Zn(OAc)_2 \bullet 2H_2O$] (27 mg, 0.13 mmol) and KO^{t}Bu 95% (29 mg, 0.25 mmol) in 10 mL of *n*-butanol was reacted in microwave for 5 min. with magnetic stirring. The reaction mixture was evaporated to dryness, dissolved in CH_2Cl_2 and filtered through Celite. The solvent was evaporated and the resulting red-purple residue was concentrated in THF and recrystallized by slow diffusion of pentane. The solid was isolated by filtration and washed with pentane (3 X 5 mL), which afforded a blue-purple powder. Yield = 134 mg (89 %). ^{1}H NMR ($CDCl_3$, 400 MHz) δ/ppm: 3.40 (s, 12 H), 3.92 (s, 12 H), 6.57 - 6.66 (m, 12 H), 6.97 (d, *J* = 8.78 Hz, 8 H), 7.44 (d, *J* = 8.78 Hz, 8 H), 7.89 (d, *J*=8.78 Hz, 8 H). ^{13}C NMR ($CDCl_3$, 100 MHz) δ/ppm: 55.01, 55.36, 72.21, 113.41, 113.42, 115.28, 126.05, 127.50, 128.31, 130.87, 143.93, 147.74, 159.28, 159.50, 160.45. Mass Spec (*m/z*); HR-ESIMS calcd for $C_{72}H_{60}N_6O_8Zn$: [M^+] 1200.3759, found: 1200.3724. Elemental Analysis: calcd: C = 71.90 %, H = 5.03 %, N = 6.99 %; found: C = 71.73 %, H = 5.22 %, N = 6.76 %.

1. 4 – Results and Discussion

Synthesis

Complexes **2a** to **5a** were obtained following literature procedure using ligand **1a**.[32] The new methodology developed to access complexes **2-5b** consist of irradiating 2 equivalents (equiv.) of the tetra-*p*-methoxyphenyl-ADPM ligand **1b** with 1 equiv. of the corresponding $M(OAc)_2 \bullet xH_2O$ (M = Co, Ni, Cu, Zn; OAc = Acetate), in presence of 2 equiv. KO^{t}Bu at 140°C in the microwave for 5 to 15 minutes, using *n*-butanol as solvent. Microwave irradiation accelerated the reaction while giving yields ranging from 89% to quantitative. The solvent, *n*-butanol, is suitable for such complexation due to its high boiling point, its stability towards side reactions and decomposition, and the ease of purification resulting from the insolubility of the product upon formation. A recrystallization was performed for each complex by slow diffusion of pentane in a saturated solution of THF to remove residual traces of ligand, after filtration of salts on Celite® in CH_2Cl_2 (DCM). Dark purple powders with tints of blue to red were isolated. Elemental analysis, ^{1}H & ^{13}C NMR (except for the paramagnetic Cu(II) complex **4b**) and HRMS all supported the conversion to corresponding homoleptic complexes. Noteworthy, the use of an aprotic solvent for MS gives the M^+ cation while a proton source such as formic acid gives mainly the MH^+ specie. Suitable single crystals for X-ray diffraction of the ligand **1b** and Co(II) complex **2b** were obtained from a double-layer of DCM and hexanes.

Electrochemistry

In the perspective of incorporating ADPM complexes in various photoactive systems, for instance as molecular probes or in light-harvesting materials, access to information concerning the energy levels of the HOMO and the LUMO becomes crucial in order to further fine-tune their properties. For instance, we can easily consider that a too low-lying LUMO level would not permit efficient electronic transfers in potential photosensitizers for dye-sensitized solar cells (DSSC) or organic photovoltaic (OPV) devices.[9,39,40] Similarly, the photophysical mechanisms implied in fluorescent sensors based on such materials might also be affected by improper energy levels, i.e. high-lying HOMO levels might oxidize in biological environments.[1] While optical properties such as absorption and emission can indicate the energy levels difference between these two orbitals, electrochemistry is able to further provide their exact position in the ground state. The effect of metal substitution from the d^7 Co(II) to the d^{10} Zn(II) in ADPM homoleptic complexes **2** to **5a-b** was compared to corresponding ligands **1a-b** by cyclic and differential pulse voltammetry techniques (CV & DPV, respectively) (Table I.1 and ESI). These techniques afford critical information concerning the electronic processes occurring and exact energies associated to their HOMO/LUMO states. To complete the study, Aza-BODIPYs **6a-b** are also presented.

Table I.1 - Electrochemical data for ADPM ligands **1a-b**, complexes **2** to **5a-b** and Aza-BODIPYs **6a-b**.

Compound	Chelate	$E_{1/2}$(Ox) [a]				$E_{1/2}$(Red) [a]		
1a	None	---	---	1.36 (137)	1.01 (91)	-0.78 (72)	-1.45 (16)	---
1b	None	---	1.30 [b, c]	1.10 [b, c]	0.71 (61)	-0.92 (106)	-1.52 (193)	---
2a	Co(II)	---	---	1.15 (102)	0.85 (97)	-0.93 (108)	-1.10 (104)	---
2b	Co(II)	1.27 [b, c]	1.21 [b, c]	0.80 (136)	0.55 (115)	-1.09 (109)	-1.25 (114)	-1.78 [b, c]
3a	Ni(II)	---	---	1.15 (111)	0.85 (106)	-0.89 (115)	-1.15 (113)	---
3b	Ni(II)	1.28 [b, c]	1.21 [b, c]	0.80[c] (111)[d]	0.56 (77)	-1.05 (86)	-1.29 (91)	-1.80 [b, c]
4a	Cu(II)	---	---	1.18 (95)	0.87 (86)	-0.46 (150)	-0.80 (88)	-1.41 (112) [e]
4b	Cu(II)	1.25 [b, c]	1.19 [b, c]	0.82 (107)	0.55 (82)	-0.59 (106)	-0.95 [c]	-1.54 [f]
5a	Zn(II)	---	---	1.15 (104)	0.86 (98)	-0.97 (111)	-1.11 (114)	---
5b	Zn(II)	1.25 [b, c]	1.22 [b, c]	0.80 (98)	0.55 (86)	-1.13 (82)	-1.25 (88)	-1.77 [b, c]
6a	BF_2^+	---	---	1.45[c] (62)[d]	1.32 (122)	-0.40 (101)	-1.19 (96)	---
6b	BF_2^+	---	1.52 [b, c]	1.34 [b, c]	0.95 [b, c]	-0.58 (107)	-1.37 (92)	---

a) Potentials are in volts vs SCE for CH_2Cl_2 deaerated solutions, 0.1 M in TBAP, recorded at 25 ± 1 °C at a sweep rate of 50 mV/s. The difference between cathodic and anodic peak potentials (mV) is given in parentheses. b) Irreversible. c) Determined by differential pulse voltammetry (DPV). d) Obtained from cyclic voltammetry (CV) before addition of ferrocene. e) Another pseudo-reversible reduction process was observed at -1.60 (133) V (see ESI). f) An irreversible reduction at -1.74 was also observed by DPV (see ESI).

First looking at the organic ligands **1a** and **1b** to establish the effect of the electron-rich *p*-methoxy-phenyl groups on the later compound, a difference in stability is clearly notable (see ESI). This higher susceptibility to decomposition for **1b** is probably the result of a more facile oxidation of the ligand bearing four electron-rich –OMe groups. This is of specific importance in the context of using derivatives based on ligand **1b** either for life science or light-harvesting system components, because they are more likely to decompose over time in such environments.[1,39,41-43] While ligand **1a** present two «pseudo-reversible» processes of one electron each in the oxidation potentials (1.01 (91) and 1.36 (137) V vs SCE, respectively) along with two other in the reduction potentials (-0.78 (72) and -1.45 (16) V, respectively) (Table I.1), the ligand **1b** bearing four *p*–methoxy-phenyl groups shows only one pseudo-reversible oxidation at 0.71 (61) V followed by two irreversible peaks (1.10 and 1.30 V, respectively). Presence of a third oxidation process in ADPM **1b** compared to **1a** seems to be accessible in the potential window of DCM due to the overall stabilization of the bonding-orbitals induced by electron rich –OMe substituents groups. On their side, reduction processes of this last ligand are «pseudo-reversible» (-0.92 (106) and -1.52 (193) V, respectively) in a similar fashion to the tetraphenyl ADPM derivative, while being more stabilized.

Assignation of the molecular orbitals (MO) implied in redox processes for ADPM **1a**-**1b** can be made putatively by comparing with electron density mapping obtained from molecular modeling reported in literature for various related ADPM and Aza-BODIPY. An *in silico* study of interest from Russo et al. present TD-DFT calculations for Aza-BODIPY

6a and related –OMe derivatives in proximal and distal positions (**6c** and **6d** respectively) (Figure 1.5).[44] Their modelization for **6a** showed an HOMO mainly based on the π-system implying the dipyrrolic core and the four phenyl rings, but with a node on the N-bridge arising from the C_2 symmetry in the molecule. Furthermore, the electron density calculated for HOMO-1 and HOMO-2 were both mainly centered on the distal phenyl rings. In the case of the LUMO, delocalization throughout the whole π-system was restored, including the N-bridge, along with a slightly higher contribution implying the BF_2^+ fragment. Noteworthy, only a moderate contribution seemed to arise from the BF_2^+ fragment in all of those calculated MOs. Based on those observations; it appears reasonable to use Aza-BODIPY **6a** as a good model for the assignation of MOs from ADPM **1a** and **1b**, especially since those three derivatives are symmetrical molecules. Our assumption seems to be also reinforced by two other *in silico* studies. One was reported in 2011 by Kobayashi *et al.*, presenting a direct comparison between the fused-ring ADPM **7** and its corresponding Aza-BODIPY derivative **8** (Figure 1.5). Modelization revealed that both corresponding HOMOs and LUMOs orbitals have a very similar electronic charge distribution.[24] Jacquemin *et al.* lately reported the other study, looking closer at the frontier orbitals of Aza-BODIPY derivative **6e** bearing a dimethylamino electro-donating group installed in proximal position through an extended π-conjugation system (Figure 1.5).[21] Calculations for HOMO-4 to HOMO and LUMO to LUMO+4 orbitals were presented and similarities are notable concerning the HOMO-2, HOMO-1, HOMO and LUMO electronic density localization previously reported by Russo *et al.* for **6a**. Noteworthy, while the LUMO of **6e** is centered

on the dipyrrolic moiety like in **6a**, the further presentation of LUMO+1 to LUMO+4 revealed that appended phenyl rings take over the electron density for those subsequent unoccupied orbitals. All those precedents in scientific literature therefore lead us to assign the first oxidation observed for both **1a** and **1b** as centered on the dipyrrolic core with charge stabilization throughout the appended phenyls; while the second and third (for **1b**) ones are more likely to be centered on the peripheral phenyl rings. For the reduction processes, the pyrrolic core seems to be the host of the first electron accepted, while peripheral phenyls take over for the second reduction.

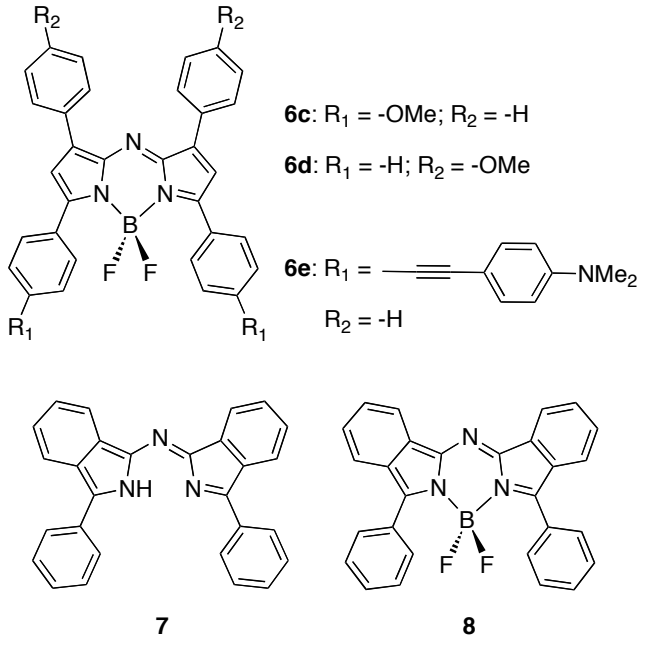

Figure 1.5 – Related ADPM and Aza-BODIPY derivatives.

Once converted into electron volt (eV), HOMO and LUMO levels are lying at -5.95 and -4.17 eV (ΔE = 1.78 eV) for tetraphenyl-ADPM **1a**, respectively, while they are at -5.66 and -4.03 eV (ΔE = 1.63 eV) for tetra-*p*-methoxyphenyl-ADPM derivative **1b** (Table I.2). A look at Figure I.6 leads to a better understanding of the electron-rich *p*-methoxyphenyl groups' effects on the energy levels of ADPM derivatives. In facts, the HOMO is easier to oxidize by about 0.29 eV in **1b** compared to **1a**. This is an indication of the additional electron density brought by –OMe substituents, whom stabilize the binding orbital. On the other hand, the first reduction of **1b** is about 0.14 eV more difficult to reduce due to the destabilization of the anti-bonding orbital. Combined, these effects decreased the energetic transition (ΔE) between the HOMO and LUMO orbitals by 0.15 eV in tetra-*p*-methoxyphenyl ligand **1b**. In other words, the absorption band of this dye should be displaced deeper in the NIR region due to a less energetic transition, as it will be further discussed in the absorption spectroscopy section.

Table I.2 - HOMO/LUMO levels (in eV) as determined by electrochemistry along with ΔE obtained from redox and optical methods for ADPM ligands **1a-b**, complexes **2** to **5a-b** and Aza-BODIPYs **6a-b**.

Compound	Chelate	HOMO [a)]	LUMO [a)]	ΔE Redox [b)]	ΔE Opt [c)]
1a	None	-5.95	-4.17	1.78	1.93
1b	None	-5.66	-4.03	1.63	1.81
2a	Co(II)	-5.80	-4.02	1.78	1.69 [d)]
2b	Co(II)	-5.49	-3.86	1.63	1.60 [d)]
3a	Ni(II)	-5.80	-4.06	1.74	1.69 [d)]
3b	Ni(II)	-5.50	-3.90	1.60	1.62 [d)]
4a	Cu(II)	-5.82	-4.49	1.33	1.76 [d)]
4b	Cu(II)	-5.49	-4.36	1.13	1.65 [d)]
5a	Zn(II)	-5.81	-3.97	1.84	1.75 [d)]
5b	Zn(II)	-5.49	-3.81	1.68	1.64 [d)]
6a	BF_2^+	-6.26	-4.54	1.72	1.83
6b	BF_2^+	-5.90	-4.36	1.54	1.71

a) Reported in eV b) Energetic difference between the HOMO and the LUMO obtained by electrochemistry in DCM solution. c) Energetic difference obtained from the conversion of the emission wavelength in DCM solution into eV using the formula $E = hc / \lambda$, otherwise stated. d) Energetic difference qualitatively obtained from the red end of the Gaussian peak of the $\lambda_{max\ shoulder}$ in DCM solution and converted in eV using the same formula as d).

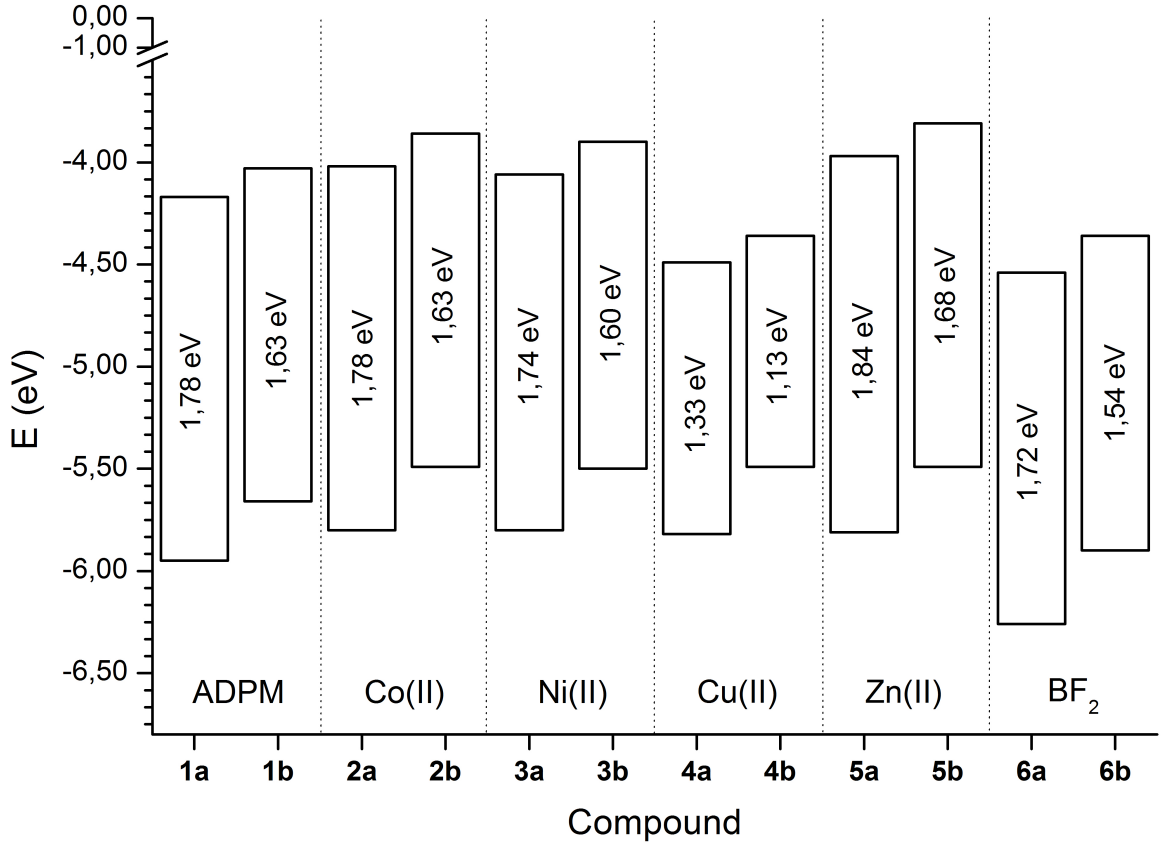

Figure 1.6 – Energetic scheme (in eV) of compounds **1** to **6** including the HOMO-LUMO difference (ΔE) as calculated by electrochemistry.

Upon coordination of the Lewis acidic BF_2^+ fragment, tetra-phenyl Aza-BODIPY **6a** present one «pseudo-reversible» oxidation process of one electron at 1.32 (122) V and one other of about half an electron at 1.45 (62) V (Table I.1), this last one interfering with the limit of the potential window of DCM in the oxidation potentials (see ESI). In the reduction potentials, two «pseudo-reversible» processes are present at -0.40 (101) and -1.19 (96) V, respectively. In general, the same number of processes is present compared to the ADPM **1a**, albeit they are all markably stabilized by the presence of the Lewis acid chelate, as can be expected. For Aza-BODIPY **6b** bearing four *p*–methoxy-phenyl groups, the three oxidation processes at 0.95, 1.34 and 1.52 V, respectively, are irreversible. The reduction processes are however «pseudo-reversible» (-0.58 (107) and -1.37 (92), respectively). Comparing the Aza-BODIPY **6b** to its ADPM **1b** derivative, the overall effect is a stabilization of both the oxidation and reduction processes upon coordination of the BF_2^+ chelate in a similar fashion to **6a**.

As mentioned previously in the assignation of redox processes of ADPMs **1a-b** from molecular modeling of various Aza-BODIPYs,[21,24,44] the first oxidation observed for both **6a** and **6b** are centered on the dipyrrolic core with charge stabilization throughout the appended phenyls; while the second and third (for **6b**) ones are more likely to be centered on the peripheral phenyl rings. For the reduction processes, the first reduction is based on the pyrrolic moiety while peripheral phenyls take over for the second one.

A closer look at the frontier orbitals of those Aza-BODIPY derivatives shows that tetra-phenyl Aza-BODIPYs **6a** present a ligand-centered HOMO harder to oxydize than the one of *p*-methoxyphenyl substituted **6b** by about 0.36 eV (-6.26 and -5.90 eV, respectively) and a ligand-centered LUMO including contributions from the BF_2^+ chelate that reduces more easily by about 0.18 eV (-4.54 and -4.36 eV, respectively) (Table I.2). This correlates perfectly with the observations made for **1a-b** ligands arising from a stabilization of the bonding orbital and a destabilization of the anti-bonding orbital induced by the –OMe groups. In addition, the presence of the BF_2^+ electropositive fragment leads to an overall stabilization of both the HOMO and the LUMO due to the Lewis base-Lewis acid interaction provided upon coordination of the chelate. For the HOMO, this stabilization is about 0.25 eV (-6.26 vs -5.95 eV for **6a** vs **1a**; -5.90 vs -5.66 eV for **6b** vs **1b**) while it is of about 0.35 eV for the LUMO (-4.54 vs -4.17 eV for **6a** vs **1a**; -4.36 vs -4.03 eV for **6b** vs **1b**). As mentioned previously, a rationalization can be made implying contribution from the BF_2^+ chelating agent in the first unoccupied molecular orbital of the Aza-BODIPYs. Actually, the computational study from Jacquemin *et al.* on Aza-BODIPY derivatives tends to support this hypothesis, as they reported for a model chromophore including only the aza-dipyrromethene central moiety a contraction of the B-N bonds and a strong elongation of the central C-N bonds of the central rings in the S_1 excited state compared to his ground state S_0.[21] Overall, the ΔE from redox measurements decreased to 1.72 eV for **6a** and 1.54 eV for **6b**, with a relative order that correlates observed emission values (Tables I.2 and I.3).

When considering the redox behavior of homoleptic complexes **2** to **5a-b**, it appears to change significantly compared to ADPM ligands **1a-b** and their corresponding boron adducts **6a-b**. The four main observations for the organometallic complexes are (Table I.2 and Figure 1.6): i) access to one additional oxidation and one reduction process for complexes **2b-5b**; ii) presence of two additional reduction processes upon coordination to Cu(II) for both **4a** and **4b** complexes; iii) a general destabilization of HOMOs to the same extend throughout the M(II) series; iv) a general stabilization of LUMOs to various extend, except for Cu(II) derivatives **4a** and **4b**. Those observations will be discussed in the following.

Looking at the effect of varying the metal center on the oxidation potentials, only a slight difference is observed among the complexes for the two first oxidation potentials. Referring to the HOMO level, complexes based on tetra-phenyl-ADPM **1a** are all lying between -5.80 to -5.82 eV (0.85 to 0.87 V) while the ones based on tetra-*p*-methoxyphenyl-ADPM **1b** are between -5.49 to -5.50 eV (0.55 to 0.56 V). Having a HOMO energy level difference ranging from 0.30 eV for complexes Co(II) **2a-b** to 0.33 eV for Cu(II) complexes **4a-b**, they all respect the relative difference of ADPM **1a** compare to **1b** along with a very similar difference (0.29 eV for the ligands). Those observations are pointing toward a ligand-based HOMO, notwithstanding slightly destabilized (about 0.15 eV) by the presence of two ADPM ligands on the same homoleptic complex. This assignation of the HOMO is also in accordance with computational modelization of Zn(II) complex **5a** reported by Gray *et al.*[31] The second oxidation process follows the exact same behavior,

with potentials ranging from 1.15 to 1.18 V for complexes based on ADPM **1a** and between 0.80 and 0.82 V for the ones based on ADPM **1b**. Therefore, this second pseudo-reversible oxidation also seems to be ligand-based. For complexes **2b**-**5b**, the third irreversible oxidation process ranging between 1.19 and 1.21 V and the fourth one (also irreversible) ranging between 1.25 and 1.28V are also pointing toward ligand-based processes as they are very similar along the M(II) series.

While oxidation processes were slightly affected by variation of the metal center throughout the series, the trend is somewhat different for the LUMO (Figure I.6) and other reduction processes observed (Tables I.1 and I.2). The presence of Co(II) induced a stabilization of the first pseudo-reversible reduction process, representing the LUMO, of 0,15 eV for complex **2a** (-4.02 eV / -0.93 V) and 0.17 eV for complex **2b** (-3.86 eV / -1.09 V) compared to their respective ADPM ligands **1a** (-4.17 eV / -0.78) and **1b** (-4.03 eV / -0.92 V). For Ni(II) based complexes, this stabilization decreased to 0.11 and 0.13 eV for **3a** (-4.06 eV / -0.89 V) and **3b** (-3.90 eV / -1.05 V), respectively. On their side, Zn(II) complexes are showing 0.20 and 0.22 eV of LUMO stabilization for **5a** (-3.97 eV / -0.97 V) and **5b** (-3.81 eV / -1.13 V), respectively. However, all complexes based on Co(II), Ni(II) and Zn(II) presented a second pseudo-reversible reduction process less stable than the one of their corresponding ADPM ligand by about 0.35 V for **1a** derivatives and 0.25 V for the ones based on **1b**. Complexes based on this last ligand are all three presenting an additional irreversible oxidation between -1.77 V for the Zn(II) complex **5b** and -1.80V for Ni(II) complex **3b**. Based on the modelization of complex **5a** by Gray *et al.* mentioned

previously,[31] all reduction processes seems to be based on the core of the ADPM ligand without significant contribution from the M(II) present. However, variation of the M(II) center seems to have an influence on the exact energy of the LUMO, without a clear trend going from the d^7 Co(II) to the d^{10} Zn(II). Finally, the combined effect of a relatively constant HOMO orbital with a fluctuating LUMO leads to ΔE_{Redox} = 1.78 eV for Co(II) complex **2a** compared to ΔE_{Redox} = 1.63 eV for **2b**. Those ΔE_{Redox} observed are exactly the same as their respective ADPM derivatives. For Ni(II) complexes, slightly smaller ΔE_{Redox} are obtained (1.74 and 1.60 eV respectively for **3a** and **3b**), while larger ones are obtained for Zn(II) complexes (1.84 and 1.68 eV respectively for **5a** and **5b**). Overall, those ΔE_{Redox} observed are following the same relative order as the one obtained from optical measurement's (Table I.3).

The case of Cu(II) complexes **4a-b** is special as the first reduction process lead to a strong destabilization (0.32 and 0.33 eV, respectively) compared to their corresponding ADPM ligands. LUMO orbitals are therefore low-lying at -4.49 eV (-0.46 V) and -4.36 eV (-0.59 V), respectively. *De facto*, the transitions between the HOMO and LUMO levels of those two complexes are the lowest observed with ΔE_{Redox} = 1.33 eV for **4a** and ΔE_{Redox} = 1.13 eV for **4b**. Such low-lying LUMOs are attributable to the Cu(II)/Cu(I) reduction process in a similar fashion to metalloporphyrin and Cu(I)-phenanthroline $[Cu(NN)_2]^+$ derivatives.[45-47] In addition, this metal-based reduction leads to geometry change in the coordination sphere from distorted tetrahedral to square planar (typical of Cu(I) complexes), expulsing one ADPM ligand into the DCM solution. This explains the small

pseudo-reversible reduction peak observed for complexes **4a-b** in CV and DPV (see ESI) around the same potentials as their corresponding ADPM ligand, i.e. at -0.80 and -0.95 V respectively. Two other pseudo-reversible processes of one electron each were observed at -1.41 (112) and -1.60 (133) V for **4a**. In the case of **4b**, those two reduction processes were irreversible (-1.54 and -1.74 V, respectively). Based on the related Co(II), Ni(II) and Zn(II) complexes, those two last reduction seems attributable to the ligand.

Overall, the electrochemistry data presented in Tables I.1-2 and resumed in Figure I.6 for ADPM coordination derivatives of the tetra-phenyl substituted **1a** and electron-richer tetra-*p*-methoxyphenyl substituted **1b** revealed important trends. First, the tetra-phenyl ADPM **1a** has a lower lying HOMO and less stable LUMO than the more electron rich ADPM **1b**, as can be expected. Also, the destabilized HOMO of the –OMe substituted ADPM **1b** leads to decomposition of the compound under redox conditions. Second, the coordination of BF_2^+ Lewis acidic fragment to obtain Aza-BODIPYs **6a** and **6b** led to a stabilization of both HOMO and LUMO orbitals. Third, the variation of the metal center along the Co(II), Ni(II), Cu(II) and Zn(II) series revealed that their HOMO is centered on the ligands and that they are almost constant for a given ligand throughout the series. On the other hand, the LUMO appears to be more affected by the replacement of the M(II) center, but presents no clear trend going from d^7 Co(II) to d^{10} Zn(II) chelate. Especially, the Cu(II) complexes **4a-b** present a Cu(II)/Cu(I) reduction based LUMO, which lead to decoordination of one ADPM ligand upon the geometrical rearrangement from distorted tetrahedral to square planar. Based on the various observations made, the use of

electrochemistry to characterize new ADPM to be developed and their coordination derivatives appears of great necessity to prepare successful systems in specified application. Hopefully, this study will provide useful insights to researchers on the substituents to install for stable ADPM derivatives in their quest for NIR chromophores.

Optical properties

To complete our study of ADPM dye derivatives in coordination chemistry, absorption and emission spectra of newly synthetized complexes **2b**-**5b** and Aza-BODIPY **6b** based on ligand **1b** were recorded (Figures 1.7 and 1.8, respectively). In a desire to standardize and complete the various data available in existing literature data for ligands **1a**, complexes **2a**-**5a** and Aza-BODIPY **6a**, record of data was made in both DCM and THF (Table I.3). All together, that information should lead to better understand trends arising from varying the electronic density of the ligand and/or the coordinated center.

The presence of four electron-rich –OMe groups on the tetra-aryl ADPM **1b** led to a bathochromic shift of 37 nm in DCM and 31 nm in THF compared to tetra-phenyl-ADPM **1a**. In fact, the λ_{max} in the red region for **1b** was of 627 nm in both solvents, compared to 590 nm in DCM and 596 nm in THF for the tetra-phenyl-ADPM **1a**. Such a bathochromic shift follows the tendency observed in literature as the presence of two *p*-methoxy substituents in the distal position gave a λ_{max} at 607 nm and at 620 nm in the proximal position (in THF).[31] Further comparison can be made between ADPM **1a** and its tetraphenyl-dipyrromethene derivative reported by Jones and coworkers.[48] In this case, a bathochromic shift of 50 nm is observed simply based on the presence of the nitrogen atom on the bridge of the ADPM. Typical of azadipyrromethene dyes, a second absorption band is observed in the 300 nm region ($\lambda_{max\ near\text{-}UV}$) arising from variable orbital contributions, mainly $\pi - \pi^*$ transitions, depending of the substituents present in the chromophore.[21] As mentioned by Jacquemin and coworkers, these orbital contributions are hard to formally

establish without *in silico* simulations. Readers interested about computational modelization of Aza-BODIPY are invited to consult very recent papers on the subject from this group.[21,49,50] Also of interest, the tetra-*p*-methoxyphenyl ADPM **1b** offers a molar absorptivity (ε) of 54 000 $M^{-1}cm^{-1}$ in THF, about 20% more than any of the other *p*-methoxy substituted or tetra-phenyl ADPMs. They are also on the same order of magnitude as what was observed by Gresser and coworkers for benzannulated ADPM derivatives that exhibit a better π-conjugation.[25] In fluorescence spectroscopy, the tetra-phenyl ADPM **1a** present an emission at 644 nm in DCM, which is slightly blue-shifted at 642 nm in more polar THF. ADPM **1b** exhibited an emission centered at 684 nm in DCM (Figure 1.8), with a larger ipsochromic effect of 6 nm compared to **1a** bringing up the emission to 678 nm in THF (ESI). Noteworthy, emission peaks are reaching up to about 850 nm in both solvents, which make ADPM **1b** an interesting candidate for NIR applications. Once converted into eV, the optical band-gap (ΔE_{Opt}) can be compared to the one obtained by electrochemistry (ΔE_{Redox}) in order to evaluate if the trends are respected. While the values of band-gap do not correspond perfectly between redox and optical measurements (1.78 vs 1.93 eV respectively for **1a** and 1.63 vs 1.81 eV for **1b**), the relative order within each method is respected (Table I.2).

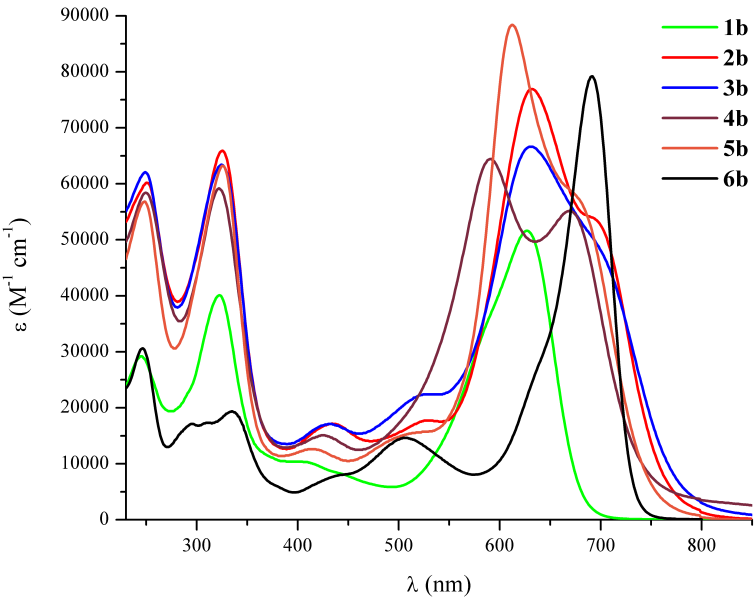

Figure 1.7 – Absorption spectra of ligand **1b**, complexes **2b** to **5b** and Aza-BODIPY **6b** in DCM.

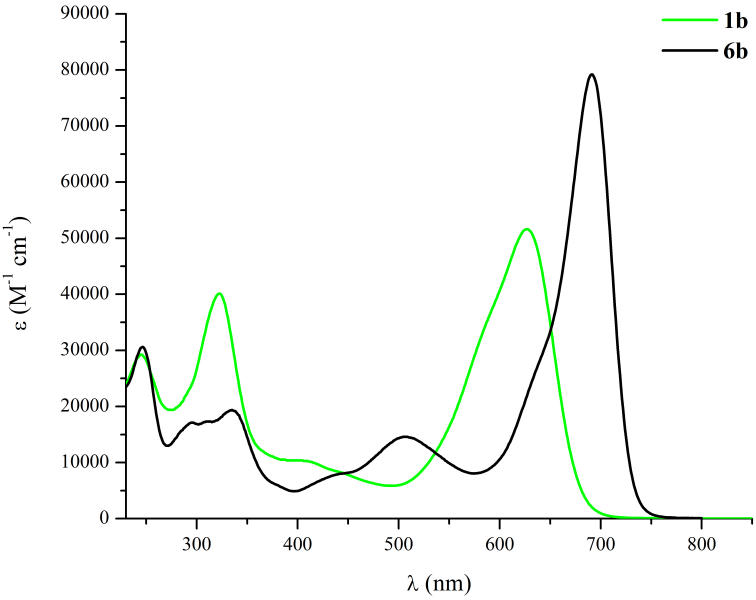

Figure 1.8 – Emission spectra of **1b** and **6b** in DCM

Table I.3 - Compiled UV/vis absorption and emission data for the ligands **1**, complexes **2** to **5** and corresponding Aza-BODIPYs **6** in deaerated solutions.

Compound	Chelate	Absorption [a][b]			Emission [a] [b] [c]
		$\lambda_{max\ near\text{-}UV}$, nm ($\varepsilon$, x$10^3$ $M^{-1}cm^{-1}$)	$\lambda_{max\ red}$, nm (ε, x10^3 $M^{-1}cm^{-1}$)	$\lambda_{shoulder}$, nm (ε, x10^3 $M^{-1}cm^{-1}$)	λ_{em}, nm
1a	None	302 (41)	596 (46)	---	644
	[d]	302 (42)	597 (47)	---	642
1b	None	322 (40)	627 (52)	---	684
	[d]	322 (41)	627 (54)	---	678
2a	Co(II)	305 (64)	603 (68)	675 (41)	---
	[d]	305 (64)	603 (68)	675 (40)	---
2b	Co(II)	325 (66)	632 (77)	691 (54)	---
	[d]	325 (63)	632 (73)	695 (51)	---
3a	Ni(II)	306 (62)	607 (58)	653 (49)	---
	[d]	306 (60)	607 (56)	655 (47)	---
3b	Ni(II)	325 (63)	631 (67)	692 (50)	---
	[d]	325 (54)	631 (58)	693 (57)	---
4a	Cu(II)	303 (57)	565 (55)	640 (51)	---
	[d]	303 (59)	566 (57)	641 (51)	---
4b	Cu(II)	322 (59)	591 (64)	670 (55)	---
	[d]	323 (63)	591 (71)	671 (58)	---
5a	Zn(II)	304 (66)	590 (88)	644 (56)	---
	[d]	303 (65)	591 (86)	642 (56)	---
5b	Zn(II)	326 (63)	612 (88)	675 (58)	---
	[d]	326 (64)	613 (90)	674 (59)	---
6a	BF_2^+	310 (25)	648 (80)	---	677
	[d]	310 (26)	651 (84)	---	678
6b	BF_2^+	335 (19)	691 (79)	---	723
	[d]	335 (19)	694 (81)	---	721

[a] in CH_2Cl_2 unless otherwise stated. [b] Acquisition at 293K. [c] Value from excitation at $\lambda_{max\ red}$. [d] in THF (for entire line).

The presence of two ligands brought into proximity by a metallic center in homoleptic complexes **2** to **5** gives rise to interesting behavior. As explained by O'Shea *et al.* for Cu(II) complex **4a,** the clear splitting of the longest wavelength band with λ values of 565 and 640 nm in DCM (slight bathochromic shift of 1 nm in THF for both λ) is indicative of the strain within the ligand.[32] The same behavior is observed for the Cu(II) complex **4b** bearing the four *p*-methoxy groups, with λ values red-shifted to 591 and 670 nm in DCM (slight bathochromic of 1 nm in THF for the second λ only). For other complexes **2**, **3** and **5a-b**, only a distinct red-shifted shoulder ($\lambda_{shoulder}$) of the main absorption band $\lambda_{max\ red}$ is observed. In that last series of complexes, only a slight shift is discernable between the $\lambda_{shoulder}$ recorded in DCM and THF, in the error margin of the measurement. Complexes **2b** to **5b** presented a bathochromic shift in DCM of $\lambda_{max\ red}$ compared to their tetra-phenyl counterpart ranging from 22 nm between Zn(II) complexes to 29 nm between Co(II) ones. As mentioned previously, the molar absorptivity of ligand **1b** was higher than for **1a** and this trend transferred to the homoleptic complexes. Through the series, M(II) complexes based on ligand **1b** exhibit a higher molar absorptivity by roughly 9 000 $M^{-1}cm^{-1}$ compared to the ones based on ADPM **1a** in DCM solution, except for Zn(II) complexes where no difference is observed. The more polar THF solution seems to yield the same overall trend, but with lower values in general than in DCM solution. Also to be mentioned, both Cu(II) complexes present an absorption spectrum in the red-region similar to their respective ligand and related M(II) complexes, which means that electronic transitions observed in that absorption region posses mainly a cyanine-like

character implying $\pi - \pi^*$ transitions.[21] This further support the idea that the first reduction process observed by electrochemistry is metal-centered on the Cu(II)/Cu(I) process. Similarly to what was reported by the groups of Gray and O'Shea in their papers on homoleptic M(II) complexes bearing ADPM derivatives, no emission was observed for the newly synthesized complexes **2b** to **5b**. Therefore, comparison of band-gap values with redox measurements need to be done based on an optical band-gap evaluated by using the intersection of the end of $\lambda_{shoulder}$ with the baseline (edge absorption) (Table I.2). Again, directly comparing values obtained by redox versus optical measurements for a given compound does not match perfectly. A systematic underestimation to various extend from the latter method is observed, still giving values that are closer compared to what was obtained from emissive compounds. However, the relative order between given M(II) complexes based on ADPM **1a** vs **1b** is consistent.

Aza-BODIPYs **6a** and **6b** absorbed in the red region ($\lambda_{max\ red}$) at 648 nm and 691 nm, respectively, in DCM solution. Measurements in THF solution give rise to a red-shift of 3 nm in both case. The bathochromic shift induced by the presence of the tetra-*p*-methoxyphenyl substituents reached 43 nm, slightly more than for the parent ADPM ligands. Noteworthy, the molar absorptivities of **6a** (84 000 $M^{-1}cm^{-1}$ in THF) and **6b** (81 000 $M^{-1}cm^{-1}$) are significantly increased compared to their ADPM precursors **1a-b**, a typical behavior in this family of chromophore.[51] In addition, the presence of four electron-rich –OMe group in **6b** gave a 46 cm^{-1} bathochromic shift in DCM to the sharp emission at 723 nm compared to tetra-phenyl **6a** (677 nm). Similar emission values were observed in

THF. All this is consistent with the shift observed in absorption, which shows potential for NIR applications if photo- and chemo-stability can be insured in the given system. Concerning the band-gaps, ΔE_{Opt} is systematically overestimated like in the case of ADPM **1a-b**. However, the relative order obtained is consistent for the two methods.

X-ray diffraction

Slow diffusion of hexanes into a CH_2Cl_2 solution at room temperature of **1b** and **2b** afforded the best single crystals for X-ray crystallography. Both compounds crystallized in the monoclinic space group $P2_1/c$ (see ESI). The molecular structure of the ligand **1b** confirms the conjugated nature of the azadipyrrole unit, with bond lengths for the bridging nitrogen to both pyrrole rings of 1.330(4) Å and 1.319(4) Å, for N2-C1 and N2-C17, respectively (Figure 1.9). All other bonds and distances are in the expected range for those found in conjugated systems of this type of chromophores. As already observed for other ADPM derivatives,[32] these structures show two very planar central pyrrolic rings (the angle of intersection between the two is negligible at 1.29(3)°) and four twisted *p*-methoxyphenyl groups. Of interest, ADPM **1b** features internal asymmetry relative to the pyrrolic rings in the solid state, which is due to tautomerism for the pyrrole hydrogen. The structure was therefore refined with a disordered hydrogen atom on N1 and N3 atoms, leading a ratio of about 1:2 in favor of N3. In addition, the distance between the centroid of the phenyl rings in position 3 of the pyrrolic ring is slightly shorter when compared to the ones in position 5 (6.29(5) Å and 7.12(5) Å, respectively). Also, the tilt between the rings formed by the azadipyrrole moiety and phenyl rings varies from 24.62(9)° for distal positions to only 18.47(8)° for proximal ones.

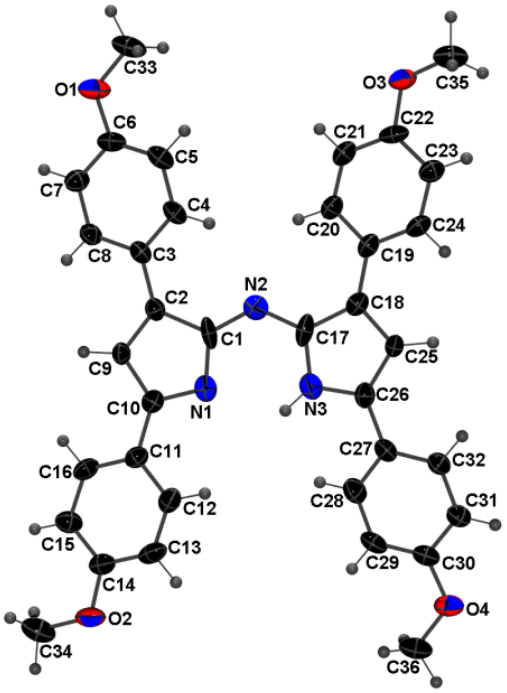

(a)

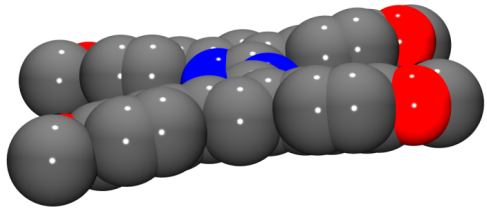

(b)

Figure 1.9 – (a) Thermal ellipsoid projection of the ligand **1b** (ellipsoids are shown at 30% probability). (b) Space-filling model of the view of L along the central plane, showing the tilt of the rings.

The hydrogen atoms have been omitted for clarity. Selected bonds and angles lengths: N1-C1 1.407(5) Å; N1-C10 1.348(4) Å; N2-C1 1.327(4) Å; N2-C17 1.319(4) Å; N3-C17 1.374(5) Å; N3-C26 1.361(4) Å; C1-N2-C17 126.5(3)°; N1-C1-N2 121.2(3)°; N2-C17-N3 122.3(3)°.

The crystal structure of the homoleptic Co(II) complex **2b** is shown in Figure 10. The two ADPM bidentate ligands **1b** force a distorted tetrahedral geometry at the metal center, with Co-N bond distances ranging from 1.975(2) Å for Co-N6 to 1.992(3) Å for Co-N4 and chelate angle of N1-Co-N3 (94.7(1)°) and N4-Co-N6 (94.5(1)°) being slightly different from each other. Other bonds distances and angles are generally very similar to those found by Gray and O'Shea for related complexes.[31,32] As expected, the chelating ligand is planar, with an angle between best-fit planes of 67°. The crystal structure of **2b** also revealed that upon coordination of the ligands, the phenyl rings orientate in a clockwise fashion (Figure 10b) although no significant π interaction was found in the crystal packing. Again, this behavior compares with similar complexes reported by Gray and O'Shea.

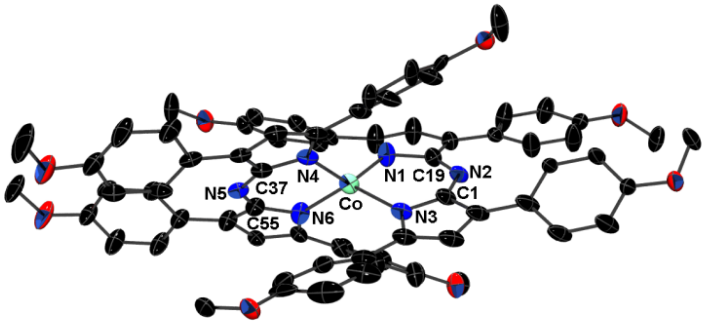

(a)

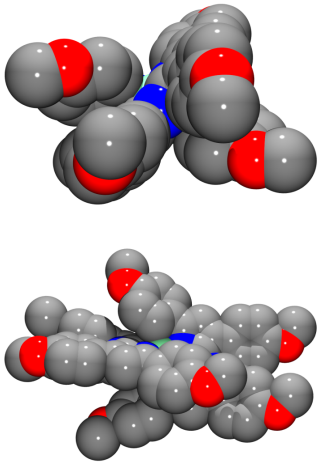

(b)

Figure 1.10 – Thermal ellipsoid projection of Co(II) complex **2b**. (a) Ellipsoids are shown at 30% probability; the labeling and the H atoms were omitted for clarity). (b) Space-filling model of the view of Co along the N2-Co-N5 plane and N1-Co-N6, showing the tilt of the rings.

The disorder over the methoxyphenyl rings - corresponding to the 30 % of occupancy factor - were omitted for clarity. The hydrogen atoms and disordered atoms have been omitted for clarity. Selected bonds and angles lengths: Co-N1 1.975(3) Å; Co-N3 1.987(3) Å; Co-N4 1.992(3) Å; Co-N6 1.975(2) Å; N1-Co-N4 106.5(1)°; N3-Co-N6 108.08(11)°; N1-Co-N6 128.6(1)°; N3 -Co-N4 128.2(1)°.

1. 5 – Conclusions

In summary, we reported herein a high-yielding microwave-assisted synthesis of four new homoleptic complexes of Co(II), Ni(II), Co(II) and Zn(II) based on the tetra-*p*-methoxyphenyl-ADPM ligand **1b**. Those complexes were put in relation with already known ADPM homoleptic complexes of the same M(II) series and related BF_2^+ chelates (Aza-BODIPY) for a better understanding of trends arising from substitution of the chelate and/or electron-donating effect of the *p*-methoxy substituents. Electrochemical characterization revealed four main observations for the organometallic complexes: i) access to one additional oxidation and one reduction process for complexes **2b-5b** compared to related ADPM **1b**; ii) presence of two additional reduction processes upon coordination to Cu(II) for both **4a** and **4b** complexes; iii) a general destabilization of HOMOs to the same extend throughout the M(II) series; iv) a general stabilization of LUMOs to various extend, except for Cu(II) derivatives **4a** and **4b**. Those two Cu(II) complexes presented a metal-centered first reduction process (Cu(II) to Cu(I)) that engender a decoordination of one ADPM ligand by geometrical rearrangement and also a lower ΔE_{Redox} compared to related complexes. Optical characterization further support this hypothesis by exhibiting similar absorption properties for Cu(II) complexes compared to Co(II), Ni(II) and Zn(II) ones and their free ligands. Such a behavior for observed electronic transitions is indicative of a cyanine-like character implying mainly $\pi - \pi^*$ transitions. As might be expected from electron rich –OMe substituents, emission of the

tetra-*p*-methoxy-ADPM **1b** and Aza-BODIPY derivative **6b** gave bathochromic shift compared to related tetra-aryl-ADPM compounds previously reported. X-Ray structures for the tetra-*p*-methoxyphenyl-ADPM ligand **1b** and related Co(II) complex **2b** was also discussed. Hopefully, this study will provide useful insights to researchers on the effect of substituents for stable ADPM derivatives in their quest for NIR chromophores.

Acknowledgements

GSH thanks the Natural Sciences and Engineering Research Council of Canada, the Centre for Self-Assembled Chemical Structures and the Université de Montréal (UdeM) for financial support. AB is thankful of NSERC, FQRNT and Saint-Jean Photochemicals Inc. (sjpc.com) for a BMP-Innovation grant and to UdeM for an excellence grant. JGF is grateful to the Canadian Postdoctoral Research Fellowship Programme (PDRF). AB is grateful to Anne-Catherine Bédard for useful scientific discussions and to Daniel Chartrand for help on X-Ray structures. The authors also thank the Combinational Chemistry, NMR, Mass Spectrometry, Elemental Analysis and X-Ray laboratories of UdeM for their help.

Associated content

Supporting Information. HR-ESIMS for newly synthesized complexes **2b** to **5b**; cyclic and differential pulse voltammograms for ADPM **1a-b**, complexes **2** to **5a-b** and Aza-BODIPYs **6a-b**; absorption spectrum in DCM for ADPM **1a**, complexes **2a** to **5a** and Aza-BODIPYs **6a**; absorption spectrum in THF for ADPM **1a-b**, complexes **2** to **5a-b** and Aza-BODIPYs **6a-b**; emission spectrum in DCM for **1a** and **6a;** emission spectrum in THF for **1a-b** and **6a-b**; crystal data and details of the structure determination for **1b** (CCDC Number 876955) and **2b** (CCDC Number 876954) along with Ortep representation of **2b** at the 50% probability level. This material is available free of charge via the Internet at http://pubs.acs.org.

1. 6 – Bibliography

(1) Boens, N.; Leen, V.; Dehaen, W. *Chem. Soc. Rev.* **2012**, *41*.

(2) Ulrich, G.; Ziessel, R.; Harriman, A. *Angew. Chem., Int. Ed.* **2008**, *47*, 1184.

(3) Smith, N. W.; Alonso, A.; Brown, C. M.; Dzyuba, S. V. *Biochem. Biophys. Res. Commun.* **2010**, *391*, 1455.

(4) Nierth, A.; Kobitski, A. Y.; Nienhaus, G. U.; Jaschke, A. *J. Am. Chem. Soc.* **2010**, *132*, 2646.

(5) Buyukcakir, O.; Bozdemir, O. A.; Kolemen, S.; Erbas, S.; Akkaya, E. U. *Org. Lett.* **2009**, *11*, 4644.

(6) Nepomnyashchii, A. B.; Bard, A. J. *Acc. Chem. Res.* **2012**.

(7) Ziessel, R.; Harriman, A. *Chem. Commun.* **2010**.

(8) Iehl, J.; Nierengarten, J.-F.; Harriman, A.; Bura, T.; Ziessel, R. *J. Am. Chem. Soc.* **2012**, *134*, 988.

(9) Kolemen, S.; Bozdemir, O. A.; Cakmak, Y.; Barin, G.; Erten-Ela, S.; Marszalek, M.; Yum, J.-H.; Zakeeruddin, S. M.; Nazeeruddin, M. K.; Gratzel, M.; Akkaya, E. U. *Chem. Sci.* **2011**, *2*, 949.

(10) Bozdemir, O. A.; Yilmaz, M. D.; Buyukcakir, O.; Siemiarczuk, A.; Tutas, M.; Akkaya, E. U. *New J. Chem.* **2010**, *34*, 151.

(11) Rio, Y.; Seitz, W.; Gouloumis, A.; Vazquez, P.; Sessler, J. L.; Guldi, D. M.; Torres, T. *Chem. - Eur. J.* **2010**, *16*, 1929.

(12) Teets, T. S.; Partyka, D. V.; Esswein, A. J.; Updegraff, J. B., III; Zeller, M.; Hunter, A. D.; Gray, T. G. *Inorg. Chem.* **2007**, *46*, 6218.

(13) Partyka, D. V.; Deligonul, N.; Washington, M. P.; Gray, T. G. *Organomet.* **2009**, *28*, 5837.

(14) Teets, T. S.; Updegraff, J. B., III; Esswein, A. J.; Gray, T. G. *Inorg. Chem.* **2009**, *48*, 8134.

(15) Loudet, A.; Burgess, K. *Chem. Rev.* **2007**, *107*, 4891.

(16) Hall, M. J.; McDonnell, S. O.; Killoran, J.; O'Shea, D. F. *J. Org. Chem.* **2005**, *70*, 5571.

(17) Yakubovskyi, V. P.; Shandura, M. P.; Kovtun, Y. P. *Synth. Commun.* **2010**, *40*, 944.

(18) Li, Y.; Dolphin, D.; Patrick, B. O. *Tetrahedron Lett.* **2010**, *51*, 811.

(19) Bellier, Q.; Dalier, F.; Jeanneau, E.; Maury, O.; Andraud, C. *New J. Chem.* **2012**, *36*, 768

(20) Amin, A. N.; El-Khouly, M. E.; Subbaiyan, N. K.; Zandler, M. E.; Fukuzumi, S.; D'Souza, F. *Chem. Commun.* **2012**, *48*, 206.

(21) Le Guennic, B.; Maury, O.; Jacquemin, D. *Phys. Chem. Chem. Phys.* **2012**, *14*.

(22) D'Souza, F.; Amin, A. N.; El-Khouly, M. E.; Subbaiyan, N. K.; Zandler, M. E.; Fukuzumi, S. *J. Am. Chem. Soc.* **2011**, *134*, 654.

(23) Batat, P.; Cantuel, M.; Jonusauskas, G.; Scarpantonio, L.; Palma, A.; O'Shea, D. F.; McClenaghan, N. D. *J. Phys. Chem. A* **2011**, *115*, 14034

(24) Lu, H.; Shimizu, S.; Mack, J.; Shen, Z.; Kobayashi, N. *Chem. - Asian J.* **2011**, *6*, 1026.

(25) Gresser, R.; Hummert, M.; Hartmann, H.; Leo, K.; Riede, M. *Chem. - Eur. J.* **2011**, *17*, 2939

(26) Gao, L.; Senevirathna, W.; Sauvé, G. v. *Org. Lett.* **2011**, *13*, 5354.

(27) Tasior, M.; Murtagh, J.; Frimannsson, D. O.; McDonnell, S. O.; O'Shea, D. F. *Org. Biomol. Chem.* **2010**, *8*, 522.

(28) Yuan, M.; Yin, X.; Zheng, H.; Ouyang, C.; Zuo, Z.; Liu, H.; Li, Y. *Chem. - Asian J.* **2009**, *4*, 707.

(29) Mueller, T.; Gresser, R.; Leo, K.; Riede, M. *Sol. Energy Mater. Sol. Cells* **2012**, *99*, 176.

(30) Leblebici, S. Y.; Catane, L.; Barclay, D. E.; Olson, T.; Chen, T. L.; Ma, B. *ACS Appl. Mater. Interfaces* **2011**, *3*, 4469.

(31) Teets, T. S.; Partyka, D. V.; Updegraff, J. B.; Gray, T. G. *Inorg. Chem.* **2008**, *47*, 2338.

(32) Palma, A.; Gallagher, J. F.; Mueller-Bunz, H.; Wolowska, J.; McInnes, E. J. L.; O'Shea, D. F. *Dalton Trans.* **2009**, 273.

(33) Rogers, M. A. T. *J. Chem. Soc. (Resumed)* **1943**, 590.

(34) Rousseau, T.; Cravino, A.; Ripaud, E.; Leriche, P.; Rihn, S.; De Nicola, A.; Ziessel, R.; Roncali, J. *Chem. Commun.* **2010**, *46*, 5082.

(35) Kubo, Y.; Watanabe, K.; Nishiyabu, R.; Hata, R.; Murakami, A.; Shoda, T.; Ota, H. *Org. Lett.* **2011**, *13*, 4574.

(36) In *Bruker Molecular Analysis Research Tool*; Bruker AXS Inc.: Madison, WI, 2009, p 53719.

(37) Sheldrick, G. M. In *Bruker Area Detector Absorption Corrections*; Bruker AXS Inc.: Madison, WI, 1996, p 53719.

(38) ; 6.12 ed.; Bruker AXS Inc.: Madison, WI, 2001, p 53719.

(39) Mishra, A.; Bäuerle, P. *Angew. Chem. Int. Ed. Engl.* **2012**, *51*, 2020.

(40) Li, Y. *Acc. Chem. Res.* **2012**, *45*, 723.

(41) Blouin, N.; Michaud, A.; Gendron, D.; Wakim, S.; Blair, E.; Neagu-Plesu, R.; Belletête, M.; Durocher, G.; Tao, Y.; Leclerc, M. *J. Am. Chem. Soc.* **2007**, *130*, 732.

(42) Zeng, L.; Jiao, C.; Huang, X.; Huang, K.-W.; Chin, W.-S.; Wu, J. *Org. Lett.* **2011**, *13*, 6026.

(43) Jørgensen, M.; Norrman, K.; Gevorgyan, S. A.; Tromholt, T.; Andreasen, B.; Krebs, F. C. *Adv. Mater.* **2012**, *24*, 580.

(44) Quartarolo, A. D.; Russo, N.; Sicilia, E. *Chem. - Eur. J.* **2006**, *12*, 6797.

(45) Smith, K. M. *Porphyrins and Metalloporphyrins*; Elsevier, New York, N.Y., 1975.

(46) Armaroli, N. *Chem. Soc. Rev.* **2001**, *30*, 113.

(47) Accorsi, G.; Armaroli, N.; Duhayon, C.; Saquet, A.; Delavaux-Nicot, B.; Welter, R.; Moudam, O.; Holler, M.; Nierengarten, J.-F. *Eur. J. Inorg. Chem.* **2010**, *2010*, 164.

(48) Guy, R.; Jones, R. *Aust. J. Chem.* **1966**, *19*, 1871.

(49) Jacquemin, D.; Planchat, A.; Adamo, C.; Mennucci, B. *J. Chem. Theo. Comp.* **2012**, *8*, 2359.

(50) Chibani, S.; Le Guennic, B.; Charaf-Eddin, A.; Maury, O.; Andraud, C.; Jacquemin, D. *J. Chem. Theo. Comp.* **2012**.

(51) Gorman, A.; Killoran, J.; O'Shea, C.; Kenna, T.; Gallagher, W. M.; O'Shea, D. F. *J. Am. Chem. Soc.* **2004**, *126*, 10619.

Partie B - Informations Supplémentaires

Figure 1.11 – HR-ESIMS of compound **2b** and its fitting with theoretical spectrum.

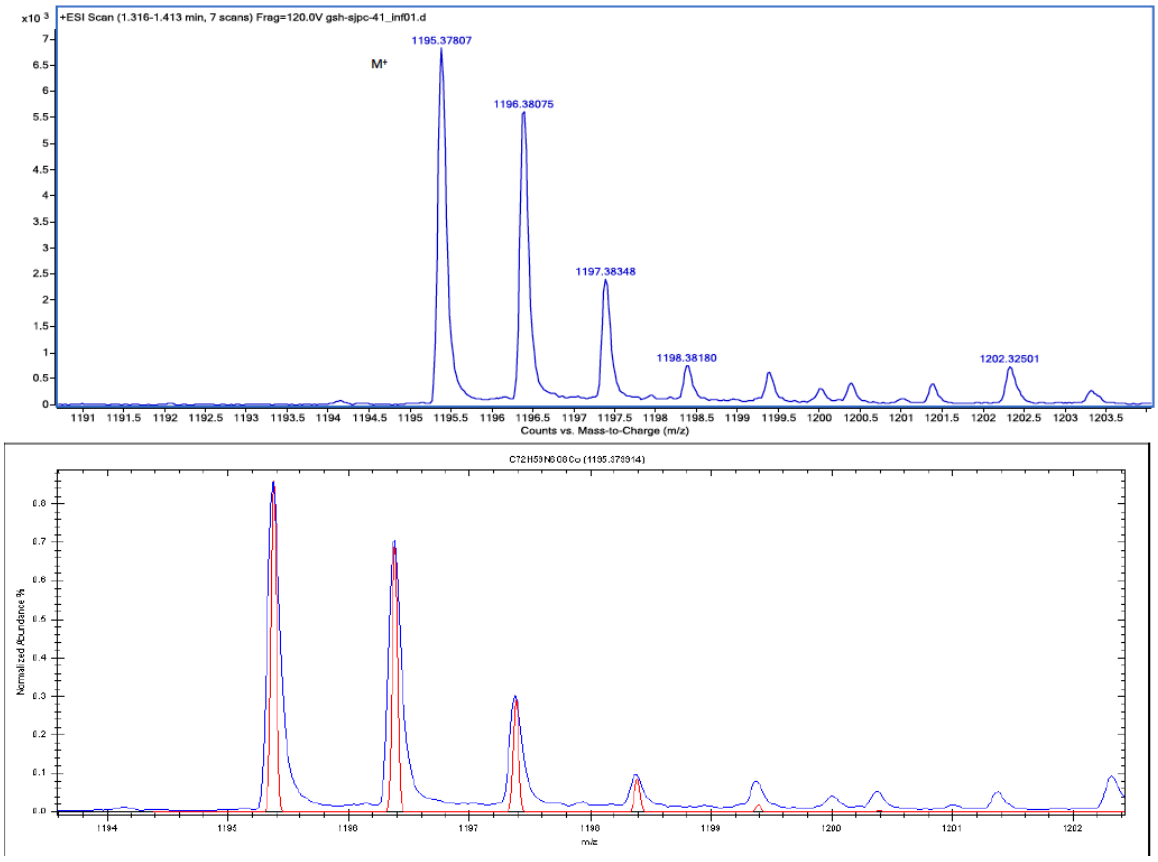

Figure 1.12 – HR-ESIMS of compound **3b** and its fitting with theoretical spectrum.

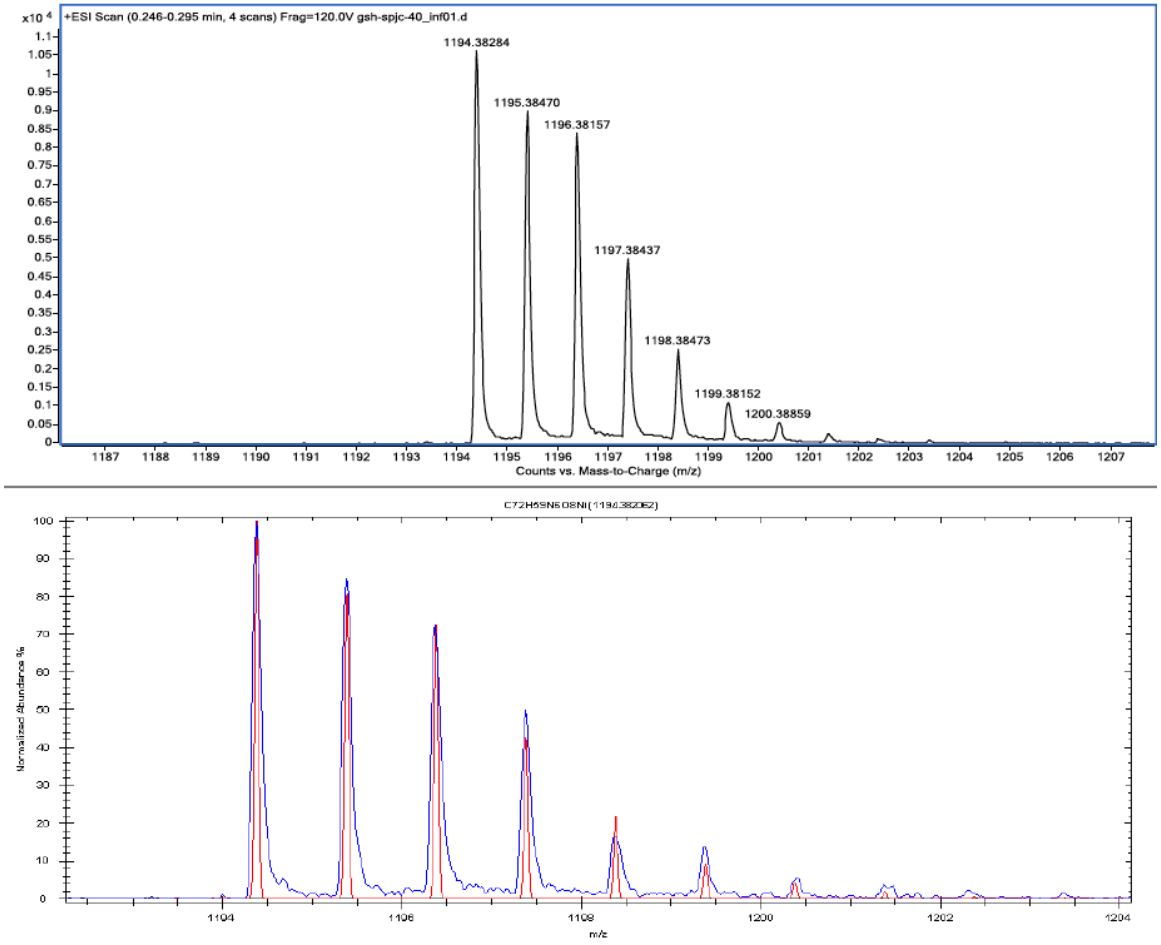

Figure 1.13 – HR-ESIMS of compound **4b** and its fitting with theoretical spectrum.

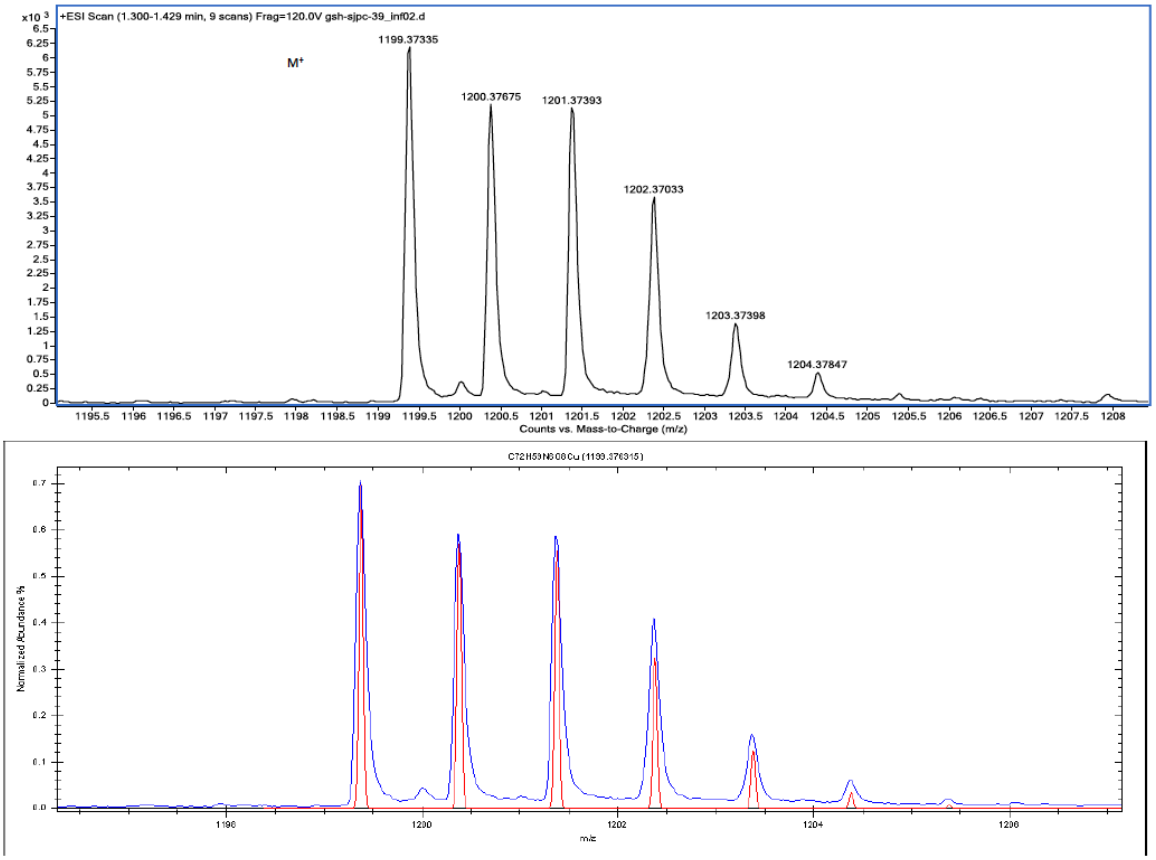

Figure 1.14 – HR-ESIMS of compound **5b** and its fitting with theoretical spectrum.

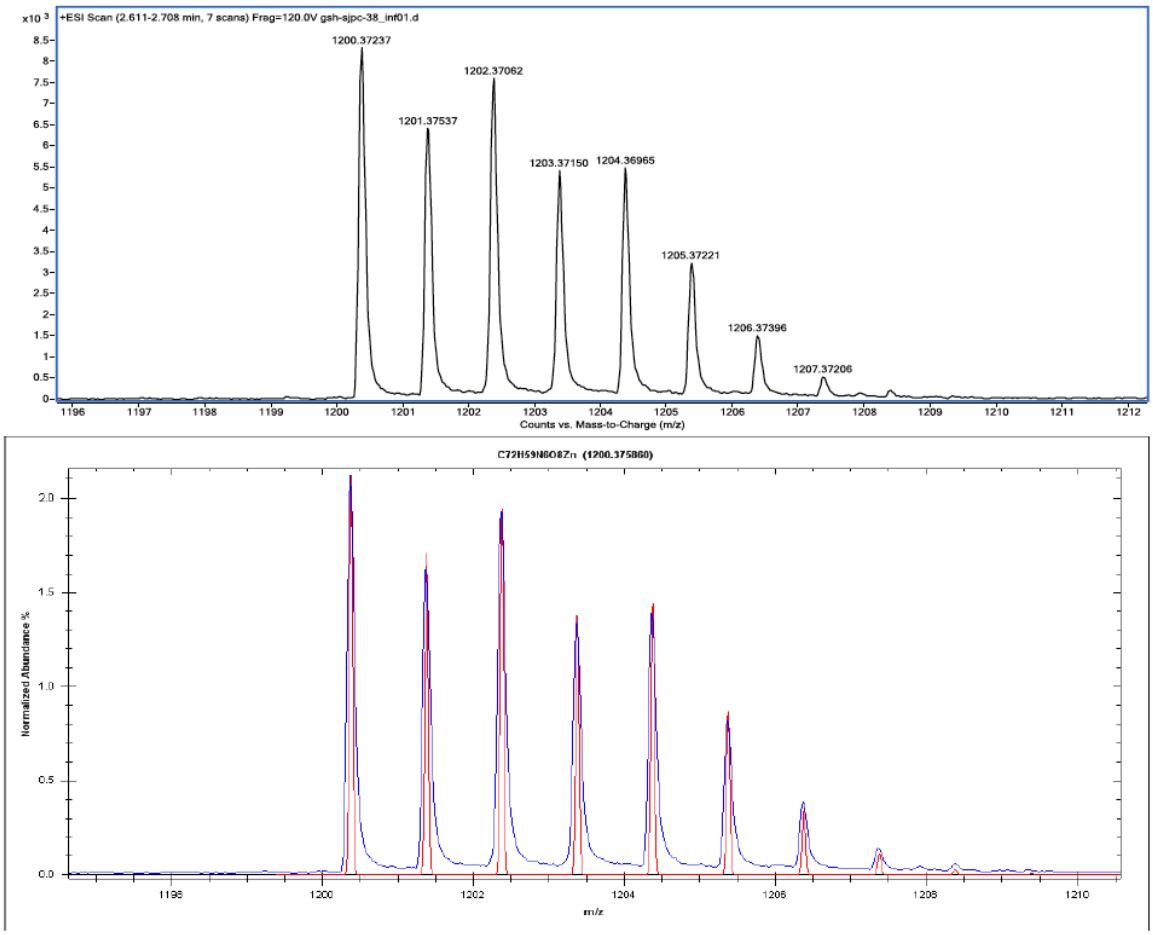

Figure 1.15 – CV of ligand **1a** with ferrocene as internal reference.
(0.46V vs SCE in DCM) (Scan rate of 50 mV/s at R.T.)

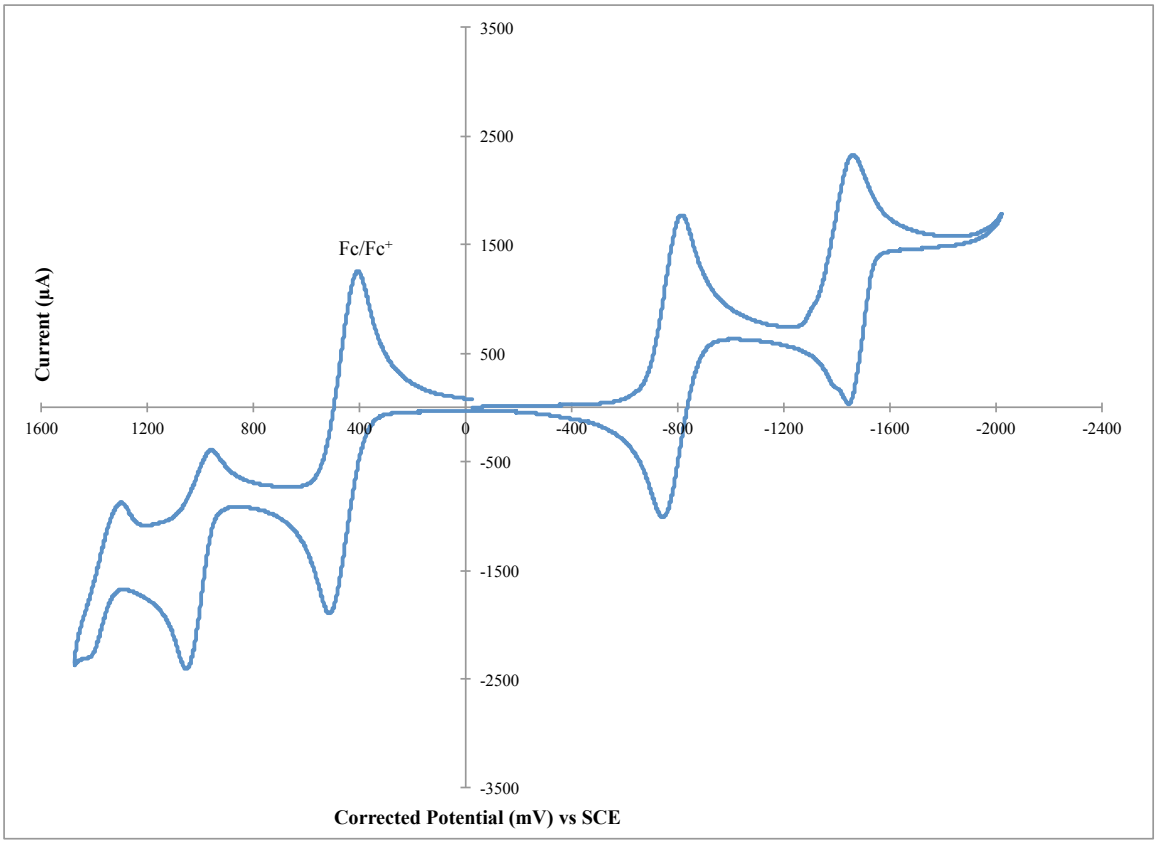

Figure 1.16 – CV of ligand **1b** with ferrocene as internal reference.
(0.46V vs SCE in DCM) (Scan rate of 50 mV/s at R.T.)

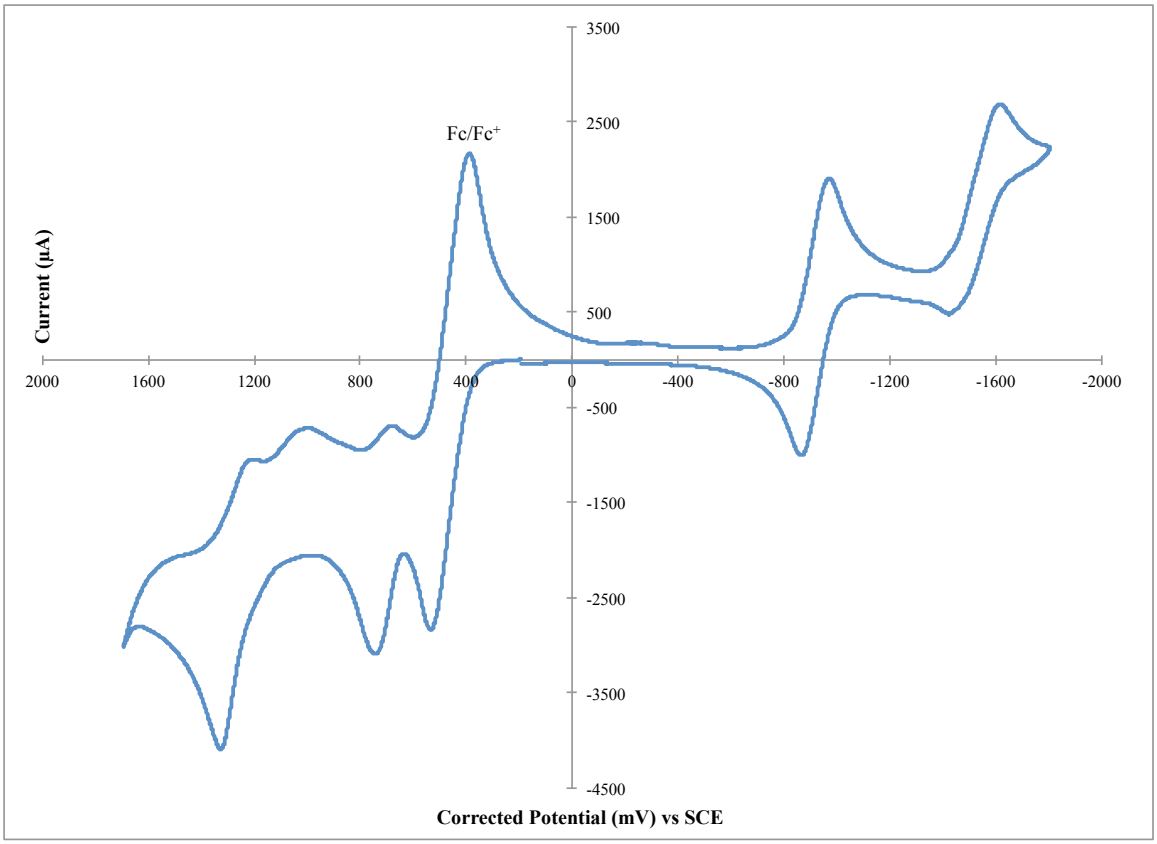

Figure 1.17 – DPV of ligand **1b** with ferrocene as internal reference.
(0.46V vs SCE in DCM) (Scan rate of 50 mV/s at R.T.)

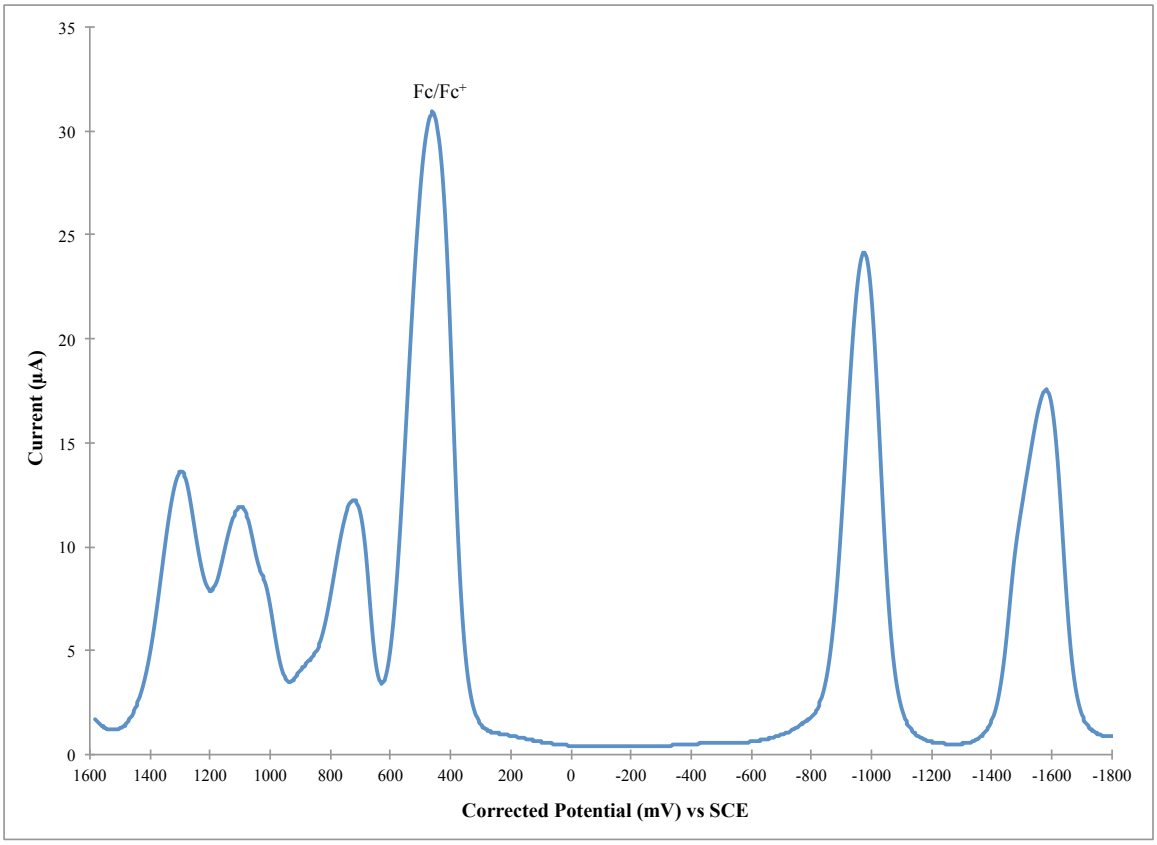

Figure 1.18 – DPV of ligand **1b** before addition of ferrocene.

(Scan rate of 50 mV/s in DCM at R.T.)

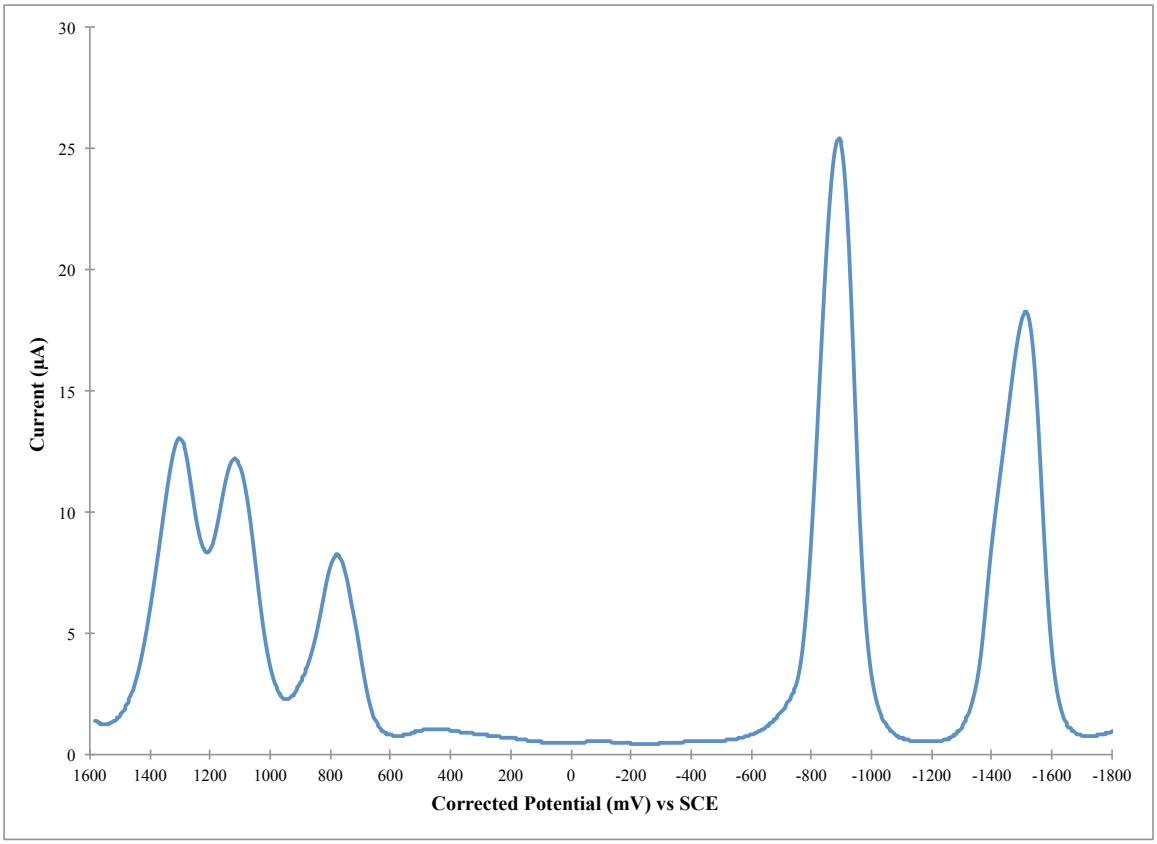

Figure 1.19 – CV of Co(II) complex **2a** with ferrocene as internal reference.
(0.46V vs SCE in DCM) (Scan rate of 50 mV/s at R.T.)

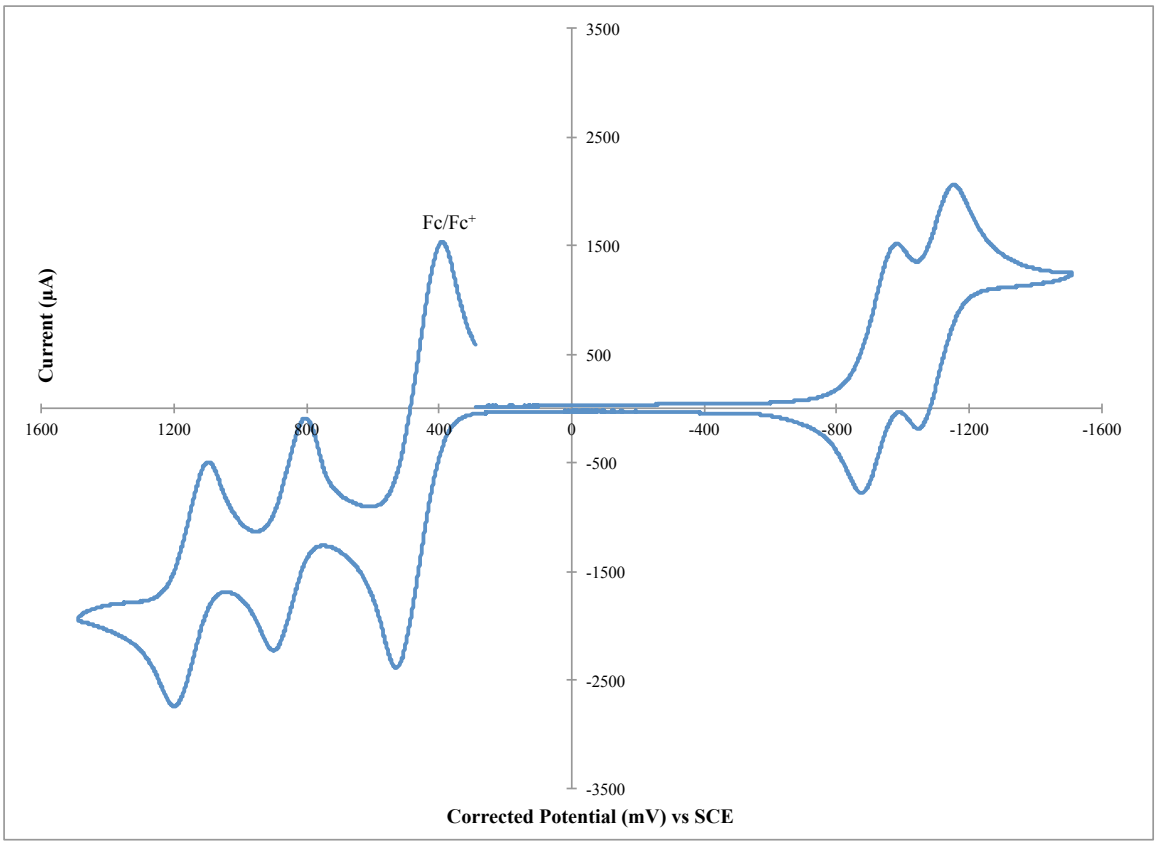

Figure 1.20 – CV of Co(II) complex **2b** with ferrocene as internal reference (0.46V vs SCE in DCM) (Scan rate of 50 mV/s at R.T.)

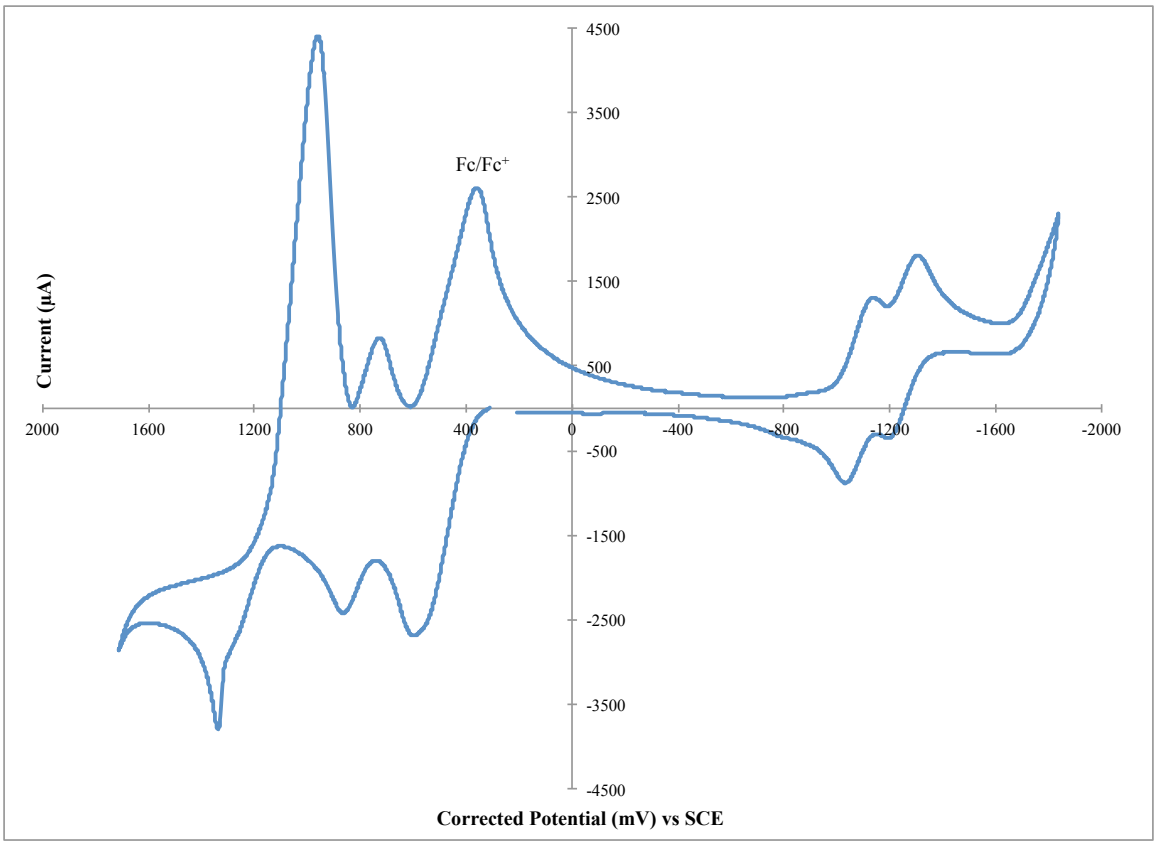

Figure 1.21 – CV of Co(II) complex **2b** before addition of ferrocene.
(Scan rate of 50 mV/s in DCM at R.T.)

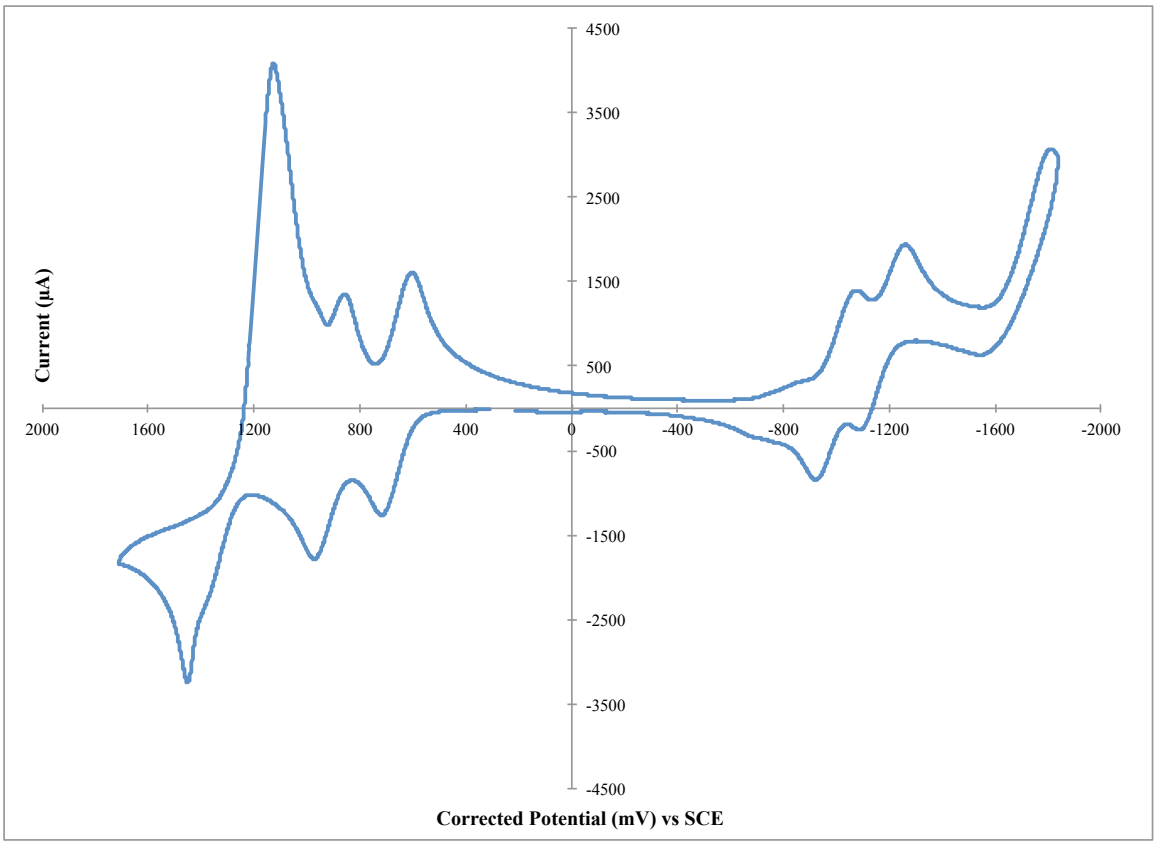

Figure 1.22 – CV of Co(II) complex **2b** in the 2 first oxidation peaks region, showing the pseudo-reversible behavior.
(Scan rate of 50 mV/s in DCM at R.T. Before addition of ferrocene)

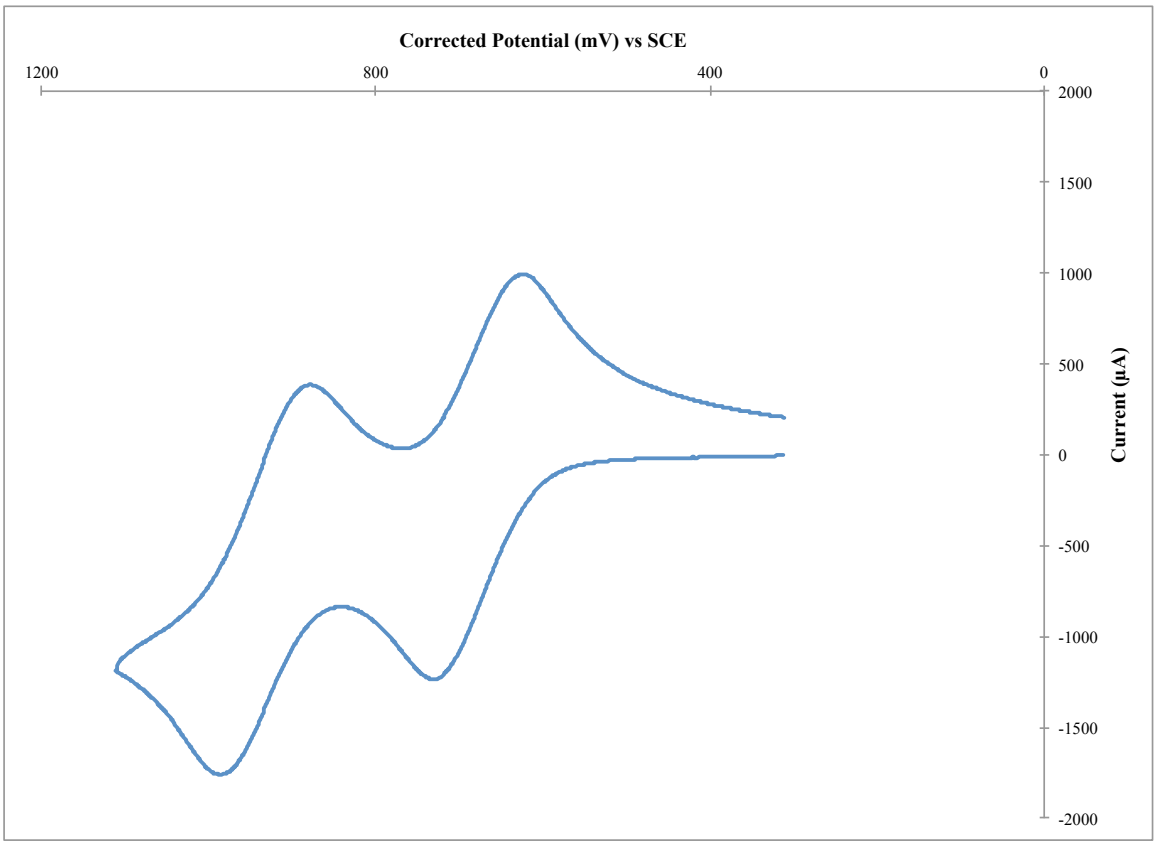

Figure 1.23 – DPV of Co(II) complex **2b** with ferrocene as internal reference (0.46V vs SCE in DCM) (Scan rate of 50 mV/s at R.T.)

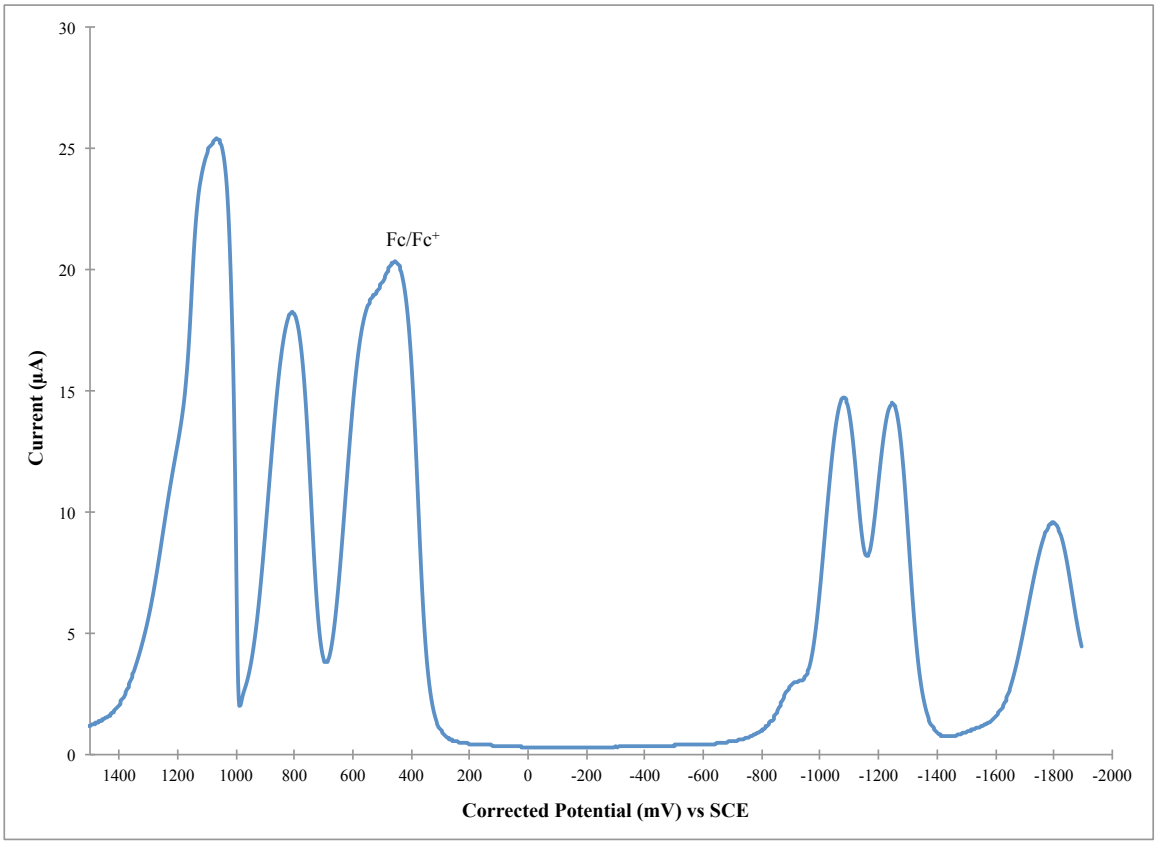

Figure 1.24 – DPV of Co(II) complex **2b** with ferrocene as internal reference in the oxidation window only; showing the presence of 2 near oxydation peaks at 1.21 and 1.27 V respectively. (0.46V vs SCE in DCM) (Scan rate of 50 mV/s at R.T.)

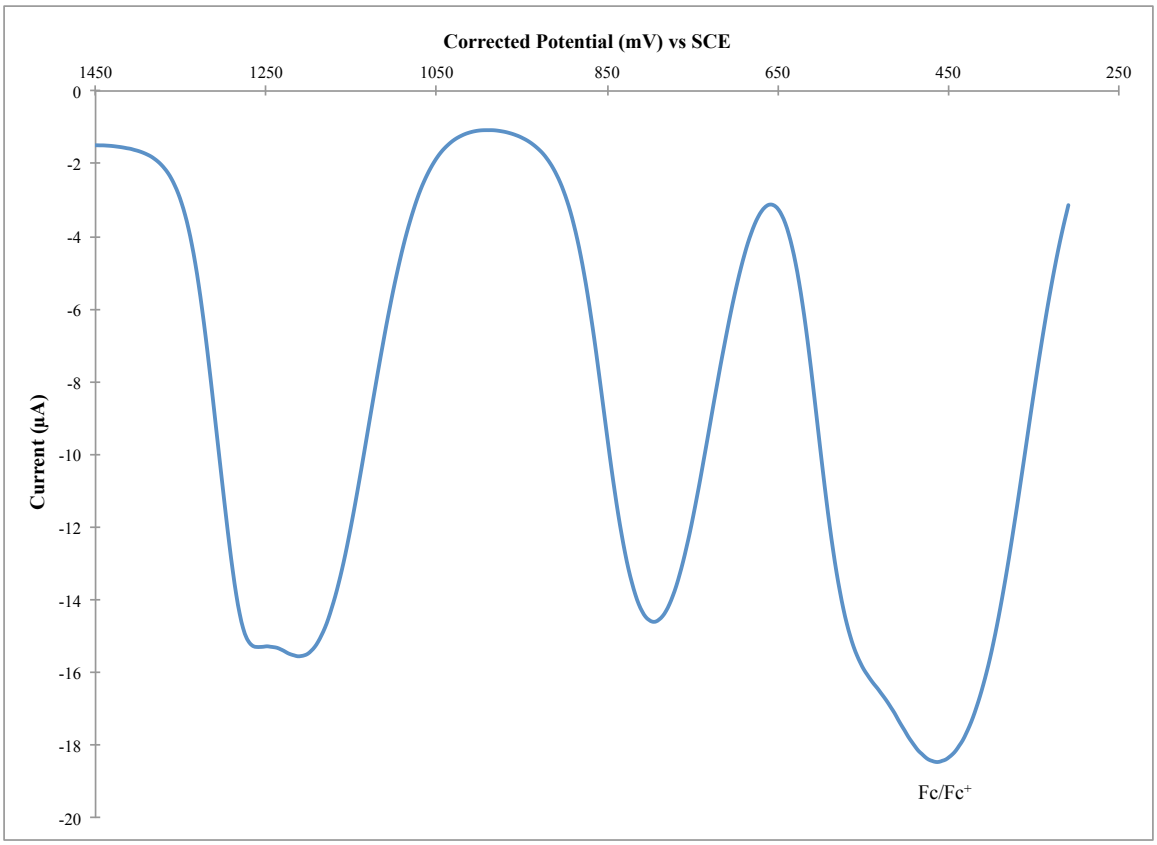

Figure 1.25 – DPV of Co(II) complex **2b** before addition of ferrocene.
(Scan rate of 50 mV/s in DCM at R.T.)

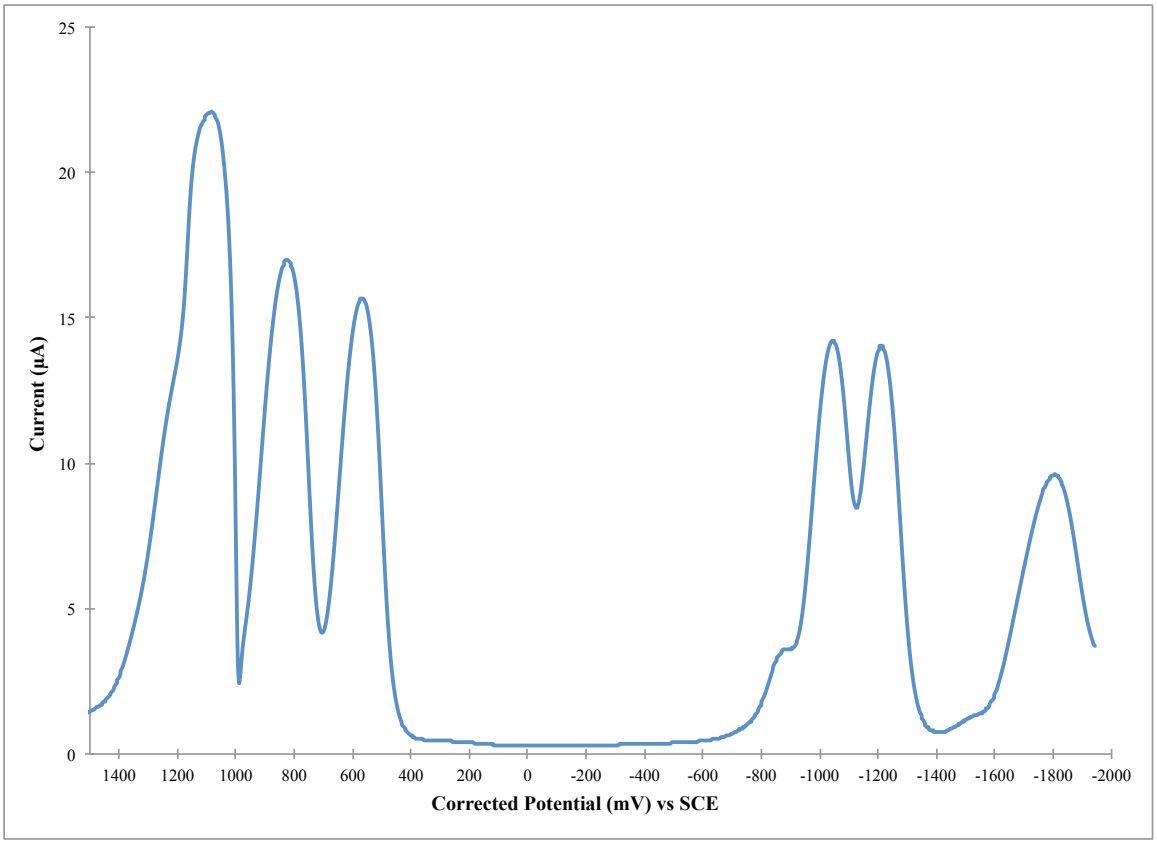

Figure 1.26 – CV of Ni(II) complex **3a** with ferrocene as internal reference.
(0.46V vs SCE in DCM) (Scan rate of 50 mV/s at R.T.)

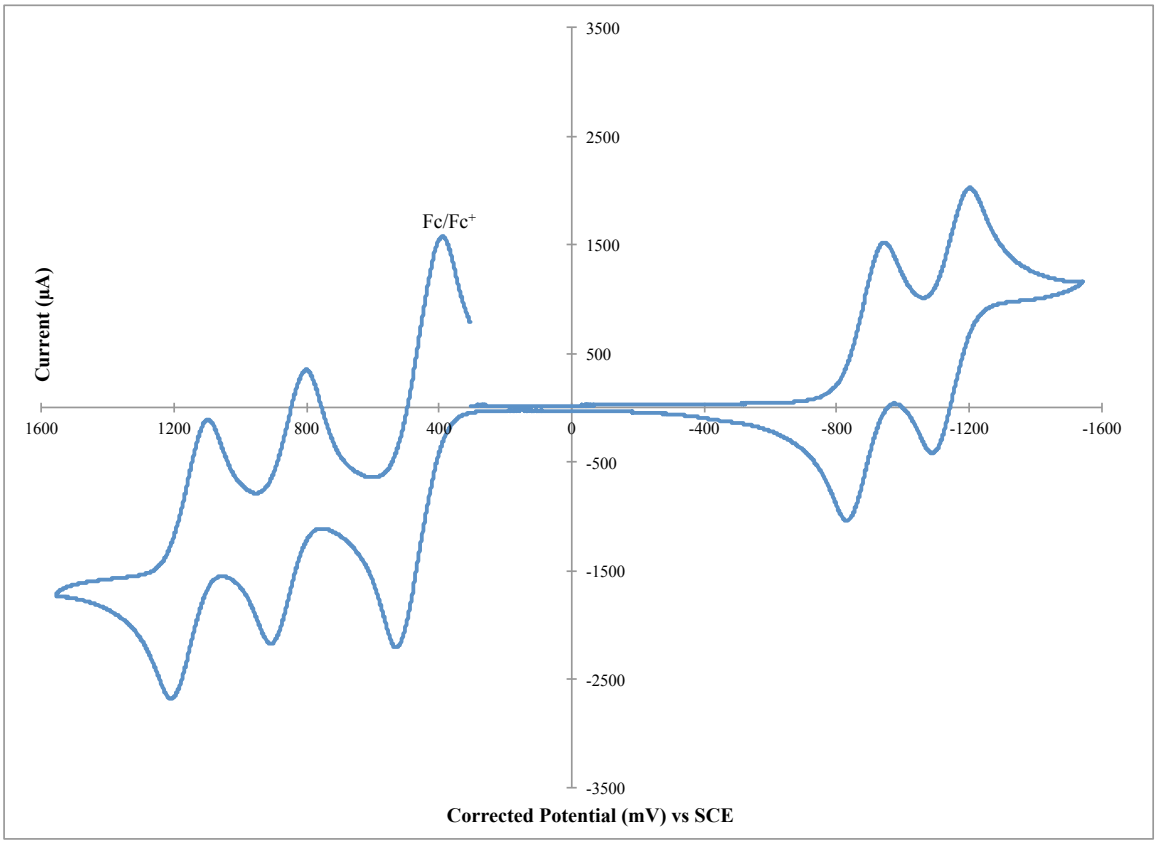

Figure 1.27 – CV of Ni(II) complex **3b** with ferrocene as internal reference (0.46V vs SCE in DCM) (Scan rate of 50 mV/s at R.T.)

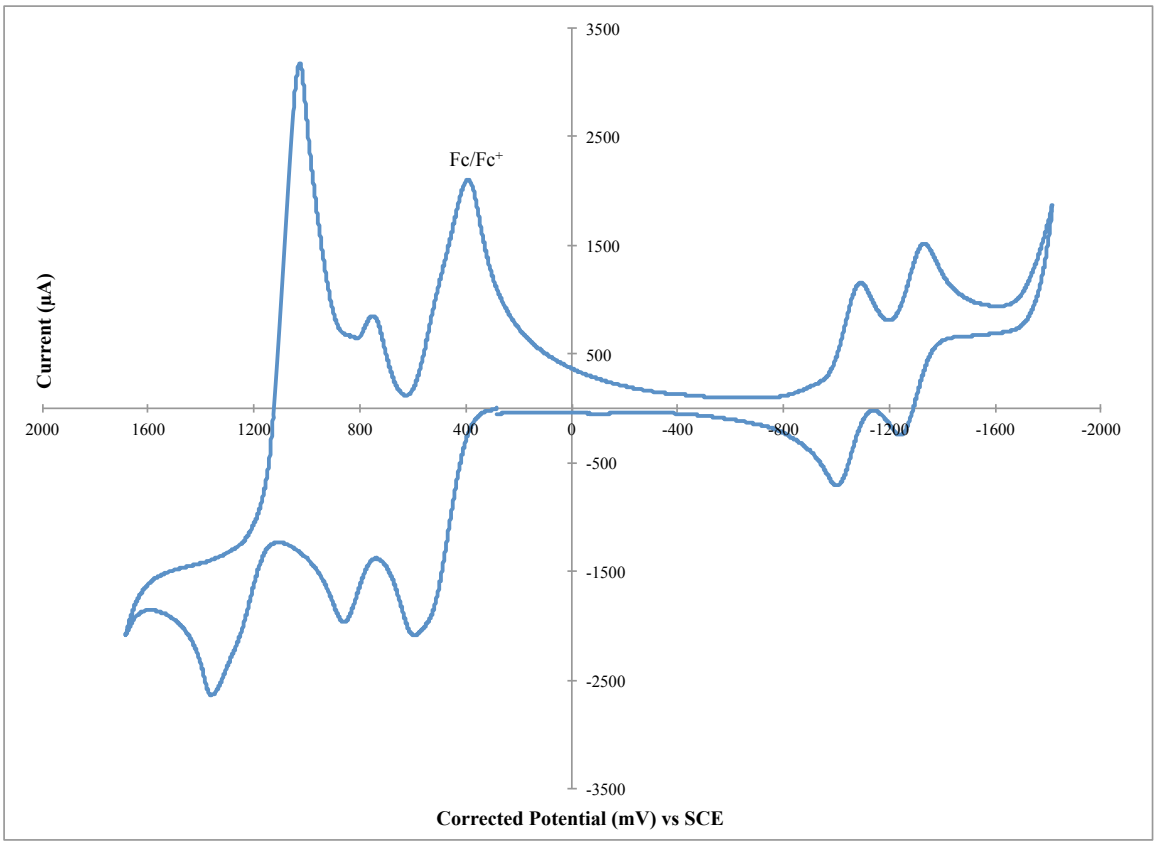

Figure 1.28 – CV of Ni(II) complex **3b** before addition of ferrocene.
(Scan rate of 50 mV/s in DCM at R.T.)

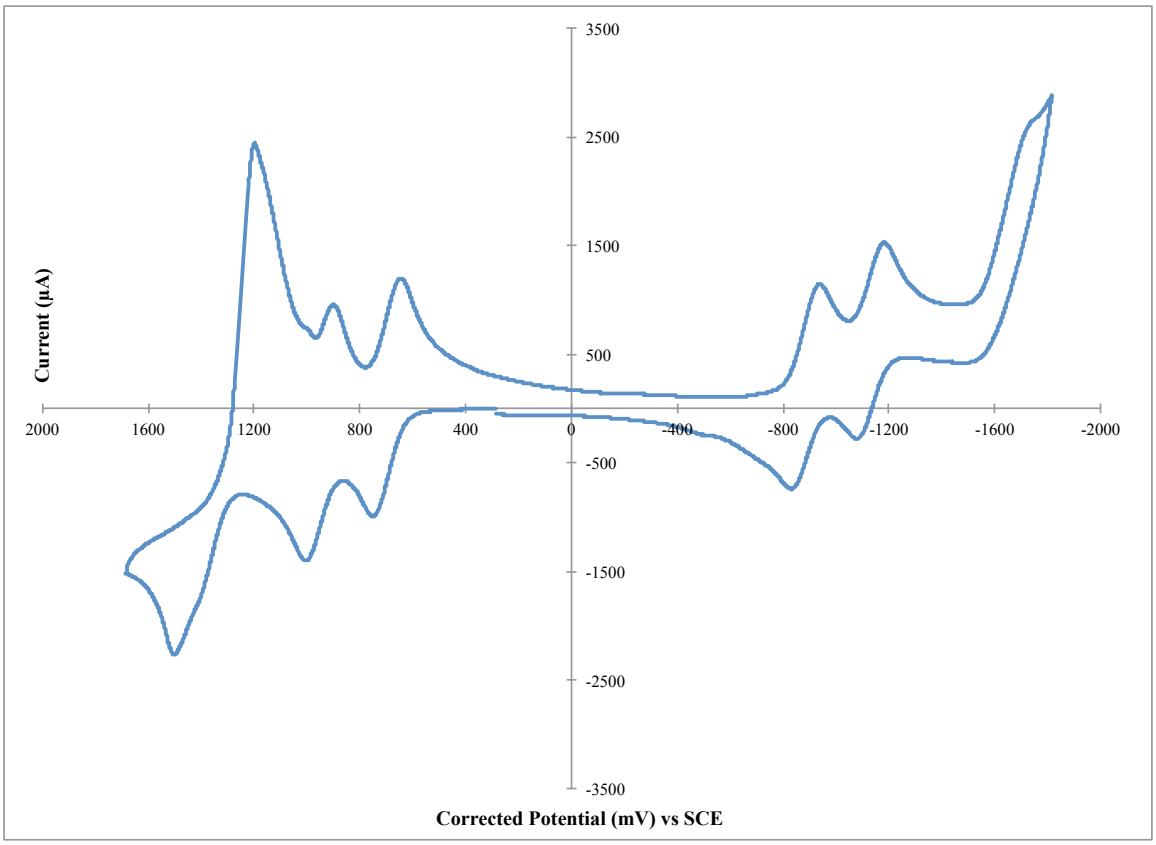

Figure 1.29 – CV of Ni(II) complex **3b** in the potential region of the 2 first oxidation peaks, showing the pseudo-reversible behavior.
(Scan rate of 50 mV/s in DCM at R.T. Before addition of ferrocene)

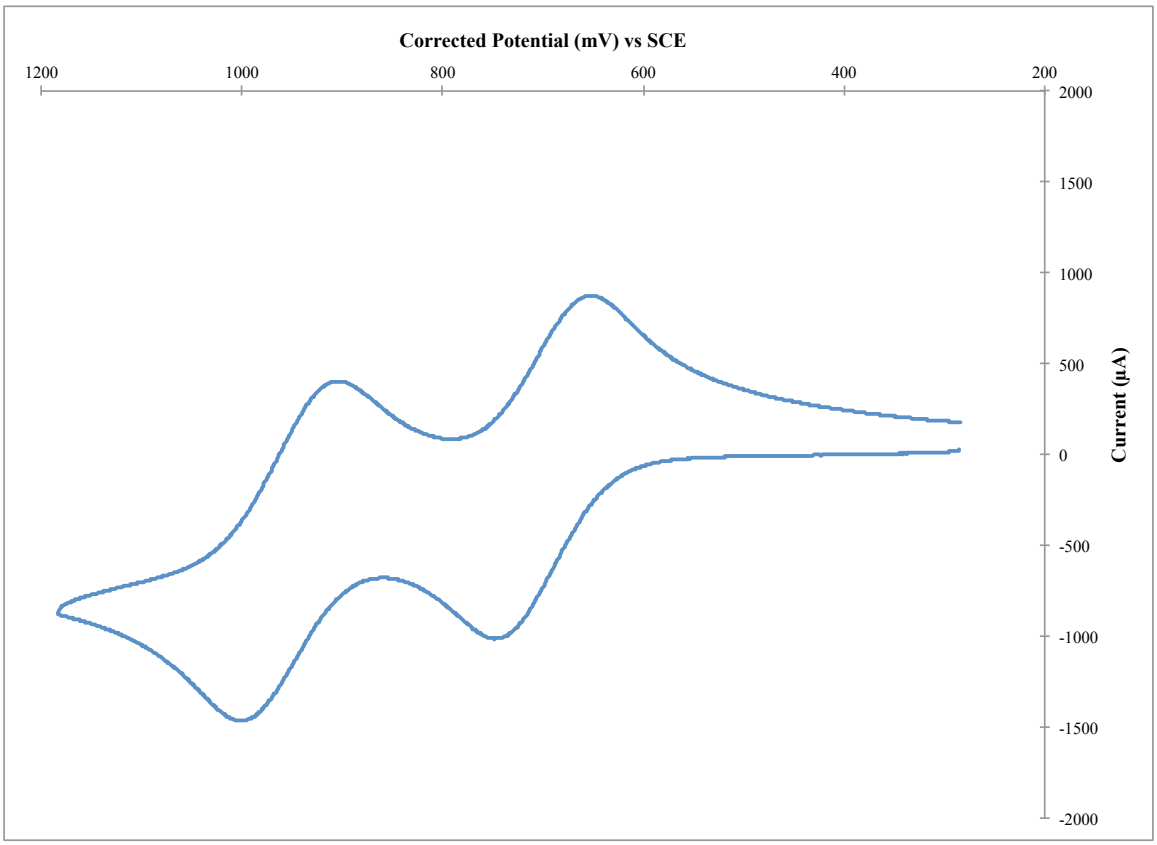

Figure 1.30 – DPV of Ni(II) complex **3b** with ferrocene as internal reference (0.46V vs SCE in DCM) (Scan rate of 50 mV/s at R.T.)

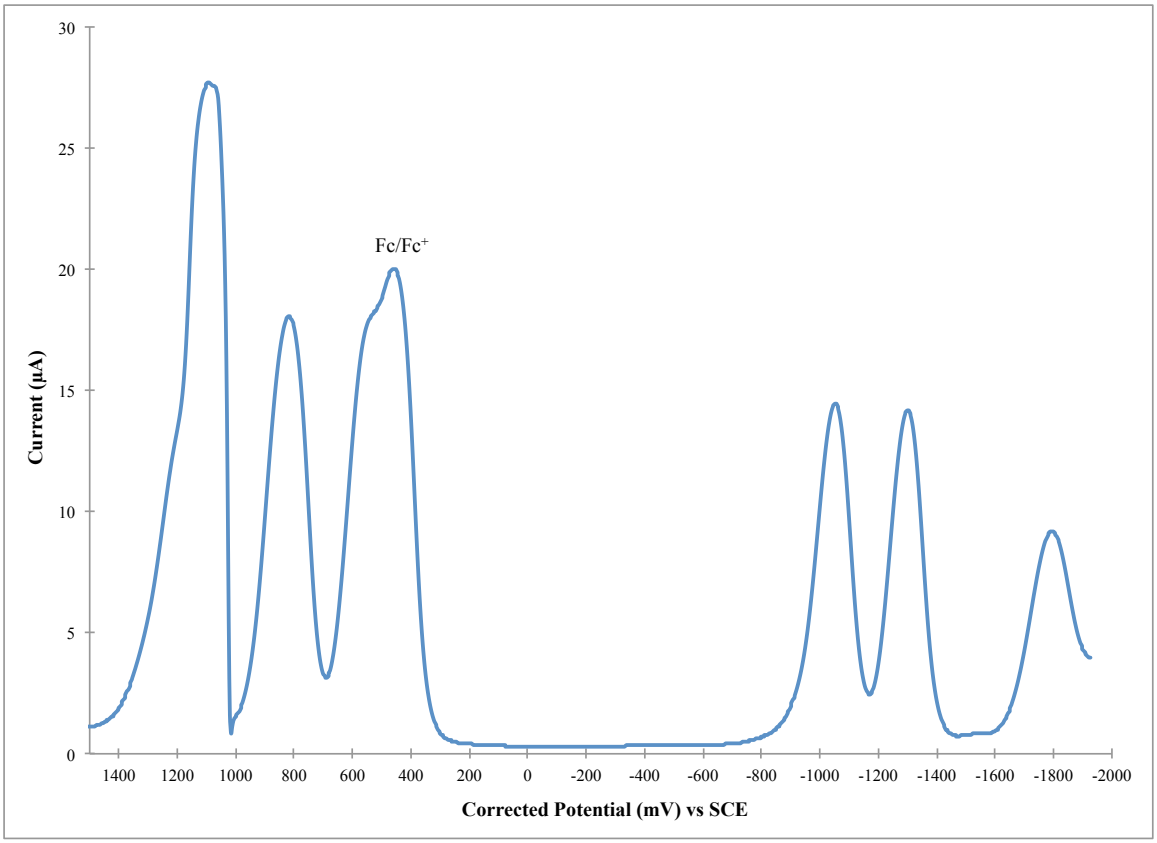

Figure 1.31 – DPV of Ni(II) complex **3b** with ferrocene as internal reference in the oxidation window only; showing the presence of 2 near oxydation peaks at 1.21 and 1.28 V respectively. (0.46V vs SCE in DCM) (Scan rate of 50 mV/s at R.T.)

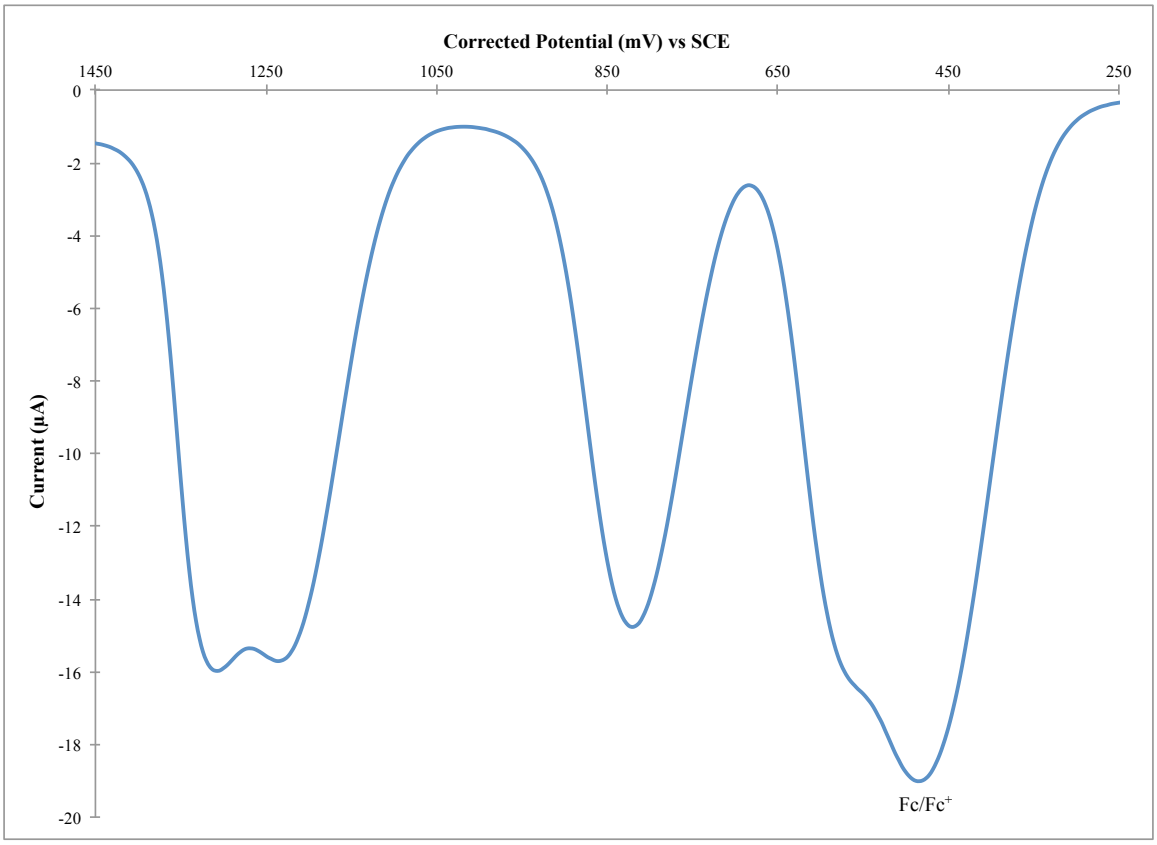

Figure 1.32 – DPV of Ni(II) complex **3b** before addition of ferrocene.
(Scan rate of 50 mV/s in DCM at R.T.)

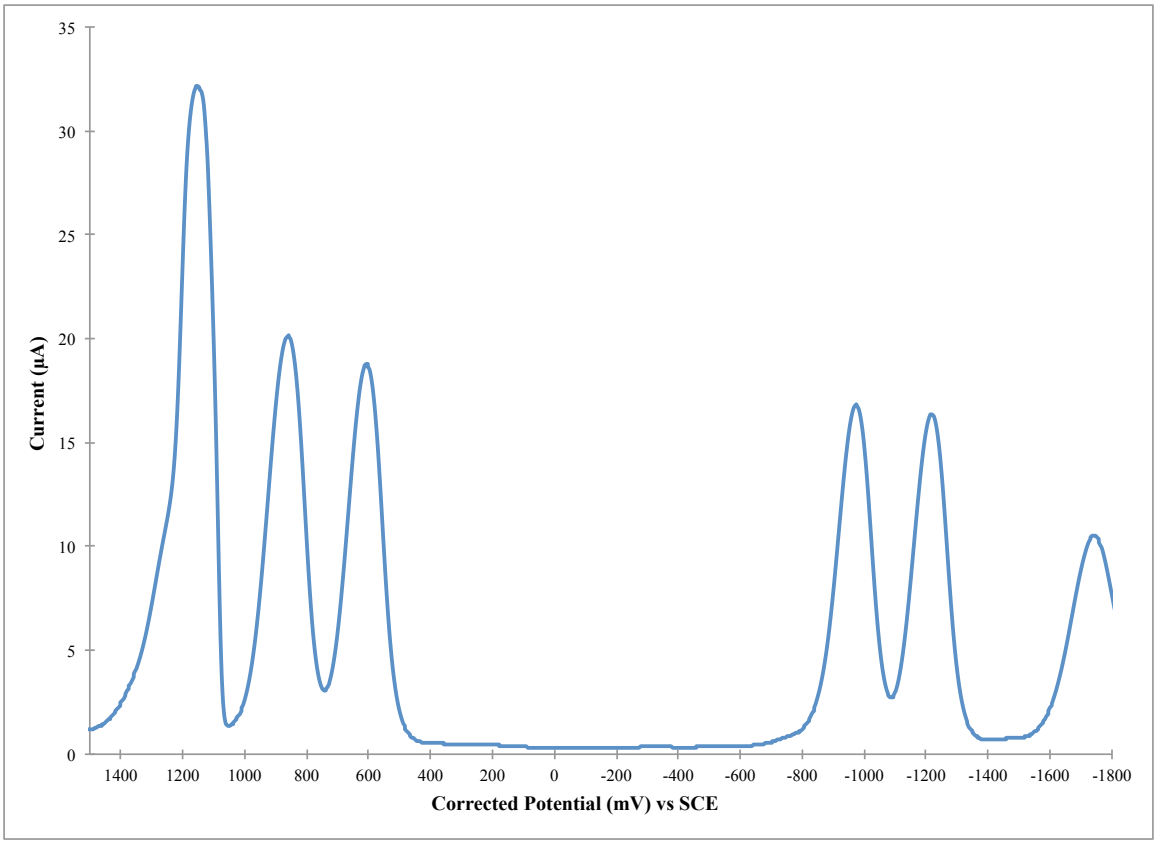

Figure 1.33 – CV of Cu(II) complex **4a** with ferrocene as internal reference.
(0.46V vs SCE in DCM) (Scan rate of 50 mV/s at R.T.)

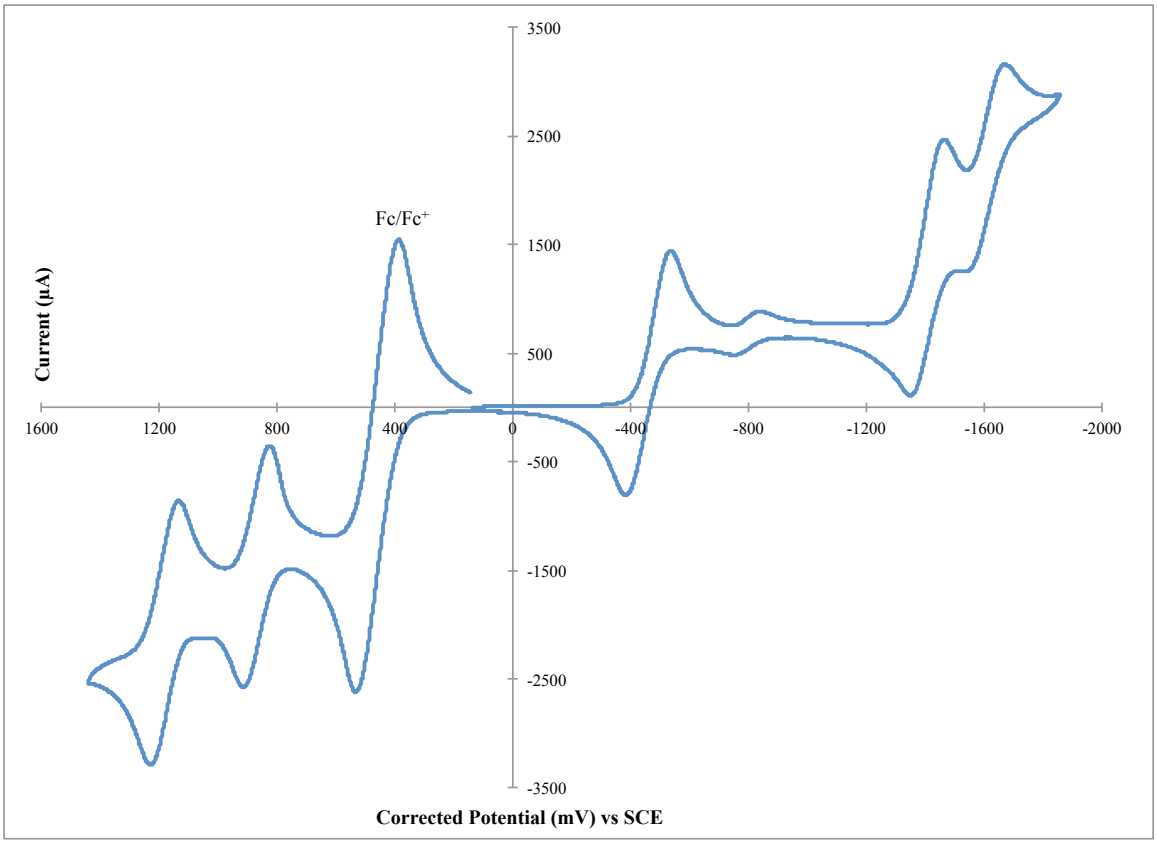

Figure 1.34 – CV of Cu(II) complex **4b** with ferrocene as internal reference (0.46V vs SCE in DCM) (Scan rate of 50 mV/s at R.T.)

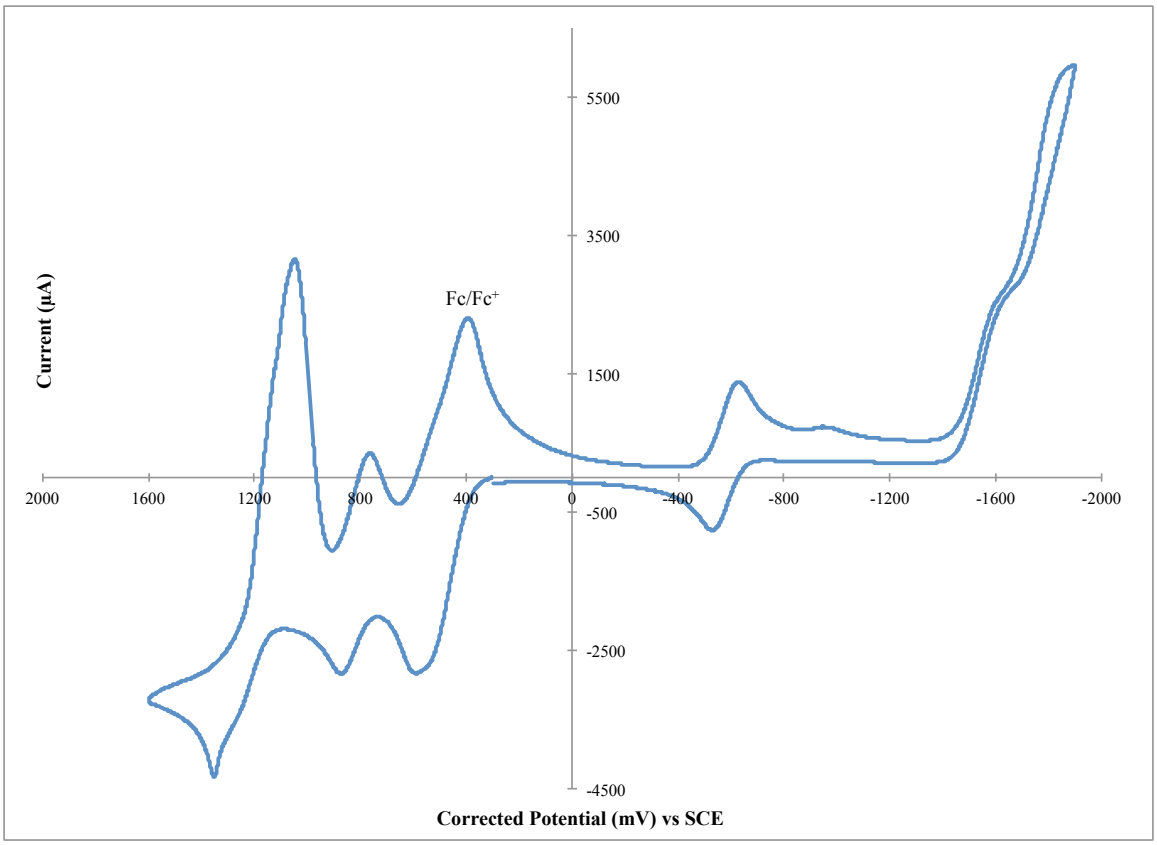

Figure 1.35 – CV of Cu(II) complex **4b** before addition of ferrocene.
(Scan rate of 50 mV/s in DCM at R.T.)

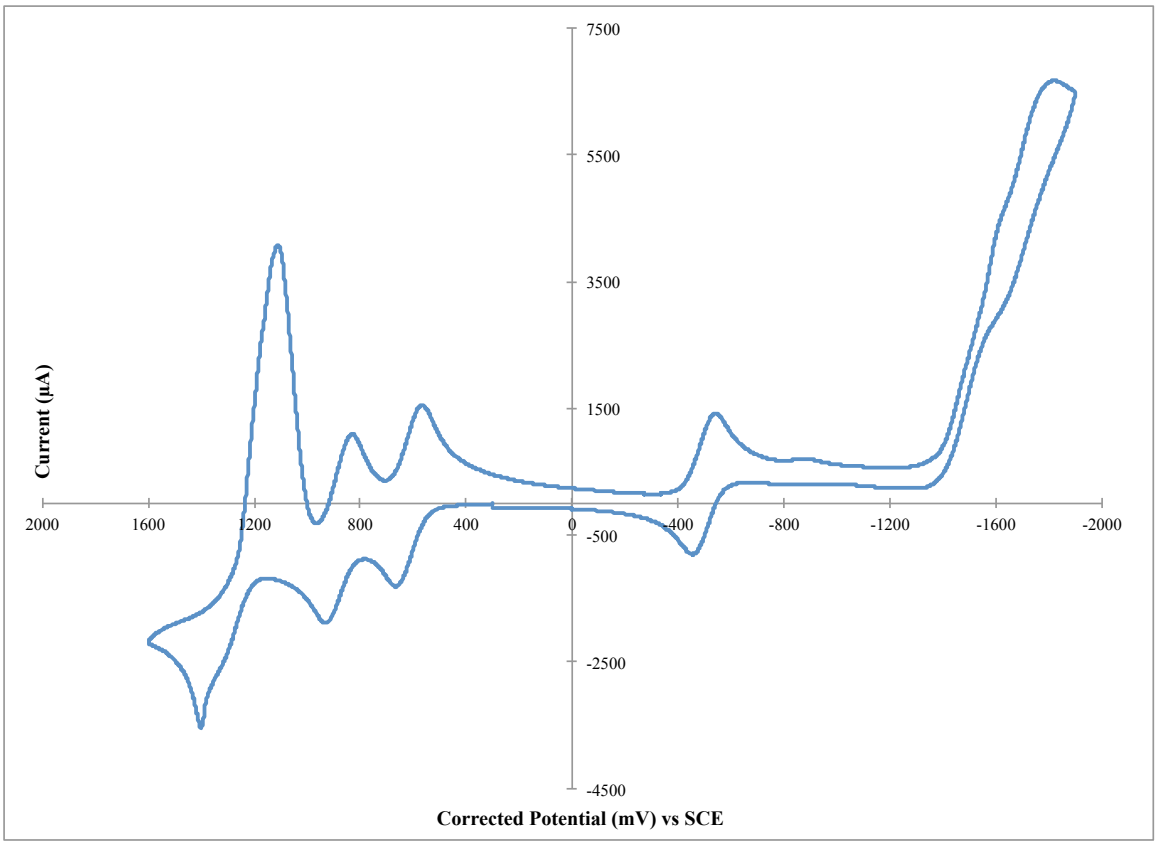

Figure 1.36 – DPV of Cu(II) complex **4b** before addition of ferrocene in the oxidation window only; showing the presence of 2 near oxydation peaks at 1.19 and 1.25 V respectively. (Scan rate of 50 mV/s at R.T.)

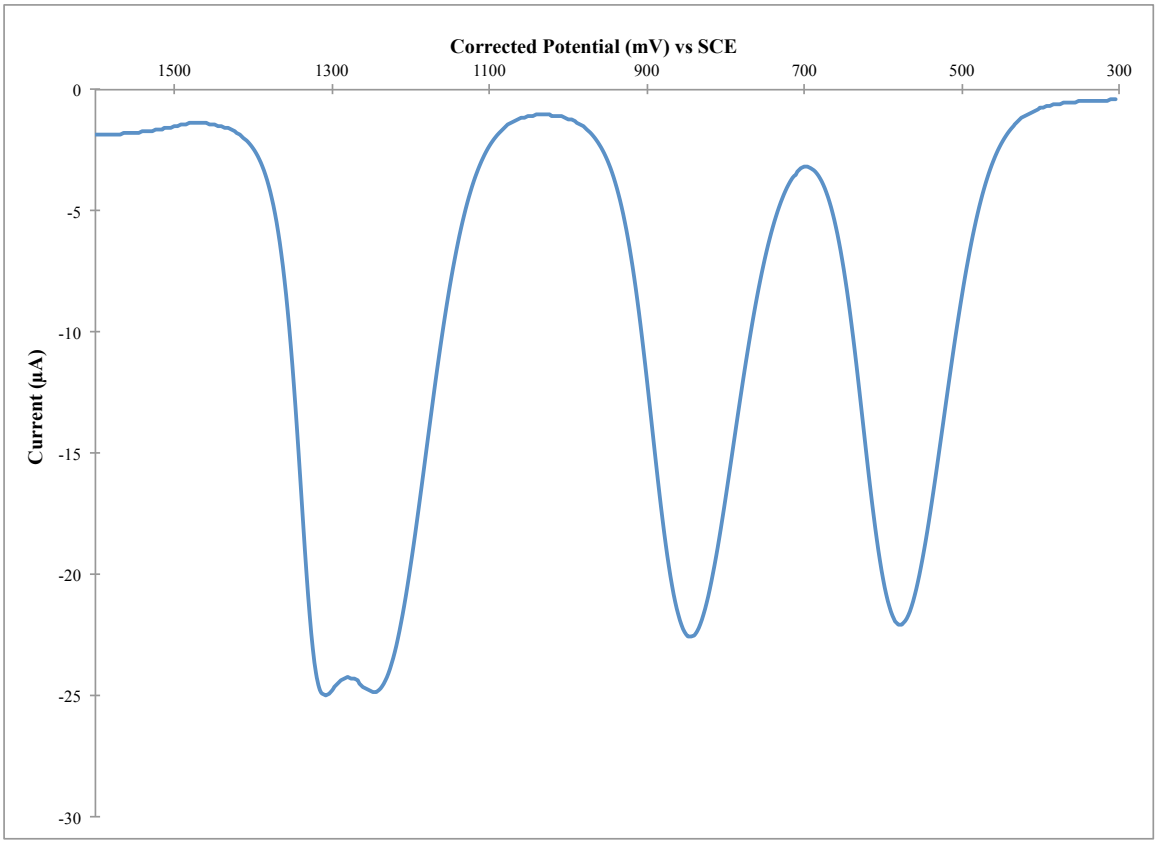

Figure 1.37 – DPV of Cu(II) complex **4b** before addition of ferrocene in the reduction window only; (Scan rate of 50 mV/s at R.T.)

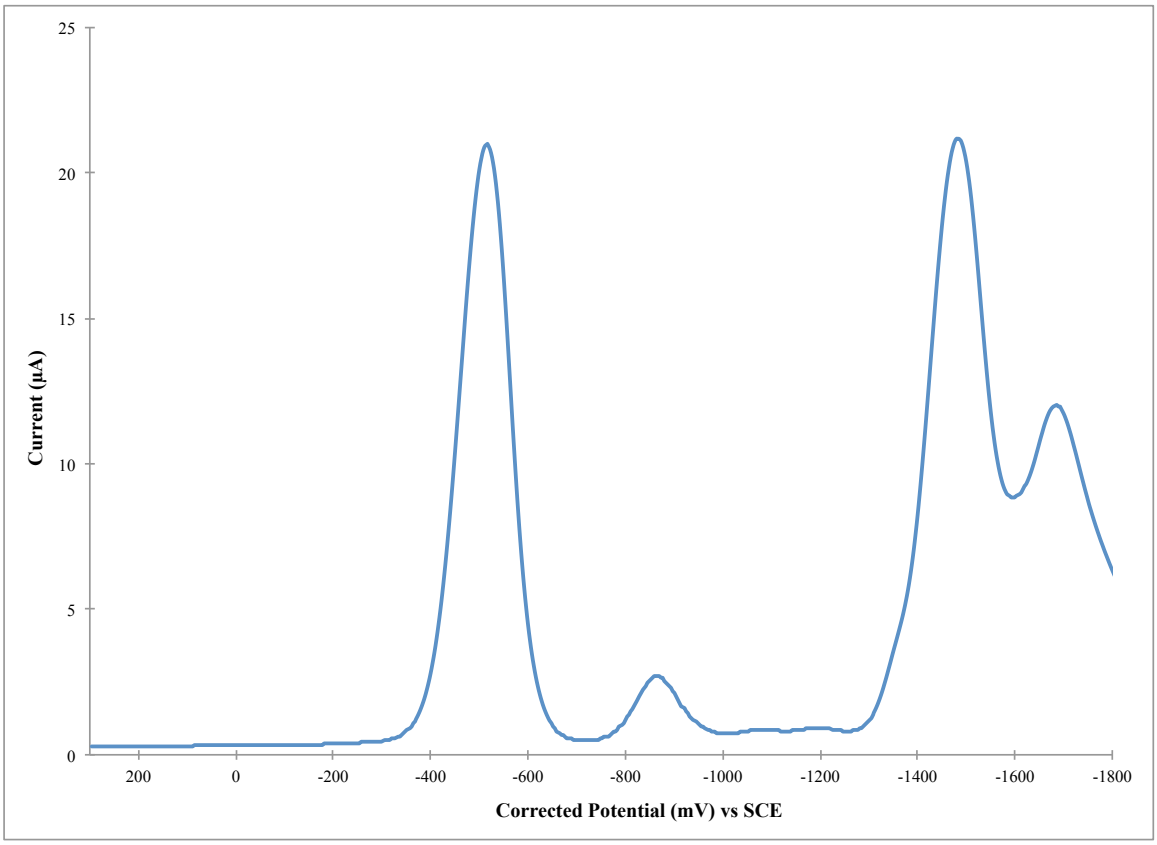

Figure 1.38 – CV of Zn(II) complex **5a** with ferrocene as internal reference.
(0.46V vs SCE in DCM) (Scan rate of 50 mV/s at R.T.)

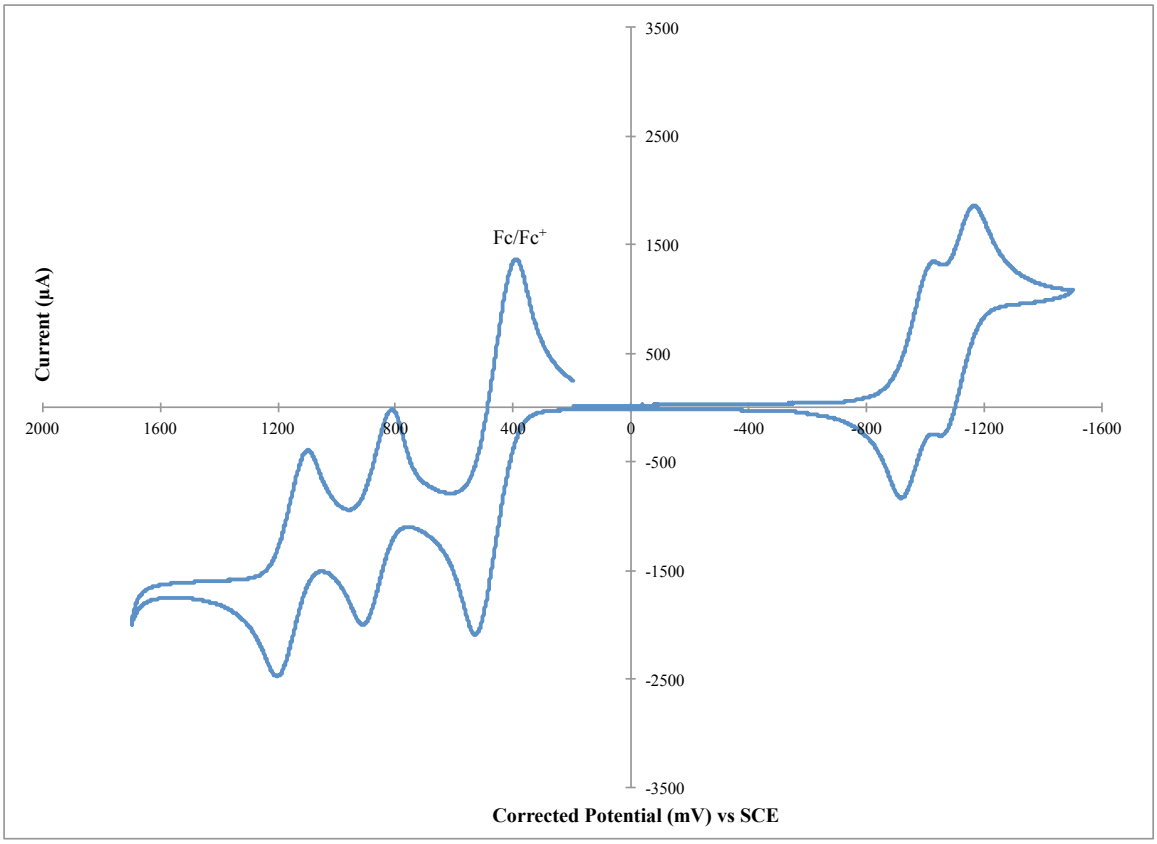

Figure 1.39 – CV of Zn(II) complex **5b** with ferrocene as internal reference (0.46V vs SCE in DCM) (Scan rate of 50 mV/s at R.T.)

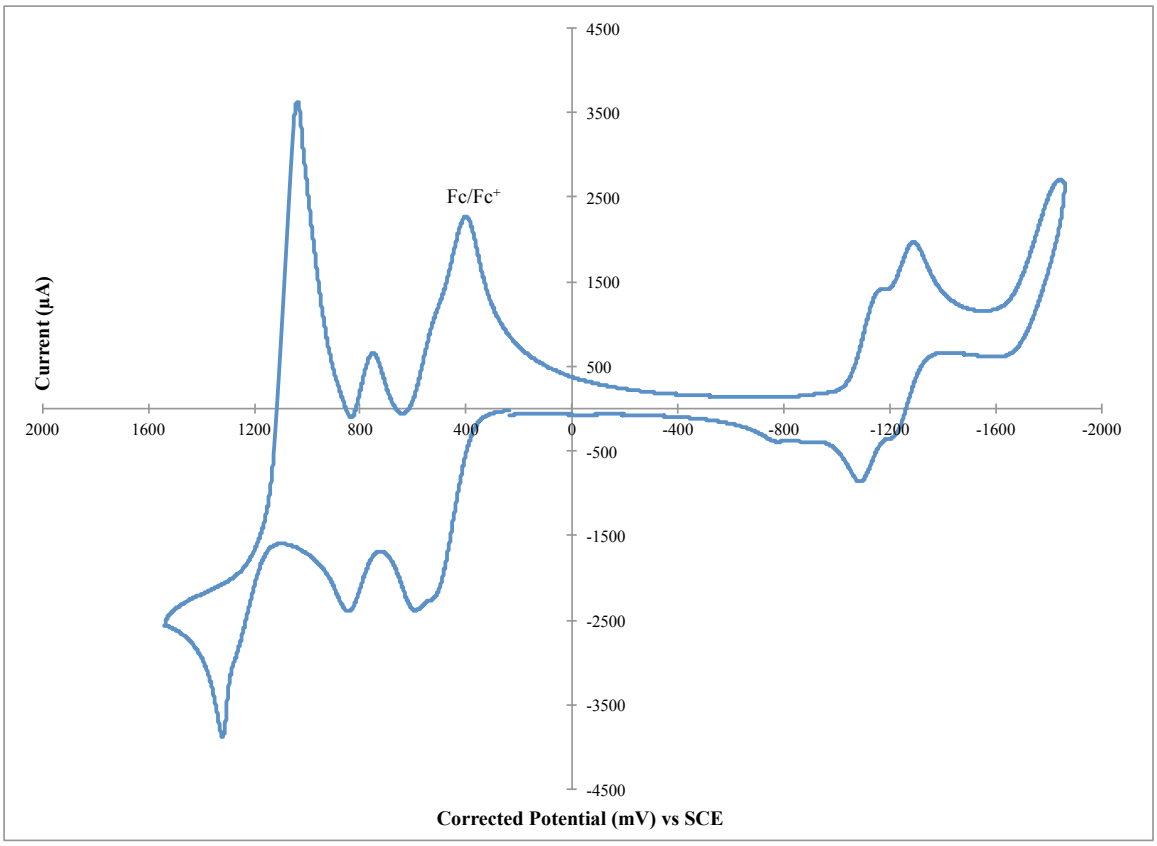

Figure 1.40 – CV of Zn(II) complex **5b** before addition of ferrocene.
(Scan rate of 50 mV/s in DCM at R.T.)

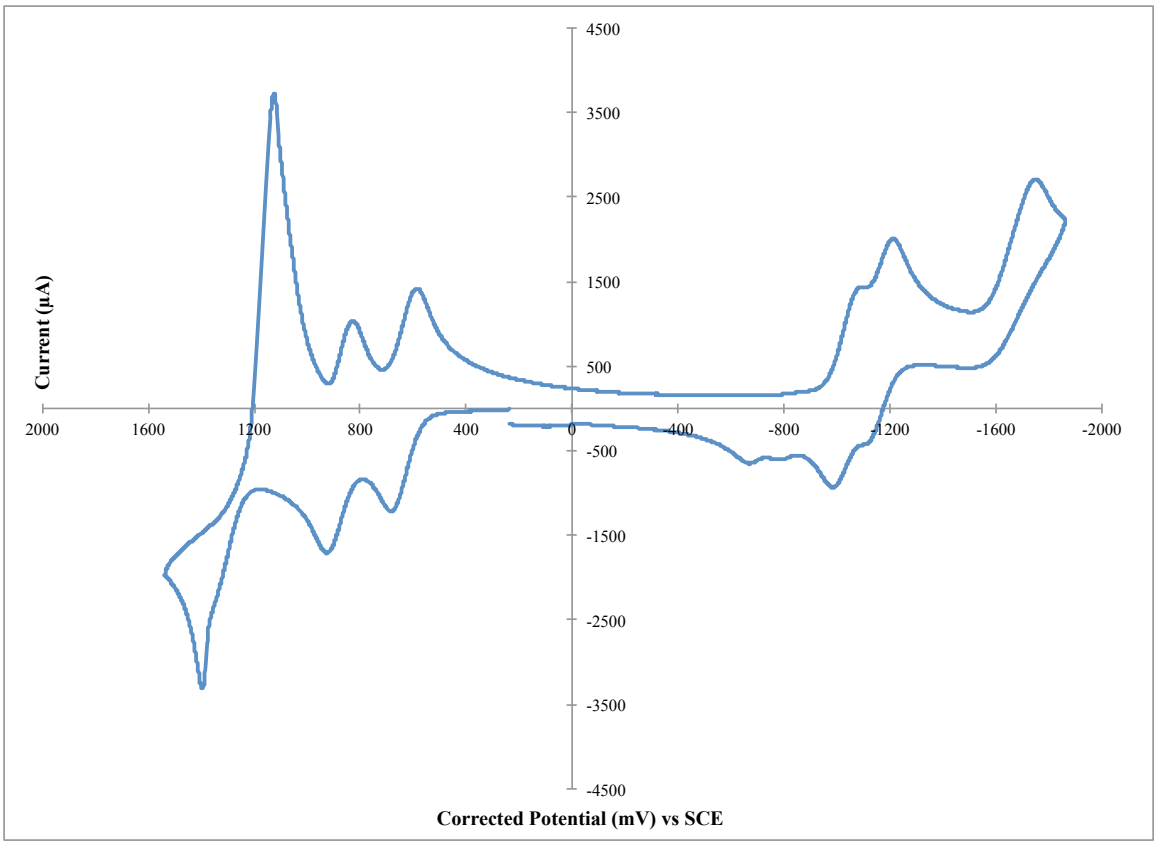

Figure 1.41 – DPV of Zn(II) complex **5b** with ferrocene as internal reference (0.46V vs SCE in DCM) (Scan rate of 50 mV/s at R.T.)

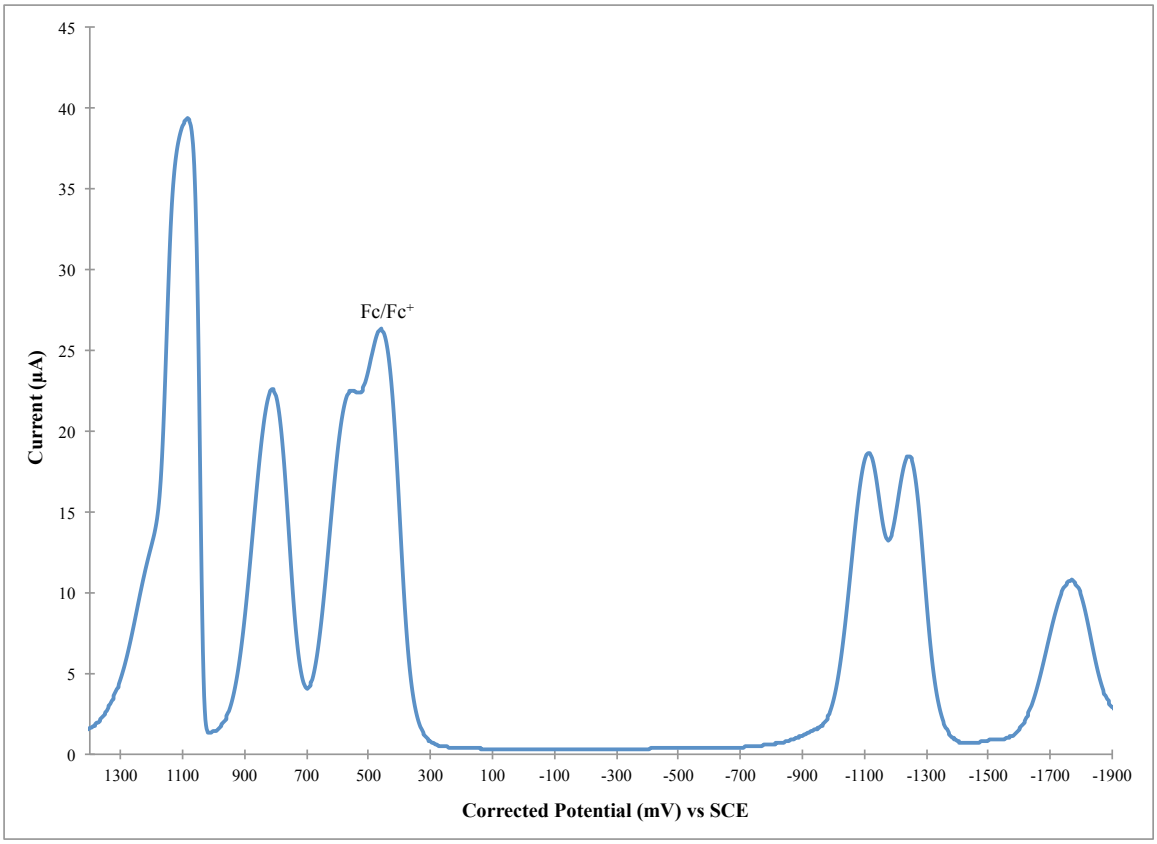

Figure 1.42 – DPV of Zn(II) complex **5b** with ferrocene as internal reference in the oxidation window only; showing the presence of 2 near oxydation peaks at 1.22 and 1.25 V respectively. (0.46V vs SCE in DCM) (Scan rate of 50 mV/s at R.T.)

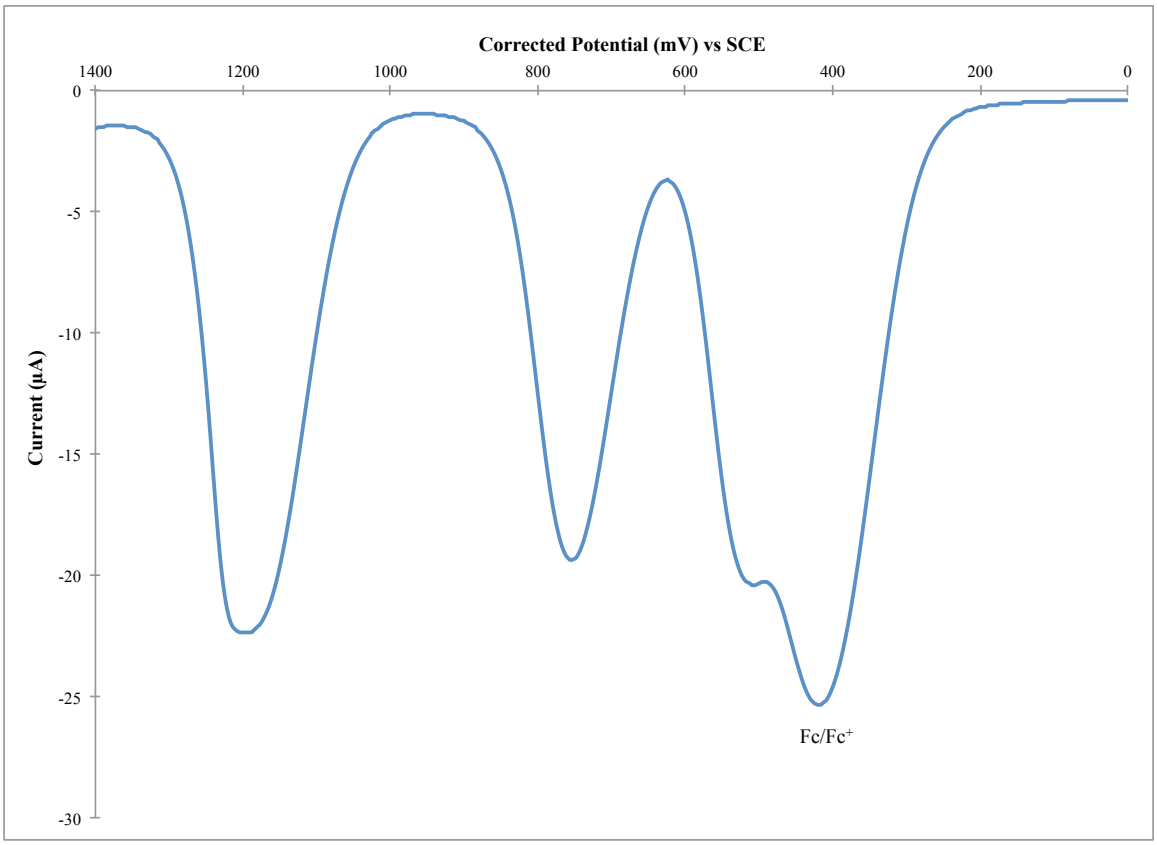

Figure 1.43 – DPV of Zn(II) complex **5b** before addition of ferrocene.
(Scan rate of 50 mV/s in DCM at R.T.)

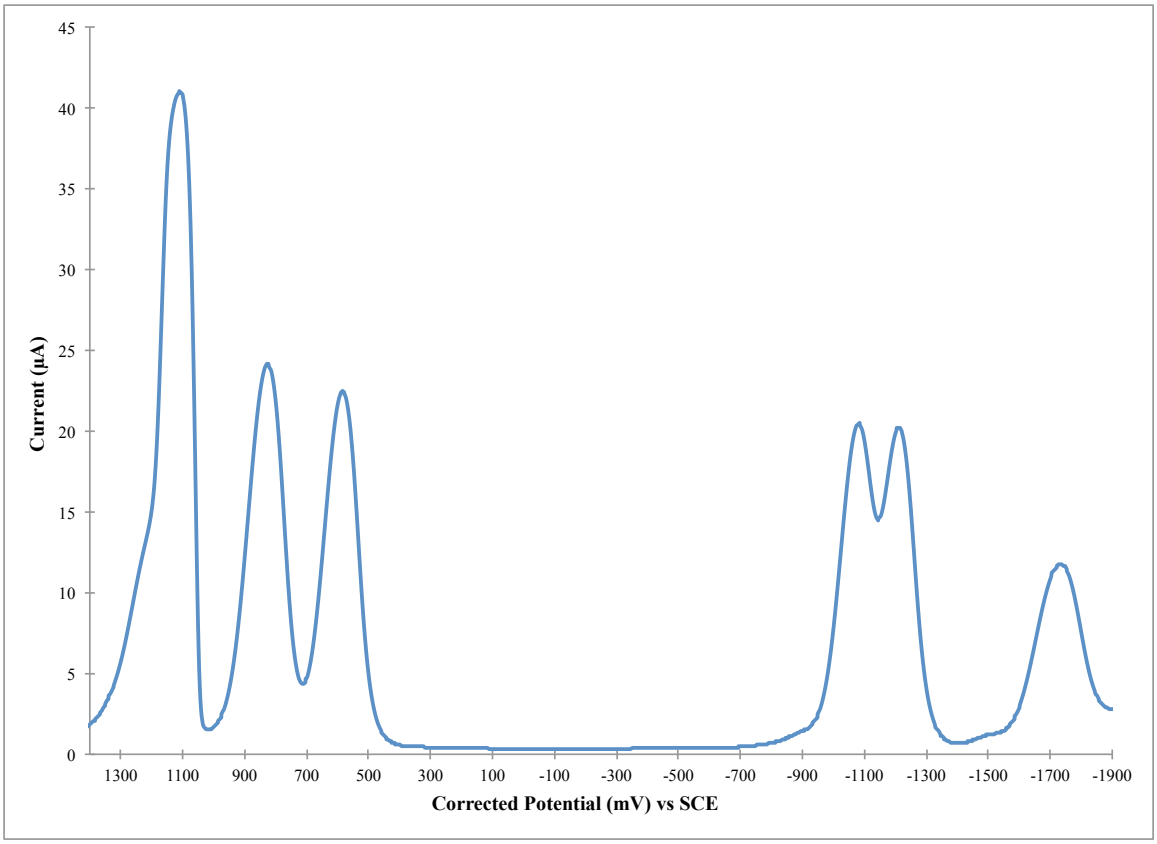

Figure 1.44 – CV of Aza-BODIPY complex **6a** with ferrocene as internal reference (0.46V vs SCE in DCM). (Scan rate of 50 mV/s at R.T.)

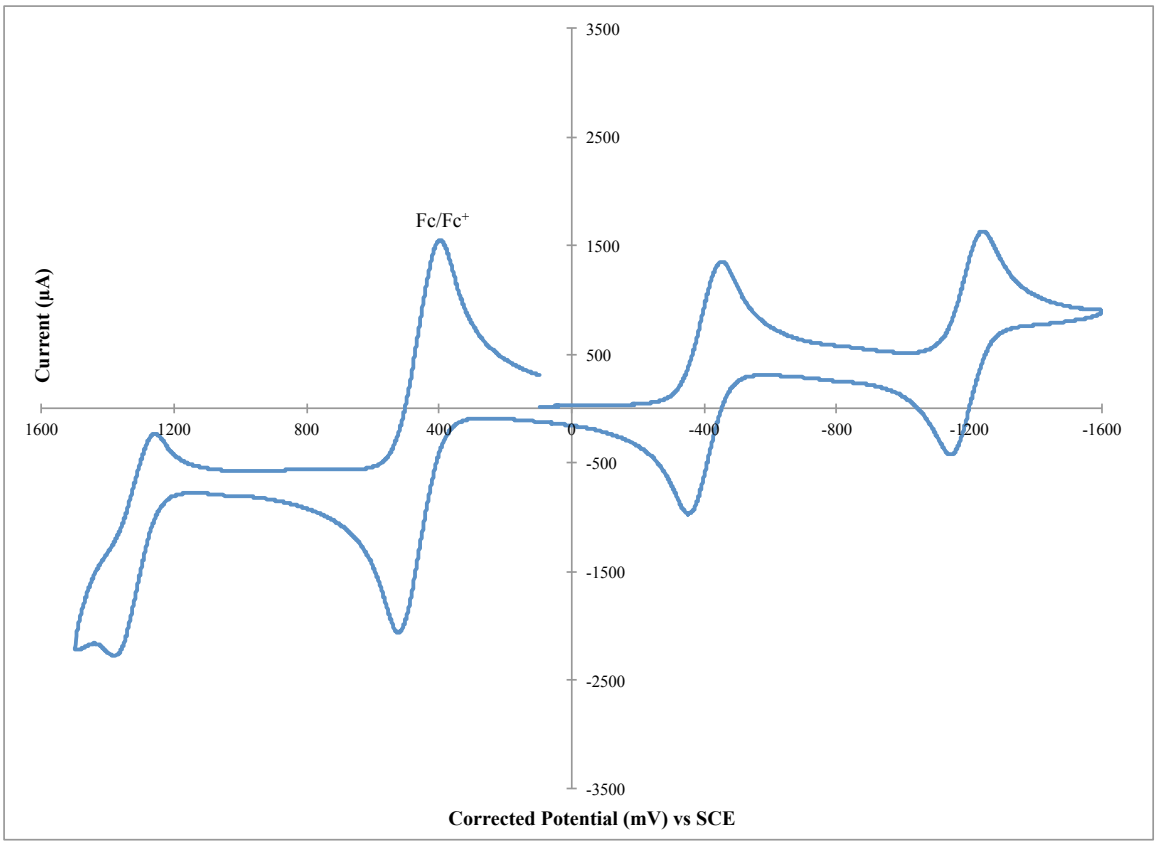

Figure 1.45 – DPV of Aza-BODIPY complex **6a** with ferrocene as internal reference (0.46V vs SCE in DCM). (Scan rate of 50 mV/s at R.T.)

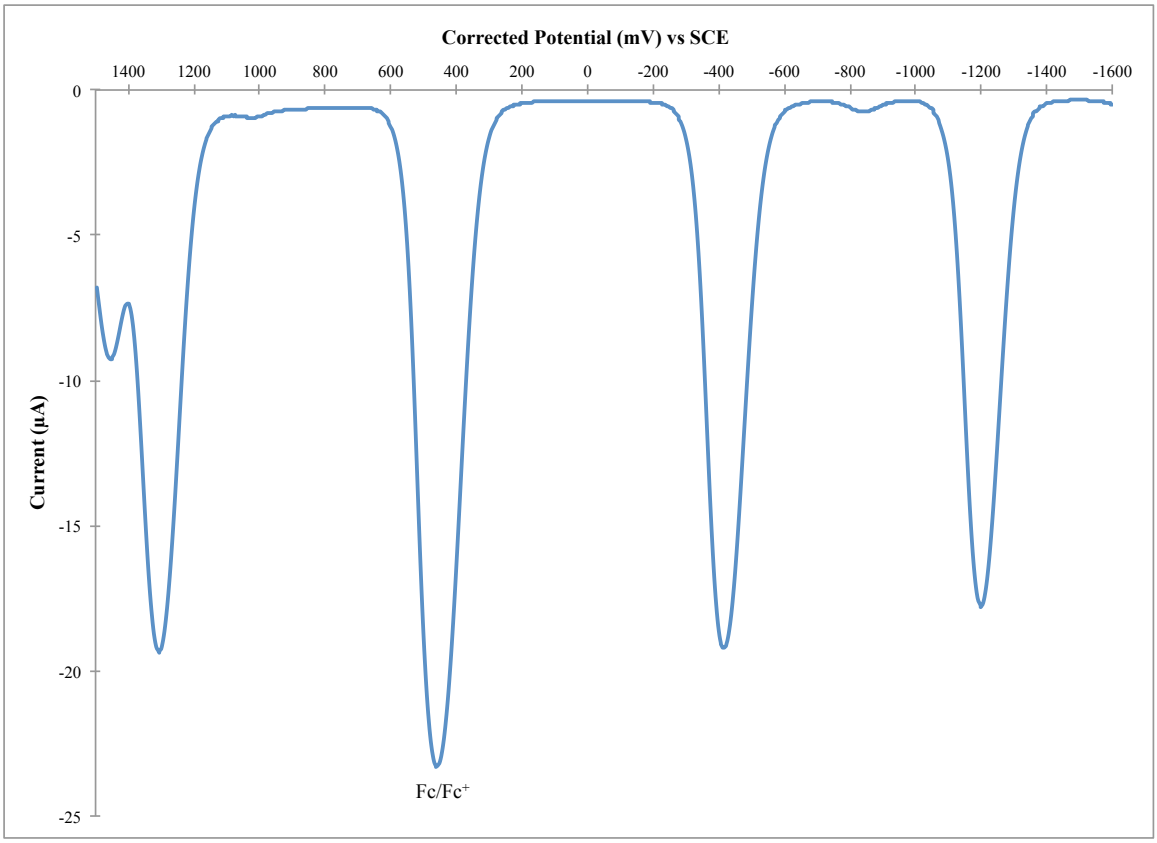

Figure 1.46 – CV of Aza-BODIPY complex **6b** with ferrocene as internal reference (0.46V vs SCE in DCM). (Scan rate of 50 mV/s at R.T.)

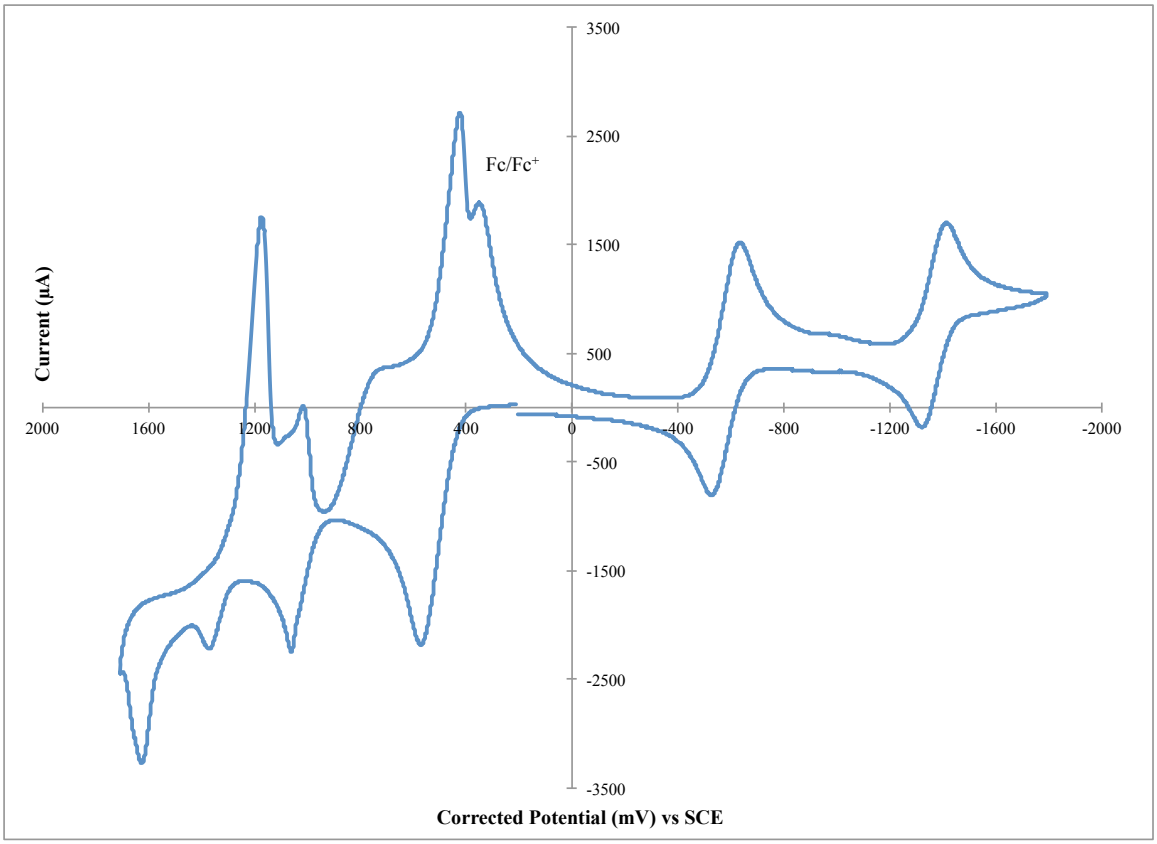

Figure 1.47 – DPV of Aza-BODIPY complex **6b** with ferrocene as internal reference (0.46V vs SCE in DCM). (Scan rate of 50 mV/s at R.T.)

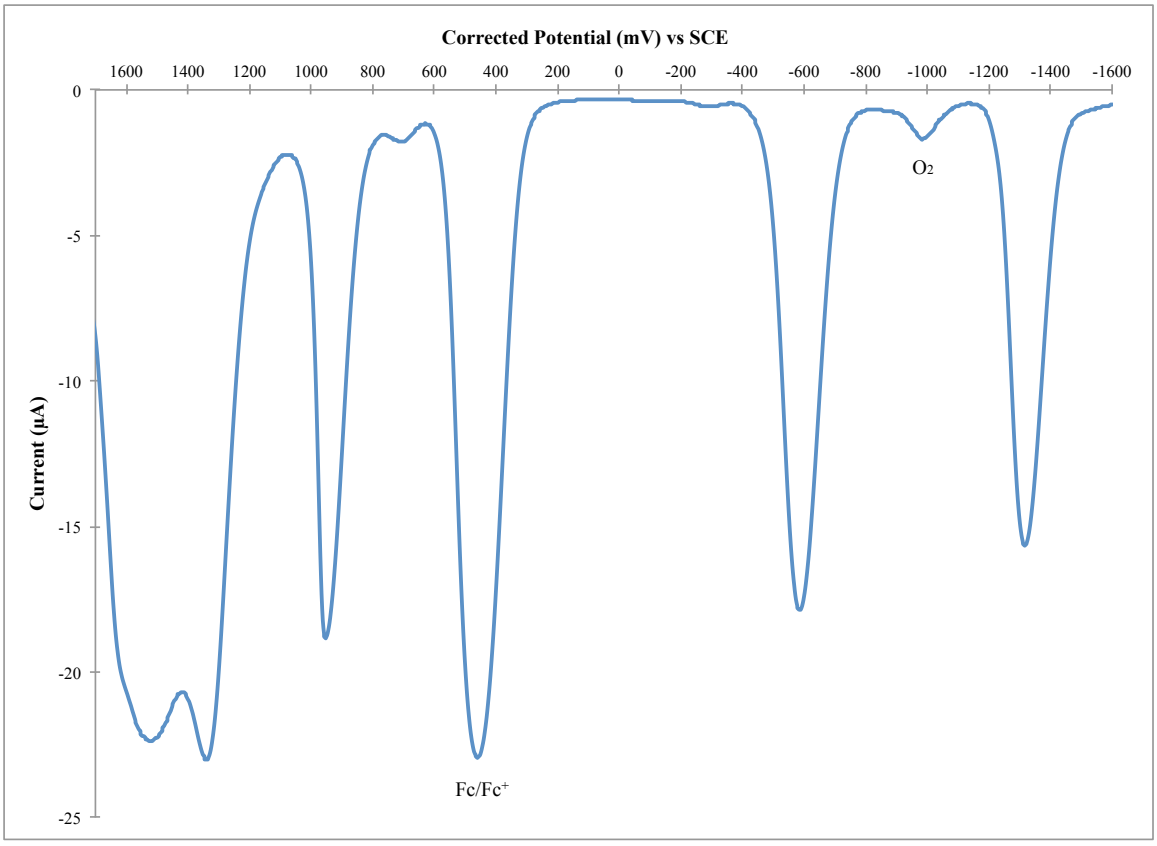

Figure 1.48 – DPV of Aza-BODIPY complex **6b** before addition of ferrocene.
(Scan rate of 50 mV/s in DCM at R.T.)

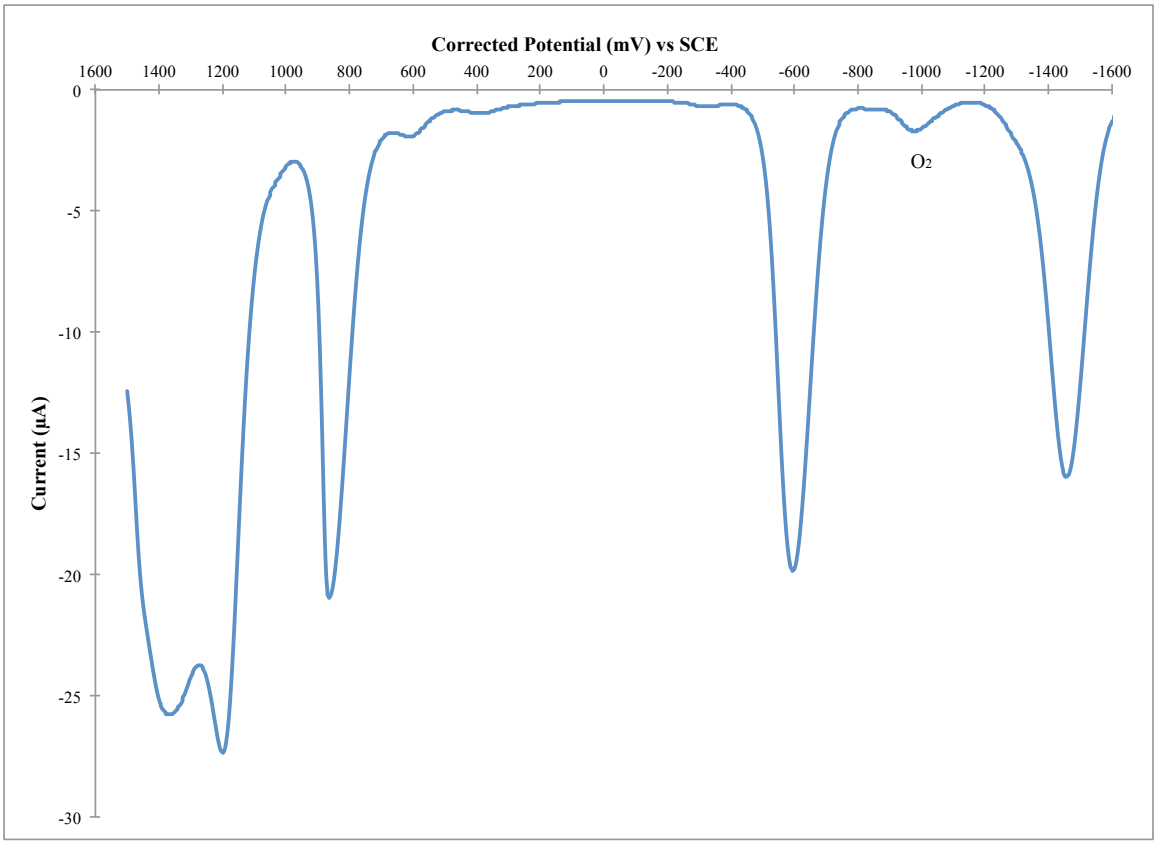

Figure 1.49 – Absorption spectra of ligand **1a**, complexes **2a** to **5a** and Aza-BODIPY **6a** in DCM solution.

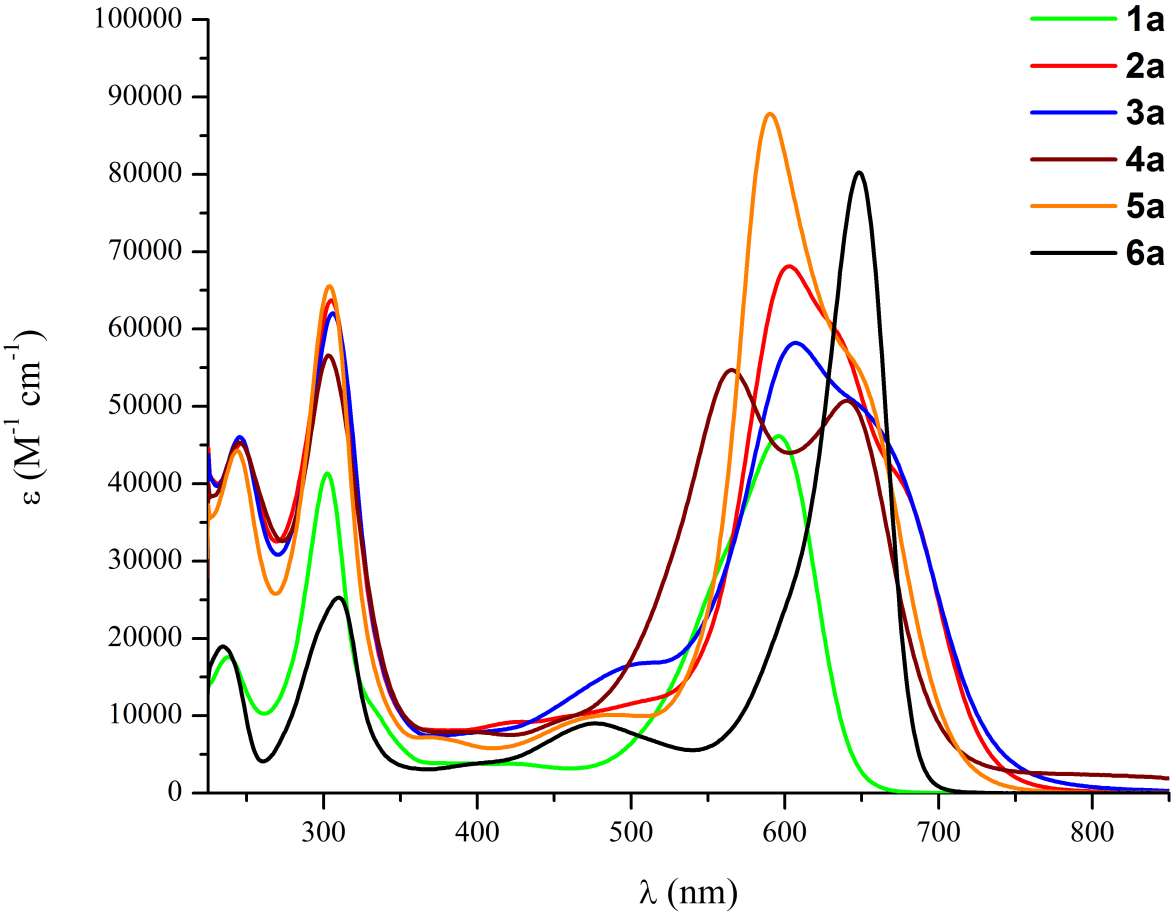

Figure 1.50 – Absorption spectra of ligand **1a**, complexes **2a** to **5a** and Aza-BODIPY **6a** in THF solution.

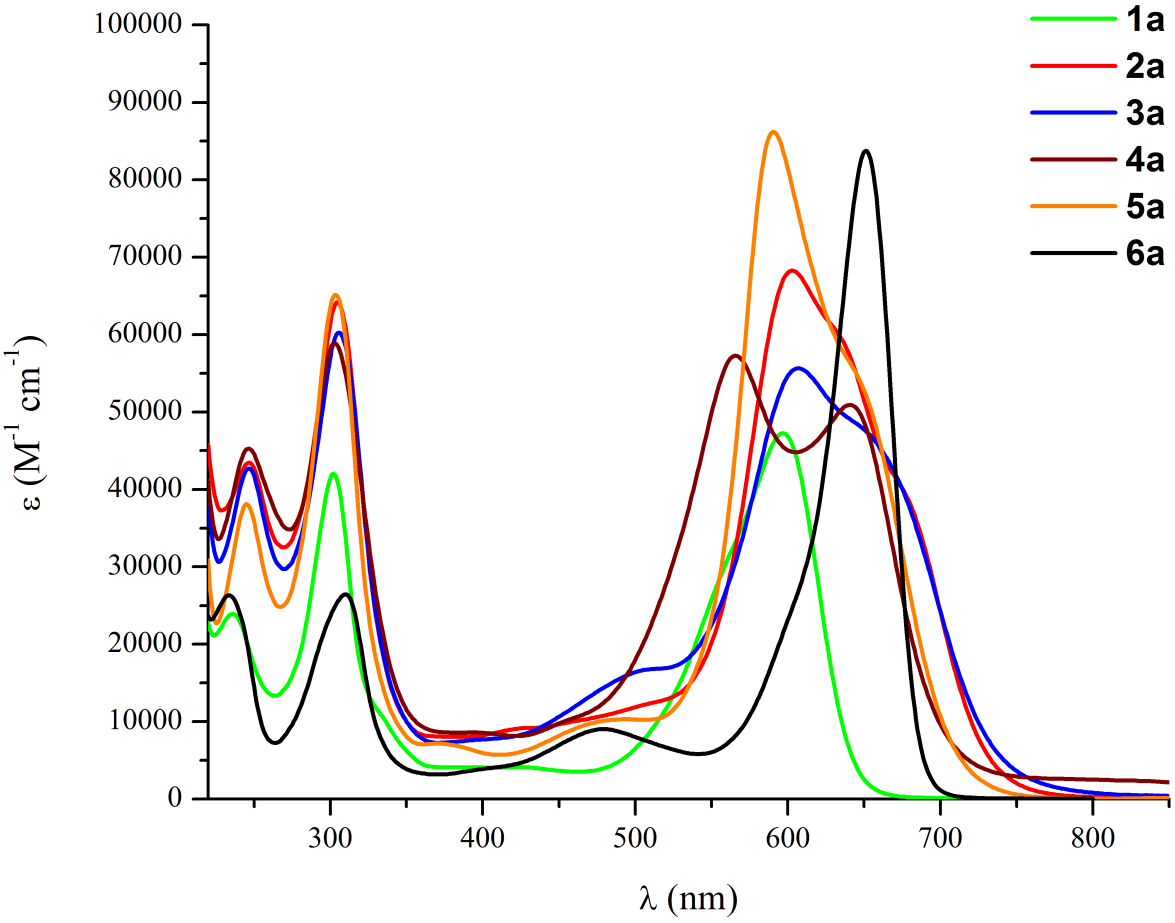

Figure 1.51 – Absorption spectra of ligand **1b**, complexes **2b** to **5b** and Aza-BODIPY **6b** in THF solution.

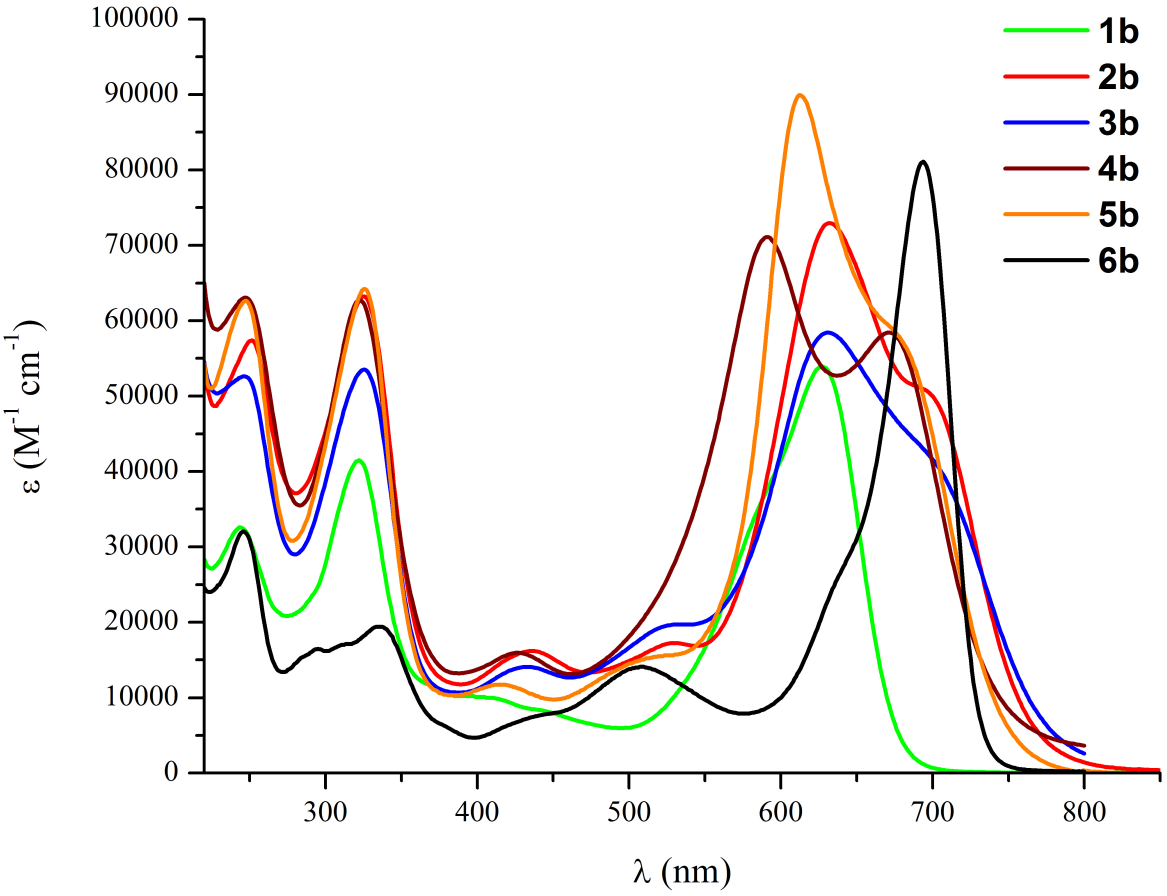

Figure 1.52 – Normalized intensity emission spectrum of **1a** and **6a** in DCM solution.

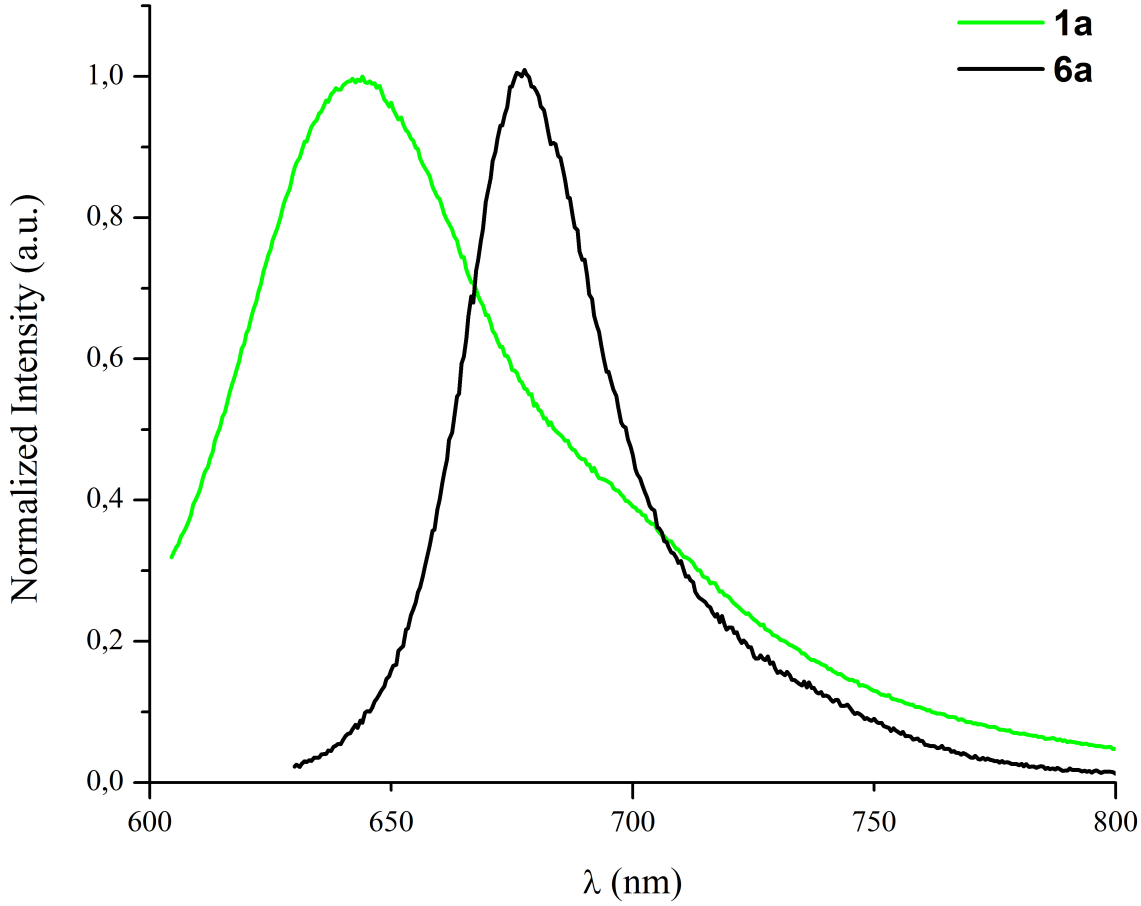

Figure 1.53 – Normalized intensity emission spectrum of **1a** and **6a** in THF solution.

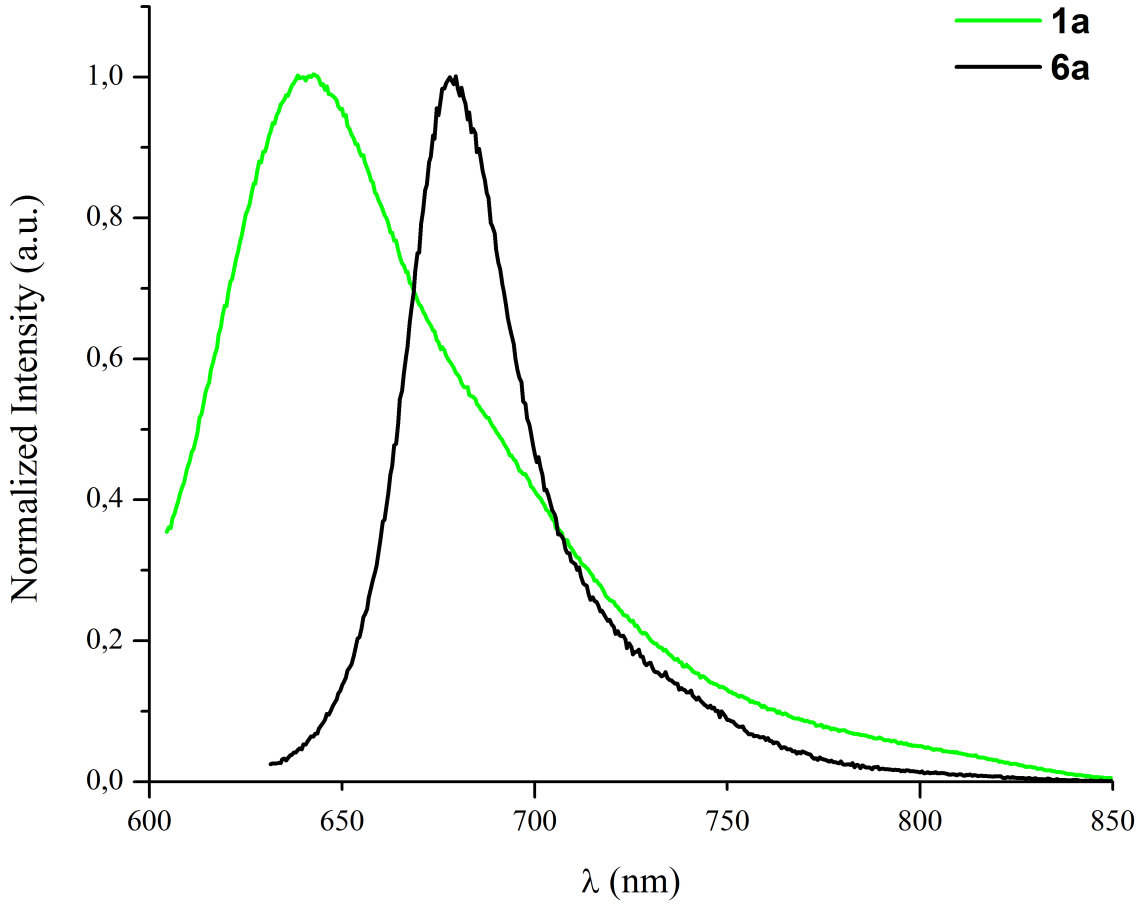

Figure 1.54 – Normalized intensity emission spectrum of **1b** and **6b** in THF solution.

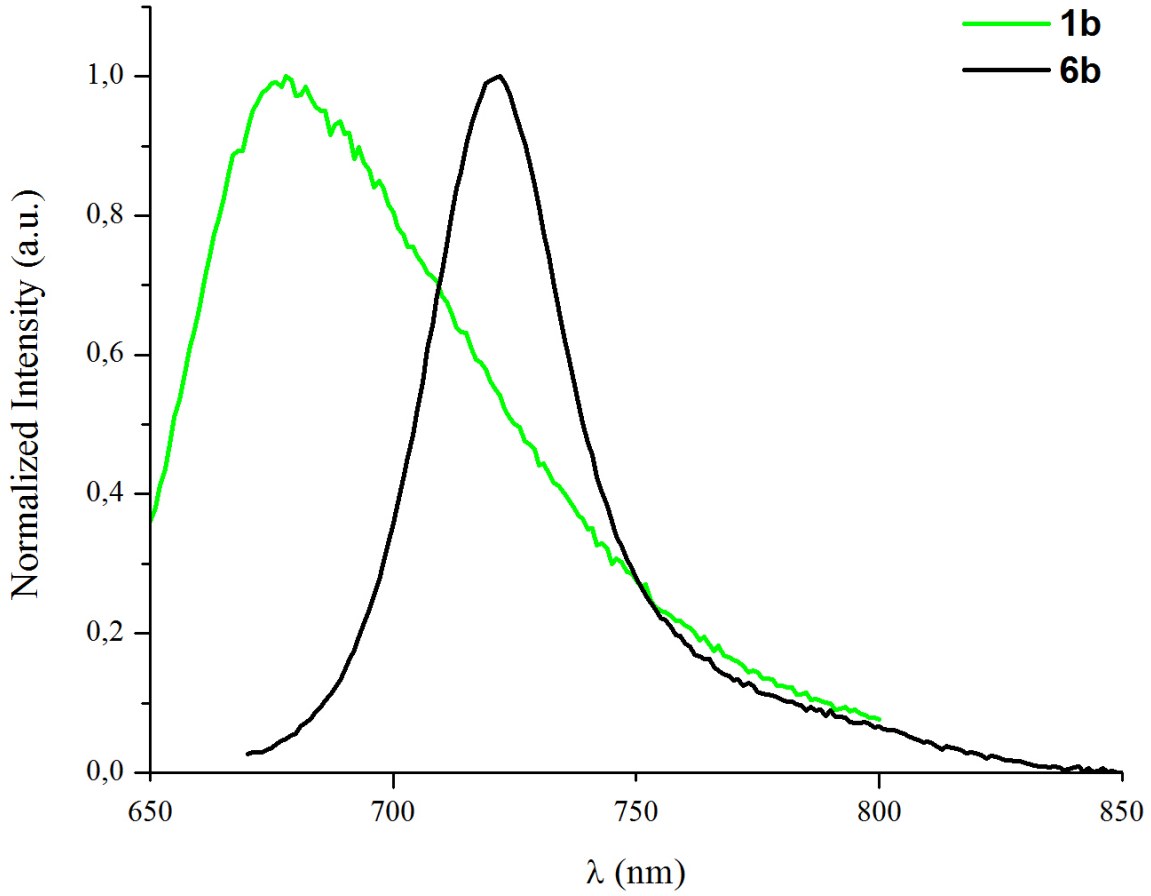

Figure 1.55 – Ortep representation of the Co(II) complex **2b** at the 50% probability level.

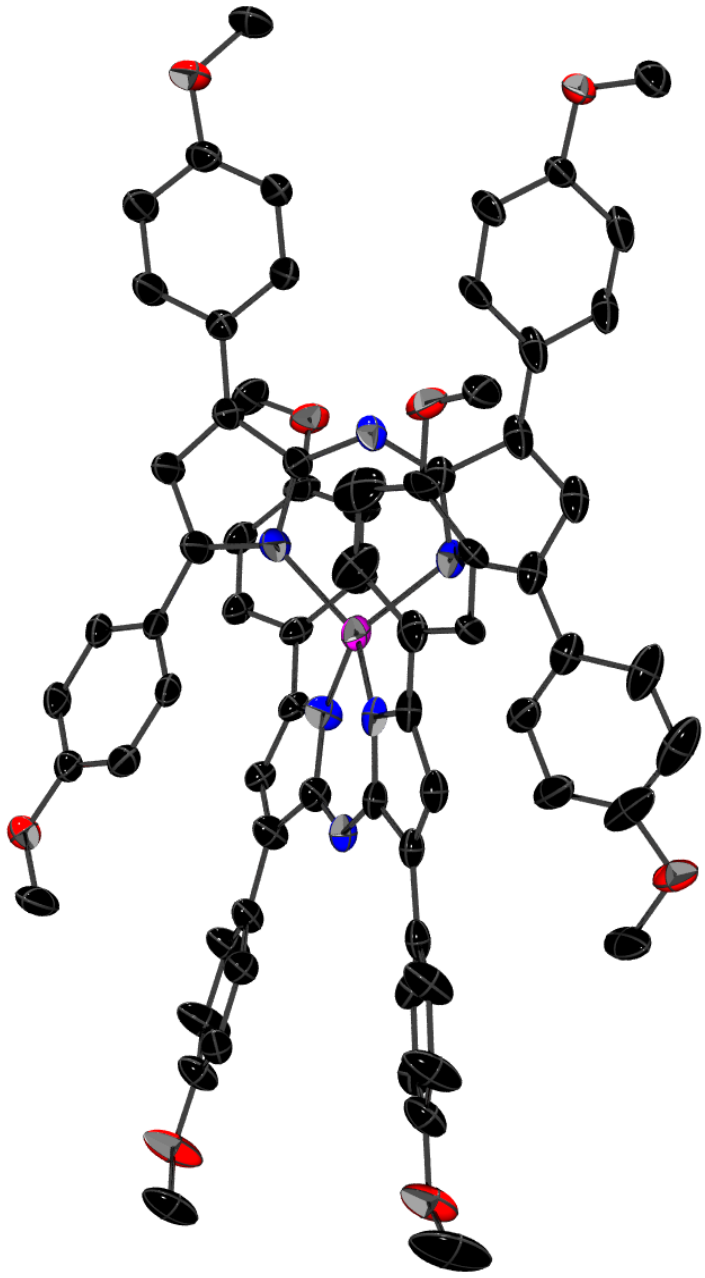

Table I.4 - Crystal Data and Details of the Structure Determination for Ligand **1b** and Co(II) Complex **2b**.

	1b	**2b**
CCDC Number	876955	876954
Formula	$C_{36}H_{31}N_3O_4$	$C_{72}H_{60}N_6O_8Co$
Mw (g/mol); $d_{calcd.}$ (g/cm^3)	569.64; 1.688	1196.19; 1.355
T (K); F(000)	150; 3696	150; 2500
Crystal System	Monoclinic	Monoclinic
Space Group	$P2_1/c$	$P2_1/c$
Unit Cell: *a* (Å)	19.4979(5)	12.2987(3)
b (Å)	7.0104(2)	14.3062(3)
c (Å)	21.2448(5)	34.1066(7)
β (°)	105.288(1)	102.219(1)
V (Å^3); Z	2801.1(1); 4	5865.0(2); 4
θ range (°); completeness	4.32-69.49; 0.991	2.65-69.83; 0.996
Refl.: collec./indep.; R_{int}	37808/5544; 0.052	121155/11031; 0.056
μ (mm^{-1})	0.713	2.822
R1(F); wR(F^2); GoF(F^2) [a]	0.0752; 0.2312; 0.98	0.0610; 0.1686; 1.038
Residual electron density	1.40; -0.37	0.50; -0.63

[a] R1(F) based on observed reflections with I>2σ(I), wR(F^2) and GoF(F^2) based on all data.

Chapitre 2

Partie A – Neutral Re(I) Complexes for Anion Sensing

Auteurs :

André Bessette[1], Samik Nag[1,2], Amlan K. Pal[1], Sofia Derossi[1] et Garry S. Hanan[1]*

[1] Département de Chimie, Université de Montréal, Pavillon J.-A. Bombardier, 5155 Decelles Avenue, Montréal, Québec, H3T-2B1, Canada;

[2] Department of Chemical Sciences, Sikkim University, Gangtok, Sikkim, India 737102.

Contributions :

- **André Bessette** : Reprise des travaux du Dr Samik Nag en optimisant chacune des étapes clés de synthèse; la caractérisation photophysique, par RMN et par HRMS; rédaction de l'article.
- Samik Nag: Instigateur du projet ayant fait la première synthèse des complexes et les études préliminaires de photophysique.
- Amlan K. Pal: Résolution de la structure rayons X d'un des intermédiaires organométalliques obtenues.
- Sofia Derossi: Aide lors des études photophysiques préliminaires du Dr Samik Nag.

Historique :

Accepté pour publication dans le journal *Supramolecular Chemistry* en tant que ‘’Full Paper’’ le 11 avril 2012. Publié sur le web le 6 août 2012; DOI : 10.1080/10610278.2012.691500

2.1 – Abstract

Anion sensing properties toward F^-, OAc^- and $H_2PO_4^-$ were studied for new mononuclear and dinuclear Re(I) complexes based on a 5-substituted phenanthroline moiety bearing a thiourea hydrogen-bonding receptor. Log($K_{1:1}$) values between 4 and 6 were obtained for the complexes by UV/vis titrations and between 3 and 5 by ^{1}H NMR titrations. The effect of hydrogen-bonding versus deprotonation of the thiourea receptor upon addition of the anions was also evaluated by UV/vis and NMR titration techniques. In addition, an X-ray structure of the Re(I) precursor complex is reported and the chirality of the mononuclear and dinuclear complexes is discussed.

2.2 – Introduction

The field of anion recognition has been growing at an impressive rate since the start of the new millennium.[1] One reason is that anions are ubiquitous throughout biological systems as they carry genetic information (DNA is a poly-anion) and the majority of enzyme substrates and co-factors are anionic.[2,3] Thus, anion binding and recognition has attracted intense interest,[1-10] and metal complexes have played an important role in anion receptor chemistry since its earliest examples.[11,12] The presence of a metal ion can introduce a range of advantageous physicochemical properties to this class of receptor.[12] Recently Gale and co-workers have shown that introduction of a transition metal into a purely organic system can enhance its anion binding capabilities dramatically.[13] While both metal-ligand interaction[11,14-16] and van der Waals interactions[8,9,17-19] are employed to study anion binding phenomena, neutral metal complexes are challenging candidates for anion binding as the electrostatic component is not an available mode of interaction. With a few exceptions of metallocene complexes,[12,20] neutral metal-based optical anion sensors are less well known. Neutral anion sensors with Re(I) as the metal centre are of particular interest, but their synthesis usually involves multiple steps.[21-24] Recently, neutral alkynylrhenium(I) tricarbonyl diimine complexes with a triarylboron moiety, which can bind to F^- with a stability constant in the range of 10^5 was reported.[25] This high binding constant is due to

the interaction between the highly Lewis acidic and electron-accepting triarylboron moiety and the electron-rich guest F^-. Another report by Lin *et al* shows that a dinuclear neutral Re(I) complex with quinoxaline-bis(sulphonamide) functionalization can be active as a good anion binder where both sulphonamide groups can orient themselves to a conducive position to form a cleft around the incoming anion.[26] A similar approach reported earlier by Beer's group to surround the anion by amide functionalities attached to a Re(I) core lead to reasonably strong binding constants (ca. between 35 and 1790 depending on the anion and the receptor system).[24,27] However, all of the receptors mentioned above were only available in multiple synthetic steps. Recently, the group of Lees circumvented this synthetic drawback by reporting the preparation of thioamide, urea and especially of readily accessible thiourea Re(I) bridged complexes, along with their use as luminescent anion receptor.[28] Herein we report the anion-binding properties of two neutral Re(I) complexes (**3** and **4**) also with a thiourea moiety as the anion receptor group, which can be synthesized very readily. A comparative anion sensing study by UV/vis and NMR titrations have been done in order to better understand the effect of hydrogen-bonding versus deprotonation of the thiourea receptor upon addition of monoanionic F^-, OAc^- and $H_2PO_4^-$ on the binding constants obtained.

2.3 – Results and Discussion

Our target ligand for combining both a bidentate binding site and a scaffold for the thiourea group was a 5-substituted phenanthroline. The reaction of 1,10-phenanthrolin-5-amine with $Re(CO)_5Br$ in refluxing toluene gave Re(I) complex **1** in 96% yield. Treatment of **1** with thiophosgene in the presence of Na_2CO_3 gave isothiocyanate functionalized Re(I) complex **2** in nearly quantitative yield. Complex **2** proved to be a good precursor for the synthesis of thiourea [$(-NH)_2C=S$] containing rhenium(I) complexes. Reaction of **2** with ten equivalents of aniline in acetone at ambient temperature and under inert atmosphere afforded the neutral Re(I) complex **3** containing thiourea receptor group in 81% yield (Figure 2.1). Under similar conditions, reaction of **2** with p-phenylenediamine in a 2:1 ratio afforded the dinuclear neutral Re(I) complex **4** with two thiourea receptor units in 60% yield. All of the complexes were characterized by NMR spectroscopy, high-resolution mass spectrometry (HRMS) and elemental analysis.

Figure 2.1 – Synthesis of the neutral Re(I) complexes: precursors **1** and **2** and thiourea receptors **3** and **4**.

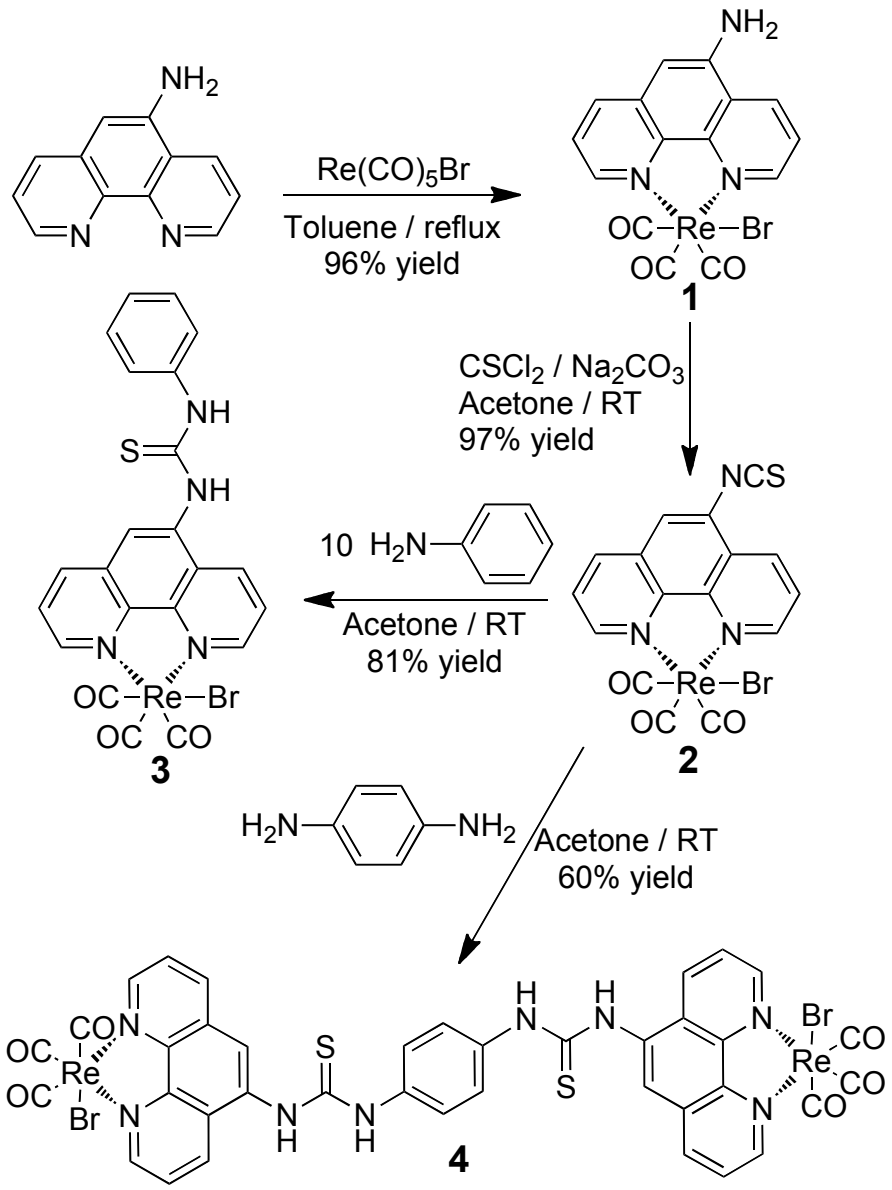

The isothiocyanate precursor **2** was further structurally characterized by X-ray crystallography (Figure 2.2). Complex **2** crystallizes in triclinic P-1 space group with an acetone molecule as solvate. Complex **2** presents an octahedral ligand arrangement with a facial tricarbonyl moiety. A bidentate diimine ligand and a bromide fill its octahedral coordination sphere. The two equatorial carbonyl ligands, the rhenium centre and aromatic rings of the phenanthroline ligand are in a nearly ideal planar arrangement. The plane containing atoms C16, N3 and S deviates from the plane formed by N1, N2, Re, C2, C3 by only 4.5^{o}. Bond lengths and angles around the metal center are comparable to those in closely related compounds (see ESI).[29,30] The C-Re bond lengths *trans* to the neutral chelating phenanthroline (1.921(4) and 1.919(3) Å) are shorter than the C-Re bond *trans* to the anionic Br ligand (1.984(4) Å) due to increased backbonding *trans* to phenanthroline. The C-O bond distances, as a consequence, show the reverse trend. Whereas the equatorial C-O bonds are 1.147(4) and 1.149(4) Å, the one *trans* to the bromide is significantly less at 1.034(5) Å. The Re-Br bond is 2.6167(7) Å whereas the two Re-N bonds are almost identical at 2.180(3) Å. The isothiocyanate group is almost linear with a N-C-S angle of 175.2(4)^{o}. The molecule is chiral on Re-atom, but the effect of this chirality is faded to affect the hydrogen bonding property of the thiocyanato group due to the long distance between the chiral Re-centre and the thiocyanate group.

Figure 2.2 – (Top) Ortep representation of **2** drawn at 50% probability level, showing a view of the molecule from above of the molecule. (Botton) Ball and stick model of two different enantiomeric views of the chiral molecule. H atoms and the solvated acetone molecule have been omitted for clarity.

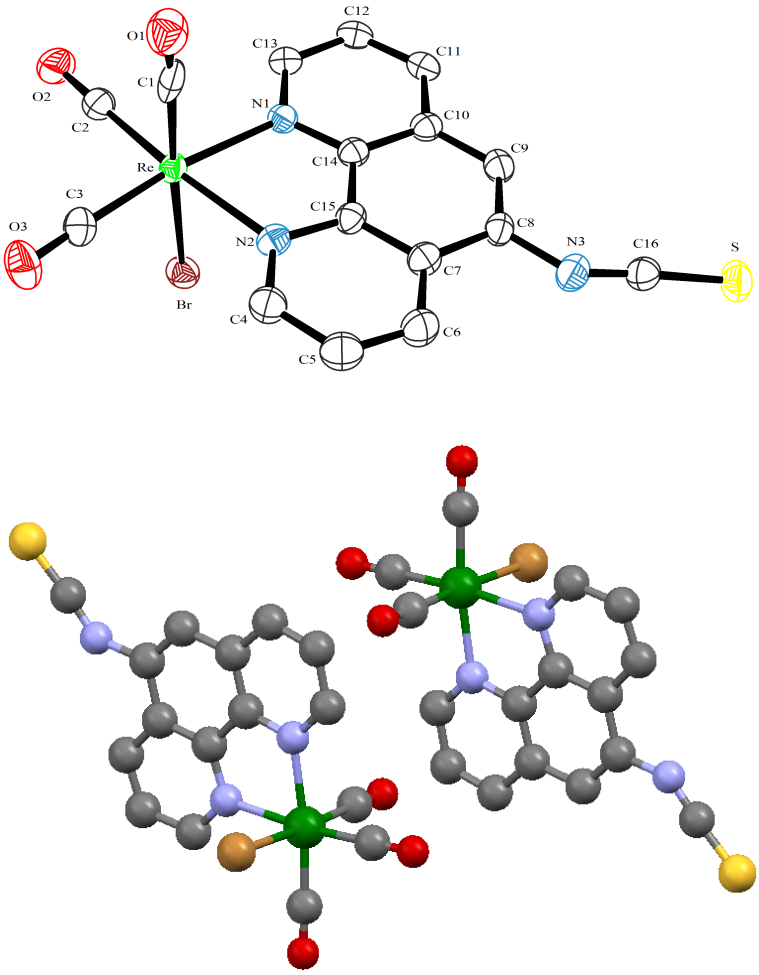

The electrochemical behavior of complexes **3** and **4** has been examined by cyclic voltammetry at a glassy carbon electrode in purified *N*,*N*'-dimethylformamide (DMF) under a dry argon atmosphere. At positive potentials, complex **3** shows an irreversible oxidation at 0.85 V vs saturated calomel electrode (SCE), attributable to the oxidation of the thiourea group, similar to that reported for the oxidation of a thiourea group of a cationic Re(I) polypyridyl complexes with thiourea receptors.[29] As the Re(I/II) oxidation couples for similar rhenium complexes are reported to appear beyond 1.8 V vs SCE, we did not observe any such couples within the solvent potential window of DMF. At negative potentials, the quasi-reversible diimine based reduction is observed at -1.38 V vs SCE. Similar values were also reported earlier for reduction of the diimine ligand in Re(I) carbonyl complexes.[31,32] For complex **4,** the irreversible oxidation and reduction are observed at 0.90 V and -1.36 V vs SCE, respectively.

The monoanionic ions F^-, OAc^- and $H_2PO_4^-$ are well known to bind to thiourea[31-36] and, therefore, we studied their binding to the Re(I) thiourea complexes (Figures 2.3 and 2.4; ESI). However, as thiourea receptors are subject to a deprotonation of relatively acid NH's when a strong conjugated anionic base like OAc^- is added,[37] efficiency of the anion sensing properties of our organometallic systems needed to be establish. In fact, Yatsimirsky *et al.* showed that deprotonation is favored in highly diluted solutions due to a ratio of H-bonded and deprotonated forms of thiourea linkage being proportional to the total receptor concentration. Similar results of acid-base reaction were also observed by Gale *et al.* for 3,4-dichloro-2,5-diamidopyrroles.[38] Consequently, we were curious to establish to which extent apparent binding constant (K_{app}) values resulting from such multi-equilibrium systems would be affected by varying the concentration from a 1.5×10^{-5} M of complexes by UV/vis to a two hundred-fold concentration of 3×10^{-3} M by NMR (Table II.1).

Figure 2.3 – a) (Top) UV/vis titrations of receptor **3** (1.5 x 10^{-5} M) with F^- in DMSO-0.5% water. Inset: corresponding titration profile at 347 nm. b) (bottom) Job plot of receptor **3** with F^- in DMSO-0.5% water at 440 nm, showing 1:1 binding

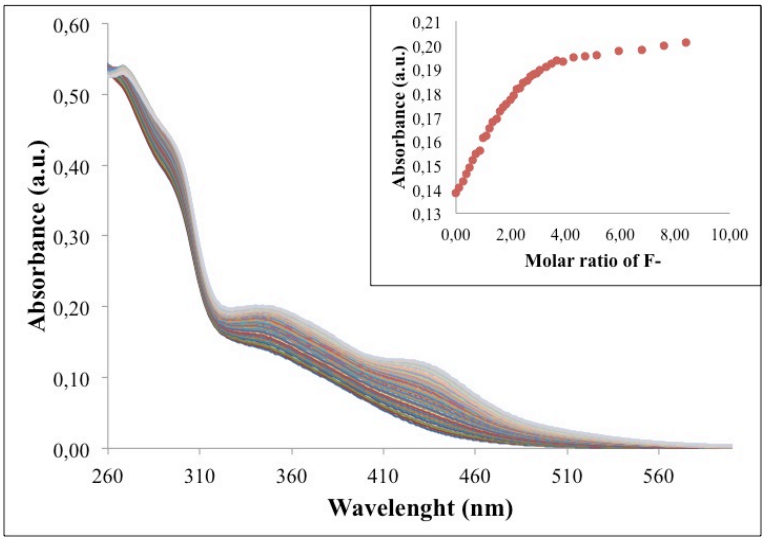

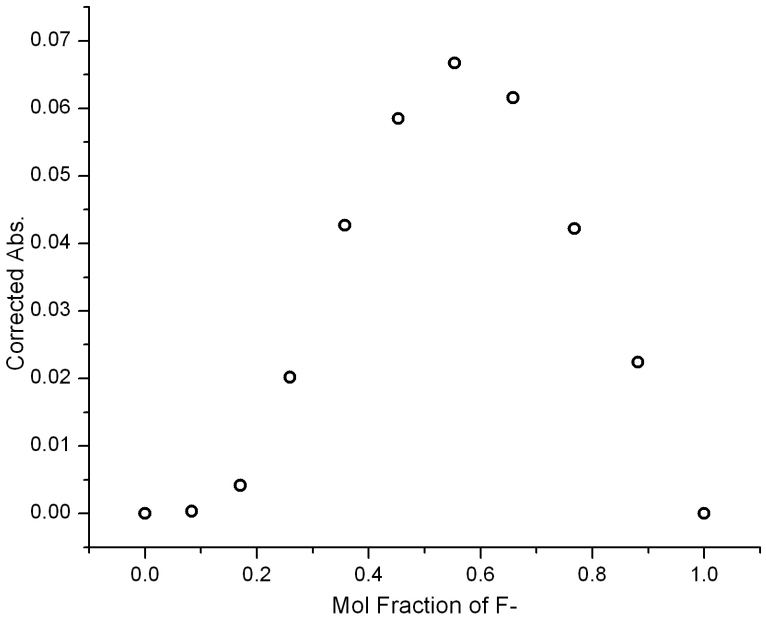

Figure 2.4 – a) (Top) UV/vis titrations of receptor **4** (1.5 x 10^{-5} M) with F- in DMSO-0.5% water. Inset: corresponding titration profile at 430 nm. b) (Bottom) Job plot of receptor **4** with F^- in DMSO-0.5% water at 450 nm, showing 1:2 receptor to anion binding.

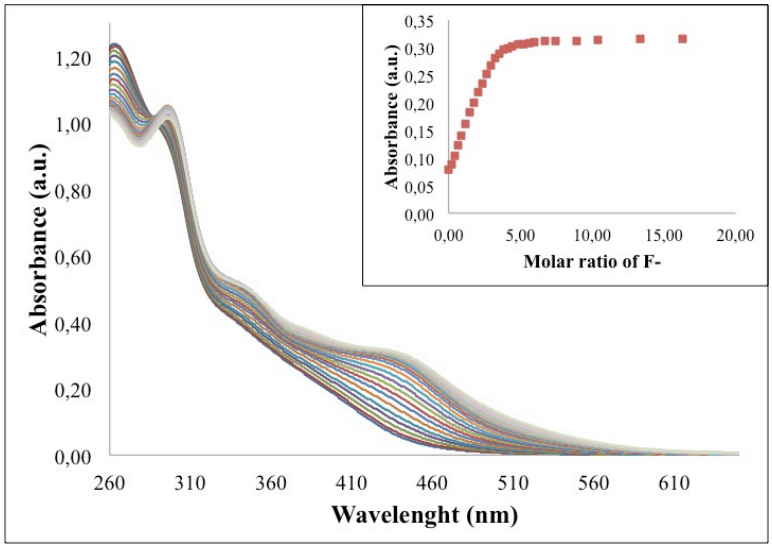

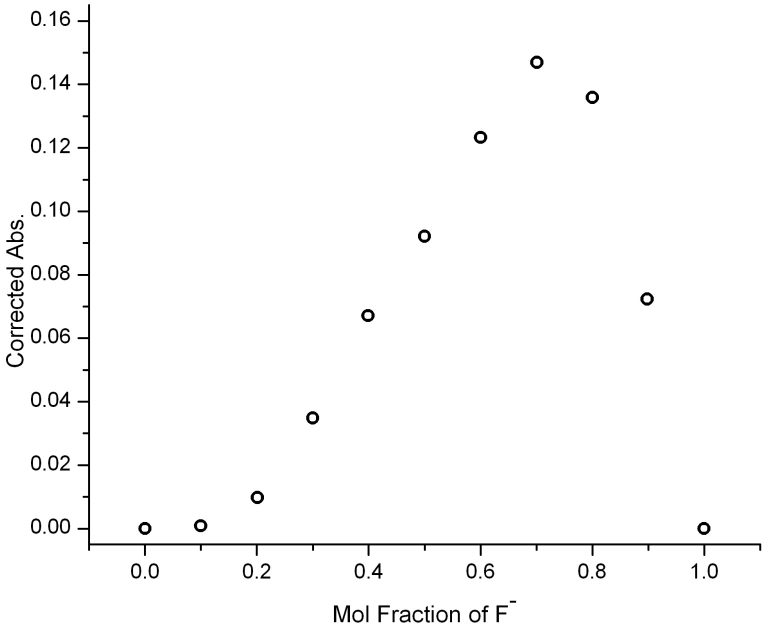

Table II.1 - Apparent binding constants (K_{app}) determined by UV/vis and NMR titrations.

		UV/vis[b][c][e]		NMR[b][d][f]		
Entry	Anion[a]	Log ($K_{1:1}$) (± 0.1)	Log ($K_{2:1}$) (± 0.1)	Log ($K_{1:1}$) (± 0.2)	Log ($K_{2:1}$) (± 0.2)	Log ($K_{3:1}$) (± 0.2)
3	F^-	4.4	NA	3.7	NA	NA
	OAc^-	5.8	NA	3.9	8.9	NA
	$H_2PO_4^-$	4.7	NA	2.8	6.2	NA
4	F^-	3.9	10.3	3.6	5.8	3.0
	OAc^-	5.4	11.2	4.8	9.0	6.1
	$H_2PO_4^-$	5.7	9.8	2.9	5.5	4.0

[a] All anions were added as their tetrabutylammonium (TBA) salts. [b] Acquisitions at 298K. [c] In DMSO - 0.5% H_2O (v/v). [d] In DMSO-*d6* - 0.5% H_2O (v/v). [e] Data fitted with the HypSpec software. [f] Data fitted with the HypNMR2008 software.

The UV/vis anion-binding studies were performed in a DMSO-0.5% water medium (Figure 2.3 and ESI). Absorption spectra of both complexes show intense intra-ligand ($\pi \rightarrow \pi^*$) absorption bands in the range 260-300 nm. The less intense absorption shoulder between 350 and 400 nm is assigned to a spin-allowed metal-to-ligand charge-transfer (^{1}MLCT) ($d\pi(Re) \rightarrow \pi^*(phen)$) transition. On addition of the F^-, OAc^- and $H_2PO_4^-$ ions as their tetrabutylammonium (TBA) salts during titration of **3** and **4,** gradual rises in the absorption at ca. 350 nm and 440 nm were observed.

The use of Job plots by UV/vis allowed a preliminary fitting of the data to a 1:1 complex: anion model for **3** (ESI) and to 1:2 for **4** (Figure 2.4 and ESI)**.** While some of the results tend to be slightly offset from the ideal fittings, eg. **3** with F^- and $H_2PO_4^-$, it appears that a deprotonation equilibra exist in the system. Moreover, it has already been established by Jurczak *et al.* that the deprotonation process on bishydrazide derivatives of isoindoline induced the development of a new band between 390-445 nm,[39] a behavior very similar to what is observe in our case around 440 nm.

UV/vis titration curves allowed for the determination of K_{app}. Values obtained in $\log(K_{app})$ for a 1:1 anion to complex **3** are 4.4 (F^-), 5.8 (OAc^-) and 4.7 ($H_2PO_4^-$). It is noteworthy that $K(OAc^-)$ /$K(H_2PO_4^-)$ is ~ 12.6 and $K(OAc^-)/K(F^-)$ is ~ 25, which demonstrates a preference for the acetate anion. The K values obtained for **3** are considerably higher than those previously reported for neutral Re(I) complexes with cleft-type amide receptors[22] and of a similar magnitude for positively charged Re(I) polypyridyl complexes with thiourea receptors.[31,40] Strong binding with neutral receptors is remarkable as favorable electrostatic interactions are usually one of the strongest contributors to anion-binding.[4-6] The Re(I) center is an excellent electron-withdrawing (EWG) group that acidifies the NH group and the extended π-conjugation of the phenanthroline stabilizes the deprotonated form of the receptor by delocalization of the charge. This combination of structural elements could be offering an increased tendency for deprotonation over H-

bonding behavior and, therefore, the apparent binding constant should be driven by basicity of the anion used. Following this idea, a quick look at the pKa table for acetic acid (4.76), hydrofluoric acid (3.17) and phosphoric acid (2.12) gives an insight that acetate anion is the strongest conjugate base of the three. Between $H_2PO_4^-$ and F^-, the latter should be stronger, but the higher solvation of unbound F^- in presence of water molecules should hinder its ability to deprotonate the thiourea group. All together, this rationalization seems to support the K_{app} obtained empirically for the mono-receptor complex **3**.

Complex **4** also shows high apparent stability constants for the three anions. Having two identical receptor sites, **4** is expected to furnish two K_{app} values, $K_{1:1}$ and $K_{2:1}$ respectively, where the latest should be lower due to disfavourable electrostatic arguments. The $\log(K_{app})$ values obtained for **4** are 3.9 and 10.3 (F^-), 5.4 and 11.2 (OAc^-); 5.7 and 9.8 ($H_2PO_4^-$). Those values are greater than the ones found for other bis-thiourea receptors,[37] although the contribution of deprotonation must also be considered. Interestingly enough, the results obtained clearly exhibit a $K_{2:1}$ between ca. 4 and 6 orders of magnitude higher than the $K_{1:1}$, which at first look might seems counterintuitive. However, a precedent in literature is known from Jurczak *et al.* where the interaction of $H_2PO_4^-$ with a mono-receptor led to a $K_{2:1}$ of three orders of magnitude higher than $K_{1:1}$ (i.e. $\log(K_{2:1}) = 7.2$ vs $\log(K_{1:1}) = 4.3$).[39] While no formal explanation for the presence of a second binding constant was reported there, it seems plausible that the presence of two hydrogens on

hydrophosphate anions can play a role, that is, multiple H-bonding with the receptor`s heteroatoms of their hydrazide linkages might add their effect to the classical NH bond interaction. In our case, as observation of the second binding constants for F^-, OAc^- or $H_2PO_4^-$ all displayed a higher value than the first one in a system where no multiple H-bonding of the anion with receptors was possible, it seems that the presence of deprotonated receptors do interfere with a good fitting of data. To further prove that idea and evaluate its impact, NMR titrations were also performed.[41]

NMR titration experiments were conducted in a 99.5% DMSO-d_6 / 0.5% H_2O solvent mixture to match with the conditions used in UV/vis tritration. As mentionned previously, a two hundred fold higher concentration of complexes **3** and **4** was used, i.e. 3 x 10^{-3} M, in order to evaluate the impact of concentration on the K_{app} observed at a suitable concentration for NMR. To keep the overall concentration of complex **3** constant throughout the titration, microliter-scale additions of a solution containing ~30 fold higher concentration of the anion as its TBA salt (1 x 10^{-1} M) over the complex were done to 0.7 mL of starting solution containing the complex alone (Figure 2.5 and ESI). Initial increments of 0.2 eq were used until 2 eq. of anion was reached, followed by 1 eq additions until the final 6 eq was reached. For complex **4**, which bears two thiourea receptor groups, the same starting concentration of complex was used, but initial increments of 0.25 eq were used until 6 eq of anion was reached, followed by 2 eq additions until the final 10 eq was

reached (Figure 2.6 and ESI). Interestingly, both complexes exhibit broadening then quick disaperance of the two NHs signals (around 10.25 ppm) upon addition of the various anions, which has been noted previously during deprotonation.[39] Based on stabilization arguments, the NH proton next to the phenanthroline moiety is the more likely to be deprotonated.

Figure 2.5 – NMR titration of receptor **3** (3 x 10^{-3} M) from 0 to 6 equivalents of OAc^- added by increments in 99.5 % DMSO-d_6 / 0.5% water. Only aromatic region is shown for clarity.

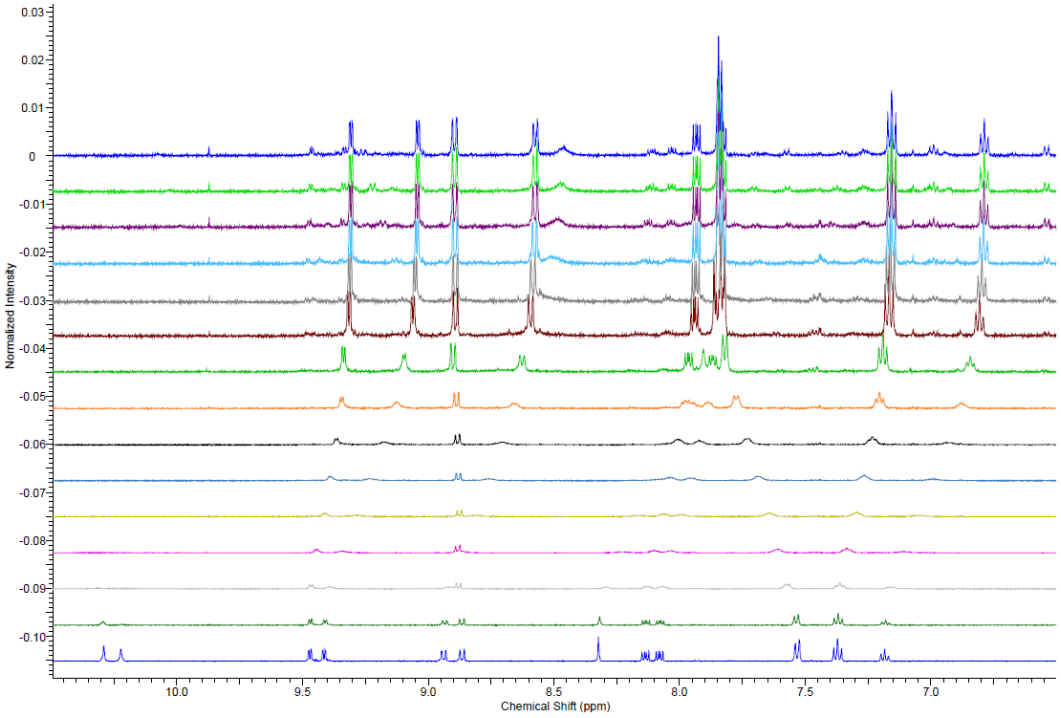

Figure 2.6 – NMR titration of receptor **4** (3 x 10^{-3} M) from 0 to 12 equivalents of OAc^- added by increments in 99.5 % DMSO-d_6 / 0.5% water. Only aromatic region is shown for clarity.

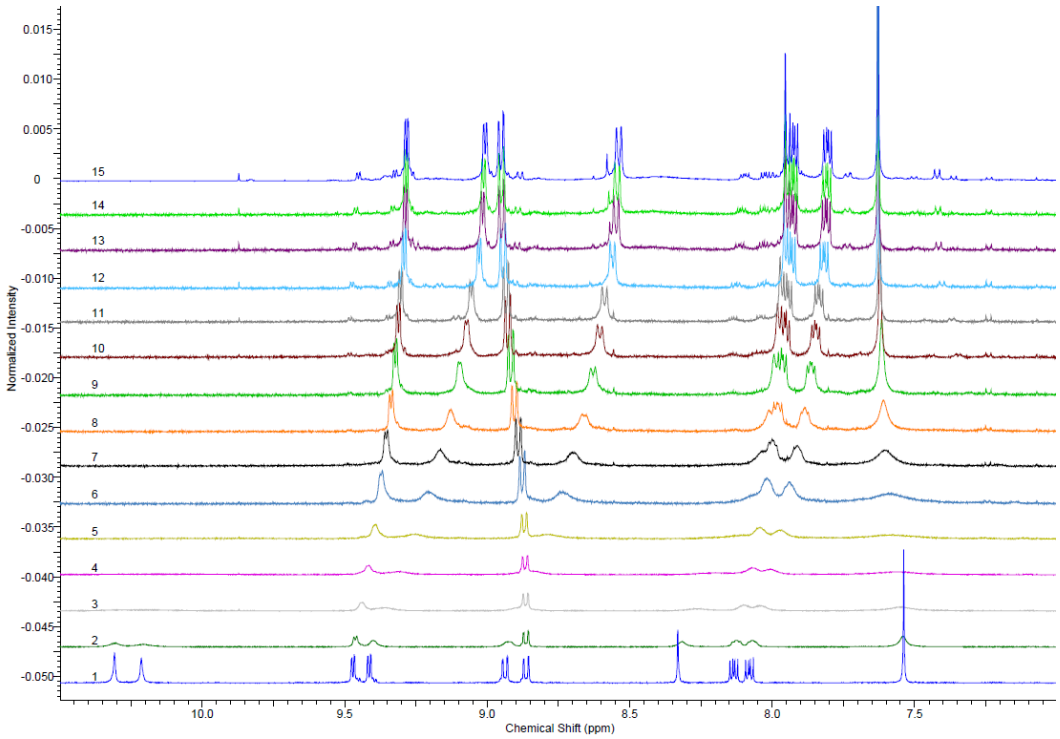

For determination of K_{app}, the three peaks showing biggest variation in ppm were used in order to diminish the potential error on the binding constant obtained. *A priori*, one might think that the protons providing higher variations in shift upon addition of anions should be the nearest to the thiourea receptor. However, peaks presenting this behavior are the ones allowing the stabilization of an electronic charge by delocalization. In this respect,

positions 3-, 7- and 9- on the phenanthroline moiety are the more sensible to receive this charge. Therefore, they should exhibit the largest shift during the titration. In complex **3**, the ^{1}H NMR shifts of positions 7 and 9, appearing at 8.94 ppm and 9.41 ppm, respectively, were studied. The H *para* (7.18 ppm) to the thiourea in the phenyl group also exhibited a large shift by NMR. For complex **4**, the peak at position 3- on the phenanthroline (8.08 ppm) replaced the *para*- one of the phenyl for K_{app} determination due to a bigger shift observed in that case. Positions 7- and 9- presented similar NMR displacements as in complex **3**.

Fitting of the data for complex **3** led to K_{app} values in the same order of magnitude as to what was obtained by UV/vis titration ($Log(K_{1:1}) = 3.7 \pm 0.2$ by NMR vs 4.4 ± 0.1 for UV/vis) for F^- (Table 2.1). However, necessity for a $K_{2:1}$ appeared to better fit data in the cases of stronger conjugate bases $H_2PO_4^-$ and OAc^-. Values of $log(K_{2:1})$ were higher than the one of one anion binding to one receptor for both OAc^- ($Log(K_{1:1}) = 3.9 \pm 0.2$; $Log(K_{2:1}) = 8.9 \pm 0.2$) and $H_2PO_4^-$ ($Log(K_{1:1}) = 2.8 \pm 0.2$; $Log(K_{2:1}) = 6.2 \pm 0.2$). Data for complex **4** (Table 2.1) are even more peculiar as they force to consider for a good fitting an association of 3 anions to one complex bearing two receptors ($K_{3:1}$). While we have no formal explanation for this unusual behaviour from a supramolecular point of view, it might only be artefacts arising from the interference of deprotonation equilibra compared to H-bonding at the concentrations required for NMR experiments. Another point to take in

consideration is the appearance in the baseline of NMR spectrums of what seems to be a new species upon addition of anions; potentially due to a decomposition phenomena leading back to the 5-amino-1,10-diaminophenanthroline derivative in basic conditions. Overall, the titrations by NMR of complexes **3** and **4** allowed a better understanding of the possible deprotonation equilibra in competition with H-bonding, as this technique offers access to structural characterization of anion interactions with the receptor at higher concentration compared to UV/vis.

Of note, titration attempts were also made using fluorescence emission quenching method, however, no useful results were obtained in order to determine K_{app}. In fact, development of a second emission peak overlapping with the one under evaluation renders the tracking of emission maxima impossible. This second peak might be the result of emission from the deprotonated receptor R^-. In any case, this behavior is an additional point which suggests that a competitive system exists in which both H-bonding and deprotonation equilibria are at play. Decomposition phenomena may also be implied, as the NMR titration experiments showed, a situation that further can affect apparent binding constants.

From a supramolecular point of view, complexes **3** and **4** should be *a priori* integrable into higher order self-assembled structures when combine with suitable H-bonding linkers. Based on that concept, the dianionic terephatalate could potentially form a dimeric structure in the case of **3** and or even a molecular triangle by combining three complexes **4** with three bridging dianions. In order to quickly test if such assemblies were easily accessible, HRMS studies by direct infusion of 2.8E-03 M solutions of both the complex and the dianion were done under the mildest ESI conditions possible. While self-assembled structures are not always stable in the HRMS due to the weak nature of H-bonding, many examples were still observed and reported in the literature. Unfortunately, complex **3** exhibited mainly the deprotonated specie [**3**-H]$^-$ at 678.9536 m/z along with a 1:1 assembly with the dianion still bearing one of the two TBA cations [**3**+Terephtalate+TBA]$^-$ at 1086.2502 m/z. For complex **4**, only the doubly deprotonated specie [**4**-2H]$^{2-}$ at 639.9224 m/z and the TBA-stabilized one [**4**+TBA-2H]$^-$ at 1522.1217 m/z were observed. Therefore, no indication of dimer or molecular triangle is reportable. However, the presence of deprotonated complexes in the HRMS for both case further support the hypothesis of a thiourea deprotonation phenomena.

2.4 – Conclusion

In conclusion, we have demonstrated in this work a very simple and high-yielding synthetic protocol for mono and polynuclear Re(I) complexes based on a 5-substituted phenanthroline moiety with thiourea linkages. An X-ray molecular structure of the precursor **2** also confirmed that these systems are inherently chiral. To the best of our knowledge, complexes **3** and **4** in our present work represent the first example of neutral Re(I) complexes with thiourea receptor groups that can be used as anion binding agents. Moreover, we have studied the tendency of thiourea receptors toward deprotonation in presence of F^-, OAc^- and $H_2PO_4^-$ to conclude such an equilibrium might be present in our systems as Re(I) center can be considered as an EWG, which greatly enhances the NH proton's acidity. In addition, delocalization into the extended π-conjugation on the phenanthroline moiety may also stabilize the negative charge generated by deprotonation. Future work will be focus toward the incorporation of such high-energy absorbing Re(I) polynuclear complexes by the developed synthetic protocol into artificial molecular antenna for light-harvesting applications.

2.5 – Experimental section

Experimental Nuclear magnetic resonance (NMR) spectra were recorded in DMSO-d_6 at room temperature (r.t.) on a Bruker AV400 spectrometer at 400 MHz for ^{1}H NMR and at 100 MHz for ^{13}C NMR. Chemical shifts are reported in part per million (ppm) relative to residual solvent protons and the carbon resonance of the solvent (1.93 and 33.5 ppm respectively for DMSO-d_6). Absorption spectra for UV-vis titration and the Job plot method were measured in DMSO-0.5% water at r.t. on a Cary 500i UV-vis-NIR spectrophotometer. Experimental uncertainties are as follows: absorption maxima, ±2 nm; molar absorption coefficient, 10%. Solvents were removed under reduced pressure using a rotary evaporator unless otherwise stated.

$Re(CO)_3Br(5\text{-}NH_2\text{-phen})$ (**1**)

To a suspension of $Re(CO)_5Br$ (406 mg, 1 mmol) in toluene (30 mL) was added the 1,10-phenanthroline-5-amine (200 mg, 1 mmol). The mixture was then stirred and refluxed for 1h, during which time an orange compound precipitated. After cooling to ambient temperature the orange precipitate was isolated by filtration and was washed with n-hexane and air dried. Yield = 525 mg. (96 %). ^{1}H NMR (DMSO-d_6, 400 MHz); 9.40 (dd, J^d = 5.0 Hz, J^d = 1.0 Hz, 1H, H), 9.11 (dd, J^d = 9.0 Hz, J^d = 1.0 Hz, 1H), 8.95 (dd, J^d = 5.0 Hz, J^d = 1.0 Hz, 1H), 8.47 (dd, J^d = 8.0 Hz, J^d = 1.0 Hz, 1H), 8.05 (dd, J^d = 8.0 Hz, J^d = 5.0 Hz, 1H), 7.78 (dd, J^d = 8.0 Hz, J^d = 5.0 Hz, 1H), 7.07 (s, 1H, H_7), 6.90 (s, 2H,-NH_2). Elemental Analysis: calc for $C_{15}H_9BrN_3O_3Re$; C = 33.04 %, H = 1.66 %, N = 7.71 %; found: C = 33.95 %, H = 1.62 %, N = 7.60 %.

$Re(CO)_3Br(5\text{-}NCS\text{-}phen)$ (**2**)

To a suspension of $Re(CO)_3Br(5\text{-}NH_2\text{-}phen)$ (240 mg, 0.45 mmol) in acetone (90 mL) was added the Na_2CO_3 (180 mg, 1.7 mmol). To the mixture was added $CSCl_2$ (0.16 mL) and stirring was continued at ambient temperature for 6h under N_2 atmosphere. The reaction mixture was then filtered and the filtrate was evaporated under reduced pressure. The resulting brownish yellow solid was dissolved in minimum volume of dichloromethane and was filtered again. Evaporation of the solvent under reduced pressure yielded the product **2** as a brownish yellow powder. Yield = 250 mg (97 %). ^{1}H NMR (DMSO-d_6, 300 MHz); 9.55 (dd, J^d = 5.0 Hz, J^d = 1.0 Hz, 1H, H), 9.45 (dd, J^d = 5.0 Hz, J^d = 1.0 Hz, 1H), 8.98 (dd, J^d = 8.0 Hz, J^d = 1.0 Hz, 1H), 8.89 (dd, J^d = 8.0 Hz, J^d = 1.0 Hz, 1H), 8.60 (s, 1H, H_7), 8.21 (dd, J^d = 8.0 Hz, J^d = 5.0 Hz, 1H), 8.11 (dd, J^d = 8.0 Hz, J^d = 5.0 Hz, 1H). Elemental Analysis: calc for $C_{16}H_7BrN_3O_3ReS.(CH_3)_2CO$; C = 35.35 %, H = 2.03 %, N = 6.51, S = 4.97 %; found: C = 35.05 %, H = 1.83 %, N = 6.28, S = 5.07 %.

$Re(CO)_3Br$(5-(NH–CS-NH-Ph)-phen) (**3**)

$Re(CO)_3Br$(5-NCS-phen) (60 mg, 0.1 mmol) was dissolved in acetone (15 mL) with stirring. To this was added aniline (20 μL, 0.1 mmol) under a N_2 atmosphere. The resulting mixture was stirred for 20h under N_2, by which time a pale yellow precipitate formed, which was filtered, washed with n-hexane and air dried. Yield = 41 mg (63 %). (^{1}H NMR (DMSO-d_6, 400 MHz); 10.31 (s, 1H, Phen-N*H*-CS-NH-Ph), 10.23 (s, 1H, Phen-NH-CS-N*H*-Ph), 9.47 (d, J^d = 5.0 Hz, 1H), 9.42 (d, J^d = 5.0 Hz, 1H), 8.94 (d, J^d = 8.0 Hz, 1H), 8.87 (d, J^d = 8.0 Hz, 1H), 8.32 (s, 1H, H_7), 8.14 (dd, J^d = 8.0 Hz, J^d = 5.0 Hz, 1H), 8.08 (dd, J^d = 8.0 Hz, J^d = 5.0 Hz, 1H), 7.53 (d, J^d = 8.0 Hz, 2H, Ph-*o*), 7.37 (t, J^t = 8.0 Hz, 2H, Ph-*m*), 7.18 (t, J^t = 7.0 Hz, 1H, Ph-*p*). Elemental Analysis: calc for $C_{22}H_{14}BrN_4O_3ReS$; C = 38.83 %, H = 2.07 %, N = 8.23, S = 4.71 %; found: C = 38.79 %, H = 1.54 %, N = 8.05, S = 4.39 %.

[$Br(CO)_3Re$(μ-phen-5-(NH–CS-NH)-5-phen)$Re(CO)_3Br$] (4)

$Re(CO)_3Br$(5-NCS-phen) (120 mg, 0.2 mmol) was dissolved in acetone (20 mL) with stirring. To this solution was added *p*-phenylenediamine (11 mg, 0.1 mmol) under a N_2 atmosphere. The resulting mixture was stirred for 24h under N_2, by which time a brownish orange precipitate formed, which was filtered, washed with n-hexane and air dried. Yield = 61 mg (60 %). (^{1}H NMR (DMSO-d_6, 400 MHz); 10.35 (s, 1H, Phen-N*H*-CS-NH-Ph), 10.25 (s, 1H, Phen-NH-CS-N*H*-Ph), 9.47 (d, J^d = 5.0 Hz, 1H), 9.41 (d, J^d = 5.0 Hz, 1H), 8.94 (d, J^d = 8.0 Hz, 1H), 8.87 (d, J^d = 8.0 Hz, 1H), 8.34 (s, 1H, H_7), 8.13 (dd, J^d = 8.0 Hz, J^d = 5.0 Hz, 1H), 8.08 (dd, J^d = 8.0 Hz, J^d = 5.0 Hz, 1H), 7.54 (s, 4H, Ph). Elemental Analysis: calc for $C_{38}H_{22}Br_2N_8O_6Re_2S_2$. C = 35.57 %, H = 1.73 %, N = 8.73, S = 5.00 %; found: C = 36.06%, H = 1.75 %, N = 8.60, S = 4.57 %.

Acknowledgement. GSH thanks the Natural Sciences and Engineering Research Council of Canada (NSERC), the Centre for Self-Assembled Chemical Structures and the Université de Montréal (UdeM) for financial support. AB thanks the NSERC, the Fonds Québécois de la Recherche sur la Nature et les Technologies and Saint-Jean Photochimie Inc. for a BMP-Innovation scholarship and UdeM for a fellowship. AB also thanks Anne-Catherine Bédard for useful scientific discussions. SN thanks the Canadian Bureau for International Education for a fellowship.

Supporting Information Available: UV/Vis and NMR titrations, corresponding titration profile and Job plots of compounds **3** and **4**; Table containing bond lengths of structurally similar compounds and CIF file for **2**. The CCDC deposit number for the X-ray crystal structure of **2** is 796139.

2.6 – Bibliography

(1) Gale, P. A. *Chemical Communications* **2011**, *47*, 82.

(2) Christianson, D. W.; Lipscomb, W. N. *Acc. Chem. Res.* **1989**, *22*, 62.

(3) Berg, J. M. *Acc. Chem. Res.* **1995**, *28*, 14.

(4) Gale, P. A.; Gunnlaugsson, T. *Chem. Soc. Rev.* **2010**, *39*, 3595.

(5) Mercer, D. J.; Loeb, S. J. *Chem. Soc. Rev.* **2010**, *39*, 3612.

(6) Li, A.-F.; Wang, J.-H.; Wang, F.; Jiang, Y.-B. *Chem. Soc. Rev.* **2010**, *39*, 3729.

(7) Beer, P. D.; Gale, P. A. *Angew. Chem., Int. Ed.* **2001**, *40*, 486.

(8) dos Santos, C. M. G.; Harte, A. J.; Quinn, S. J.; Gunnlaugsson, T. *Coord. Chem. Rev.* **2008**, *252*, 2512.

(9) Rice, C. R. *Coord. Chem. Rev.* **2006**, *250*, 3190.

(10) Wenzel, M.; Hiscock, J. R.; Gale, P. A. *Chem. Soc. Rev.* **2012**, *41*, 480.

(11) Bondy, C. R.; Loeb, S. J. *Coord. Chem. Rev.* **2003**, *240*, 77.

(12) Bayly, S.; Beer, P. In *Recognition of Anions*; Vilar, R., Ed.; Springer Berlin / Heidelberg: 2008; Vol. 129, p 45.

(13) Caltagirone, C.; Mulas, A.; Isaia, F.; Lippolis, V.; Gale, P. A.; Light, M. E. *Chemical Communications (Cambridge, United Kingdom)* **2009**, 6279.

(14) De Santis, G.; Fabbrizzi, L.; Licchelli, M.; Poggi, A.; Taglietti, A. *Angewandte Chemie International Edition in English* **1996**, *35*, 202.

(15) Fabbrizzi, L.; Licchelli, M.; Mancin, F.; Pizzeghello, M.; Rabaioli, G.; Taglietti, A.; Tecilla, P.; Tonellato, U. *Chemistry – A European Journal* **2002**, *8*, 94.

(16) Fabbrizzi, L.; Licchelli, M.; Pallavicini, P.; Parodi, L.; Taglietti, A. *Fluorescent Sensors for and with Transition Metals*; John Wiley & Sons, Ltd., 2007.

(17) Bondy, C. R.; Gale, P. A.; Loeb, S. J. *Journal of the American Chemical Society* **2004**, *126*, 5030.

(18) Fisher, M. G.; Gale, P. A.; Light, M. E.; Loeb, S. J. *Chem. Commun.* **2008**, 5695.

(19) dos Santos, C. M. G.; Gunnlaugsson, T. *Dalton Transactions* **2009**, 4712.

(20) Basurto, S.; Riant, O.; Moreno, D.; Rojo, J.; Torroba, T. *The Journal of Organic Chemistry* **2007**, *72*, 4673.

(21) Beer, P. D.; Cooper, J. B. *Chem. Commun.* **1998**, 129.

(22) Beer, P. D.; Dent, S. W.; Hobbs, G. S.; Wear, T. J. *Chem. Commun.* **1997**, 99.

(23) Beer, P. D.; Drew, M. G. B.; Hesek, D.; Shade, M.; Szemes, F. *Chem. Commun.* **1996**, 2161.

(24) Beer, P. D.; Timoshenko, V.; Maestri, M.; Passaniti, P.; Balzani, V. *Chem. Commun.* **1999**, 1755.

(25) Lam, S.-T.; Zhu, N.; Yam, V. W.-W. *Inorg. Chem.* **2009**, *48*, 9664.

(26) Lin, T.-P.; Chen, C.-Y.; Wen, Y.-S.; Sun, S.-S. *Inorg. Chem.* **2007**, *46*, 9201.

(27) Cooper, J. B.; Drew, M. G. B.; Beer, P. D. *J. Chem. Soc., Dalton Trans.* **2001**, 392.

(28) Odago, M. O.; Hoffman, A. E.; Carpenter, R. L.; Tse, D. C. T.; Sun, S.-S.; Lees, A. J. *Inorg. Chim. Acta* **2011**, *374*, 558.

(29) Kurz, P.; Probst, B.; Spingler, B.; Alberto, R. *European Journal of Inorganic Chemistry* **2006**, *2006*, 2966.

(30) Lundin, N. J.; Walsh, P. J.; Howell, S. L.; McGarvey, J. J.; Blackman, A. G.; Gordon, K. C. *Inorg. Chem.* **2005**, *44*, 3551.

(31) Lo, K. K.-W.; Lau, J. S.-Y.; Fong, V. W.-Y.; Zhu, N. *Organomet.* **2004**, *23*, 1098.

(32) Si, Z.; Li, X.; Li, X.; Zhang, H. *Journal of Organometallic Chemistry* **2009**, *694*, 3742.

(33) Gunnlaugsson, T.; Davis, A. P.; Glynn, M. *Chem. Commun.* **2001**, 2556.

(34) Gunnlaugsson, T.; Kruger, P. E.; Jensen, P.; Tierney, J.; Ali, H. D. P.; Hussey, G. M. *The Journal of Organic Chemistry* **2005**, *70*, 10875.

(35) Lee, D. H.; Lee, H. Y.; Lee, K. H.; Hong, J.-I. *Chem. Commun.* **2001**, 1188.

(36) Nishizawa, S.; Kaneda, H.; Uchida, T.; Teramae, N. *Journal of the Chemical Society, Perkin Transactions 2* **1998**, 2325.

(37) Perez-Casas, C.; Yatsimirsky, A. K. *The Journal of Organic Chemistry* **2008**, *73*, 2275.

(38) Camiolo, S.; Gale, P. A.; Hursthouse, M. B.; Light, M. E.; Shi, A. J. *Chem. Commun.* **2002**, 758.

(39) Dydio, P. Ç.; Zielinski, T.; Jurczak, J. *The Journal of Organic Chemistry* **2009**, *74*, 1525.

(40) Lo, K. K.-W.; Lau, J. S.-Y.; Lo, D. K.-K.; Lo, L. T.-L. *Eur. J. Inorg. Chem.* **2006**, *2006*, 4054.

(41) Gunnlaugsson, T.; Davis, A. P.; O'Brien, J. E.; Glynn, M. *Org. Biomol. Chem.* **2005**, *3*, 48.

Partie B - Informations Supplémentaires

Table II.2 - Bond lengths of structurally similar compounds.

Compound (CCDC no.)	Ceq-Re (esd)	Ceq-Re (esd)	Cax-Re (esd)	Ceq-Oeq (esd)	Ceq-Oeq (esd)	Cax-Oax (esd)	Re-Br (esd)	Re-N (avg)
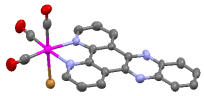 299063	1.925 (16)	1.927 (18)	1.952 (16)	1.152 (19)	1.15 (2)	1.101 (17)	2.6391 (16)	2.182
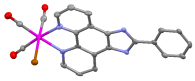 606330	1.939 (6)	1.939 (7)	1.895 (4)	1.151 (9)	1.152 (7)	1.133 (4)	2.5852 (18)	2.183
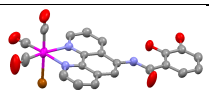 648123	1.920 (8)	1.894 (8)	1.934 (8)	1.142 (8)	1.161 (9)	1.072 (8)	2.6254 (8)	2.176

Figure 2.7 – UV-Vis titrations of receptor **3** with $H_2PO_4^-$ in DMSO-0.5% water. Inset: corresponding titration profile at 347 nm.

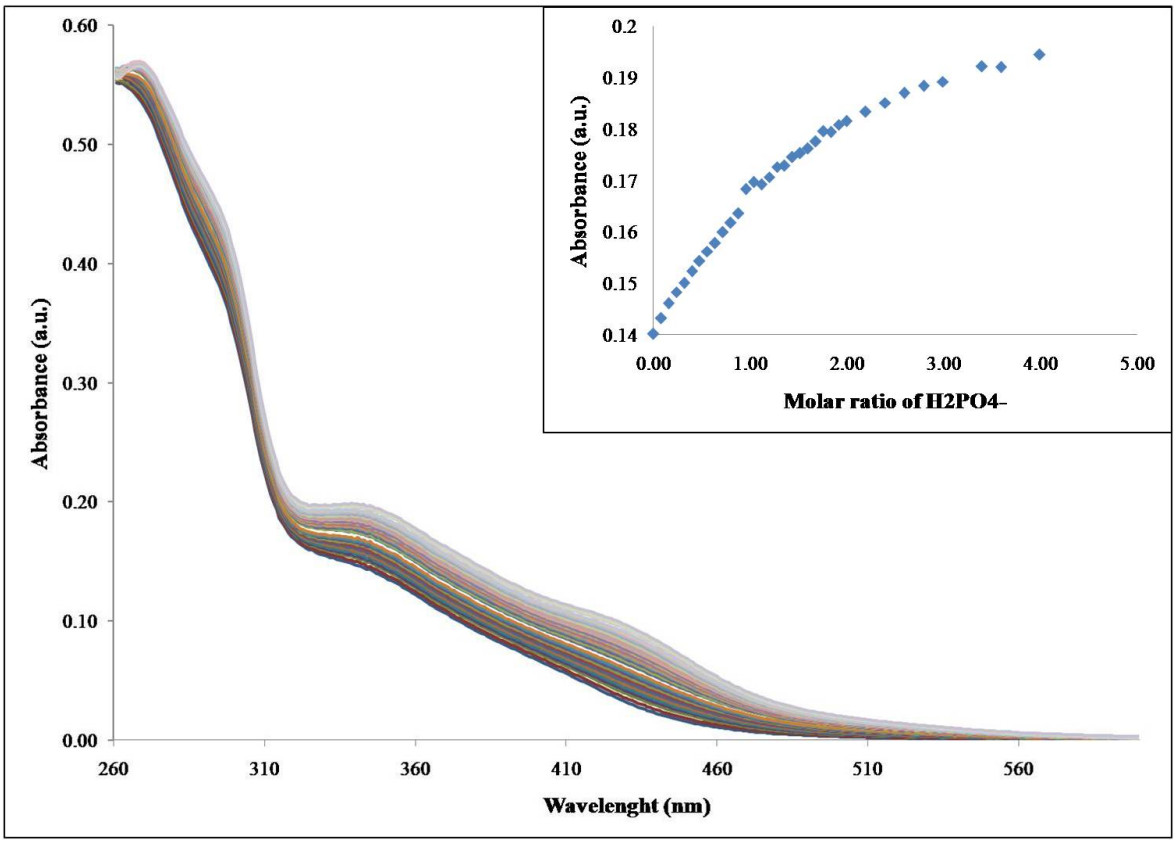

Figure 2.8 – Job plot of receptor **3** with $H_2PO_4^-$ in DMSO-0.5% water at 450 nm, showing 1:1 binding.

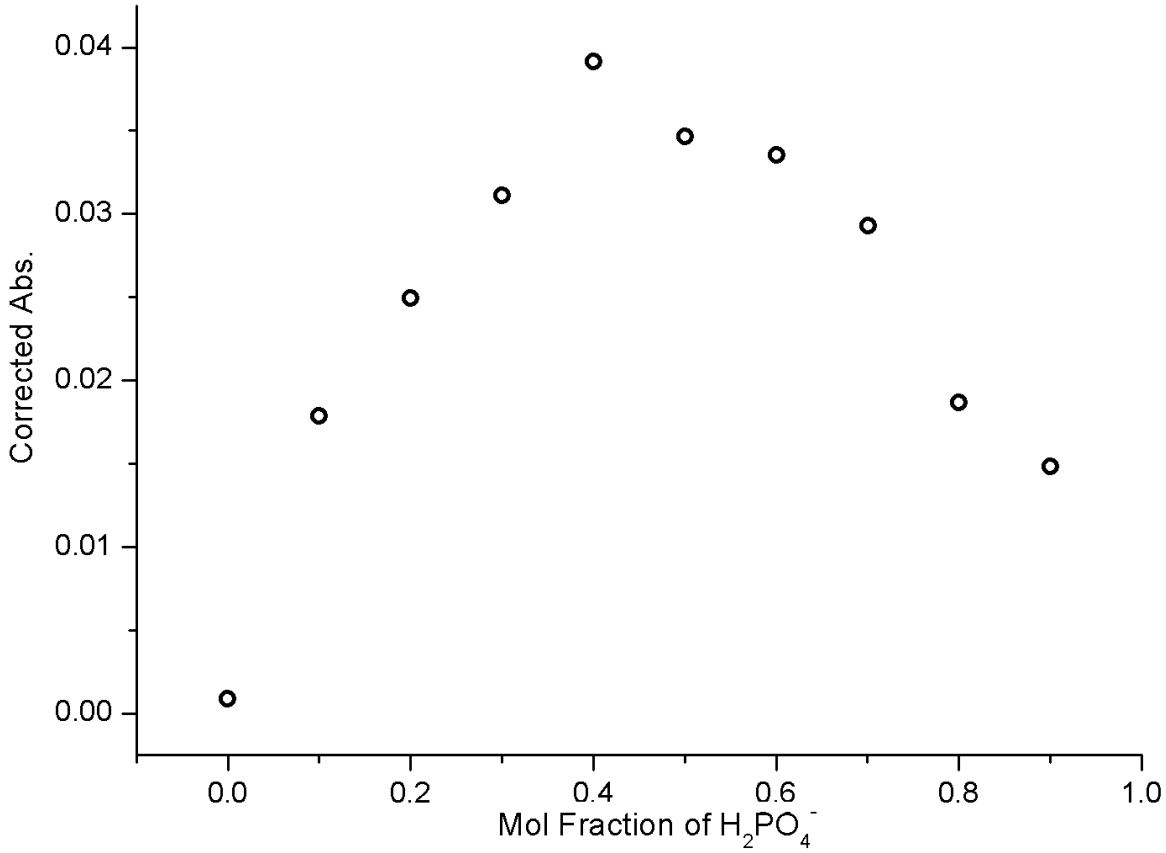

Figure 2.9 – UV-Vis titrations of receptor **3** with OAc^- in DMSO-0.5% water. Inset: corresponding titration profile at 347 nm.

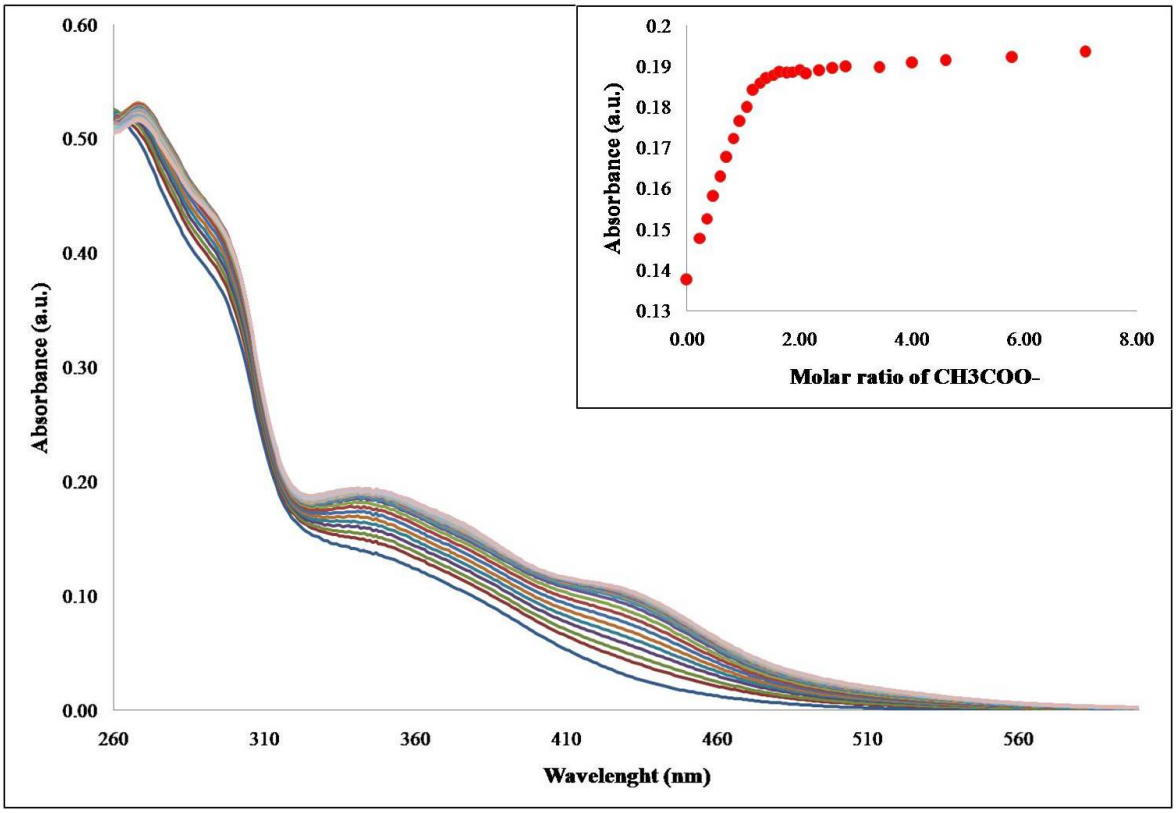

Figure 2.10 – Job plot of receptor **3** with OAc^- in DMSO-0.5% water at 450 nm, showing 1:1 binding.

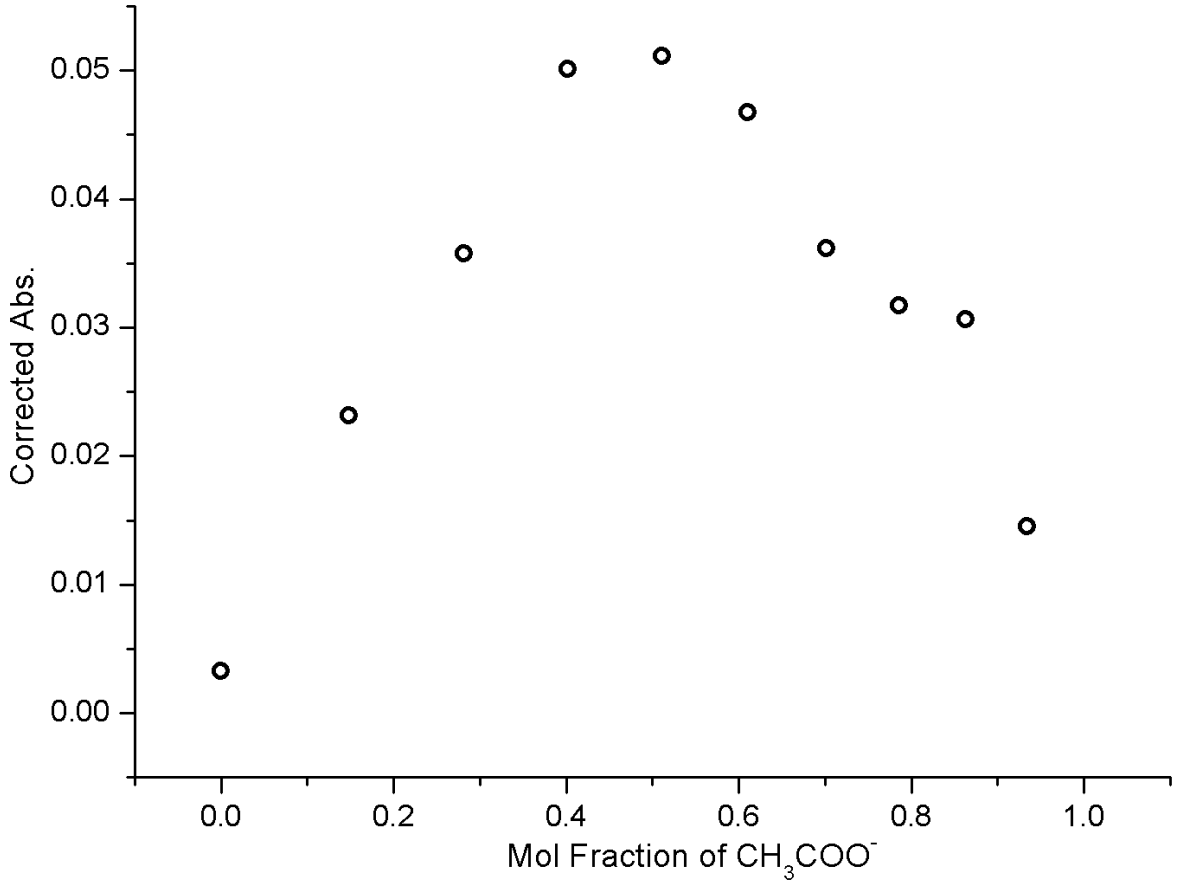

Figure 2.11 – UV-vis titrations of receptor **4** with $H_2PO_4^-$ in DMSO-0.5% water. Inset: corresponding titration profile at 430 nm.

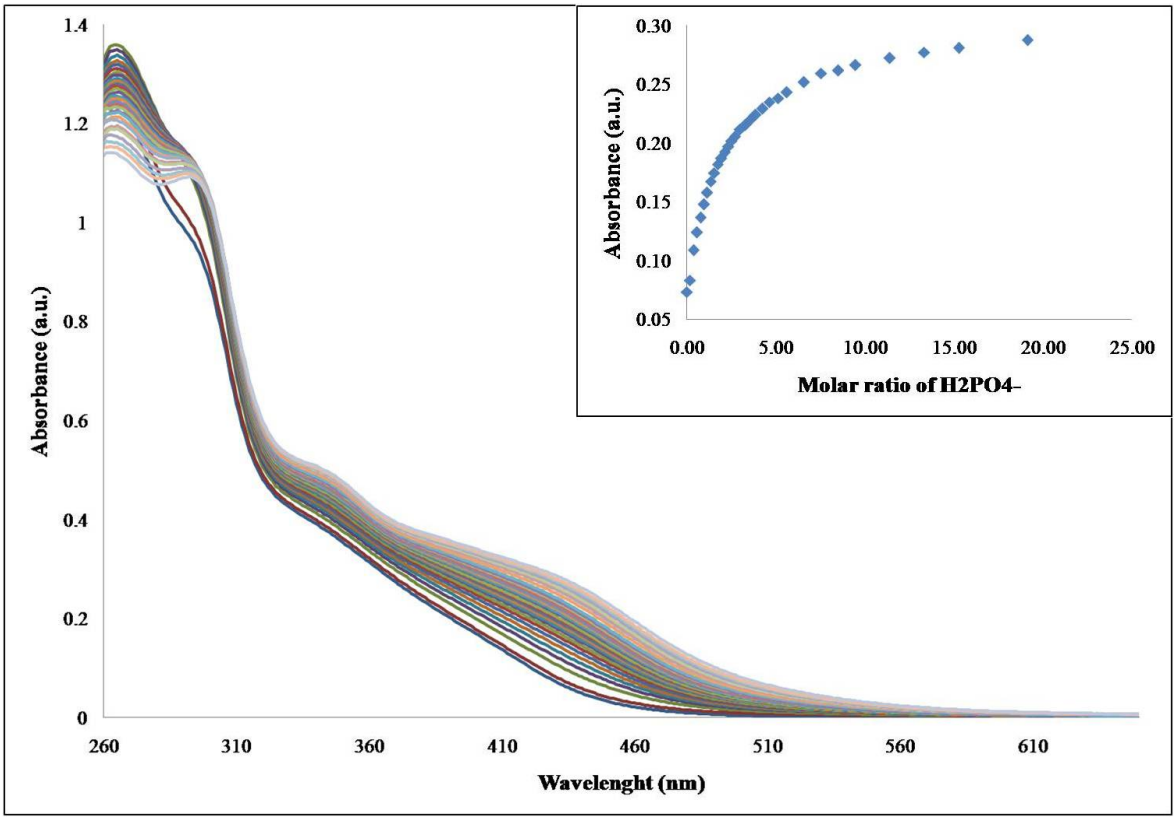

Figure 2.12 – Job plot of receptor **4** with $H_2PO_4^-$ in DMSO-0.5% water at 500 nm, showing 1:2 binding.

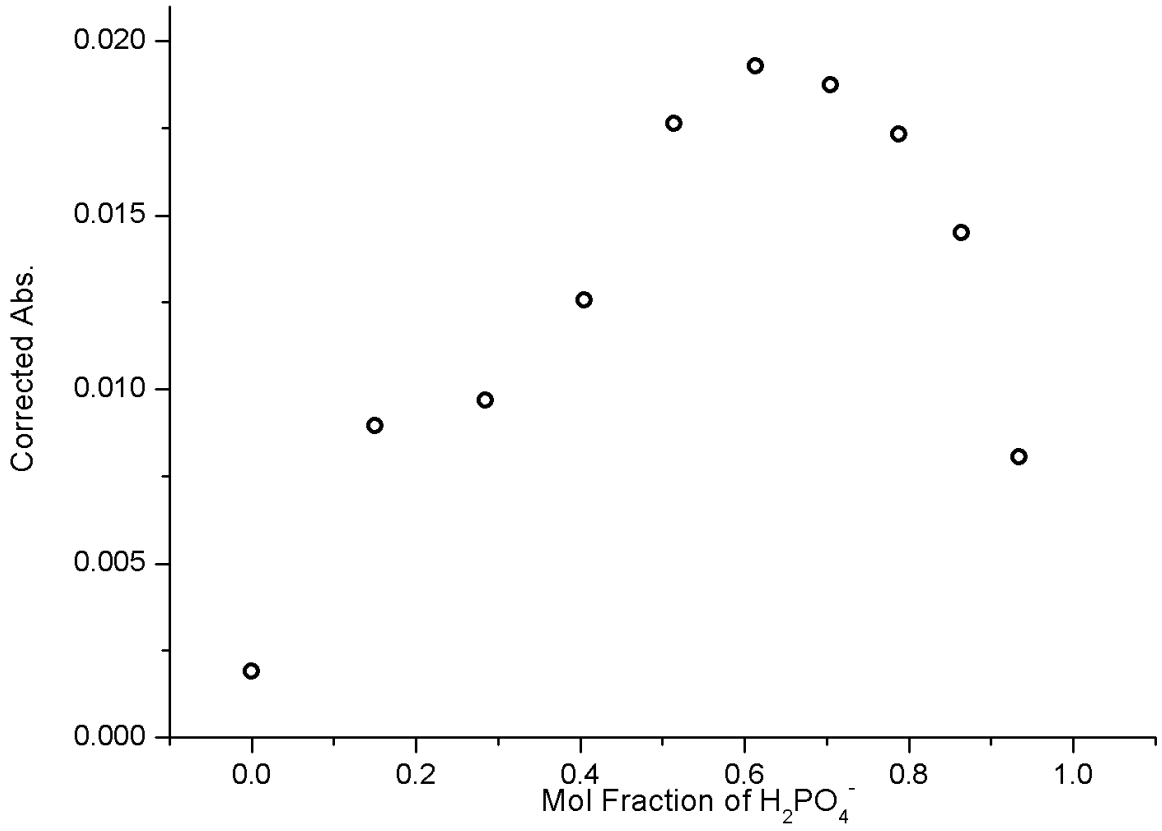

Figure 2.13 – UV-vis titrations of receptor **4** with OAc^- in DMSO-0.5% water. Inset: corresponding titration profile.

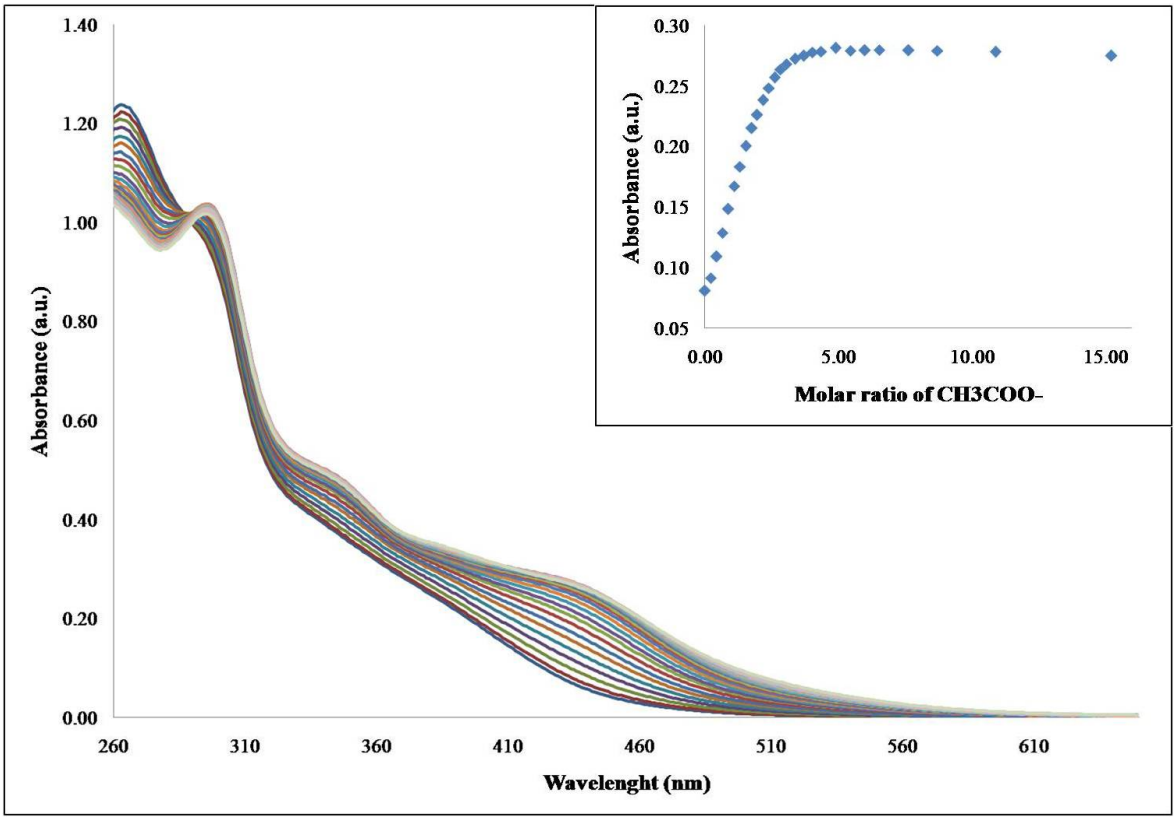

Figure 2.14 – Job plot of receptor **4** with OAc^- in DMSO-0.5% water at 450 nm, showing 1:2 binding.

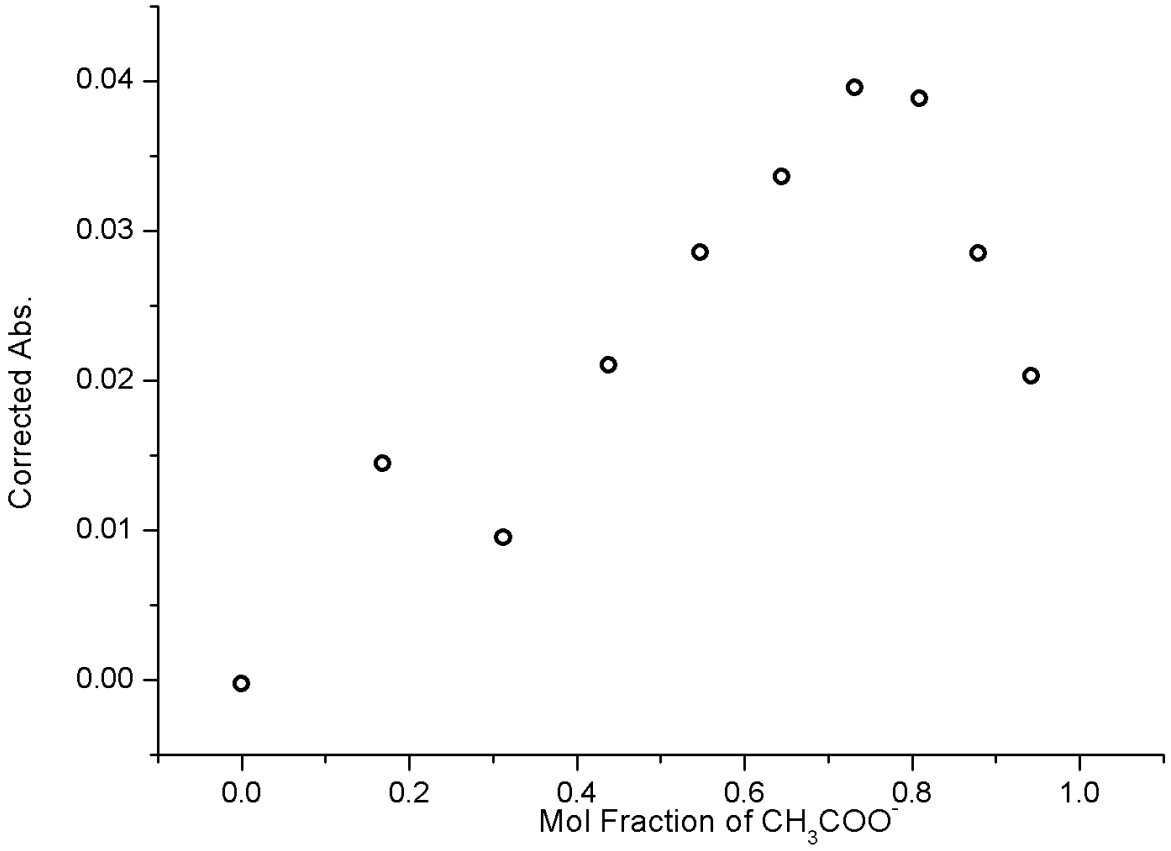

Figure 2.15 – NMR titration of receptor **3** ($3x10^{-3}$ M) from 0 to 6 equivalents of F^- added by increments in 99.5 % DMSO-d_6 / 0.5% water. Only aromatic region is shown for clarity.

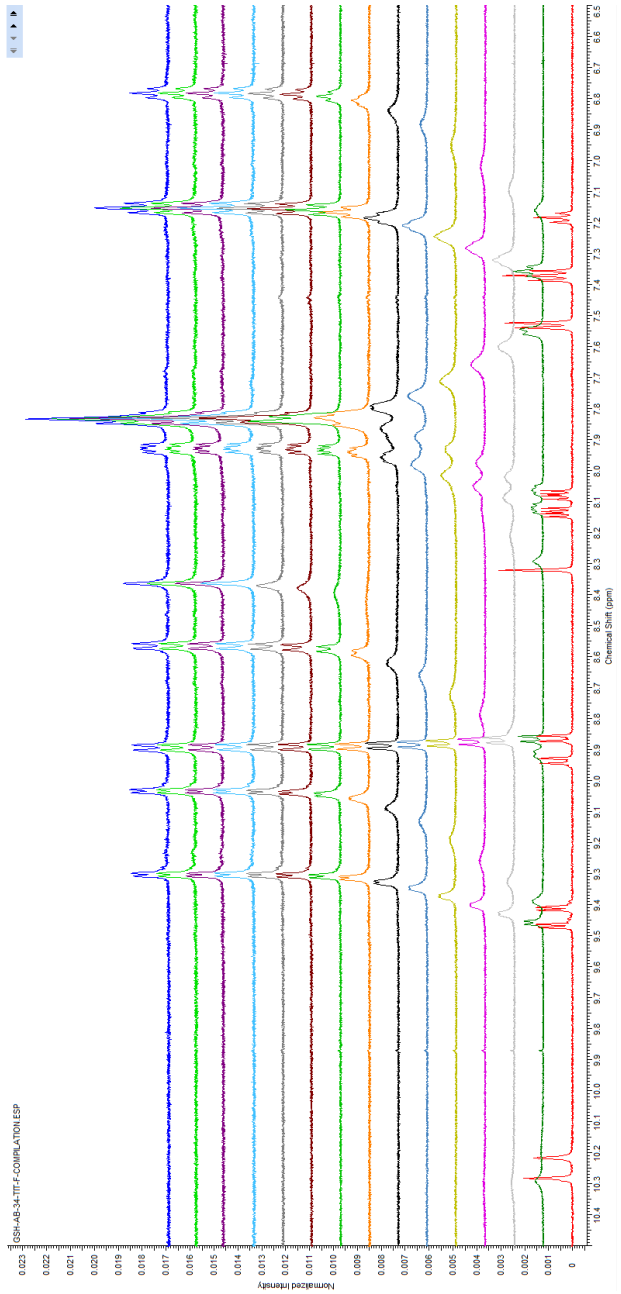

Figure 2.16 – NMR titration of receptor **3** ($3x10^{-3}$ M) from 0 to 6 equivalents of $H_2PO_4^-$ added by increments in 99.5 % DMSO-d_6 / 0.5% water. Only aromatic region is shown for clarity.

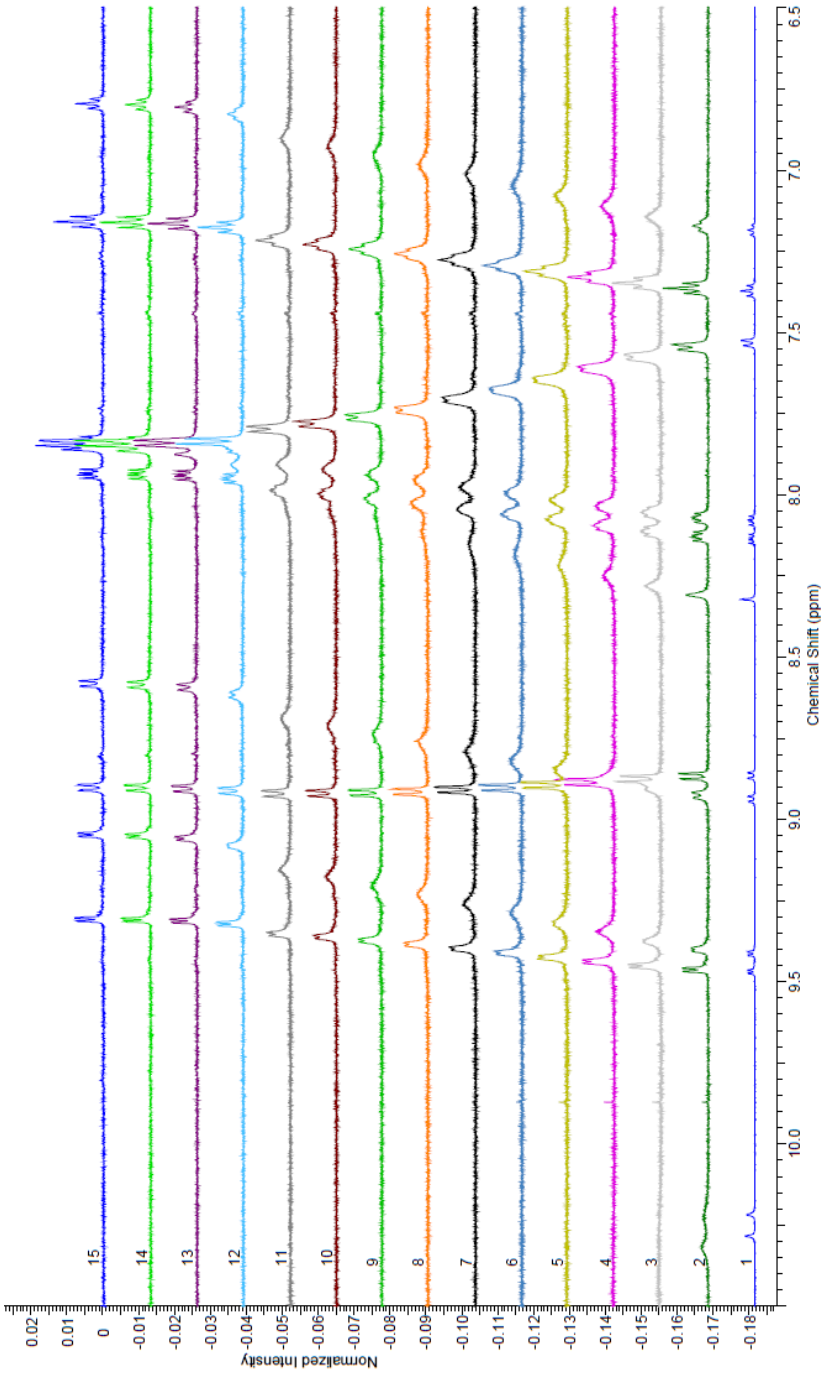

Figure 2.17 – NMR titration of receptor **4** ($3x10^{-3}$ M) from 0 to 12 equivalents of F^- added by increments in 99.5 % DMSO-d_6 / 0.5% water. Only aromatic region is shown for clarity.

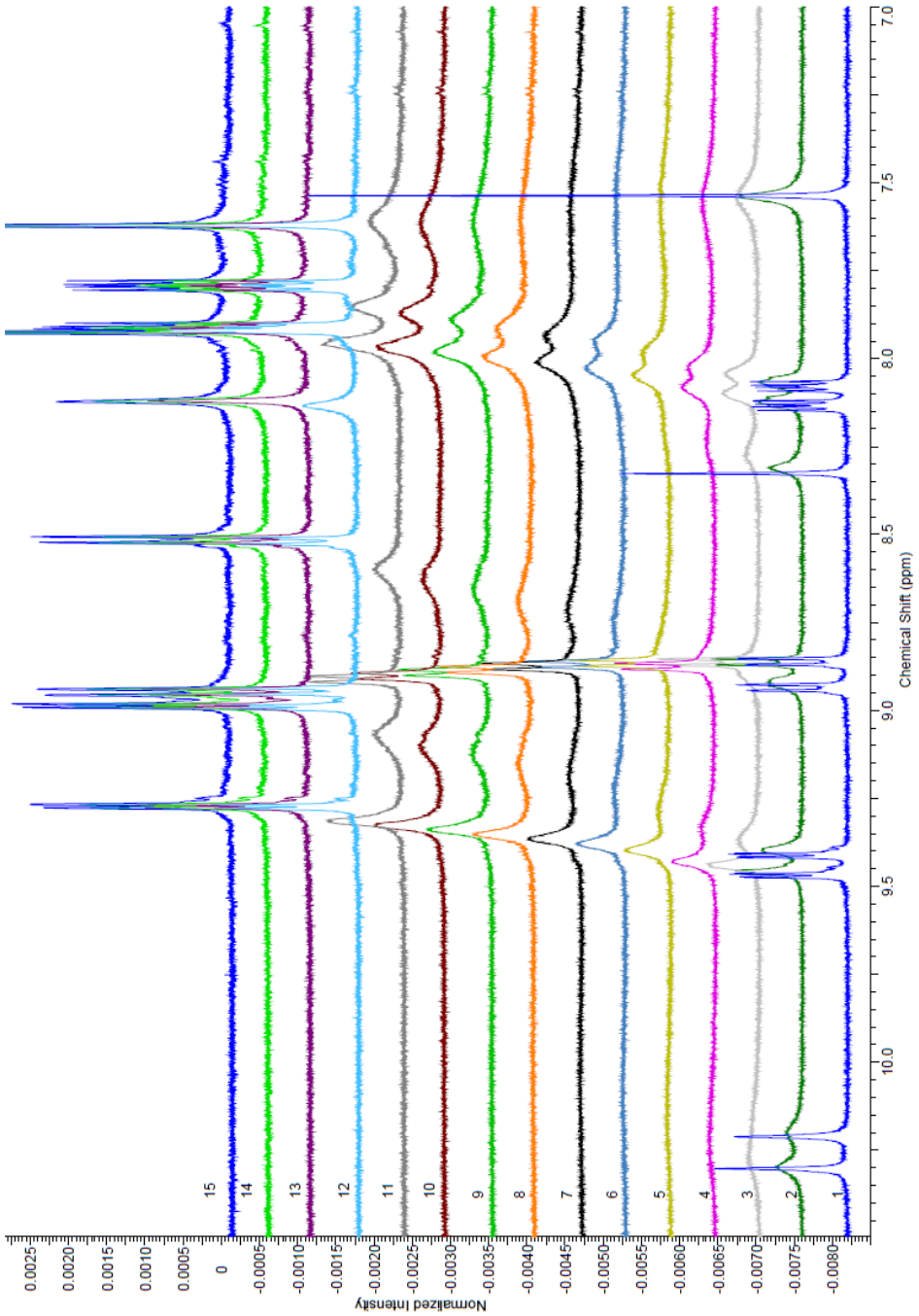

Figure 2.18 – NMR titration of receptor **4** ($3x10^{-3}$ M) from 0 to 12 equivalents of $H_2PO_4^-$ added by increments in 99.5 % DMSO-d_6 / 0.5% water. Only aromatic region is shown for clarity.

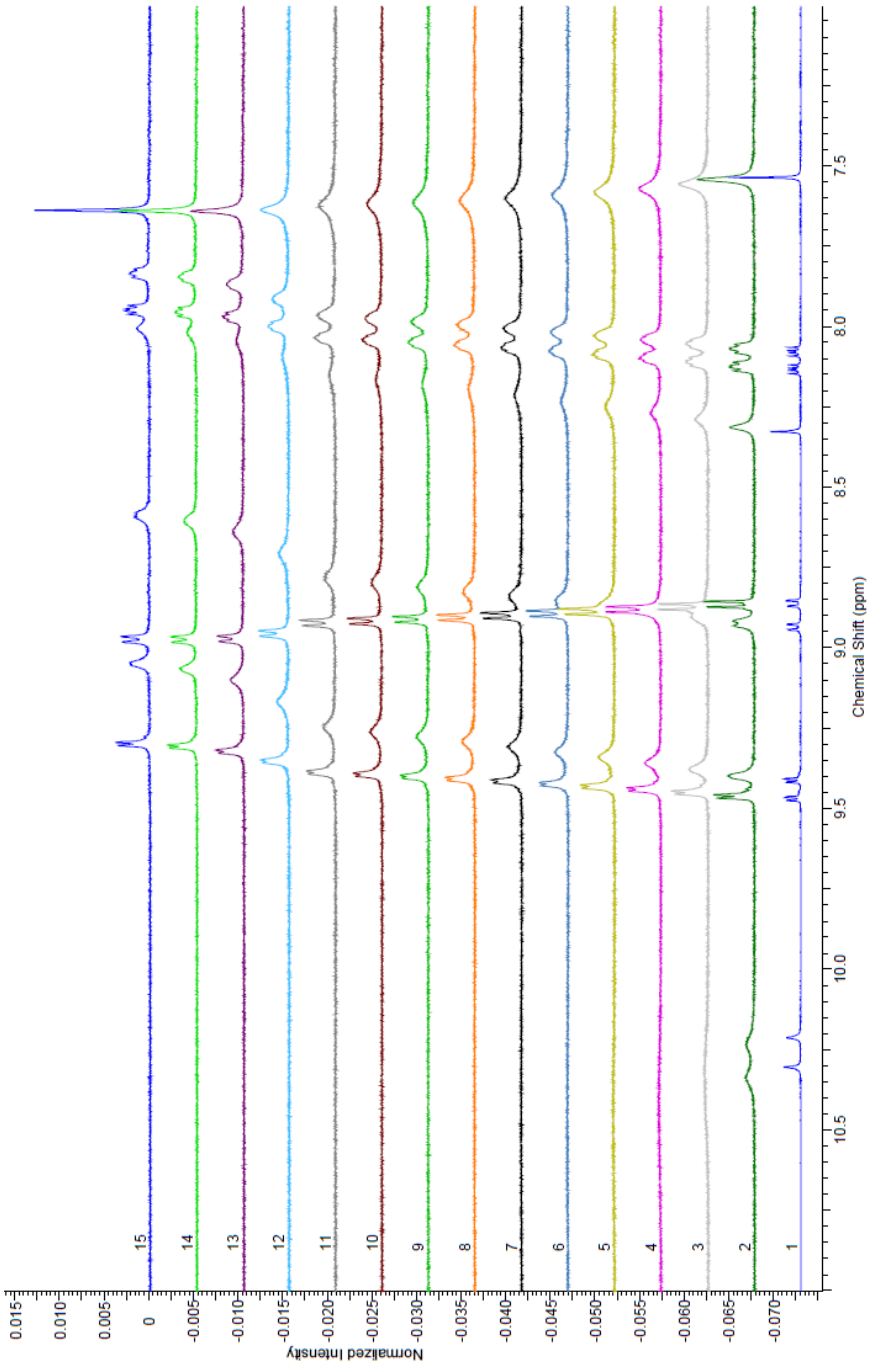

Figure 2.19 – HRMS by direct infusion in negative mode of a $2.8x10^{-3}$ M solution of complex **3** and the dianion terephtalate as its TBA salt in 20% Acetone / 80% DMSO.

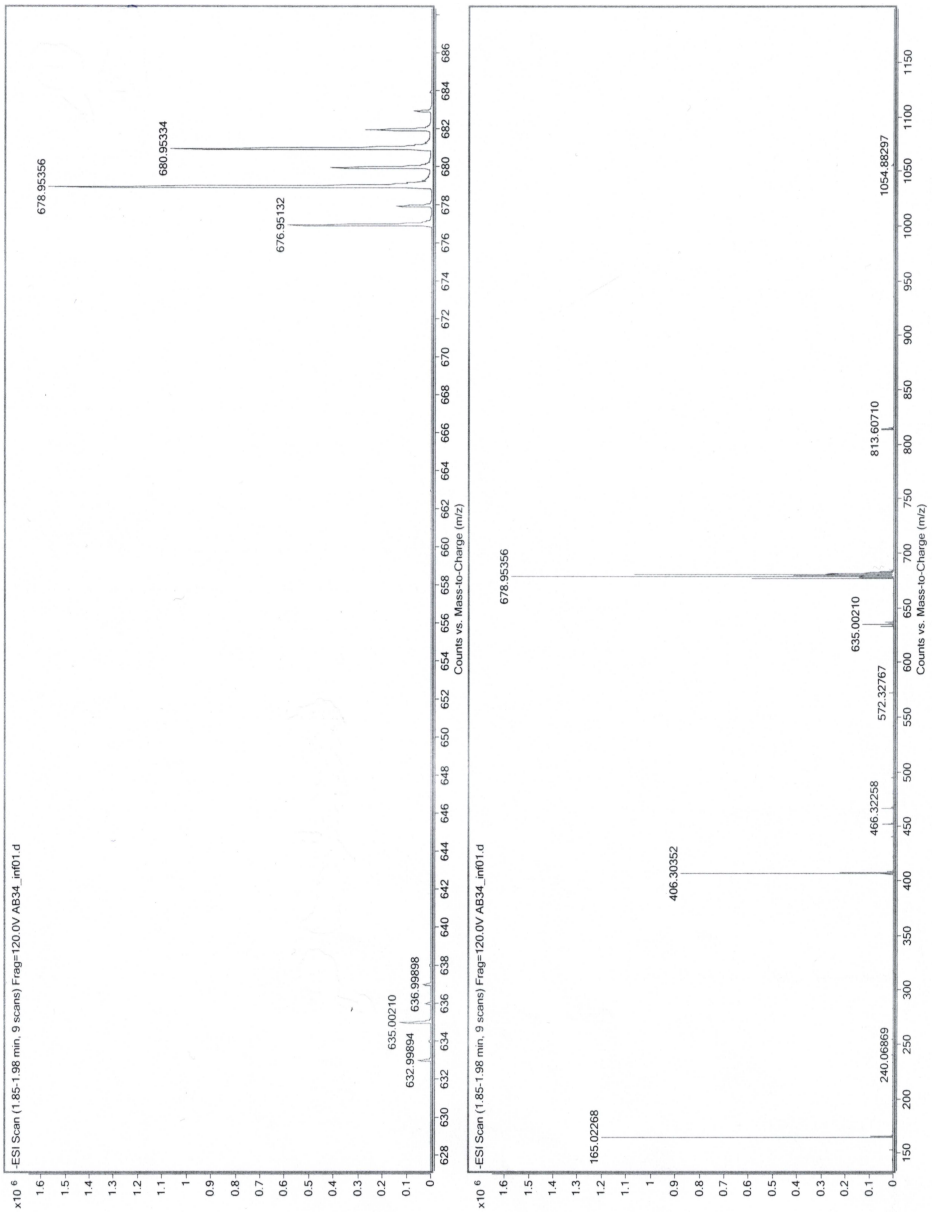

Result shown the presence of deprotonated specie $[\mathbf{3}\text{-H}]^-$ at 678.9536 m/z along with a 1:1 assembly with the dianion still bearing one of the two TBA cations $[\mathbf{3}\text{+Terephtalate+TBA}]^-$ at 1086.2502 m/z.

Figure 2.20 – Expension of the 1:1 assembly with the dianion still bearing one of the two TBA cations [**3**+Terephtalate+TBA]$^-$ at 1086.2502 m/z (Top) and its match with the theoretical isotopic patern (Bottom).

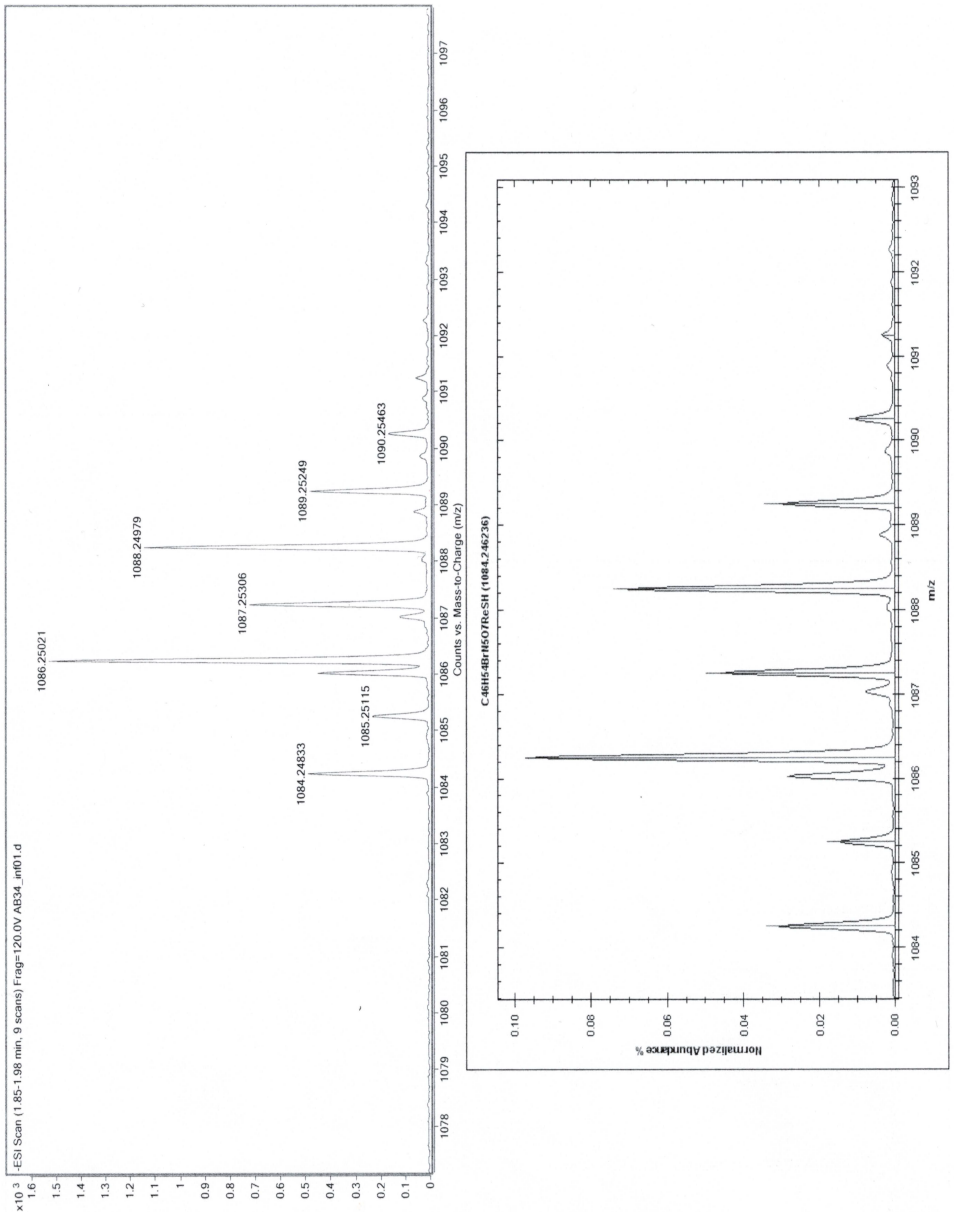

Figure 2.21 – HRMS by direct infusion in negative mode of a 2.8×10^{-3} M solution of complex **4** and the dianion terephtalate as its TBA salt in 20% Acetone / 80% DMSO.

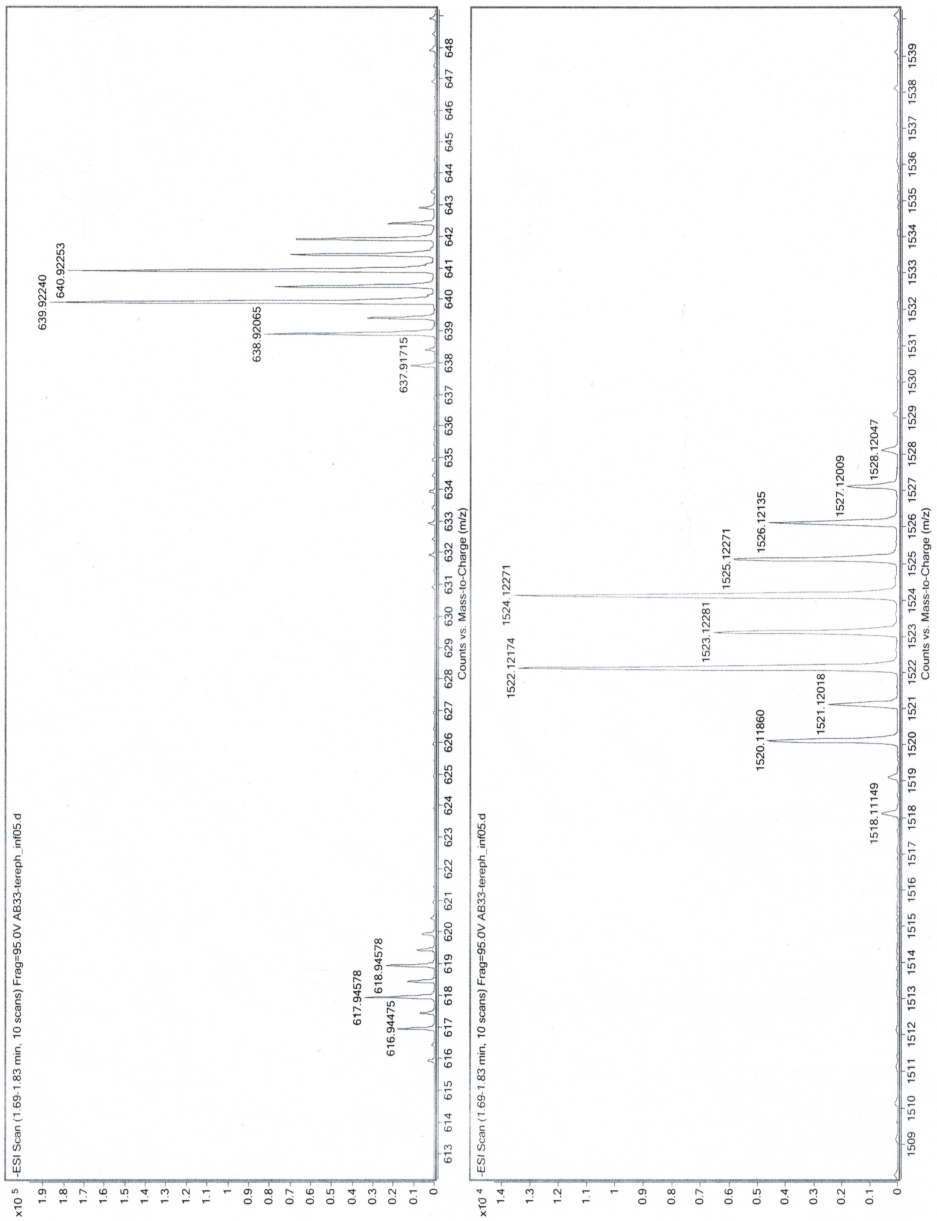

Results shown the doubly deprotonated species [**4**-2H]$^{2-}$ at 639.9224 m/z (Top) and the TBA-stabilized one [**4**+TBA-2H]$^{-}$ at 1522.1217 m/z (Bottom).

Conclusion

Présentés dans le contexte général du développement de nouveaux matériaux organométalliques dans le domaine de la conversion d'énergie solaire, les travaux de ce mémoire ont été effectués selon deux grands axes d'application, soit le photovoltaïque et les capteurs d'énergie pour la photoproduction d'hydrogène. À la lueur de ce qui y a été présenté, il apparaît clairement que la caractérisation poussée des complexes organométalliques préparés est d'une importance capitale dans le but de s'assurer de leur stabilité à long terme, peu importe l'application envisagée. Cela s'est révélé par la tendance à la décomposition des complexes homoleptiques de Co(II), Ni(II), Cu(II) et Zn(II) basés sur le ligand électron-riche tétra-*p*-méthoxyphényl-ADPM lorsque soumis à des conditions d'oxydoréduction et par la déprotonation des liens thio-urée dans les complexes neutres de Re(I) lorsque soumis à des conditions rendues basiques par la présence de bases conjuguées anioniques. Cela étant mentionné, il n'en demeure pas moins que les informations recueillies dans le cadre de ces travaux s'avèrent d'un vif intérêt pour le design des générations futures de ces familles de composés.

Plus particulièrement, le chapitre 1 portant sur l'étude comparative de complexes homoleptiques de M(II) basés sur la famille de chromophores azadipyrrométhènes révèle un potentiel marqué en OPV dû aux niveaux énergétiques contrôlables et à la panchromaticité obtenue s'étendant jusqu'à la limite du NIR.[1] La caractérisation électrochimique a démontré que l'ensemble des composés arborant le tétra-*p*-

méthoxyphényl-ADPM présentent un comportement moins stable qu'avec le tétraphényl-ADPM, tant pour les composés de coordination de M(II) ou BF_2^+ que dans le cas du ligand lui-même. Malgré cela, leurs niveaux énergétiques ainsi que leur E_g semblaient plus intéressants du point de vue photovoltaïque.[2,3] La caractérisation photophysique a quant à elle révélé que les nouveaux complexes basés sur le tétra-*p*-méthoxyphényl-ADPM vont plus loin dans le NIR que ce qui avait été rapporté précédemment pour ceux moins riche électroniquement.[4,5] La rationalisation des effets de la coordination d'un centre métallique M(II) et/ou de la richesse électronique du ligand permettent de penser à différentes améliorations pour les rendre optimaux en OPV.

Une piste d'amélioration à envisager semble être la modification du ligand ADPM pour tenter de le rendre moins vulnérable aux conditions d'oxydoréduction tout en préservant les propriétés photophysiques d'intérêt. Pour ce faire, il apparaît d'intérêt d'étudier l'effet d'avoir les groupements methoxy en position proximale ou distale (Figure C.1) pour identifier quelle position possède la plus grande influence sur les niveaux énergétiques obtenus. Cela pourrait permettre de déterminer si l'une de ces positions rend le ligand plus vulnérable à la décomposition. De façon similaire, l'étude de groupements fortement électro-donneurs tels les $–NR_2$ ou électro-attracteurs tels les $–NO_2$ et les –CN pourrait aussi s'avérer valable (Figure C.1). En effet, il pourrait ainsi être intéressant de faire l'électrochimie de composés possédant des ligands appauvris électroniquement pour voir les deux extrêmes et comprendre comment la combinaison de groupements électron-riches et électron-pauvres permettra un ajustement fin des niveaux énergétiques.

Conclusion

Figure C.1 – Exemples de ligands ADPM intéressants à investiguer.

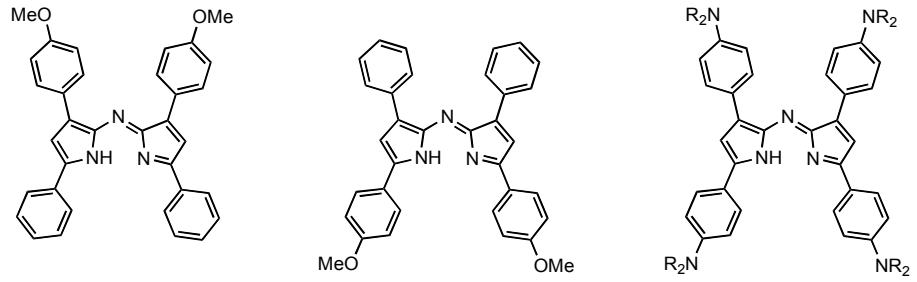

ADPM électron-riche

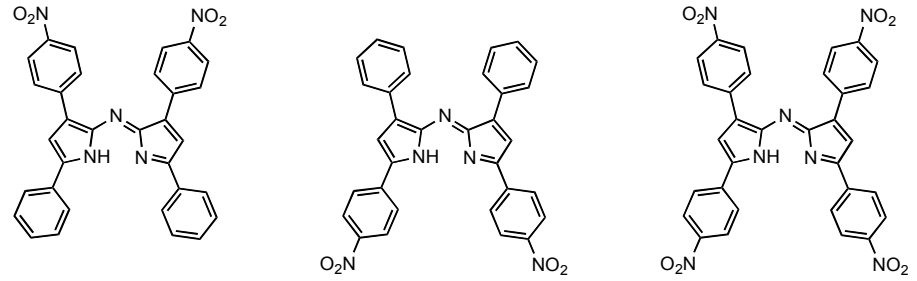

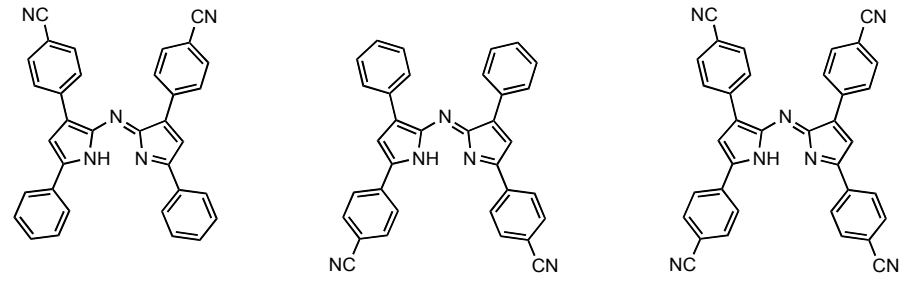

ADPM électron-pauvre

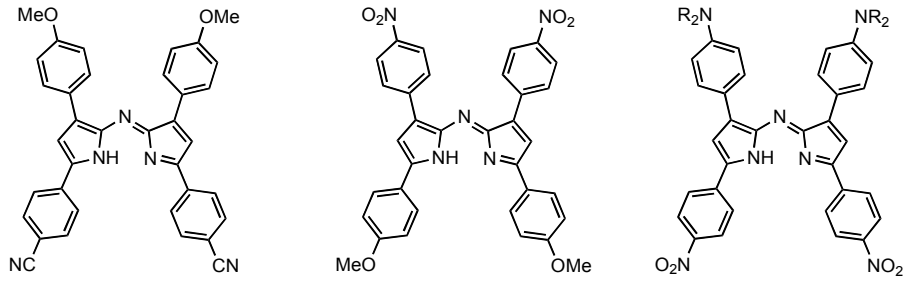

Combinaison

Parmi les autres travaux envisageables pour les composés organométalliques homoleptiques à base de la famille de ligand ADPM, notons leur incorporation réelle dans des cellules solaires en tant que matériau donneur de façon similaire à ce qui a été rapporté récemment par la compagnie Heliatek GmbH,[6] le groupe de Ma[7] ou encore par le groupe de Ziessel avec des dérivés DPM.[8,9] Leur utilisation en tant que photosensibilisateur pour BHJSC est aussi d'intérêt, comme l'a démontré Kubo *et coll.* avec des DPM.[10] Moyennant quelques modifications structurales, l'emploi de complexes organométalliques à base d'ADPM pourra aussi servir en DSSC comme plusieurs groupes de recherche l'ont démontré avec les DPM.[11-13]

De façon plus large, l'emploi du ligand ADPM est aussi possible avec d'autres métaux que les Co(II), Ni(II), Cu(II) et Zn(II) étudiés dans cette maîtrise. Par exemple, des dérivés d'ADPM ont été employé avec les métaux univalents Cu(I), Ag(I) et Au(I) par le groupe de Gray.[14,15] Bien que ces composés aient présenté des propriétés photophysiques intéressantes, leur instabilité dans les conditions atmosphériques ambiantes les rend moins intéressants du point de vue de la fabrication de dispositifs de conversion d'énergie solaire. En revanche, un composé neutre de fac-tricarbonyle Re(I) tétraphényl-ADPM stable à l'air possédant un ligand THF labile (Figure C.2) qui est substituable, notamment par des ligands à base de thiophène et de pyridine, semble présenter des caractéristiques intéressantes pour la conversion d'énergie solaire.[16] En effet, des dérivés de ce composé neutre de Re(I) pourraient être utilisables pour la préparation d'antennes moléculaires pour la photoproduction d'hydrogène. La Figure C.3 présente un exemple de dérivé envisageable dans lequel une tétra-pyridine-porphyrine sert de point d'ancrage à quatre complexes de

Re(I) basés sur un ligand ADPM. La coordination additionnelle d'un métal au centre de la porphyrine pourrait servir à relier cette antenne moléculaire au centre réactionnel ou bien à un dérivé de fullerène pour en étudier les propriétés de transfert énergétique comme l'ont fait Torres *et coll.* avec un BODIPY (Figure C.4).[17]

Figure C.2 – Composé neutre fac-tricarbonyle Re(I) tétraphényl-ADPM possédant un ligand THF labile.[16]

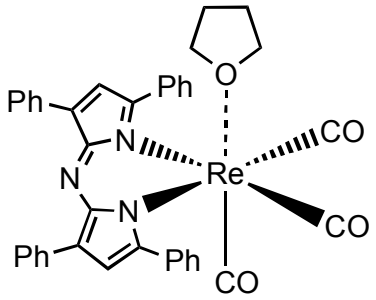

Figure C.3 – Exemple d'antenne moléculaire basé sur quatre composés neutres fac-tricarbonyle Re(I) tétra-aryle-ADPM liés à une tétra-pyridine-porphyrine.

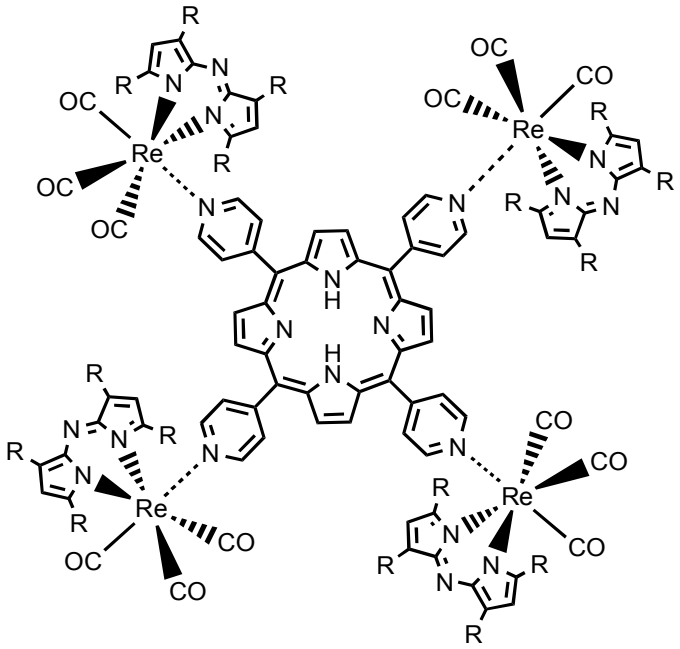

Figure C.4 – Assemblage supramoléculaire de type D-A d'un BODIPY substitué en périphérie d'une phtalocyanine de Zn(II) coordonnant un dérivé fullerène.[17]

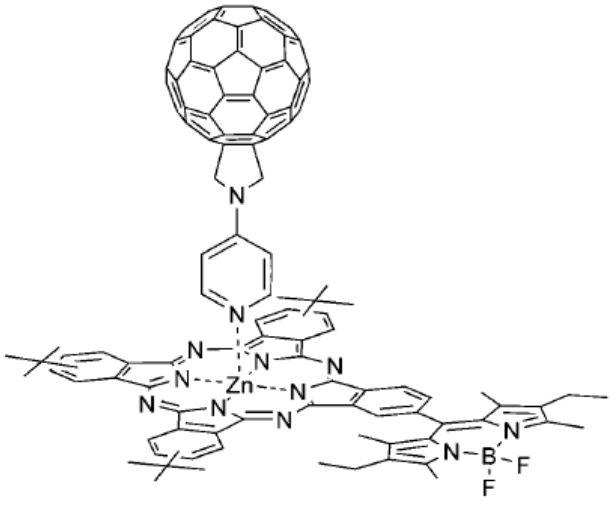

Le deuxième article présenté dans ce mémoire introduit aussi des complexes neutres à base de Re(I) qui pourraient être utilisés pour la formation d'antennes moléculaires dans des systèmes d'architecture plus complexes pour la photoproduction d'hydrogène (cf. Figure I.6). L'autoassemblage d'un complexe bimétallique est assurément un pas dans cette direction. Tout comme dans le cas d'applications en OPV, il demeure important de s'assurer du comportement électrochimique des complexes préparés avant de les intégrer dans des systèmes de photosynthèse artificielle complexes. L'électrochimie a donc été effectuée avec les nouveaux complexes neutres préparés et n'a pas révélé de signe de décomposition marqué. Toutefois, il a été démontré que la présence des liens thio-urée rend les systèmes basés sur cette stratégie synthétique vulnérables à la variation de pH. En effet, la déprotonation observée lors des études de détection d'anion permet de réitérer l'importance de bien caractériser les nouveaux matériaux organométalliques développés pour s'assurer de leur stabilité avant de les intégrer dans des systèmes d'architecture complexe. De son côté, la caractérisation UV/Vis laisse tout de même croire que le noyau Re(I) phénanthroline est intéressant en tant que chromophore absorbant à haute énergie dans le contexte des antennes moléculaires. Elle a aussi montré qu'un changement marqué dans les bandes d'absorption se produit lors de la déprotonation, ce qui n'est pas souhaitable pour une application de ce type. Face à un tel inconvénient d'instabilité, deux pistes de solution mériteraient de l'attention en tant que travaux futurs.

Premièrement, le remplacement du lien thio-urée par un lien urée pourrait contribuer à augmenter la stabilité du système tout en maintenant la possibilité de faire de la détection d'anions (Figure C.5). Cette proposition provient du fait que les orbitales vides

du soufre dans le thio-urée stabilisent mieux la charge négative générée lors de la déprotonation que celle de l'oxygène dans l'urée, ce qui rend les protons liés à ce dernier groupement moins acides (pKa urée = 27 vs pKa thio-urée = 21). En contrepartie, la formation du groupement urée peut s'avérer moins aisée que celle de la thio-urée. Pour remédier à cela tout en augmentant la délocalisation électronique à travers tout l'assemblage, il apparaît intéressant de considérer l'utilisation de la chimie «clic».[18] Par exemple, la Figure C.6 présente un complexe bimétallique qui pourrait être assemblé par une cycloaddition [3+2] catalysée par le Cu(I) de type Huisgen formant un triazole à partir d'un azide et d'un alcyne.[19,20] Seul inconvénient de cette méthode à haut rendement synthétique et conditions de réaction douces, les composés résultants ne pourraient pas être utilisé pour l'application de senseur d'anion.

Figure C.5 – Complexe bimétallique de Re(I) phénanthroline basé sur le lien urée.

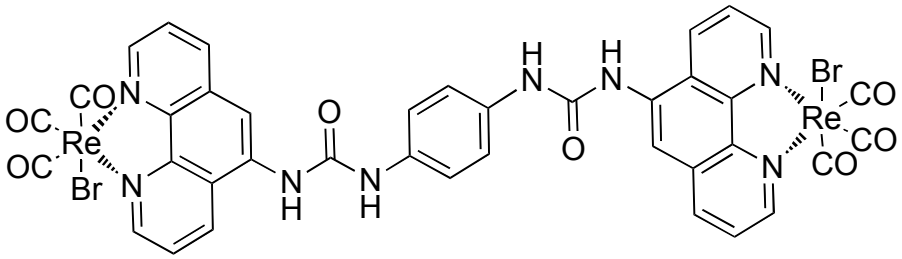

Figure C.6 – Complexe bimétallique de Re(I) phénanthroline basé sur la chimie «clic».

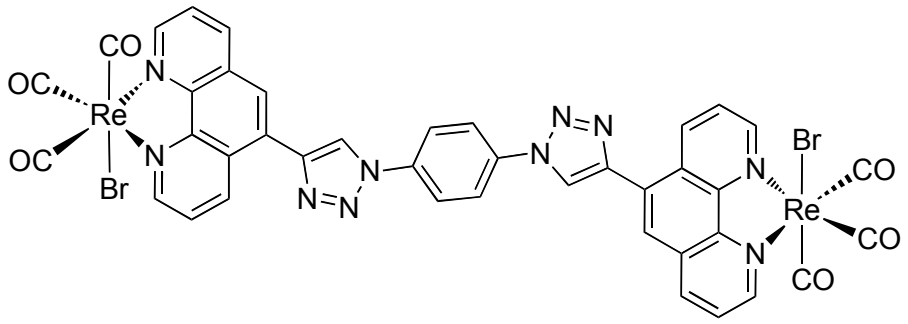

La deuxième stratégie à envisager pour l'amélioration de la stabilité des complexes obtenus tout en préservant les liens thio-urée serait d'installer des groupements électron-donneurs aux positions 3-, 7- et 9- du noyau phénanthroline. Tel que mentionné dans le chapitre 2, ce sont ces positions qui sont les plus susceptibles de recevoir la charge négative par délocalisation en cas de déprotonation. Ainsi, l'ajout de groupements tels des amines, des alcool ou bien des méthoxy pourrait donc permettre de redonner de la densité électronique dans le système conjugué et ainsi diminuer l'effet électro-attracteur du centre métallique de Re(I).

Voici donc ce qui conclut ce mémoire axé sur le développement de nouveaux matériaux organométalliques pour des applications dans le domaine de la conversion d'énergie solaire. Les travaux présentés ici constituent une brique supplémentaire qui s'ajoute à la déjà vaste structure des sciences dans ce domaine. Espérons qu'elle saura inspirer d'autres chercheurs dans la quête d'un monde carburant aux énergies renouvelables.

Bibliographie de la conclusion

(1) Tel que mentionné dans la note de l'Introduction, l'appellation du domaine "photovoltaïque organique" doit être prise au sens large et peut inclure la présence de complexes organométalliques dans la fabrication des cellules solaires en découlant. En effet, cette appellation commune dans le milieu scientifique est historiquement basée sur son opposition à la photovoltaïque à base de semi-conducteurs inorganiques, par exemple les cellules solaires faites de silicium cristallin.

(2) Li, Y. *Acc. Chem. Res.* **2012**, *45*, 723.

(3) Mishra, A.; Bäuerle, P. *Angew. Chem. Int. Ed. Engl.* **2012**, *51*, 2020.

(4) Teets, T. S.; Partyka, D. V.; Updegraff, J. B.; Gray, T. G. *Inorg. Chem.* **2008**, *47*, 2338.

(5) Palma, A.; Gallagher, J. F.; Mueller-Bunz, H.; Wolowska, J.; McInnes, E. J. L.; O'Shea, D. F. *Dalton Trans.* **2009**, 273.

(6) Mueller, T.; Gresser, R.; Leo, K.; Riede, M. *Sol. Energy Mater. Sol. Cells* **2012**, *99*, 176.

(7) Leblebici, S. Y.; Catane, L.; Barclay, D. E.; Olson, T.; Chen, T. L.; Ma, B. *ACS Appl. Mater. Interfaces* **2011**, *3*, 4469.

(8) Bura, T.; Leclerc, N.; Fall, S.; Lévêque, P.; Heiser, T.; Ziessel, R. *Org. Lett.* **2011**, *13*, 6030.

(9) Rousseau, T.; Cravino, A.; Ripaud, E.; Leriche, P.; Rihn, S.; De Nicola, A.; Ziessel, R.; Roncali, J. *Chem. Commun.* **2010**, *46*, 5082.

(10) Kubo, Y.; Watanabe, K.; Nishiyabu, R.; Hata, R.; Murakami, A.; Shoda, T.; Ota, H. *Org. Lett.* **2011**, *13*, 4574.

(11) Warnan, J.; Buchet, F.; Pellegrin, Y.; Blart, E.; Odobel, F. *Org. Lett.* **2011**, *13*, 3944.

(12) Kolemen, S.; Bozdemir, O. A.; Cakmak, Y.; Barin, G.; Erten-Ela, S.; Marszalek, M.; Yum, J.-H.; Zakeeruddin, S. M.; Nazeeruddin, M. K.; Gratzel, M.; Akkaya, E. U. *Chem. Sci.* **2011**, *2*, 949.

(13) Erten-Ela, S.; Yilmaz, M. D.; Icli, B.; Dede, Y.; Icli, S.; Akkaya, E. U. *Org. Lett.* **2008**, *10*, 3299.

(14) Teets, T. S.; Partyka, D. V.; Esswein, A. J.; Updegraff, J. B., III; Zeller, M.; Hunter, A. D.; Gray, T. G. *Inorg. Chem.* **2007**, *46*, 6218.

(15) Teets, T. S.; Updegraff, J. B., III; Esswein, A. J.; Gray, T. G. *Inorg. Chem.* **2009**, *48*, 8134.

(16) Partyka, D. V.; Deligonul, N.; Washington, M. P.; Gray, T. G. *Organomet.* **2009**, *28*, 5837.

(17) Rio, Y.; Seitz, W.; Gouloumis, A.; Vazquez, P.; Sessler, J. L.; Guldi, D. M.; Torres, T. *Chem. - Eur. J.* **2010**, *16*, 1929.

(18) Iha, R. K.; Wooley, K. L.; Nyström, A. M.; Burke, D. J.; Kade, M. J.; Hawker, C. J. *Chem. Rev.* **2009**, *109*, 5620.

(19) Meldal, M.; Tornoe, C. W. *Chem. Rev.* **2008**, *108*, 2952.
(20) Amblard, F.; Cho, J. H.; Schinazi, R. F. *Chem. Rev.* **2009**, *109*, 4207.

Annexe I – Structures cristallographiques

Les structures cristallographiques présentées ici ont été déposées dans la banque de données du CCDC.

Références :

- SAINT (2006) Release 7.34A; Integration Software for Single Crystal Data. Bruker AXS Inc., Madison, WI 53719-1173.
- Sheldrick, G.M. (1996). SADABS, Bruker Area Detector Absorption Corrections. Bruker AXS Inc., Madison, WI 53719-1173.
- Sheldrick, G.M. (2008). Acta Cryst. A64, 112-122.
- SHELXTL (2001) version 6.12; Bruker Analytical X-ray Systems Inc., Madison, WI 53719-1173.
- APEX2 (2009) ; Bruker Molecular Analysis Research Tool. Bruker AXS Inc., Madison, WI 53719-1173.
- Spek, A.L. (2008). PLATON, A Multipurpose Crystallographic Tool, Utrecht University, Utrecht, The Netherlands.
- Maris, T. (2004). UdMX, University of Montréal, Montréal, QC, Canada.
- XPREP (2008) Version 2008/2; X-ray data Preparation and Reciprocal space Exploration Program. Bruker AXS Inc., Madison, WI 53719-1173.

Table AI.1 – Détails des études de diffraction des rayons X pour les composés **1b** et **2b** (Chapitre 1)

	1b	**2b**
CCDC Number	876955	876954
Formula	C36 H31 N3 O4	C72 H60 Co N6 O8
Mw (g/mol); $d_{calcd.}$ (g/cm^3)	569.64; 1.688	1196.19; 1.355
T (K); F(000)	150; 3696	150; 2500
Crystal System	Monoclinic	Monoclinic
Space Group	$P2_1/c$	$P2_1/c$
Unit Cell: *a* (Å)	19.4979(5)	12.2987(3)
b (Å)	7.0104(2)	14.3062(3)
c (Å)	21.2448(5)	34.1066(7)
β (°)	105.2881(15)	102.219(1)
V (Å^3); Z	2801.15(13) 4	5865.0(2); 4
θ range (°); completeness	4.32-69.49; 0.991	2.65-69.83; 0.996
Refl.: collec./indep.; R_{int}	37808/ 5544; 0.52	121155/11031; 0.056
μ (mm^{-1})	0.713	2.822
R1(F); wR(F^2); GoF(F^2) [a]	0.0752;0.2312;0.98	0.0610; 0.0971; 1.038
Residual electron density	1.40; -0.37	0.50; -0.63

[a] R1(F) based on observed reflections with I>2σ(I), wR(F^2) and GoF(F^2) based on all data.

Figure AI.1 – Représentation Ortep au niveau de probabilité 50% avec numérotation complète du composé **1b**, incluant les hydrogènes désordonnés dans un ratio 1:2 sur N1 et N3 respectivement.

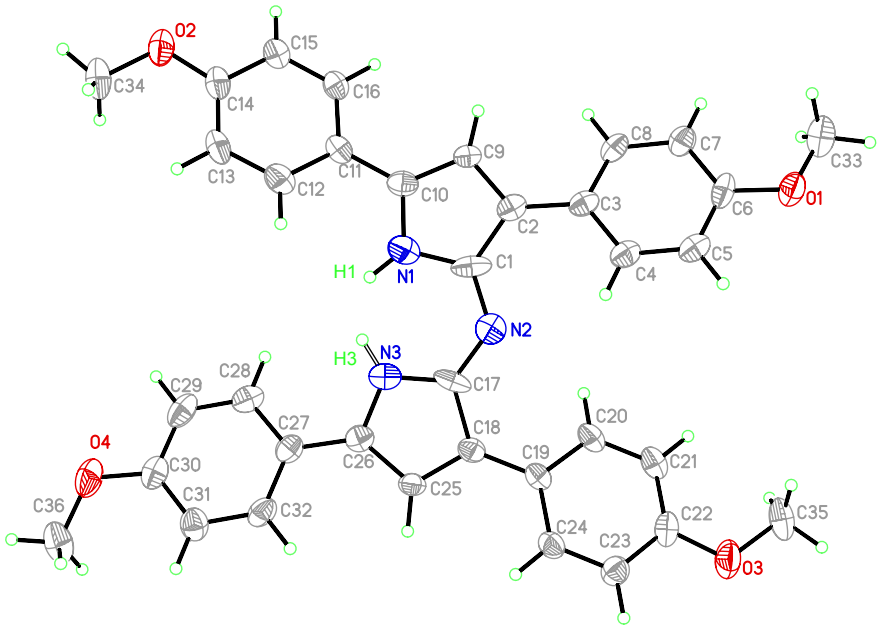

Table AI.2 – Liste des longueurs de liens et des angles pour le composé **1b**.

O1—C6	1.363 (4)	C15—C16	1.378 (4)
O1—C33	1.409 (4)	C15—H15	0.9500
O2—C14	1.364 (4)	C16—H16	0.9500
O2—C34	1.421 (4)	C18—C25	1.395 (4)
O3—C22	1.366 (4)	C18—C19	1.457 (4)
O3—C35	1.424 (4)	C19—C20	1.406 (4)
O4—C30	1.362 (4)	C19—C24	1.414 (4)
O4—C36	1.432 (5)	C20—C21	1.389 (5)
N1—C10	1.348 (4)	C20—H20	0.9500
N1—C1	1.407 (5)	C21—C22	1.388 (5)
N1—H1	0.8800	C21—H21	0.9500
N2—C17	1.319 (4)	C22—C23	1.396 (4)
N2—C1	1.327 (4)	C23—C24	1.376 (4)
N3—C26	1.361 (4)	C23—H23	0.9500
N3—C17	1.374 (5)	C24—H24	0.9500
N3—H3	0.8800	C25—C26	1.419 (4)
C1—C2	1.452 (4)	C25—H25	0.9500
C17—C18	1.452 (4)	C26—C27	1.452 (4)
C2—C9	1.378 (4)	C27—C28	1.392 (4)
C2—C3	1.458 (4)	C27—C32	1.393 (4)
C3—C8	1.394 (4)	C28—C29	1.380 (5)
C3—C4	1.407 (4)	C28—H28	0.9500
C4—C5	1.369 (4)	C29—C30	1.391 (5)
C4—H4	0.9500	C29—H29	0.9500
C5—C6	1.392 (5)	C30—C31	1.381 (5)
C5—H5	0.9500	C31—C32	1.402 (5)

C6—C7	1.396 (4)	C31—H31	0.9500
C7—C8	1.378 (4)	C32—H32	0.9500
C7—H7	0.9500	C33—H33A	0.9800
C8—H8	0.9500	C33—H33B	0.9800
C9—C10	1.426 (4)	C33—H33C	0.9800
C9—H9	0.9500	C34—H34A	0.9800
C10—C11	1.462 (4)	C34—H34B	0.9800
C11—C12	1.389 (4)	C34—H34C	0.9800
C11—C16	1.403 (4)	C35—H35A	0.9800
C12—C13	1.387 (5)	C35—H35B	0.9800
C12—H12	0.9500	C35—H35C	0.9800
C13—C14	1.399 (5)	C36—H36A	0.9800
C13—H13	0.9500	C36—H36B	0.9800
C14—C15	1.386 (4)	C36—H36C	0.9800
Angles			
C6—O1—C33	117.6 (3)	C20—C19—C18	122.4 (3)
C14—O2—C34	118.4 (3)	C24—C19—C18	120.6 (3)
C22—O3—C35	118.3 (3)	C21—C20—C19	121.9 (3)
C30—O4—C36	117.6 (3)	C21—C20—H20	119.1
C10—N1—C1	104.8 (3)	C19—C20—H20	119.1
C10—N1—H1	127.6	C22—C21—C20	119.4 (3)
C1—N1—H1	127.6	C22—C21—H21	120.3
C17—N2—C1	126.5 (3)	C20—C21—H21	120.3
C26—N3—C17	108.4 (3)	O3—C22—C21	124.3 (3)
C26—N3—H3	125.8	O3—C22—C23	115.5 (3)
C17—N3—H3	125.8	C21—C22—C23	120.2 (3)
N2—C1—N1	121.2 (3)	C24—C23—C22	120.1 (3)

N2—C1—C2	128.0 (4)	C24—C23—H23	120.0
N1—C1—C2	110.8 (3)	C22—C23—H23	120.0
N2—C17—N3	122.3 (3)	C23—C24—C19	121.4 (3)
N2—C17—C18	128.1 (3)	C23—C24—H24	119.3
N3—C17—C18	109.5 (3)	C19—C24—H24	119.3
C9—C2—C1	104.7 (3)	C18—C25—C26	109.0 (3)
C9—C2—C3	127.7 (3)	C18—C25—H25	125.5
C1—C2—C3	127.5 (3)	C26—C25—H25	125.5
C8—C3—C4	117.4 (3)	N3—C26—C25	108.7 (3)
C8—C3—C2	120.4 (3)	N3—C26—C27	120.8 (3)
C4—C3—C2	122.2 (3)	C25—C26—C27	130.5 (3)
C5—C4—C3	121.2 (3)	C28—C27—C32	117.7 (3)
C5—C4—H4	119.4	C28—C27—C26	122.4 (3)
C3—C4—H4	119.4	C32—C27—C26	119.8 (3)
C4—C5—C6	120.4 (3)	C29—C28—C27	121.1 (3)
C4—C5—H5	119.8	C29—C28—H28	119.4
C6—C5—H5	119.8	C27—C28—H28	119.4
O1—C6—C5	116.0 (3)	C28—C29—C30	120.9 (3)
O1—C6—C7	124.4 (3)	C28—C29—H29	119.6
C5—C6—C7	119.6 (3)	C30—C29—H29	119.6
C8—C7—C6	119.3 (3)	O4—C30—C31	125.0 (3)
C8—C7—H7	120.4	O4—C30—C29	115.8 (3)
C6—C7—H7	120.4	C31—C30—C29	119.2 (3)
C7—C8—C3	122.1 (3)	C30—C31—C32	119.6 (3)
C7—C8—H8	119.0	C30—C31—H31	120.2
C3—C8—H8	119.0	C32—C31—H31	120.2
C2—C9—C10	107.8 (3)	C27—C32—C31	121.5 (3)

C2—C9—H9	126.1	C27—C32—H32	119.3
C10—C9—H9	126.1	C31—C32—H32	119.3
N1—C10—C9	112.0 (3)	O1—C33—H33A	109.5
N1—C10—C11	119.2 (3)	O1—C33—H33B	109.5
C9—C10—C11	128.8 (3)	H33A—C33—H33B	109.5
C12—C11—C16	117.7 (3)	O1—C33—H33C	109.5
C12—C11—C10	122.0 (3)	H33A—C33—H33C	109.5
C16—C11—C10	120.3 (3)	H33B—C33—H33C	109.5
C13—C12—C11	122.4 (3)	O2—C34—H34A	109.5
C13—C12—H12	118.8	O2—C34—H34B	109.5
C11—C12—H12	118.8	H34A—C34—H34B	109.5
C12—C13—C14	118.7 (3)	O2—C34—H34C	109.5
C12—C13—H13	120.6	H34A—C34—H34C	109.5
C14—C13—H13	120.6	H34B—C34—H34C	109.5
O2—C14—C15	116.3 (3)	O3—C35—H35A	109.5
O2—C14—C13	123.9 (3)	O3—C35—H35B	109.5
C15—C14—C13	119.9 (3)	H35A—C35—H35B	109.5
C16—C15—C14	120.5 (3)	O3—C35—H35C	109.5
C16—C15—H15	119.7	H35A—C35—H35C	109.5
C14—C15—H15	119.7	H35B—C35—H35C	109.5
C15—C16—C11	120.9 (3)	O4—C36—H36A	109.5
C15—C16—H16	119.6	O4—C36—H36B	109.5
C11—C16—H16	119.6	H36A—C36—H36B	109.5
C25—C18—C17	104.4 (3)	O4—C36—H36C	109.5
C25—C18—C19	128.3 (3)	H36A—C36—H36C	109.5
C17—C18—C19	127.3 (3)	H36B—C36—H36C	109.5

Figure AI.2 – Représentations Ortep au niveau de probabilité 30% avec numérotation complète du composé **2b**.

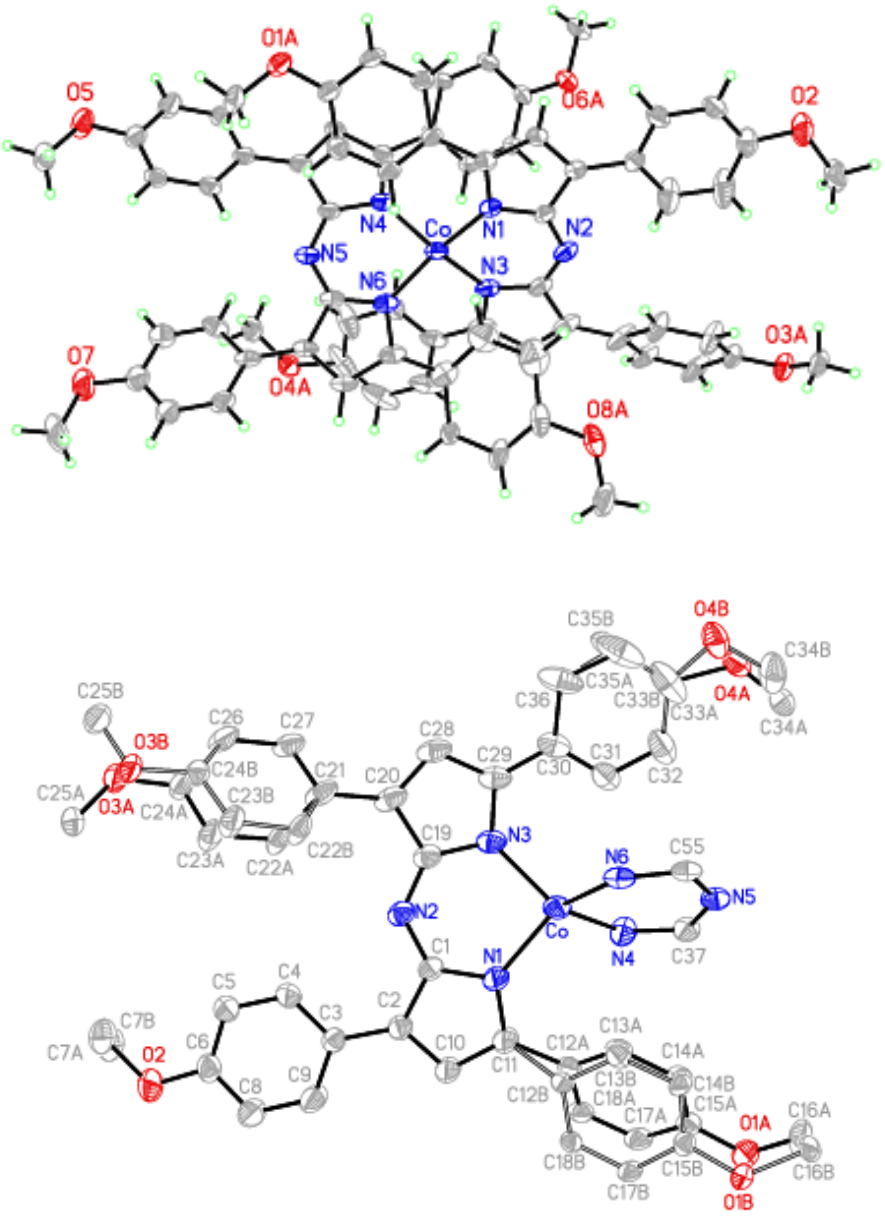

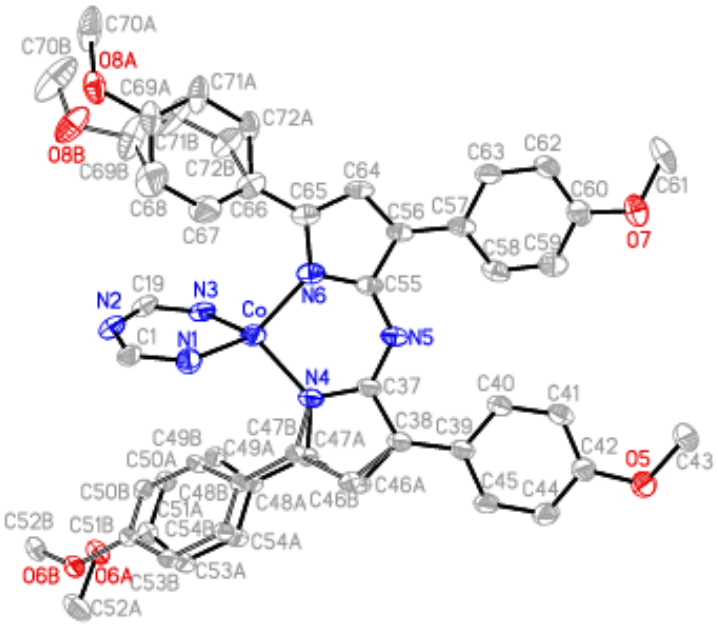
C70A
C70B
O8A
C69A
C71A
C72A
O8B
C71B
C69B
C72B
C68
C66
C67
C65
C64
C56
C57
C63
C62
C60
C61
O7
C58
C59
C19
N3
N2
Co
N6
C55
C1
N1
N5
N4
C37
C40
C41
C38
C39
C49B
C47B
C47A
C42
O5
C43
C50A
C49A
C50B
C48B
C46A
C45
C44
C51A
C48A
C46B
C52B
C51B
C54B
C54A
O6B
O6A
C53A
C53B
C52A

Table AI.3 – Liste des longueurs de liens et des angles pour le composé **2b**.

Co—N6	1.974 (3)	C25A—H25B	0.9800
Co—N1	1.975 (3)	C25A—H25C	0.9800
Co—N3	1.987 (3)	O3B—C24B	1.357 (12)
Co—N4	1.992 (3)	O3B—C25B	1.408 (12)
O2—C6	1.368 (4)	C22B—C23B	1.365 (18)
O2—C7B	1.403 (12)	C22B—H22B	0.9500
O2—C7A	1.495 (8)	C23B—C24B	1.402 (16)
C30—C31	1.385 (5)	C23B—H23B	0.9500
C30—C36	1.396 (5)	C24B—C26	1.458 (11)
C30—C29	1.456 (5)	C25B—H25D	0.9800
C31—C32	1.378 (5)	C25B—H25E	0.9800
C31—H31	0.9500	C25B—H25F	0.9800
C32—C33A	1.374 (16)	C26—C27	1.379 (5)
C32—C33B	1.436 (13)	C26—H26	0.9500
C32—H32	0.9500	C27—H27	0.9500
C36—C35B	1.334 (12)	C28—C29	1.414 (5)
C36—C35A	1.387 (17)	C28—H28	0.9500
C36—H36	0.9500	C37—C38	1.449 (4)
O4A—C34A	1.440 (15)	C38—C46A	1.356 (6)
O4A—C33A	1.58 (2)	C38—C39	1.458 (4)
C34A—H34A	0.9800	C38—C46B	1.515 (14)
C34A—H34B	0.9800	C39—C45	1.379 (5)
C34A—H34C	0.9800	C39—C40	1.395 (4)
C33A—C35A	1.397 (19)	C40—C41	1.378 (4)
C35A—H35A	0.9500	C40—H40	0.9500
O4B—C33B	1.332 (11)	C41—C42	1.360 (5)

O4B—C34B	1.429 (10)	C41—H41	0.9500
C33B—C35B	1.372 (15)	C42—C44	1.394 (5)
C34B—H34D	0.9800	C43—H43A	0.9800
C34B—H34E	0.9800	C43—H43B	0.9800
C34B—H34F	0.9800	C43—H43C	0.9800
C35B—H35B	0.9500	C44—C45	1.369 (5)
O5—C42	1.370 (4)	C44—H44	0.9500
O5—C43	1.433 (4)	C45—H45	0.9500
O7—C60	1.371 (5)	C46A—C47A	1.396 (8)
O7—C61	1.435 (6)	C46A—H46A	0.9500
N1—C11	1.340 (4)	C47A—C48A	1.459 (7)
N1—C1	1.399 (4)	O6A—C51A	1.368 (5)
N2—C1	1.323 (4)	O6A—C52A	1.430 (6)
N2—C19	1.328 (4)	C48A—C54A	1.391 (6)
N3—C29	1.360 (4)	C48A—C49A	1.408 (7)
N3—C19	1.396 (4)	C49A—C50A	1.373 (6)
N4—C47A	1.361 (6)	C49A—H49A	0.9500
N4—C37	1.392 (4)	C50A—C51A	1.380 (6)
N4—C47B	1.430 (12)	C50A—H50A	0.9500
N5—C37	1.321 (4)	C51A—C53A	1.387 (7)
N5—C55	1.330 (4)	C52A—H52A	0.9800
N6—C65	1.358 (4)	C52A—H52B	0.9800
N6—C55	1.394 (4)	C52A—H52C	0.9800
C1—C2	1.452 (4)	C53A—C54A	1.392 (6)
C2—C10	1.364 (4)	C53A—H53A	0.9500
C2—C3	1.471 (4)	C54A—H54A	0.9500
C3—C4	1.362 (5)	O6B—C51B	1.380 (11)

C3—C9	1.365 (5)	O6B—C52B	1.401 (13)
C4—C5	1.379 (6)	C48B—C49B	1.387 (13)
C4—H4	0.9500	C48B—C54B	1.409 (13)
C5—C6	1.380 (6)	C48B—C47B	1.466 (15)
C5—H5	0.9500	C49B—C50B	1.386 (13)
C6—C8	1.341 (5)	C49B—H49B	0.9500
C7A—H7A	0.9800	C50B—C51B	1.400 (14)
C7A—H7B	0.9800	C50B—H50B	0.9500
C7A—H7C	0.9800	C51B—C53B	1.373 (13)
C7B—H7D	0.9800	C53B—C54B	1.368 (12)
C7B—H7E	0.9800	C53B—H53B	0.9500
C7B—H7F	0.9800	C54B—H54B	0.9500
C8—C9	1.382 (5)	C46B—C47B	1.429 (18)
C8—H8	0.9500	C46B—H46B	0.9500
C9—H9	0.9500	C52B—H52D	0.9800
C10—C11	1.418 (5)	C52B—H52E	0.9800
C10—H10	0.9500	C52B—H52F	0.9800
C11—C12A	1.470 (6)	C55—C56	1.445 (4)
C11—C12B	1.562 (10)	C56—C64	1.373 (4)
O1A—C15A	1.368 (5)	C56—C57	1.467 (5)
O1A—C16A	1.410 (13)	C57—C63	1.376 (4)
C12A—C13A	1.391 (13)	C57—C58	1.389 (5)
C12A—C18A	1.395 (6)	C58—C59	1.375 (5)
C13A—C14A	1.385 (15)	C58—H58	0.9500
C13A—H13A	0.9500	C59—C60	1.368 (5)
C14A—C15A	1.387 (10)	C59—H59	0.9500
C14A—H14A	0.9500	C60—C62	1.370 (6)

C15A—C17A	1.386 (7)	C61—H61A	0.9800
C16A—H16A	0.9800	C61—H61B	0.9800
C16A—H16B	0.9800	C61—H61C	0.9800
C16A—H16C	0.9800	C62—C63	1.378 (6)
C17A—C18A	1.380 (6)	C62—H62	0.9500
C17A—H17A	0.9500	C63—H63	0.9500
C18A—H18A	0.9500	C64—C65	1.412 (5)
O1B—C15B	1.368 (11)	C64—H64	0.9500
O1B—C16B	1.50 (3)	C65—C66	1.451 (5)
C12B—C18b	1.402 (12)	C66—C72B	1.329 (13)
C12B—C13B	1.41 (3)	C66—C67	1.399 (5)
C13B—C14B	1.37 (3)	C66—C72A	1.461 (10)
C13B—H13B	0.9500	C67—C68	1.373 (6)
C14B—C15B	1.37 (2)	C67—H67	0.9500
C14B—H14B	0.9500	C68—C69B	1.264 (12)
C17b—C18b	1.363 (12)	C68—C69A	1.496 (9)
C17b—C15B	1.390 (13)	C68—H68	0.9500
C17b—H18B	0.9500	C70A—O8A	1.415 (10)
C18b—H17B	0.9500	C70A—H70A	0.9800
C16B—H16D	0.9800	C70A—H70B	0.9800
C16B—H16E	0.9800	C70A—H70C	0.9800
C16B—H16F	0.9800	O8A—C69A	1.426 (9)
C19—C20	1.442 (4)	C69A—C71A	1.359 (10)
C20—C28	1.379 (5)	C71A—C72A	1.383 (12)
C20—C21	1.468 (5)	C71A—H71A	0.9500
C21—C27	1.389 (5)	C72A—H72A	0.9500
C21—C22A	1.430 (8)	O8B—C69B	1.377 (14)

C21—C22B	1.442 (13)	O8B—C70B	1.411 (15)
O3A—C24A	1.366 (7)	C69B—C71B	1.36 (2)
O3A—C25A	1.422 (7)	C70B—H70D	0.9800
C22A—C23A	1.388 (10)	C70B—H70E	0.9800
C22A—H22A	0.9500	C70B—H70F	0.9800
C23A—C24A	1.370 (9)	C71B—C72B	1.351 (19)
C23A—H23A	0.9500	C71B—H71B	0.9500
C24A—C26	1.424 (7)	C72B—H72B	0.9500
C25A—H25A	0.9800		
Angles			
N6—Co—N1	128.69 (12)	H25D—C25B—H25E	109.5
N6—Co—N3	108.07 (10)	O3B—C25B—H25F	109.5
N1—Co—N3	94.72 (11)	H25D—C25B—H25F	109.5
N6—Co—N4	94.49 (11)	H25E—C25B—H25F	109.5
N1—Co—N4	106.56 (11)	C27—C26—C24A	124.2 (4)
N3—Co—N4	128.24 (12)	C27—C26—C24B	108.9 (5)
C6—O2—C7B	122.6 (8)	C27—C26—H26	117.9
C6—O2—C7A	112.4 (4)	C24A—C26—H26	117.9
C31—C30—C36	117.2 (4)	C24B—C26—H26	123.9
C31—C30—C29	121.8 (3)	C26—C27—C21	122.1 (3)
C36—C30—C29	121.0 (4)	C26—C27—H27	118.9
C32—C31—C30	121.8 (4)	C21—C27—H27	118.9
C32—C31—H31	119.1	C20—C28—C29	108.3 (3)
C30—C31—H31	119.1	C20—C28—H28	125.8
C33A—C32—C31	120.9 (9)	C29—C28—H28	125.8
C31—C32—C33B	116.6 (7)	N3—C29—C28	110.2 (3)

C33A—C32—H32	119.6	N3—C29—C30	122.4 (3)
C31—C32—H32	119.6	C28—C29—C30	127.3 (3)
C33B—C32—H32	121.4	N5—C37—N4	126.7 (3)
C35B—C36—C35A	5 (4)	N5—C37—C38	123.8 (3)
C35B—C36—C30	123.5 (7)	N4—C37—C38	109.6 (2)
C35A—C36—C30	119.4 (9)	C46A—C38—C37	106.1 (3)
C35B—C36—H36	116.1	C46A—C38—C39	126.4 (4)
C35A—C36—H36	120.3	C37—C38—C39	127.3 (3)
C30—C36—H36	120.3	C37—C38—C46B	100.7 (5)
C34A—O4A—C33A	129.3 (9)	C39—C38—C46B	127.8 (5)
C32—C33A—C35A	115.2 (15)	C45—C39—C40	116.9 (3)
C32—C33A—O4A	108.0 (13)	C45—C39—C38	119.7 (3)
C35A—C33A—O4A	133.4 (14)	C40—C39—C38	123.3 (3)
C36—C35A—C33A	121.8 (18)	C41—C40—C39	122.5 (3)
C36—C35A—H35A	119.1	C41—C40—H40	118.7
C33A—C35A—H35A	119.1	C39—C40—H40	118.7
C33B—O4B—C34B	109.0 (9)	C42—C41—C40	119.2 (3)
O4B—C33B—C35B	106.0 (11)	C42—C41—H41	120.4
O4B—C33B—C32	131.5 (11)	C40—C41—H41	120.4
C35B—C33B—C32	120.1 (10)	C41—C42—O5	124.5 (3)
O4B—C34B—H34D	109.5	C41—C42—C44	119.5 (3)
O4B—C34B—H34E	109.5	O5—C42—C44	116.0 (3)
H34D—C34B—H34E	109.5	O5—C43—H43A	109.5
O4B—C34B—H34F	109.5	O5—C43—H43B	109.5
H34D—C34B—H34F	109.5	H43A—C43—H43B	109.5
H34E—C34B—H34F	109.5	O5—C43—H43C	109.5
C36—C35B—C33B	118.0 (12)	H43A—C43—H43C	109.5

C36—C35B—H35B	121.0	H43B—C43—H43C	109.5
C33B—C35B—H35B	121.0	C45—C44—C42	120.6 (3)
C42—O5—C43	117.2 (3)	C45—C44—H44	119.7
C60—O7—C61	117.1 (4)	C42—C44—H44	119.7
C11—N1—C1	106.4 (3)	C44—C45—C39	121.2 (3)
C11—N1—Co	130.1 (2)	C44—C45—H45	119.4
C1—N1—Co	121.8 (2)	C39—C45—H45	119.4
C1—N2—C19	127.2 (3)	C38—C46A—C47A	107.1 (5)
C29—N3—C19	106.5 (3)	C38—C46A—H46A	126.4
C29—N3—Co	131.9 (2)	C47A—C46A—H46A	126.4
C19—N3—Co	119.8 (2)	N4—C47A—C46A	112.7 (5)
C47A—N4—C37	104.1 (3)	N4—C47A—C48A	119.1 (4)
C37—N4—C47B	109.9 (5)	C46A—C47A—C48A	128.1 (5)
C47A—N4—Co	134.0 (3)	C51A—O6A—C52A	117.0 (4)
C37—N4—Co	120.9 (2)	C54A—C48A—C49A	117.3 (4)
C47B—N4—Co	117.0 (5)	C54A—C48A—C47A	121.3 (4)
C37—N5—C55	126.9 (3)	C49A—C48A—C47A	121.4 (4)
C65—N6—C55	106.0 (3)	C50A—C49A—C48A	121.4 (4)
C65—N6—Co	131.3 (2)	C50A—C49A—H49A	119.3
C55—N6—Co	120.53 (19)	C48A—C49A—H49A	119.3
N2—C1—N1	126.4 (3)	C49A—C50A—C51A	120.4 (5)
N2—C1—C2	124.0 (3)	C49A—C50A—H50A	119.8
N1—C1—C2	109.6 (3)	C51A—C50A—H50A	119.8
C10—C2—C1	104.6 (3)	O6A—C51A—C50A	115.7 (4)
C10—C2—C3	126.4 (3)	O6A—C51A—C53A	124.6 (4)
C1—C2—C3	129.0 (3)	C50A—C51A—C53A	119.7 (4)
C4—C3—C9	115.7 (3)	C51A—C53A—C54A	119.8 (4)

C4—C3—C2	123.1 (3)	C51A—C53A—H53A	120.1
C9—C3—C2	121.1 (3)	C54A—C53A—H53A	120.1
C3—C4—C5	122.3 (4)	C48A—C54A—C53A	121.3 (4)
C3—C4—H4	118.8	C48A—C54A—H54A	119.3
C5—C4—H4	118.8	C53A—C54A—H54A	119.3
C4—C5—C6	120.2 (4)	C51B—O6B—C52B	118.7 (8)
C4—C5—H5	119.9	C49B—C48B—C54B	117.5 (8)
C6—C5—H5	119.9	C49B—C48B—C47B	122.1 (9)
C8—C6—O2	116.8 (3)	C54B—C48B—C47B	120.3 (9)
C8—C6—C5	118.2 (3)	C50B—C49B—C48B	122.1 (9)
O2—C6—C5	124.9 (3)	C50B—C49B—H49B	118.9
O2—C7A—H7A	109.5	C48B—C49B—H49B	118.9
O2—C7A—H7B	109.5	C49B—C50B—C51B	118.3 (9)
O2—C7A—H7C	109.5	C49B—C50B—H50B	120.8
O2—C7B—H7D	109.5	C51B—C50B—H50B	120.8
O2—C7B—H7E	109.5	C53B—C51B—O6B	116.0 (8)
H7D—C7B—H7E	109.5	C53B—C51B—C50B	120.7 (8)
O2—C7B—H7F	109.5	O6B—C51B—C50B	123.2 (8)
H7D—C7B—H7F	109.5	C54B—C53B—C51B	120.1 (9)
H7E—C7B—H7F	109.5	C54B—C53B—H53B	120.0
C6—C8—C9	120.3 (4)	C51B—C53B—H53B	120.0
C6—C8—H8	119.9	C53B—C54B—C48B	121.3 (9)
C9—C8—H8	119.9	C53B—C54B—H54B	119.4
C3—C9—C8	123.1 (3)	C48B—C54B—H54B	119.4
C3—C9—H9	118.5	C47B—C46B—C38	110.5 (10)
C8—C9—H9	118.5	C47B—C46B—H46B	124.7
C2—C10—C11	109.1 (3)	C38—C46B—H46B	124.7

C2—C10—H10	125.5	C46B—C47B—N4	104.6 (10)
C11—C10—H10	125.5	C46B—C47B—C48B	125.3 (11)
N1—C11—C10	110.3 (3)	N4—C47B—C48B	128.2 (9)
N1—C11—C12A	122.0 (3)	O6B—C52B—H52D	109.5
C10—C11—C12A	127.1 (3)	O6B—C52B—H52E	109.5
N1—C11—C12B	124.8 (4)	H52D—C52B—H52E	109.5
C10—C11—C12B	118.2 (5)	O6B—C52B—H52F	109.5
C15A—O1A—C16A	114.6 (6)	H52D—C52B—H52F	109.5
C13A—C12A—C18A	118.8 (6)	H52E—C52B—H52F	109.5
C13A—C12A—C11	118.6 (6)	N5—C55—N6	127.0 (3)
C18A—C12A—C11	122.3 (4)	N5—C55—C56	123.3 (3)
C14A—C13A—C12A	120.2 (8)	N6—C55—C56	109.5 (3)
C14A—C13A—H13A	119.9	C64—C56—C55	105.6 (3)
C12A—C13A—H13A	119.9	C64—C56—C57	127.9 (3)
C13A—C14A—C15A	120.7 (8)	C55—C56—C57	126.3 (3)
C13A—C14A—H14A	119.6	C63—C57—C58	115.7 (3)
C15A—C14A—H14A	119.6	C63—C57—C56	120.8 (3)
O1A—C15A—C17A	115.6 (4)	C58—C57—C56	123.5 (3)
O1A—C15A—C14A	125.3 (6)	C59—C58—C57	121.9 (3)
C17A—C15A—C14A	119.1 (6)	C59—C58—H58	119.0
C18A—C17A—C15A	120.5 (4)	C57—C58—H58	119.0
C18A—C17A—H17A	119.8	C60—C59—C58	120.8 (4)
C15A—C17A—H17A	119.8	C60—C59—H59	119.6
C17A—C18A—C12A	120.6 (5)	C58—C59—H59	119.6
C17A—C18A—H18A	119.7	C59—C60—C62	118.5 (4)
C12A—C18A—H18A	119.7	C59—C60—O7	116.0 (4)
C15B—O1B—C16B	123.2 (14)	C62—C60—O7	125.5 (3)

C18b—C12B—C13B	115.0 (13)	O7—C61—H61A	109.5
C18b—C12B—C11	117.6 (7)	O7—C61—H61B	109.5
C13B—C12B—C11	123.1 (12)	H61A—C61—H61B	109.5
C14B—C13B—C12B	125 (2)	O7—C61—H61C	109.5
C14B—C13B—H13B	117.6	H61A—C61—H61C	109.5
C12B—C13B—H13B	117.6	H61B—C61—H61C	109.5
C15B—C14B—C13B	116.9 (17)	C60—C62—C63	120.2 (3)
C15B—C14B—H14B	121.5	C60—C62—H62	119.9
C13B—C14B—H14B	121.5	C63—C62—H62	119.9
C18b—C17b—C15B	120.4 (8)	C57—C63—C62	122.8 (4)
C18b—C17b—H18B	119.8	C57—C63—H63	118.6
C15B—C17b—H18B	119.8	C62—C63—H63	118.6
C17b—C18b—C12B	121.4 (8)	C56—C64—C65	107.9 (3)
C17b—C18b—H17B	119.3	C56—C64—H64	126.0
C12B—C18b—H17B	119.3	C65—C64—H64	126.0
C14B—C15B—O1B	123.6 (11)	N6—C65—C64	110.8 (3)
C14B—C15B—C17b	121.5 (10)	N6—C65—C66	122.0 (3)
O1B—C15B—C17b	114.8 (8)	C64—C65—C66	127.0 (3)
O1B—C16B—H16D	109.5	C72B—C66—C67	105.5 (8)
O1B—C16B—H16E	109.5	C72B—C66—C65	131.6 (7)
H16D—C16B—H16E	109.5	C67—C66—C65	121.2 (3)
O1B—C16B—H16F	109.5	C67—C66—C72A	122.8 (4)
H16D—C16B—H16F	109.5	C65—C66—C72A	115.2 (4)
H16E—C16B—H16F	109.5	C68—C67—C66	120.1 (4)
N2—C19—N3	127.6 (3)	C68—C67—H67	119.9
N2—C19—C20	122.8 (3)	C66—C67—H67	119.9
N3—C19—C20	109.5 (3)	C69B—C68—C67	129.6 (8)

C28—C20—C19	105.4 (3)	C67—C68—C69A	115.7 (5)
C28—C20—C21	127.9 (3)	C69B—C68—H68	104.7
C19—C20—C21	126.6 (3)	C67—C68—H68	122.1
C27—C21—C22A	111.6 (4)	C69A—C68—H68	122.1
C27—C21—C22B	125.6 (6)	C70A—O8A—C69A	120.3 (5)
C27—C21—C20	122.0 (3)	C71A—C69A—O8A	121.3 (7)
C22A—C21—C20	126.1 (4)	C71A—C69A—C68	123.5 (7)
C22B—C21—C20	108.3 (5)	O8A—C69A—C68	115.1 (6)
C24A—O3A—C25A	116.3 (5)	C69A—C71A—C72A	120.5 (8)
C23A—C22A—C21	126.6 (6)	C69A—C71A—H71A	119.7
C23A—C22A—H22A	116.7	C72A—C71A—H71A	119.7
C21—C22A—H22A	116.7	C71A—C72A—C66	116.6 (6)
C24A—C23A—C22A	119.9 (7)	C71A—C72A—H72A	121.7
C24A—C23A—H23A	120.0	C66—C72A—H72A	121.7
C22A—C23A—H23A	120.0	C69B—O8B—C70B	108.4 (12)
O3A—C24A—C23A	124.6 (6)	C68—C69B—C71B	111.3 (9)
O3A—C24A—C26	120.6 (5)	C68—C69B—O8B	112.3 (12)
C23A—C24A—C26	114.3 (6)	C71B—C69B—O8B	136.1 (12)
C24B—O3B—C25B	118.2 (7)	O8B—C70B—H70D	109.5
C23B—C22B—C21	110.0 (9)	O8B—C70B—H70E	109.5
C23B—C22B—H22B	125.0	H70D—C70B—H70E	109.5
C21—C22B—H22B	125.0	O8B—C70B—H70F	109.5
C22B—C23B—C24B	122.7 (12)	H70D—C70B—H70F	109.5
C22B—C23B—H23B	118.6	H70E—C70B—H70F	109.5
C24B—C23B—H23B	118.6	C72B—C71B—C69B	118.0 (11)
O3B—C24B—C23B	117.8 (9)	C72B—C71B—H71B	121.0
O3B—C24B—C26	115.0 (8)	C69B—C71B—H71B	121.0

C23B—C24B—C26	125.3 (9)	C66—C72B—C71B	132.9 (12)
O3B—C25B—H25D	109.5	C66—C72B—H72B	113.5
O3B—C25B—H25E	109.5	C71B—C72B—H72B	113.5

Table AII.4 – Détails de l'étude de diffraction des rayons X pour le composé **2** (chapitre 2).

		2 [a]
CCDC Number		796139
Formula		C_{19} H_{13} N_3 O_4 S Br Re
M_w (g/mol); F(000)		645.49; 612
Crystal color and form		Dark Orange block
Crystal size (mm)		0.28 x 0.27 x 0.21
T (K); wavelength		150; 0.71073
Crystal System		triclinic
Space Group		P-1
Unit Cell:	a (Å)	9.074(2)
	b (Å)	11.115(3)
	c (Å)	11.68(3)
	α (°)	74.904(4)
	β (°)	73.291(4)
	γ (°)	67.379(3)
V (Å^3); Z; $d_{calcd.}$ (g/cm^3)		1026.4(5); 2; 2.089
θ range (°); completeness		1.85-29.13; 0.999
Collected reflections; R_σ		50051; 0.0157
Unique reflections; R_{int}		5517; 0.0384
Restraints; Parameters		0; 264

μ (mm^{-1}); Abs. Corr.	7.998; multi-scan
R1(F); $wR(F^2)$ [$I > 4\sigma(I)$]	0.0231; 0.0616
R1(F); $wR(F^2)$ (all data)	0.0244; 0.0621
$GoF(F^2)$	1.056
Residual electron density (max; min) $e^-/Å^3$	1.47; -1.55
Flack parameter	n.a.

[a] Bruker/AXS Smart 6000 (4K) diffractometer (Mirror Montel 200-monochromated Cu Kα radiation, FR591 Rotating Anode).

Figure AII.3 – Représentation Ortep au niveau de probabilité 50% avec numérotation complète du composé **2**.

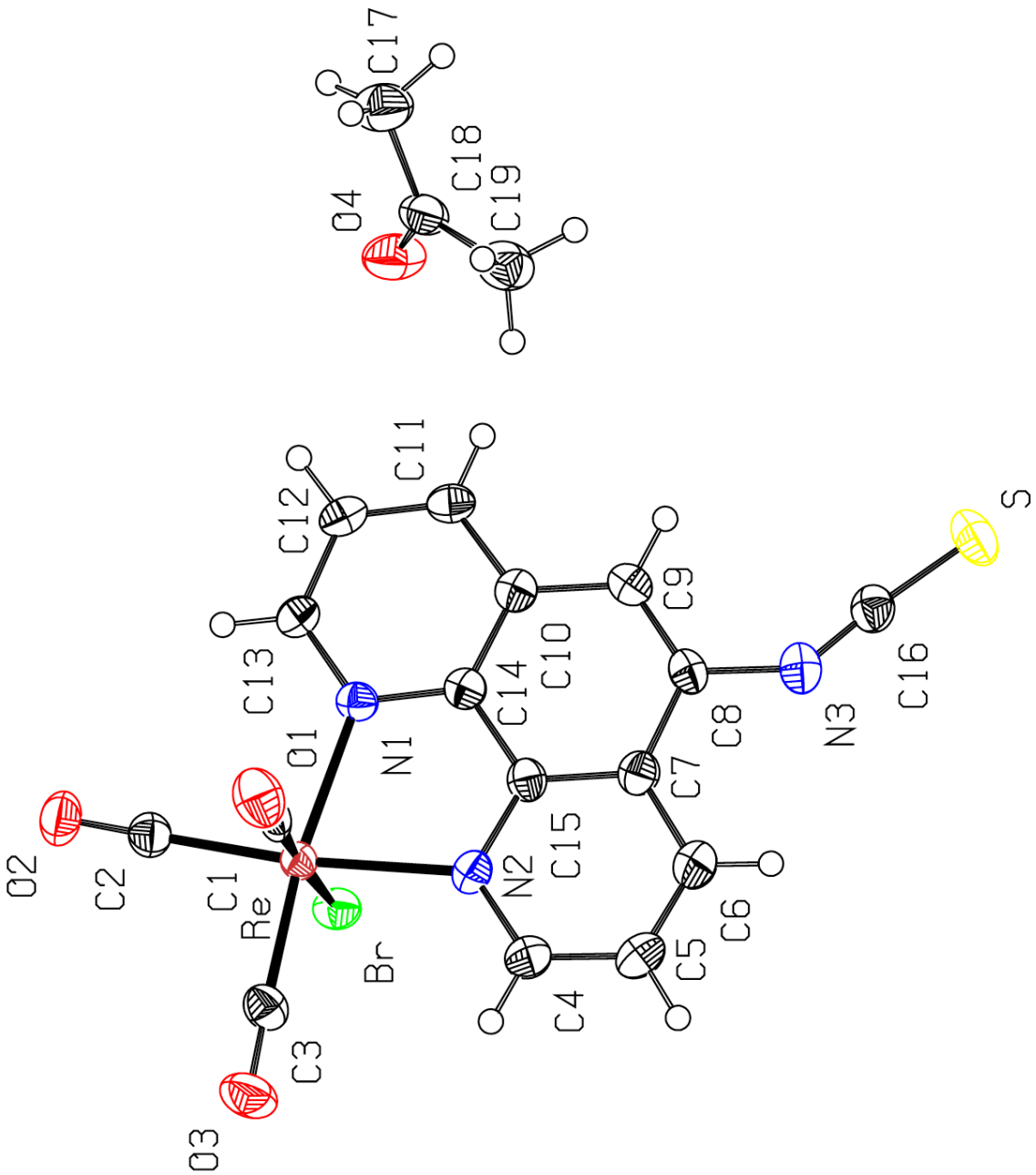

Table AII.5 – Liste des longueurs de liens et des angles pour le composé **2**.

Re-C(2)	1.919(3)
Re-C(3)	1.921(4)
Re-C(1)	1.984(4)
Re-N(1)	2.179(3)
Re-N(2)	2.181(3)
Re-Br	2.6167(7)
S-C(16)	1.565(4)
O(1)-C(1)	1.034(5)
O(2)-C(2)	1.147(4)
O(3)-C(3)	1.149(4)
N(1)-C(13)	1.341(4)
N(1)-C(14)	1.361(4)
N(2)-C(4)	1.331(4)
N(2)-C(15)	1.371(4)
N(3)-C(16)	1.186(5)
N(3)-C(8)	1.407(4)
C(4)-C(5)	1.407(5)
C(5)-C(6)	1.358(6)
C(6)-C(7)	1.401(5)
C(7)-C(15)	1.402(4)
C(7)-C(8)	1.442(5)
C(8)-C(9)	1.347(5)
C(9)-C(10)	1.428(4)
C(10)-C(14)	1.406(4)
C(10)-C(11)	1.407(4)
C(11)-C(12)	1.356(5)
C(12)-C(13)	1.403(5)
C(14)-C(15)	1.426(4)
O(4)-C(18)	1.212(5)
C(17)-C(18)	1.496(6)
C(18)-C(19)	1.495(5)

C(2)-RE-C(3)	89.56(15)
C(2)-RE-C(1)	88.90(14)
C(3)-RE-C(1)	90.72(14)
C(2)-RE-N(1)	97.37(13)
C(3)-RE-N(1)	172.64(12)
C(1)-RE-N(1)	91.88(12)
C(2)-RE-N(2)	172.71(12)
C(3)-RE-N(2)	97.29(13)
C(1)-RE-N(2)	93.47(12)
N(1)-RE-N(2)	75.68(10)
C(2)-RE-BR	92.44(10)
C(3)-RE-BR	91.71(11)
C(1)-RE-BR	177.22(9)
N(1)-RE-BR	85.54(7)
N(2)-RE-BR	84.90(8)
C(13)-N(1)-C(14)	117.9(3)
C(13)-N(1)-RE	126.9(2)
C(14)-N(1)-RE	115.2(2)
C(4)-N(2)-C(15)	118.1(3)
C(4)-N(2)-RE	127.2(2)
C(15)-N(2)-RE	114.7(2)
C(16)-N(3)-C(8)	140.3(3)
O(1)-C(1)-RE	177.3(3)
O(2)-C(2)-RE	178.9(3)
O(3)-C(3)-RE	178.4(4)
N(2)-C(4)-C(5)	122.2(3)
C(6)-C(5)-C(4)	119.8(3)
C(5)-C(6)-C(7)	119.7(3)
C(6)-C(7)-C(15)	117.7(3)
C(6)-C(7)-C(8)	124.5(3)
C(15)-C(7)-C(8)	117.8(3)
C(9)-C(8)-N(3)	121.6(3)
C(9)-C(8)-C(7)	122.1(3)
N(3)-C(8)-C(7)	116.3(3)
C(8)-C(9)-C(10)	120.7(3)
C(14)-C(10)-C(11)	117.7(3)
C(14)-C(10)-C(9)	118.9(3)
C(11)-C(10)-C(9)	123.4(3)
C(12)-C(11)-C(10)	119.7(3)
C(11)-C(12)-C(13)	119.6(3)
N(1)-C(13)-C(12)	122.5(3)
N(1)-C(14)-C(10)	122.6(3)
N(1)-C(14)-C(15)	117.2(3)
C(10)-C(14)-C(15)	120.3(3)
N(2)-C(15)-C(7)	122.5(3)
N(2)-C(15)-C(14)	117.2(3)
C(7)-C(15)-C(14)	120.3(3)
N(3)-C(16)-S	175.2(3)
O(4)-C(18)-C(19)	121.8(4)
O(4)-C(18)-C(17)	121.8(4)
C(19)-C(18)-C(17)	116.4(4)